Université de Montréal

Searching for dark matter with superheated liquid detectors

par
Arthur Plante

Département de Physique
Faculté des arts et des sciences

Thèse présentée à la Faculté des études supérieures
en vue de l'obtention du grade de Philosophiæ Doctor (Ph.D.)
en physique

Mars, 2019

© Arthur Plante, 2019.

Université de Montréal
Faculté des études supérieures

Cette thèse intitulée:

Searching for dark matter with superheated liquid detectors

présentée par:

Arthur Plante

a été évaluée par un jury composé des personnes suivantes:

François Schiettekatte ,	président-rapporteur
Viktor Zacek,	directeur de recherche
Thomas Brunner ,	membre du jury

Thèse acceptée le: X May 2019

RÉSUMÉ

De nos jours, l'une des questions fondamentales en physique des particules est la nature de la matière sombre. Les expériences PICASSO et PICO sont deux expériences de détection directe de matière sombre qui sont situées à SNOLAB qui utilisent des chambres à bulles remplies de fréons surchauffés. La collaboration PICASSO a mis sur pied la première expérience à utiliser des chambres à bulles dans le but spécifique de détecter la matière sombre et à de plus découvert l'existence de la discrimination acoustique entre les neutrons et les particules alpha. Le dernier résultat de l'expérience PICASSO a été publié en 2017 et possède, jusqu'à ce jour, la meilleure limite sur la section efficace d'interaction entre la matière sombre et la matière baryonique qui dépend du spin pour des masses de WIMPs inférieure à 5 GeV/c^2 avec une limite de $\sigma_p^{SD} = 7 \times 10^{-2}$ pb (90% C.L). Depuis la fusion des collaborations PICASSO et PICO, l'expérience PICO détient la meilleure limite au monde pour toute autre masse de WIMP et dont la meilleure limite correspond à $\sigma_p^{SD} = 2.5 \times 10^{-5}$ pb (90% C.L) pour des WIMP de 25 GeV/c^2. Actuellement, la collaboration PICO est en train de construire le détecteur PICO40L dont le bruit de fond dû aux neutrons sera radicalement diminué par un facteur $\sim$50 et qui sert de prototype pour le design et la construction du prochain détecteur, PICO500, qui contiendra environ 500L de fréon.

Cette thèse présentera tout d'abord les aspects théoriques de la matière sombre, c'est-à-dire les preuves de son existence (Chap. 2), les particules candidates les plus probables (Chap. 3), ainsi que les spectres des énergies de reculs et le taux de comptage attendu dans un détecteur de matière sombre (Chap. 4). Ces chapitres seront suivis de la présentation de la technique de détection de matière sombre avec des chambres à bulles contenant des liquides en surchauffe (Chap. 5) en plus des descriptions des détecteurs PICASSO et PICO (Chap. 6 & 7) ainsi que de l'étalonnage de ces détecteurs (Chap. 8) et de leurs résultats (Chap. 9 & 10). Par la suite, les résultats des simulations du bruit de fond de PICO40L dû aux neutrons seront présentés (Chap. 11) de même que la présentation du rôle de l'expérience PICO dans le contexte de la théorie effective (Effective Field

Theory) de la matière sombre (Chap. 12). Finalement, la recherche et le développement actuel et futur de l'expérience PICO, par exemple, la description de PICO500 ainsi que la possibilité d'utiliser du $C_2H_2F_4$ comme liquide actif seront présentés dans le dernier chapitre (Chap. 13).

Mots clés: Matière sombre, détecteurs à liquide surchauffées, simulation, PICO, PICASSO, WIMPs.

ABSTRACT

One of the most prominent questions in the fields of particle physics and cosmology is the nature of dark matter which comprises 85% of the total mass of the universe. The PICASSO and PICO experiments are both direct detection experiments situated at SNOLAB that use the superheated liquid or bubble chamber technique to search for dark matter. The PICASSO collaboration pioneered the use of this technique for dark matter searches, and moreover, discovered an important background suppression feature: the acoustic alpha-neutron discrimination. The last PICASSO result was published in 2017 and still holds to this day the best spin-dependent cross-section limit of 7×10^{-2} pb (90% C.L.) for weakly interacting dark matter candidates (WIMPs) with a mass of 4 GeV/c^2 [1]. Since the merger of PICASSO and COUPP into PICO, PICO holds the world best limit on WIMP cross sections with the most stringent spin-dependent limit of 2.5×10^{-5} pb (90% C.L) at 25 GeV/c^2 set by the recent PICO60 detector result [2]. The PICO collaboration is currently building a new detector called PICO40L with a significantly improved design which will allow to substantially decrease the neutron background by a factor of $\sim$50, and pave the way forward for the next stage, PICO500, which will contain approximately 500L of superheated liquid.

The present work presents first the observational and theoretical framework of dark matter searches, i.e., its proof of existence (Chap. 2), the most probable particle candidates (Chap. 3), as well as its expected recoil spectra and count rates in typical dark matter detectors (Chap. 4). It will be followed by a description of the superheated liquid technique (Chap. 5), by the description of the PICASSO and PICO detectors (Chap. 6 & 7), of their calibrations and common backgrounds (Chap. 8). In Chap. 9 & 10, the final PICASSO result are presented together with the most recent PICO dark matter limits. A GEANT4 simulation of the PICO40L neutron background will then be described in detail (Chap. 11), along with a discussion of the physic reach of PICO within the context of the effective field theory description of dark matter (Chap. 12). Finally, this thesis concludes with the current and future research and development program of the PICO

collaboration, such as the future PICO500 detector, and the exciting possibility of using $C_2H_2F_4$ as an active target (Chap. 13).

Key words: Dark matter, PICO, PICASSO, WIMPs, GEANT4, SNOLAB.

CONTENTS

LIST OF TABLES

LIST OF FIGURES

LIST OF APPENDICES

LIST OF ABBREVIATIONS

WIMP	Weakly Interacting Massive Particle
MSSM	Minimal SuperSymmetric Model
CDM	Cold Dark Matter
SDp	Spin-Dependent proton
SDn	Spin-Dependent neutron
SI	Spin-Independent
MACHO	Massive Astronomical Compact Halo Objects
LNGS	Laboratori Nazionali del Gran Sasso
PV	Pressure Vessel
IV	Inner Vessel
OV	Outer Vessel
LHC	Large Hadron Collider
MCMC	Markov Chain Monte Carlo
EFT	Effective Field Theory
AP	Acoustic Power
CMB	Cosmic Microwave Background

REMERCIEMENTS

J'aimerais tout d'abord remercier mon directeur de recherche Viktor Zacek de m'avoir donné l'opportunité d'avoir un si grand rôle durant la dernière analyse du projet PICASSO. Son encadrement, ses conseils, ses idées et son optimisme ont été source de motivation tout au long de ma thèse. J'adresse également mes remerciements aux membres du jury d'avoir pris le temps de lire cette thèse.

Je voudrais aussi remercier particulièrement mon collègue et ami Wen Chao Chen de m'avoir grandement aidé à l'élaboration et aux vérifications des simulations GEANT4. Je veux aussi remercier Alan Robinson pour son aide et les nombreuses discussions concernant le bruit de fond des détecteurs PICO. Merci aussi à Mathieu de m'avoir aidé à apprendre les rudiments de la physique expérimentale et d'avoir été un collègue et un ami tout au long de mes études supérieures. Je souhaite également souligner l'incroyable contribution de Simon qui fut un formidable relecteur/correcteur. Merci à tous les membres présents et passés de la collaboration PICASSO et PICO pour leur contribution aux deux expériences. Merci à tous les étudiants PICASSO et PICO que j'ai côtoyés. Merci à mes collègues et amis du Bunker, Olivia, Fabrice, Merlin, Matthieu, Frédéric D., Frédérick T., Frédéric G., Simon et François pour les nombreuses discussions sérieuses et moins sérieuses.

Je veux également dire merci à ma famille et mes amis pour leur soutien qui m'a été indispensable tout au long de ma thèse. Je tiens à exprimer ma profonde gratitude à mes parents et ma conjointe Sabrina Morel pour m'avoir encouragé de façon inconditionnelle.

PERSONAL CONTRIBUTIONS

My contributions to the PICASSO and PICO experiments cover various aspects of both project. For the most part, my work involved performing data analysis as well as Monte Carlo simulations, while also being in charge of several data taking campaigns with the PICO 0.1 calibration chamber.

One of these calibrations consisted of measuring the detector response to 22 keV neutrons with a SbBe source at a 2 keV threshold, which is currently the lowest energy threshold neutron calibration measurement. This measurement is presented in Sect. 8.5.2 of Chap. 8 and is crucial for the determination the WIMP detection efficiency of C_3F_8 at low energy thresholds.

The central part of my work consisted of the analysis of data recorded by PICASSO between March 2012 and January 2014. I was in charge of establishing the WIMP-nucleon cross section limits as well as the fiducial volumes of each of the 32 detectors which required to set novel and strict criteria used to define the fiducial cuts. These fiducials cuts introduced new systematic uncertainties that I had to quantify such as the effect of the position of the source during the neutron calibration.

The second part of my Ph.D. is the interpretation of the role of fluorine in dark matter searches within the context of the Effective Field Theory of dark matter (EFT). My work consisted in understanding the various theoretical models and to write programming codes to compute relevant quantities in order to extract useful information from the models.

One crucial information when searching for WIMPs is the expected background in the detector in particular to neutrons, α, and gamma. My contribution to the future analysis of the PICO40L detector was to predict the neutron background due to the contamination of ^{235}U, ^{238}U, and ^{232}Th inside the components of the detector. I performed

simulations of the neutron spectrum produced by each relevant PICO40L components in order to predict the number of single and multiple events per year. Furthermore, I developed a new semi-automatic approach that reduced the time required to include geometrical structures in GEANT4 and greatly decreased the probability of introducing human errors.

CHAPTER 1

INTRODUCTION

Dark matter is an unknown type of matter composed of particles beyond the Standard Model of particle physics. Its presence in the universe is currently known only via its gravitational influence on stars, galaxies, large scale structures of the Universe and on the Cosmic Microwave Background (CMB). Based on the analysis of these observations, the so-called Lambda Cold Dark Matter model or Corcondance Model predicts that 4.9% of the universe consists of ordinary matter, 26.84% of dark matter and 68.47% of dark energy [3]. Dark matter was postulated for the first time in 1933 by F. Zwicky [4] to explain the orbital velocity of galaxies in clusters of galaxies. Since then, several theories beyond the Standard Model of elementary particles have emerged and propose different suitable candidates that respect the various observations. These candidate particles are grouped under the generic name of Weakly Interacting Massive Particles (WIMP) [5]. In particular, one of the emerging models, the Minimal Supersymmetric Standard Model (MSSM), proposes a particle, the neutralino, χ, which is stable, massive, electrically neutral and interacts with matter with a strength of the order of the electroweak interaction [6].

The goal of the PICASSO [1]and PICO experiments [2] is to detect dark matter by employing the superheated liquid (SHL) technique, similar to that used in classic bubble chambers. In PICASSO detectors, the SHL is dispersed in the form of microscopic droplets of C_4F_{10}, while PICO detectors are filled with a bulk fluid of C_3F_8. The WIMP-freon interaction consists of an elastic collision between a WIMP and a ^{19}F or ^{12}C nucleus, which deposits small amounts of energy in the keV range. These recoil nuclei will then produce phase transitions in the SHL, which is accompanied by an acoustic emission that is captured by piezoelectric sensors. The energy required to induce a phase transition depends on the energy threshold of the SHL which is controled by setting the temperature and operating pressure of the detector, and thus PICASSO and PICO detec-

tors are energy threshold detectors that can reach sensitivities as low as a few keVs. The challenge in detecting dark matter lies in the weak strength of the interactions between WIMPs and matter resulting in an expected count rate at a level of 10 events/tonne/year or even smaller. It is therefore vital to build detectors with large active mass to increase the probability of interactions, and to provide the experimental setup with adequate radiation shielding against cosmic rays, neutrons, and gammas in order to isolate rare WIMP events.

In this thesis, the observations that proved the existence of dark matter and the description of the several candidate particles in agreement with those observations such as the neutralino will all be described in Chap. 2& 3. There are three possible avenues to detect dark matter, it can be detected indirectly by measuring the decay products of annihilating dark matter in the sun or the center of galaxies, it can be produced at accelerator facilities, and lastly, it can be directly detected through WIMP-nucleon interactions in detectors installed in underground laboratories (Chap. 4). All three possibilities will be presented, but since PICASSO and PICO are direct detection experiments using SHL detectors, special emphasis will be put on this technique (Chap. 5 , 6& 7). Another difficulty for dark matter searches is the presence of backgrounds due to Standard Model particles, and thus the extensive calibration measurements performed with neutrons, alpha particles and gammas will be detailed in Chap. 8.

In 2017, PICASSO published its final WIMP search result and hence a complete chapter is dedicated to the description of the analysis that was performed (Chap. 9). PICO recently published its latest dark matter search with PICO60 (Chap. 10) and the collaboration is currently installing its latest detector, PICO40L. GEANT4 simulations which aim to predict the expected neutron background of PICO40L are described in Chap. 11. Furthermore, the WIMP-nucleon interactions in the context of an Effective Field Theory approach are discussed with an emphasis on the special role of fluorinated targets in the discovery of dark matter (Chap. 12). To conclude this thesis, the current and future activities of the PICO collaboration such as the upcoming PICO500 detector,

the possibility of detecting supernova neutrinos, as well as the possibility to use $C_2H_2F_4$ to increase the WIMP sensitivity to lower mass WIMPs are presented in Chap. 13.

CHAPTER 2

DARK MATTER IN THE UNIVERSE

Nowadays, the existence of dark matter is well established, and the most widely accepted explanation regarding its nature is that it is composed of WIMPs (Weakly Interacting Massive Particle) [5]. Currently, the detection of dark matter and the understanding of the interaction between baryonic matter and dark matter are among the most active research areas in particle physics. First, in this chapter, the basics of the cosmological standard model (Lambda-Cold Dark Matter model) will be presented. This model is crucial to the development of any dark matter searches as it proves, beyond any doubt, the existence of dark matter. Then, various measurements highlighting its presence in the Universe will be presented as well as the various possible candidates. A discussion of the MSSM (Minimal SuperSymmetric Model) will follow which offers one possible explanation regarding the nature of dark matter and its interaction with baryonic matter [6].

2.1 Lambda Cold Dark Matter model

The Lambda-CDM model (Cold Dark Matter) is a cosmological model that describes the Universe and is in agreement with the current observations. It starts from the cosmological principle which states that the Universe is homogeneous, i.e., its appearance is the same independently of the position of the observer in the Universe, and is isotropic, i.e., its appearance is independent of the direction of observation. In this model, the equation describing the evolution of the Universe is the Friedmann's equation which is given by the following expression:

$$(\dot{a}/a)^2 = k/a^2 + (8\pi G/3)\rho_{tot}, \tag{2.1}$$

where $a(t)$ is the scale factor, G is the gravitational constant and ρ_{tot} is the density of mass-energy in the Universe, which is the sum of all contributing components of the

Universe:

$$\rho_{tot} = \rho_M + \rho_{rad} + \rho_\Lambda, \tag{2.2}$$

where ρ_M is the total density of matter including baryonic and non-baryonic matter, ρ_{rad} is the density of the radiation and ρ_Λ is the dark energy density. The dark energy density is a parameter whose addition to the Friedmann equation is allowed by General relativity.

The parameter k describes the curvature of space-time and can take values of +1, 0 or -1 depending on the geometry of the Universe. The first term of eq. 2.1 is the Hubble parameter that represents the expansion rate of the Universe, or, in other words, the rate at which the astronomical objects present in the Universe are moving away from each other. At the present cosmological time, the Hubble parameter becomes Hubble's constant and is equal to

$$H_0 = h \cdot 100\,\mathrm{kms}^{-1}\mathrm{Mpc}^{-1}, \tag{2.3}$$

where $h = 0.6766 \pm 0.0042$ [3] is a renormalization parameter of the expansion rate. This renormalization is introduced to relegate the uncertainties of the experimental value to a constant and then the usual values are expressed according to h. A priori, the parameter k that describes the curvature of the Universe is unknown, however, in the case where k = 0, which means that the Universe is flat, the Friedmann equation makes it possible to obtain the critical density of the Universe, ρ_c, which is equal to [3]:

$$\rho_c = \frac{3H_0^2}{8\pi G} = 1.05368(11)10^5 h^2 GeVc^{-2}cm^{-3}, \tag{2.4}$$

By using ρ_c, the relative densities of the components of the Universe are defined by Ω_i:

$$\Omega_i = \rho_i/\rho_c \tag{2.5}$$

Finally, Ω_{tot} is expressed with the Friedmann equation as:

$$\Omega_{tot} - 1 = \frac{k}{H^2 a^2}. \tag{2.6}$$

In this way, the experimental measurements of Ω_{tot} are directly connected to the curvature parameter k. As an example, if the total density (ρ_{tot}) is larger than the critical density, one obtains an open Universe. Other possible cases are shown in Table 2.I.

k = 1	closed	$\rho_{tot} < \rho_c$	$\Omega_{tot} < 1$
k = 0	flat	$\rho_{tot} = \rho_c$	$\Omega_{tot} = 1$
k = -1	open	$\rho_{tot} > \rho_c$	$\Omega_{tot} > 1$

Table 2.I – Possible geometries of the Universe according to the curvature parameter of the space k and the values of ρ_{tot} and Ω_{tot} consequently obtained.

2.2 Observational evidences of dark matter

By studying astronomical objects, various inconsistencies between the astronomical models and observations were noted and attributed to the presence of dark matter. These inconsistencies arise from the general properties of dark matter: it is non-radiative and it interacts gravitationally with baryonic matter. In the following sections, the results of astronomical and cosmological measurements proving the existence of the dark matter are presented.

2.2.1 Distribution of galaxy velocities in clusters

The dark matter problem was formed in 1933 following observations of the Coma cluster made by the astronomer Fritz Zwicky [4]. By measuring the speed of galaxies at the periphery of the cluster by Doppler shift and using the Viriel theorem, he estimated its mass. This mass was compared to the visible mass obtained by considering the total number of galaxies contained in the cluster and their respective brightness. He found that the visible mass was 400 times smaller than the mass estimated by the Viriel theorem [7]. This so-called invisible mass required to explain the speed of galaxies far from the

center of the cluster was named "dark matter" by Zwicky.

2.2.2 Rotations curves of spiral galaxies

It was only in the 1970s that a second observation supported the dark matter hypothesis proposed by Fritz Zwicky. Vera Rubin measured the speed of hydrogen clouds and stars in the Andromeda galaxy at the periphery and outside the bright region of the galaxy by Doppler shift. She then compared the result with Newtonian dynamics which states that the speed of the stars decreases as a function of their distance from the center of the galaxy if the mass of the galaxy is concentrated in its center. The analysis of the results showed that the speed of the hydrogen clouds remained almost constant as a function of the distance from the center as shown in Fig. 2.1 [8].

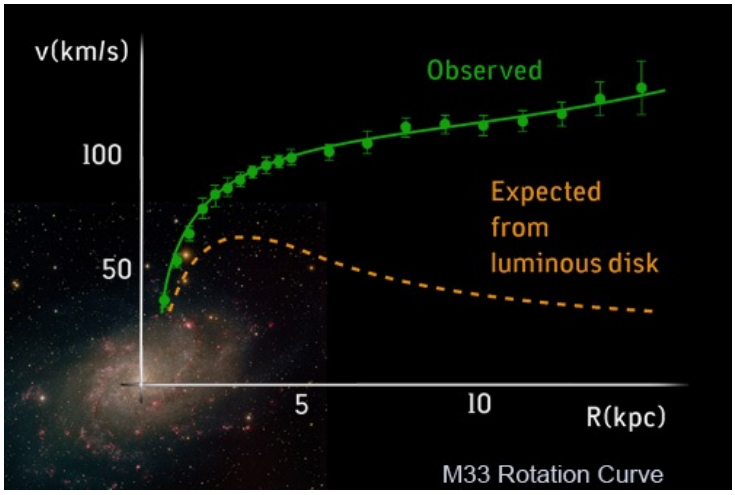

Figure 2.1 – Observed rotation speed of the M33 galaxy according to the distance from its center compared to that predicted by the theory [8].

To remedy this inconsistency with the Newtonian theory, Vera Rubin concluded that the galaxy had to contain dark matter in increasing quantity when moving away from the center. The rotational speed of an object in a stable orbit of radius r inside the luminous disk of a galaxy decreases as $v \propto \sqrt{M(r)/r}$ where $M(r)$ is the mass inside the orbit. In the case where the orbit is located outside of the luminous disk, the velocity goes as $v \propto \sqrt{(1/r)}$ if all the matter is contained inside of the bright disk. In most galaxies,

on the other hand, the measured velocity remains fairly constant, even out to regions far from the bright center. It implies the existence of a halo of dark matter having a mass density proportional to the inverse of radius squared:

$$\rho_{halo} \propto \frac{1}{r^2}. \tag{2.7}$$

2.2.3 Gravitational lensing

An important prediction of general relativity applied to astronomy is the modification of the trajectory of the radiation emitted by the celestial bodies. This phenomenon called gravitational lensing effect is divided into two categories; strong and weak. The strong gravitational lensing effect occurs when an object is behind a massive star and its light, from the Earth's point of view, is curved and produces several images of the same object [9]. Such a phenomenon happens when a quasar, an extremely luminous active galactic nucleus, and a galaxy are on the same line of sight as shown in Fig. 2.2.

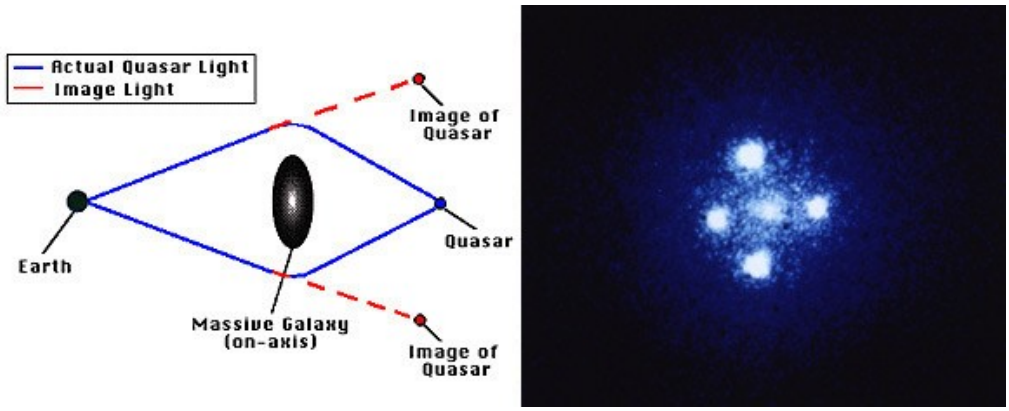

Figure 2.2 – Left: diagram of the gravitational lensing effect generated by a galaxy on the image of a distant quasar. Right: the image of a quasar, taken by the Hubble telescope, modified by the gravitational lens effect [10].

Since ordinary matter and dark matter contribute to the curvature of space-time, by measuring the brightness pattern of the distorted image of the quasar, an estimate of the distribution of total (visible + dark) matter around the galaxy is extracted. Thus, knowing where the baryonic matter is located in the galaxy, it is possible to find the contribution

and distribution of dark matter.

The most famous weak gravitational lens phenomenon was observed during the collision of the Bullet cluster. When the two sub-clusters collided, the stars of the galaxies were very little affected and were only slowed down gravitationally and their mass was reconstructed using their emitted light. On the other hand, the warm gases interacted strongly which heated them up to 10^6 K such that their emitted X-rays allowed to reconstruct the collision region [11]. Finally, dark matter, which moves freely, is detected by the deformation of the form of the objects in the background by the gravitational lens effect. The result of the collision is shown in Fig. 2.3.

Figure 2.3 – Image of the Bullet Cluster following the collision of two sub-cluster. The hot gas is shown in red, and the presence of dark matter highlighted by the gravitational lens effect is shown in blue [11].

Unlike the strong gravitational lens effect where large distortions of images of astronomical objects take place, the weak gravitational lens effect only slightly distorts the images and requires a large number of sources to quantify the mass in the foreground. The light sources will appear larger and flattened, however, galaxies are intrinsically flattened by a factor ranging from 3 to 300 times larger than the flattening caused by the gravitational lens effect depending on the mass in the foreground. It is, therefore,

necessary to have a large number of sources to perform a statistical analysis showing a consistent distortion of the shape of the objects in the background. This analysis was carried out for the Bullet cluster and allowed to reconstruct the location of dark matter in Fig. 2.3. It also determined that the quantity of dark matter must be 49 times larger than the luminous mass observed [11].

2.2.4 Inhomogeneity of the cosmic microwave background

The cosmic microwave background (CMB) is formed of photons released at the age of recombination, 380 000 years after the Big Bang when neutral hydrogen was formed and the Universe became transparent to photons. Today, these photons are present in the form of a characteristic black body spectrum with a temperature of $T_0 = 2.72548 \pm$ 00057 K [12] corresponding to a density that is equal to $\Omega_K = 0.0007 \pm 0.0019$[3]. However, the measurements made to map the sky have revealed inhomogeneities of the order 10^{-5} K which demonstrates that the CMB is not perfectly isotropic as shown in Fig. 2.4 [13].

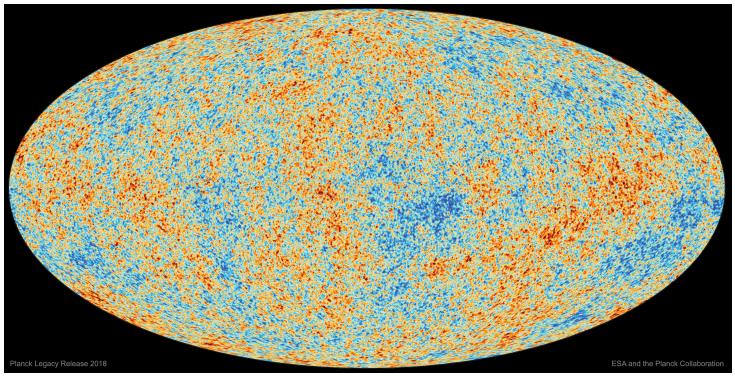

Figure 2.4 – Map of the celestial sphere showing the temperature fluctuations of the CMB radiation whose origin is from the surface of the last scattering. This measurement was taken by the Planck satellite over five years. The differences of color represent temperature variations of the order of 0.0002 Kelvin [13].

Those anisotropies are the result of quantum fluctuations present before the period of inflation and whose effects are still imprinted in the electron-baryon plasma at the time of recombination. In such a plasma, acoustic oscillations occurred which were due to

the compression of the baryon-photon fluid by gravity and the expansion of the fluid by radiation pressure exerted by the photons [14]. There were regions where the density of baryons was relatively higher than in other regions in which deeper gravitational potential wells were formed. On the other hand, there were regions of lower baryon density where the radiation pressure dominated. These potentials created oscillations of the photon temperature which increases when the plasma contracts and decreases in the opposite case. When photons left the plasma, their temperature was frozen, and thus the photons that were in a potential well with a low density of baryons left with a higher average temperature than those who were in a potential well with a high baryon density. Recent experiences, such as Planck [3] and WMAP [15], measured the temperature differences of the cosmic microwave background at different angular scales. These anisotropies can be analyzed by decomposing them into spherical harmonics whose amplitudes give the angular power spectrum C_l^{TT} which contains the essential information on cosmological parameters such as the densities of each component of the Universe. The amplitude C_l^{TT} is obtained with eq. 2.8 [16]:

$$C_l^{TT} = \frac{1}{(2l+1)} \Sigma |a_{lm}|^2, \tag{2.8}$$

where l represents the order of the multipoles and a_{lm} are the amplitude coefficients of each mode. The temperature power spectrum is given by the following expression:

$$\Delta T^2 = \frac{l(l+1)C_l^{TT}}{2\pi}, \tag{2.9}$$

and is shown in Fig. 2.5 [3]. The first peak appears at $l = 200$, and its position depends on the curvature of space. If the curvature was negative, the position of the peak would move towards greater values of l without changing the shape of the peak. Thus, the experimental measurements showed that the curvature of space is flat with $\Omega_{tot} = 1$. Moreover, three additional peaks are distinguishable, and they give information regarding the relative amount of dark and baryonic matter. From the height of the first peak one obtains the baryonic density, while the height of the third acoustic peak allows to

infer the relative density of dark matter in the Universe [3]:

$$\begin{aligned} \Omega_b h^2 &= 0.02237 \pm 0.00015, \\ \Omega_b &= 0.04930 \pm 0.00033, \\ \Omega_{DM} h^2 &= 0.1200 \pm 0.0012, \\ \Omega_{DM} &= 0.2621 \pm 0.0026. \end{aligned}$$

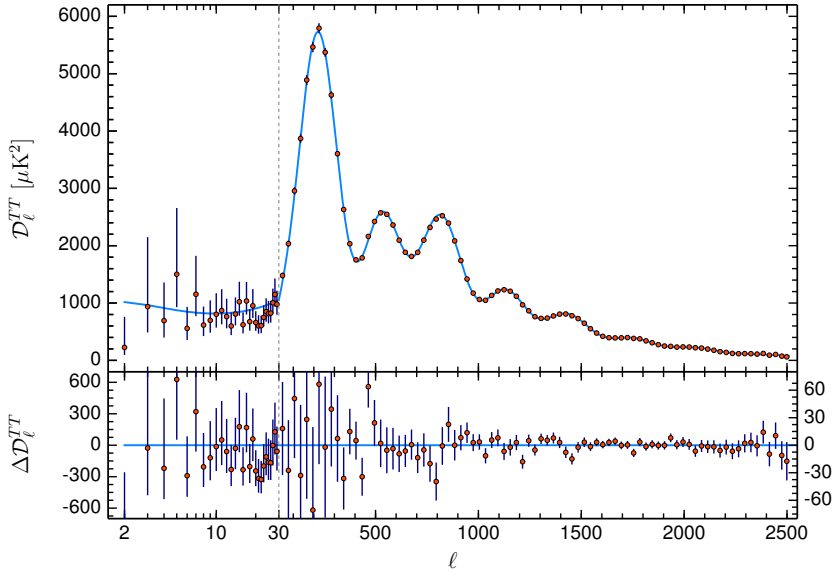

Figure 2.5 – Angular power spectrum of temperature fluctuations measured by the Planck observatory. The blue line represents the best fit to the standard cosmological model compatible with a flat Universe [3].

From these results, the proportion of each component of the Universe is presented in the diagram of Fig. 2.6

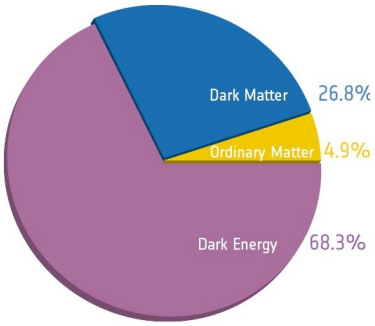

Figure 2.6 – Percentage of each mass-energy contribution present in the Universe measured by the Planck observatory [17].

2.2.5 Primordial nucleosynthesis BBN (Big Bang nucleosynthesis)

The primordial nucleosynthesis is a period in the history of the Universe that took place between 10 seconds and 20 minutes after the Big Bang. It was during this period that the production of light nuclei happened such as deuterium, ^{3}He, ^{7}Li and ^{4}He [16]. This period is very sensitive the ratio of the neutron and proton number densities initially present (ρ_n/ρ_p) and on the neutron lifetime. This ratio depends on the mass difference between the proton and the neutron, Q = 1.293 MeV, as well as the temperature T:

$$\rho_n/\rho_p = e^{-Q/T} \tag{2.10}$$

One second after the Big Bang, the Universe cooled down enough and reached a temperature of $T_{fr} \approx 1$ MeV (freeze-out temperature). At that time, the Hubble expansion became larger than the neutron-proton conversion rate ($\Gamma_{n\leftrightarrow p}$), and thus the ratio ρ_n/ρ_p was fixed to a value of $\sim$ 1/6. Subsequently, since free neutrons are unstable with a half-life of 611.0 ± 1.0 s, it reduced the ratio to $\sim$ 1/7. When the temperature decreased further, several reactions occurred that all depended on the baryon density which is usually normalized to the photon relic density:

$$\eta = \eta_b/\eta_\gamma, \tag{2.11}$$

where η_b/η_γ is the baryon-to-photon ratio. The relative abundances of light nuclei are expressed by defining: $\eta^{10} = 10^{10}\eta$, where η_γ is set by the current CMB measurements. The first reaction to take place is the production of deuterium by the reaction p(n, γ)D. However, photodissociation of deuterium is superior to deuterium production. It is only when the condition

$$\eta^{-1} e^{-\Delta_D/T} > 1 \tag{2.12}$$

is respected that photodissociation of deuterium becomes inferior to the deuterium production. The left-hand term of the last equation represents the baryon to photon ratio that has an energy greater than the photodissociation energy. The term Δ_D represents the binding energy of deuterium, $\Delta_D = 2.23$ MeV. The condition from the previous equation is satisfied when T $\approx$ 0.1 MeV. When this temperature is reached, the proportion of deuterium with an energy greater than the photodissociation energy is larger than the proportion of deuterium with an energy lower than the photodissociation energy, thus the majority of deuterium is stable. Several other reactions take place during this period. A diagram that shows those reactions is presented in Fig. 2.7. Since nuclei with mass numbers of 5 and 8 are not stable, the formation of heavier nuclei is not possible. Furthermore, the Coulomb barrier greatly disadvantages the following reactions: ^{3}He (^{4}He, γ)^{7}Li and ^{3}He(^{4}He, γ)^{7}Be who could, in turn, have created heavier nuclei by other reactions. Since ^{4}He is the most stable nucleus among these light nuclei, all free neutrons will end their lives inside a ^{4}He nucleus. Therefore it can be assumed with a very good approximation that all the free neutrons present during the "Freeze out" will create ^{4}He and any remaining protons will create neutral hydrogen.

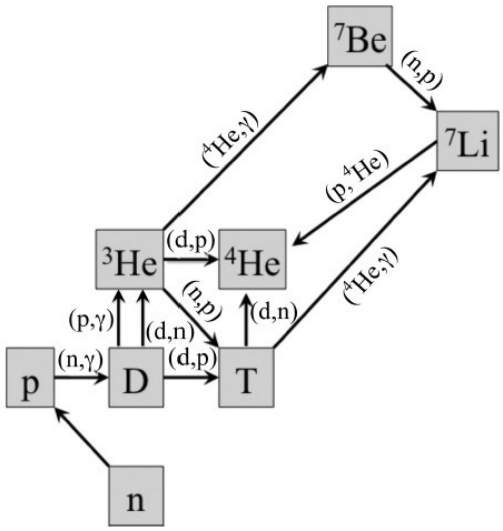

Figure 2.7 – Disintegration scheme and production of light elements present during the nucleosynthesis of the Big Bang [18].

Since each ^{4}He contains two neutrons; $N_{^4He} = N_n/2$, the primordial mass fraction of ^{4}He, $Y_p \equiv \rho(^4\text{He})/\rho_b$ is given by the following equation:

$$Y_p = \frac{2N_n}{N_n + N_p} = \frac{2(\rho_n/\rho_p)}{(1+\rho_n/\rho_p} = 0.245 \pm 0.003. \tag{2.13}$$

However, this value depends very little on the reaction rates, but directly on the value of ρ_n/ρ_p which in turn directly depends on the lifetime of the neutron. When every cross section of every process in Fig. 2.7 are known, one can predict the abundances of ^{4}He, D, ^{3}He and ^{7}Li as a function of the baryon/photon (η) ratio in a similar manner as the result shown in eq. 2.13. All these abundances are presented in Fig. 2.8 [19] [18] as a function of η and agree with one another for $5.8 \leq \eta_{10} \leq 6.6$ (95% C. L.). Using η_γ, which is determined by the CMB measurements, one obtains that $\rho_b = (3.9 - 4.6) \times 10^{-31} g$ cm^{-3} or using the fact that $\Omega_b = \rho_b/\rho_{crit} \approx (\eta^{10} h^{-2})/274$:

$$\Omega_b = (0.021 - 0.024) h^{-2} \tag{2.14}$$

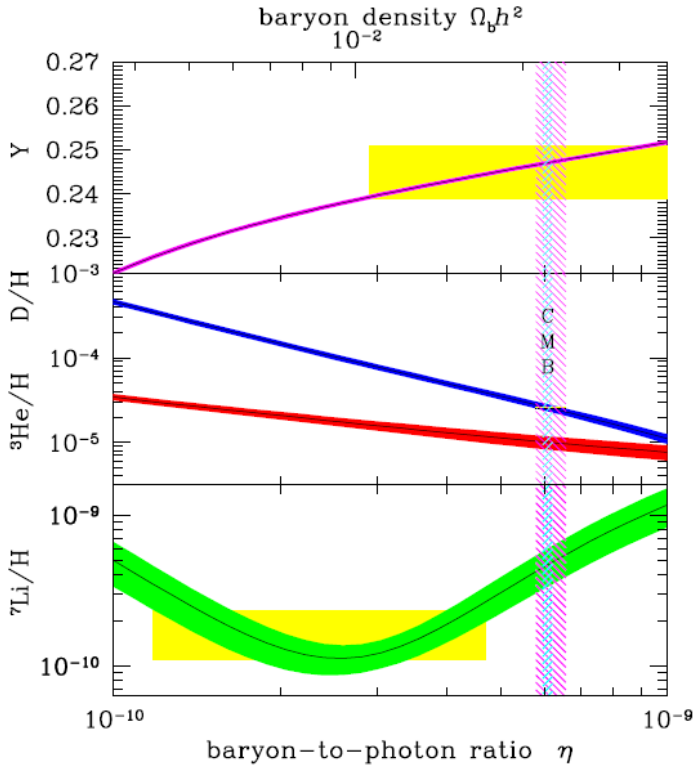

Figure 2.8 – Abundance of ^{4}He, D, ^{3}He and ^{7}Li predicted by the primordial nucleosynthesis model. The yellow boxes represent the observed abundances values of the light elements relative to the number of photons. The blue vertical band indicates the CMB measurements of the baryon density, while the large purple band indicates the BBN concordance range (both at 95% confidence level) [18].

The evaluation of Ω_b inferred by the BBN model is totally independent of the result made via the CMB measurement, and both values are in perfect agreement (eq. 2.10 & eq. 2.14) as shown by the overlapping CMB (blue) and BBN (purple) bands shown in Fig. 2.8. The primordial mass fraction of ^{4}He, D, ^{3}He agree with the theoretical calculation, as shown in Fig. 2.8. Thus the BBN model is another independent proof of the existence of non-baryonic dark matter. However, it is not the case for the ^{7}Li and this disagrement is known as the Lithium Problem and might be due to new physics [20].

2.2.6 The WIMP miracle

In the early Universe, WIMPs are believed to be abundant and in thermal equilibrium which resulted in an equal number of WIMP annihilation and production interactions [21]. As the Universe expanded and cooled down, the temperature became lower than the rest mass of WIMP particles, and thus, WIMP production was not possible anymore. As a result, the WIMP abundance decreased exponentially until the annihilation reaction fell below the Hubble expansion rate H. At this point, the WIMPs abundance "freeze-out" and retained a relic cosmological abundance. Mathematically, this process is best described quantitatively via the Boltzmann equation

$$\frac{dn_\chi}{dt} + 3Hn_\chi = - < \sigma_A v > [(n_\chi)^2 - (n_\chi^{eq})^2], \tag{2.15}$$

where $< \sigma_A v >$ is the thermally averaged total cross section for the annihilation of $\chi\bar{\chi}$ into lighter particles times the relative velocity v, and n_χ and n_χ^{eq} are the number density of WIMP particles due to the annihilation and production reaction, respectively [21]. This equation can only be resolved numerically and yields the following approximation by assuming an energy independent annihilation cross section σ_A:

$$\Omega_\chi^2 h^2 = m_\chi n_\chi / \rho_c \simeq (3 \times 10^{-27}\,\mathrm{cm^3\,s^{-1}} / < \sigma_A v >). \tag{2.16}$$

Fig. 2.9 shows the time evolution of the comoving number density as a function of m_χ/T, i.e., the number density with the expansion of the Universe factored out such that n_χ stays constant once annihilation cross section rate drops below the expansion rate. The quantity m_χ/T increases as a function of time since the temperature decreases as the Universe expands. Without the expansion of the Universe, the WIMP abundance (N_{EQ}) in Fig. 2.9 would keep decreasing exponentially. For larger annihilation cross section, the resulting WIMP relic abundance decreases, and consequently, in order to match the relative dark matter density $\Omega_D M h^2 = 0.1200 \pm 0.0012$ [3], the dark matter annihilation cross section must be $\simeq 3 \times 10^{-26} cm^3 s^{-1}$ which is of the same order of magnitude as

the weak interaction and is referred as the WIMP canonical annihilation cross section. This coincidence was coined the “WIMP Miracle” and gives another argument in favor of WIMPs as the most likely dark matter candidate.

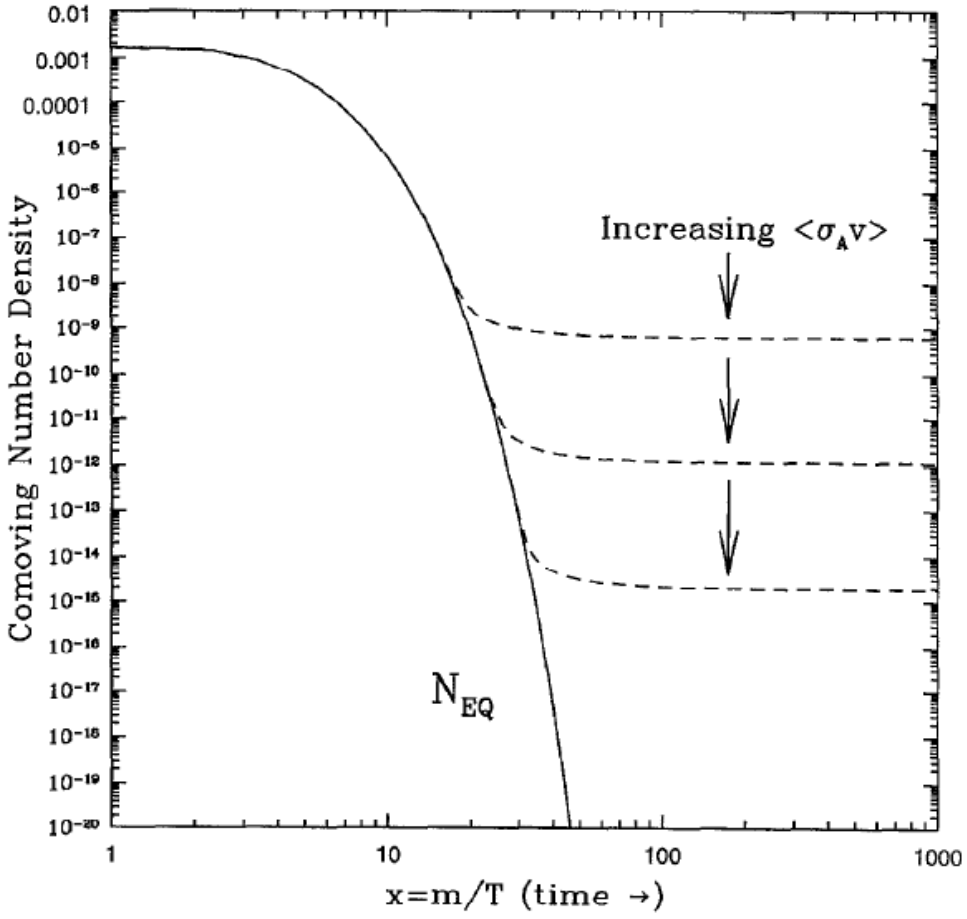

Figure 2.9 – Comoving number density of WIMPs versus time [22].

2.2.7 21 cm line

A 21-cm photon is emitted when an electron in a hydrogen atom transits from the triplet state to the singlet state which has a different energy levels due to the hyperfine splitting caused by the electron and proton magnetic moments. Since hyperfine splitting is extremely small, the lifetime of the triplet state is 1.1×10^{7} years. Today, 21-cm photons created in the early Universe have red-shifted considerably, similarly to the CMB,

and can also be detected. The observed frequency of the 21-cm photon is given by: $\nu = 1.420/(1+z)$ MHz, where z is the redshift. Hence, the 21-cm line shifts to radio frequencies of 30-200 MHz during the first billion years after the Big Bang [23]. Since the CMB contains 21-cm photons, their abundance can vary at a given redshift due to the interaction of the CMB with hydrogen clouds that can absorb or emit 21-cm photons. If there are less 21-cm photons at a specific redshift, it means that during this period, hydrogen clouds were absorbing 21-cm photons.

For the first time in 2018, an absorption spectrum was measured by the EDGES collaboration [24] which revealed strong discrepancies between the theoretically expected absorption in regions near z = 18 that correspond to the strong absorption that occurred just after the creation of the first stars [23]. The experimental result is presented in Fig. 2.10 and shows the brightness temperature T_{21}(K) versus redshift z. When T_{21} is less then 0, it means that there was an absorption of 21-cm photons, while if it is higher than 0, there is an emission. The equation for T_{21} is the following:

$$T_{21} = 27 x_{HI}(1-\delta)\Big(\frac{\Omega_b h^2}{0.023}\Big)\Big(\frac{0.5}{\Omega_m h^2}\Big)^{\frac{1}{2}}\Big(\frac{1+z}{10}\Big)^{\frac{1}{2}} \times \Big(\frac{T_{CMB}}{T_s}\Big)\,\mathrm{mK}, \tag{2.17}$$

where x_{HI} is the neutral fraction of hydrogen, δ_b is the fractional overdensity in baryons $T_S = \frac{n_1}{n_0} = 3e^{(-T_*/T_{spin})}$ is the spin temperature of the 21-cm line, where $T_* = 0.0681$ K is the temperature corresponding to the 21-cm wavelength, while n_1 and n_0 are the number densities of electrons in the triplet and singlet states, respectively. If T_{spin} is higher than T_{CMB}, it means that there is an emission of 21-cm photons.

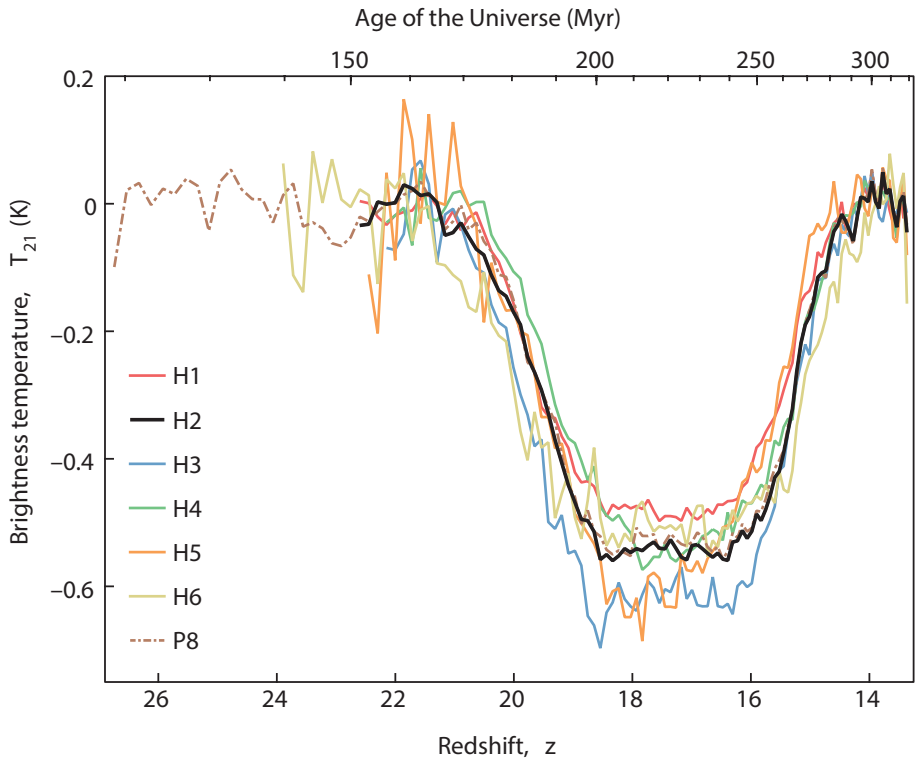

Figure 2.10 – The 21-cm temperature profile measured by the EDGES experiment for several detector configurations [24].

There are multiple mechanisms that can affect T_{spin} and each of them can both excite and de-excite the 21-cm hyperfine line of an hydrogen atom: absorption/emission of 21-cm photons from CMB interactions, collisions with other hydrogen atoms (HH), free electrons (He), and protons (Hp), and scattering of Ly α photons. T_{spin} can be written as follow [25]:

$$T_{spin}^{-1} = \frac{T_{CMB}^{-1} + x_\alpha T_K^{-1} + x_c T_K^{-1}}{1 + x_\alpha + x_c}, \tag{2.18}$$

where x_c, x_α are the coupling coefficients due to atomic collisions and scattering of Lyα photons, respectively, and T_K is the gaz temperature. Fig. 2.11 shows how T_{21} varies theoretically as a function of the redshift.

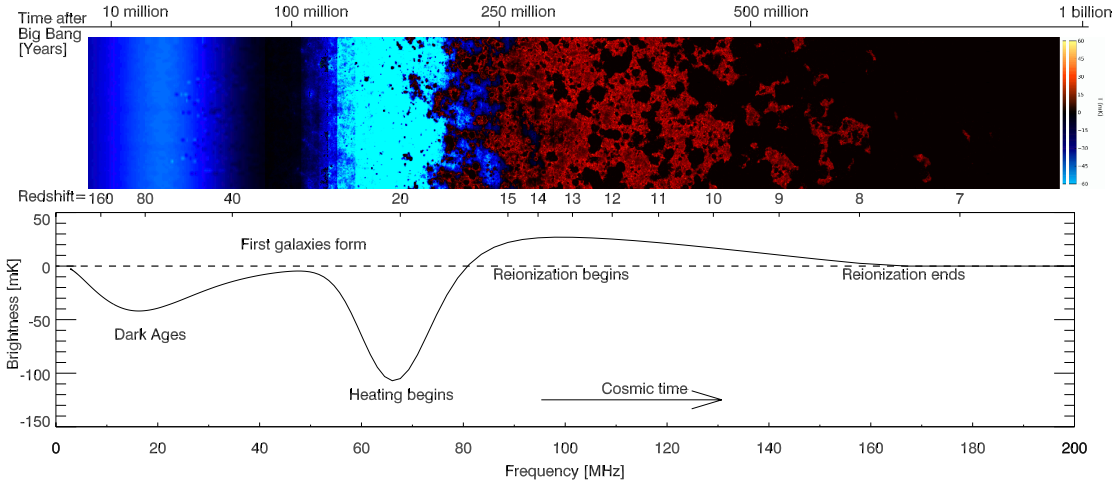

Figure 2.11 – The top plot shows the time evolution of the 21-cm brightness , where the coloration indicates the strength of the brightness. The bottom plot shows the expected evolution of the 21-cm brightness (T_{21}). Note that there is considerable uncertainty due to the unknown properties of the first galaxies [23].

The EDGES measurements correspond to the period enclosed by the appearance of the first stars ($z = 30$) and the beginning of the Reionization period ($z = 15$). The photons emitted by the first stars interacted with hydrogen clouds and induced a coupling between T_{spin} and T_K such that T_{spin} gradually reached T_K . Due to the expansion of the Universe, T_K kept decreasing proportionally to $(1+z)^2$, while T_{CMB} decreased proportionally to $(1+z)$. Therefore, when T_{spin} coupled to T_K, the gas temperature was much lower than T_{CMB} and thus T_{spin} was also much lower than T_{CMB} which results in an absorption ($T_{spin} < T_{CMB}$, eq. 2.17). Current theoretical model predict that the lowest T_{21} value is approximately -240 mK [26]. However, the EDGES experiment measured a brightness equal to -500 mK and even as low as -600 mK for certain detector configurations. To verify this signal, various experiments are currently being built that will remeasure the same signal: Large-Aperture Experiment to Detect the Dark Ages (LEDA) [27], the Sonda Cosmológica de las Islas para la Detección de Hidrógeno Neutro (SCI-HI) [28], the Probing Radio Intensity at high z from Marion (PRIZM) [29], and the Shaped Antenna measurement of the background Radio Spectrum 2 (SARAS 2) [30].

One hypothesis that was tested is whether dark matter could cool down T_K. Those calculations are performed in [31] and the conclusion is that it cannot since it would need a WIMP-proton cross section much higher than the current direct dark matter limits. However, a more exotic model could explain it [31]. This model requires that 1% of the dark matter is millicharged and that those particles would have a high enough cross section to cool down the IGM.

While dark matter cannot provide this extra cooling, it could provide extra heating to the gas. Indeed, dark matter annihilation products can interact with the gas and increase its temperature exactly like the photons produced by the first stars. Therefore, the temperature T_{21} measured by EDGES constrains the annihilation cross section of dark matter because if it is too high, it increases T_{21} and consequently T_{21} could not be as low as $\approx -500\,\mathrm{mK}$ as it was measured by the EDGES collaboration [24]. Thus, WIMP annihilation limits can be set and compared to the WIMP canonical annihilation cross section of $\simeq 3 \times 10^{-26}\,\mathrm{cm^3 s^{-1}}$. If the limit on the WIMP annihilation set by this 21-cm measurement is smaller than the canonical annihilation cross section for certain WIMP masses, it results in the exclusion of certain WIMP masses by the EDGES result. These results were published in [32] and exclude WIMP masses between 3 - 30 $\mathrm{GeV/c^2}$.

CHAPTER 3

DARK MATTER CANDIDATES

The different characteristics of dark matter that were highlighted by astrophysical observations serve as constraints to develop theoretical models that propose dark matter candidate particles. In this section, the various candidates and their characteristics will be presented.

3.1 Baryonic dark matter

Since dark matter does not emit radiation, one of the solutions proposed is the existence of a large number of astronomical objects formed of baryonic matter. These objects, called MACHOs (Massive Astronomical Compact Halo Objects), could be black holes, neutron stars, brown dwarfs, white dwarfs or planets in free orbit. They could be detected by microlensing, that is, when they pass an observable star, they bend the path of light. Therefore, searches for this effect were performed by the MACHO [33] and Eros [34] collaborations. Although the experiments measured more accurately the amount of ordinary matter in the universe, MACHOs alone are not present in sufficient quantity to account for the observed cosmological phenomena.

3.2 The axions

Axions are particles that have been theorized to account for the absence of CP violation in the strong interaction [35]. They are also good candidates for dark matter since they are non-relativistic particles and interact weakly with baryonic matter. They have very small masses ranging from 10^{-6} to 1 eV/c^2 and could have formed a Bose-Einstein condensate in sufficient quantity to account for the invisible matter measured by the different astronomical observations.

The axion is a hypothetical particle that weakly interacts with baryonic matter. It is

a pseudo-scalar particle that could solve multiple problems in particle physics. Besides being a possible dark matter particle candidate, it could also explain the absence of CP-violation in QCD and explain the absence of the neutron electric dipole moment. QCD has a natural CP-violation term in its Lagrangian [16]:

$$L_\Theta = -\bar{\Theta}(\alpha_s/8\pi)G^{\mu\nu a}\tilde{G}^a_{\mu\nu}, \tag{3.1}$$

where $\bar{\Theta}$: -$\pi \leq \bar{\Theta} \leq +\pi$ is the effective parameter after diagonalizing quark masses, $\tilde{G}^a_{\mu\nu}$ is the color field strength tensor. The current experimental measurements of the neutron electric dipole moment constrain the value of $\bar{\Theta}$ to $\leq 10^{-10}$, although if the axion is not responsible for the absence of the neutron electric dipole moment, $\bar{\Theta}$ could be of order 1 [36]. One possible explanation and proposition to resolve those issues is to add a new particle called the axion which arises naturally through the spontaneously broken global Peccei-Quinn symmetry. The addition of this particle changes the Lagrangian:

$$L_\Theta = \left(\frac{\phi_A}{f_A} - \bar{\Theta}\right)\alpha_s/8\pi G^{\mu\nu a}\tilde{G}^a_{\mu\nu}, \tag{3.2}$$

where ϕ_A is the axion field and f_A the axion decay constant. Hence to restore CP symmetry, i.e. $L_\Theta =$

$$\phi_A = \bar{\Theta} f_A. \tag{3.3}$$

Furthermore, the axion mass can be obtained following complex QCD calculation which yields the following estimate for the axion mass:

$$m_A = 5.70(7)\left(\frac{10^9 \text{GeV}}{f_A}\right)\text{meV}, \tag{3.4}$$

which depends exclusively on the coupling parameter f_A. Current experiments are mostly searching for axions by exploiting the photon-axion coupling. There are two main axion models: KSVZ [37][38] and DFSZ [39][40]. Each predict an axion-to-

photon coupling that depends on the mass of the axion. The coupling for the KSVZ and DFSZ models are, respectively [41]:

$$g_{a\gamma\gamma}^{KSVZ} \approx 0.38 \frac{m_a}{\mathrm{GeV}^2}, \tag{3.5}$$

$$g_{a\gamma\gamma}^{DFSZ} \approx 0.14 \frac{m_a}{\mathrm{GeV}^2}. \tag{3.6}$$

If the axion is the dark matter particle seen in the universe, its abundance depends on whether the symmetry is broken before or after inflation. In both cases, the current models predict masses of a few μ eV up to hundreds of μ eV.

Several particle physics experiments that exploit the coupling between photons and axions and are already running. The first experiment to reach sensitivity to KSVZ and DFSZ axions is ADMX [42]. A more recent experiment with possible reach to the two models is the HAYSTAC experiment [43]. Several other types of experiment also provide limits on the axion coupling. The current limits are presented in Fig. 3.1 [16], where the yellow band shows the theoretical predictions for both KSVZ and DFSZ. The leftmost green band on this figure is the limit obtained by ADMX, while the rightmost green band was obtained by the HAYSTAC experiment.

3.3 The MOND theory

A solution that does not require particles to explain the problem of the invisible matter is called MOND (MOdified Newtonian Dynamics) and it proposes to modify Newton's equations [44]. The initial goal of this theory was to explain the rotation curves of spiral galaxies showing a constant velocity as a function of distance from the center of the galaxy. This theory, proposed in 1983 by Mordechai Milgrom, agrees with Newton's laws for high accelerations but would change this same law for small

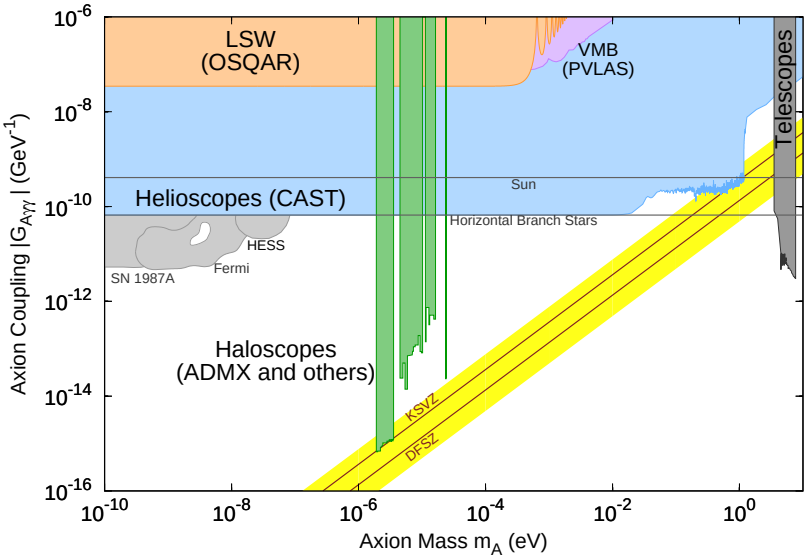

Figure 3.1 – Exclusion plot for axion-like particles [16]. The left most green band is the limit obtained by ADMX [42], while the right most green band was obtained by the HAYSTAC [43] experiment. The yellow band shows the KSVZ and DFSZ predictions. The limit

accelerations. Newton's second law is modified in the following way:

$$F = m\mu\left(\frac{a}{a_0}\right)a \tag{3.7}$$

where μ is a function of a and a_0 that interpolates between $\mu(\mathrm{x}) = \mathrm{x}$ for $\mathrm{x} \ll 1$ and $\mu(\infty) = 1$, a_0 is a natural constant, $a_0 \approx 10^{-10}\mathrm{ms}^{-2}$. In this way, the rotation speed of galaxies would no longer depend on the distance to which the object is located. On the other hand, in the case of the Bullet cluster collision, the gravitational lens effect localizes dark matter distributions at a different point which is not the center of mass of the visible mass, which cannot be explained by the MOND theory [45]. In order to solve this discrepancy, the addition of non-baryonic matter is necessary. The same argument holds for the CMB power spectrum, i.e., MOND alone is not able to reproduce the measured data [45].

3.4 Hot dark matter

Hot dark matter is made of particles that go to relativistic speeds. The main candidate for this type of matter is the neutrino. These particles satisfy the condition of very weak interactions with matter. There was also a period in the history of the universe at which neutrinos have escaped as the photons did. Just like the CMB the imprint left by those neutrinos is called CνB (Cosmic Neutrino Background), but has not been observed yet. The number density of photons can be related to the number density of neutrinos, as well as the neutrino and CMB temperature ($T_{C\nu B}$ and T_{CMB}) [16]:

$$n_\nu = \frac{4/11}{n_\gamma},\ T_{C\nu B} = (4/11)^{1/3} T_{CMB}. \tag{3.8}$$

It is also possible to obtain the physical density of neutrinos:

$$\Omega_\nu = N_{eff} \frac{7}{8} \left(\frac{4}{11} \right)^{4/3} \Omega_\gamma, \tag{3.9}$$

where $N_{eff} = 3.046$ [46] which corresponds to the number of families of neutrinos measured experimentally.

Moreover, from these results, an upper limit on the sum of the neutrinos masses is obtained [13]:

$$\Sigma m_\nu < 0.23\ eV/c^2\ 95\%\ \text{C. L.} \tag{3.10}$$

The formation of the universe as it can be seen today suggests that the smallest structures were formed first and then large structures such as superclusters were generated. Indeed, observations have shown that small structures such as galaxies are more abundant than large structures. However, if dark matter is constituted exclusively of neutrinos which have very small masses and are highly relativistic, they would have first generated large structures that would then have fragmented to form small structures such as galaxies. As a result, neutrinos alone cannot form dark matter. However, heavy sterile neutrinos with a mass of $48 - 300\,\text{keV}$ are a possible dark matter candidate that could be

detected through neutrino-electron scattering [47].

3.5 Cold dark matter

This type of matter is heavy, relativistic, non-baryonic with a mass of the order of 1 to 1000 times the mass of the proton and are compatible with the known history of the formation of the structures in the universe [5]. These particles are called WIMP (Weakly Interacting Massive Particles) and they interact very weakly at the order of the cross-section of the electroweak interaction, which makes them very difficult to detect. Several theoretical models that describe WIMPs exist and one of these models is the Minimal Supersymmetric Standard Model (MSSM) [6] which is an extension of the Standard Model. This model predicts a stable, neutral and heavy particle called neutralino which could be compatible with cosmological observations.

3.6 Supersymmetry

Supersymmetry is a theory that predicts a superpartner for each of the known particles of the Standard Model [48]. Half-integer spin fermions have superpartners with integer spins. Likewise, bosons, which are particles with integer spin, have superpartners with half-integer spin. Such a theory would make it possible to unify the coupling constants of the three forces contained in the Standard Model; the electromagnetic force, the strong and the weak force. However, this symmetry requires superpartners to have a mass much larger than the masses of the particles of the Standard Model. From this theory, several models have been created such as the Minimal Supersymmetric Standard Model (MSSM). The different models include a particle called LSP (Lightest Supersymmetric Particle) that is a quantum superposition of neutral superpartners of the standard model bosons. The LSP is called the neutralino, is the lightest particle, and thus is stable.

3.7 The MSSM and the neutralino

The expected mass of superparticles is 10 to 100 times the mass of the proton [6]. Thus, to produce these particles with a particle accelerator, a very large amount ($\approx$ TeV) of center of mass energy is required which could be made available at the LHC (Large Hadron Collider). An important feature of the MSSM is the concept of R parity which implies the stability of the LSP. The R-parity is defined by the following relation [48]:

$$P_R = (-1)^{3B+L+2s}, \tag{3.11}$$

where s is the spin, B is the baryon number, and L is the lepton number. Therefore, all Standard Model and supersymmetric particles have R-parity equal to +1 and -1 respectively. Hence, the LSP cannot decay without violating the R-parity and is thus stable. The LSP satisfies the required properties prescribed for dark matter and would possess a mass of $1-100\,\mathrm{GeV}/c^2$. The neutralino is a Majorana fermion composed by a linear combination of zino (Z boson), photino (photon) and higgsino (neutral Higgs) [16]:

$$\chi^0 = \alpha_1\tilde{\gamma} + \alpha_2\tilde{Z} + \alpha_3\tilde{H}, \tag{3.12}$$

where α are the mixing parameters, $\tilde{\gamma}$ is the photino, $\tilde{Z}$ is the zino and $\tilde{H}$ is the higgsino, respectively.

3.8 Asymmetric dark matter

Asymmetric dark matter is a recent idea, and an extension of the asymmetry between matter and antimatter in the Universe applied to dark matter. It suggests an asymmetry between dark matter and dark antimatter [49]. This concept is based on the observation that the densities of dark matter and baryonic matter are very close to one another: $\rho_{DM}/\rho_B \approx 5$ [3] and this even though they are not connected by any mechanism. However, in the case where both types of matter are asymmetrical, it is possible to find a

relation:

$$n_\chi - n_{\bar{\chi}} \approx n_b - n_{\bar{b}}, \tag{3.13}$$

where n_χ, $n_{\bar{\chi}}$ are the densities of dark matter and anti-dark matter, and n_b, $n_{\bar{b}}$ are the baryonic matter and antimatter densities. Since $\rho_{DM}/\rho_B \approx 5$ and assuming eq. 3.13 one obtains that $m_\chi \approx 5\, m_p \approx 5\,\mathrm{GeV/c^2}$ which therefore suggests that dark matter is composed of particles with a mass of 5 GeV/c^2. Initially, the asymmetry could be present only in normal matter or only in dark matter or simultaneously in both types. For a relationship to exist between the asymmetry present in dark matter and ordinary matter, there must be a means of communication between the two types of matter. Although this interaction is unknown, it follows that the asymmetry remains unchanged once the interaction between the two sectors is cut off. From this general idea, many models try to explain the asymmetry between matter and antimatter with cross sections of the same order of magnitude as that of WIMPs.

CHAPTER 4

DETECTION OF DARK MATTER

Dark matter can interact via three different processes with Standard Model particles and each of them is illustrated in the diagram of Fig. 4.1 and described below:

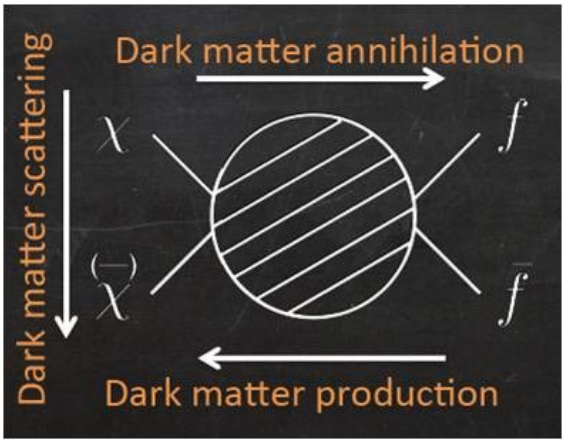

Figure 4.1 – Diagram showing the three detection processes of dark matter.

Indirect detection consists of measuring the annihilation products of dark matter into particles of the Standard Model and compares the fluxes of these particles to the fluxes predicted by cosmic models. Direct detection seeks to measure the energy deposited following an elastic scattering of a dark matter particle on a nucleus or electron. The last dark matter detection technique relies on the production of dark matter by accelerators like the LHC following the collision of two Standard Model particles. Since the lightest SUSY particle is stable in the MSSM, the dark matter signature in a detector like ATLAS or CMS would be a collision where the reconstructed energy would not be equal to the energy of the initial collision, i.e., with an amount of missing energy.

4.1 The WIMP in the universe and in the Milky Way

During the Big Bang, the energy available to form particles was sufficiently large to produce all the particles present in the MSSM. Then, all supersymmetric particles disintegrated into the neutralino, the LSP. Today, neutralinos should be present in very large quantities in the universe and should be bound gravitationally around galaxies in the form of dark matter halos. In fact, before the formation of galaxies, neutralinos have agglomerated due to the gravitational force and have created gravitational potential wells where later galaxies formed. Once these halos are formed and stable, WIMPs follow a Maxwellian distribution velocity around the galaxies. Knowing the speed of the Sun around the Milky Way, the WIMPs' velocity distribution with respect to the Earth is given by [50]:

$$f(\vec{v},\vec{v_E}) = e^{\frac{-(\vec{v}+\vec{v_E})}{v_0^2}}, \tag{4.1}$$

where v is the WIMPs' velocity, $v_0 = 230$ kms^{-1} is the average rotation speed of the Sun with respect to the centre of the galaxy and $v_E = 244$ kms^{-1} is the speed of the Earth with respect to the halo of dark matter. There is a maximum speed above which neutralinos will escape from the galaxy; $v_{esc} = 544$ kms^{-1}. Furthermore, eq. 4.1 is a general Maxwellian distribution that does not take into account this escape velocity. To obtain the relevant velocity distribution of WIMPs that detectors are sensitive to, one has to evaluate the differential particle density [50]:

$$dn = \frac{n_0}{k} f(v, v_E) d^3v, \tag{4.2}$$

where k is a normalization constant such that

$$\int_b^a dn = n_0. \tag{4.3}$$

n_0 is therefore the mean dark matter particle number density (ρ_χ / M_χ) with a velocity between a and b. The normalizing factor, k, is obtained by evaluating the following

general integral:

$$k = \int_0^{2\pi} d\phi \int_{-1}^{+1} d(cos\theta) \int_b^a f(v, v_E) v^2 dv. \tag{4.4}$$

The relevant case for WIMP searches on the Earth in the Milky Way Galaxy is for velocities between $b = 0$ and $a = v_{esc}$ and is equal to:

$$k_1 = (\pi v_0^2)^{3/2} \left[erf\left(\frac{v_{esc}}{v_0}\right) - \frac{2}{\pi^{1/2}} \frac{v_{esc}}{v_0} e^{\frac{-v_{esc}^2}{v_0^2}} \right] \tag{4.5}$$

Therefore, when calculating any WIMP recoil spectrum, the Maxwellian distribution has to be normalized by k_1 in order to take into account only the WIMPs that have a velocity between 0 and v_{esc}. This last equation will be relevant in the following section which is dedicated to the calculation of the recoil energy spectrum following WIMP-nucleon elastic scattering. For an observer on Earth, the velocity distribution has an important consequence; the number of neutralinos crossing Earth increases when the Earth travels in the same direction as the Sun and decreases in the opposite case as is shown in Fig. 4.2.

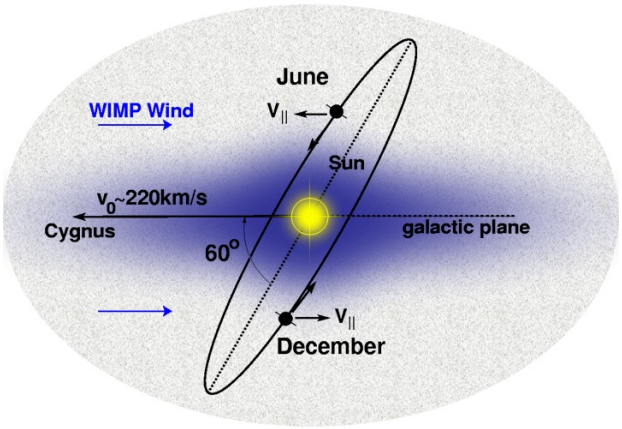

Figure 4.2 – Diagram of the origin of an annual modulation of the WIMPs flux [51].

Thus, since v_E varies sinusoidally during a terrestrial year, it results in a sinusoidal modulation of the number of WIMPs crossing the Earth and is a function of the speed

parallel to the direction of the Sun in the galaxy. This component has an amplitude of 30 km/s and generates a maximum on June 1st and a minimum on December 1st. By collecting enough data over many years, it should be possible to see this modulation over several annual cycles. Such an observation would be a unique signature of dark matter.

4.2 Direct detection

When WIMPs pass through baryonic matter, they can interact with it by elastic collisions described by the following Lagrangian [52]:

$$L = \sqrt{2}G_F[\bar{\chi}\gamma^{\mu}\gamma_5\chi(a_p\bar{p}\gamma_{\mu}\gamma_5 p + a_n\bar{n}\gamma_{\mu}\gamma_5 n)] + \bar{\chi}\chi(f_p\bar{p}p + f_n\bar{n}n), \tag{4.6}$$

where G_F is the Fermi constant, p, n and χ are the wave functions of the proton, neutron and neutralino respectively, a_n and a_p are respectively the coupling constants of the proton and neutron in the spin-dependent sector, while f_n and f_p are the neutron and proton coupling constants in the spin-independent sector. The first term is responsible for spin-dependent interactions while the latter describes spin-independent interactions. From this Lagrangian, one obtains the interaction cross section between a WIMP and a nucleus:

$$\sigma_A = 4G_F^2\left(\frac{M_{\chi}M_N}{M_{\chi}+M_N}\right)^2 C_A F(q^2), \tag{4.7}$$

where M_{χ} is the WIMP mass, M_N is the mass of the nucleus, C_A is an enhancement factor that depends on the type of interaction (SD or SI) and $F(q^2)$ is a form factor depending on the momentum transfer $q = \sqrt{2M_N E_R}$. Due to the G_F coupling, the WIMP-nucleon elastic scattering cross section is typically of the order of 10^{-39} to 10^{-50} cm^{-2}. This results in a cross section compatible with the current density of dark matter ($\Omega_c = 0.2621 \pm 0.0026$ [3]). The form factor reflects the overlap of the WIMP and nucleus wave functions. This form factor depends on the mass of the nucleus and the recoil energy, which in turn depends on the WIMP mass and its speed. The shape factors of several different nuclei are presented in Fig. 4.3 as a function of the recoil energy.

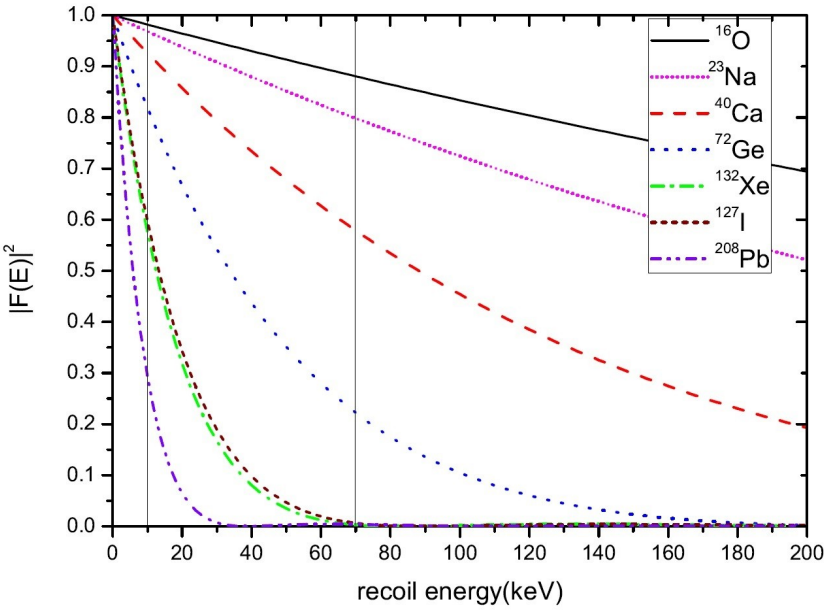

Figure 4.3 – Form factors for different nuclei based on recoil energy [53].

From this figure, we can see that the form factor decreases with increasing atomic weight (A). In the case of light nuclei, the form factor is close to 1 and varies very little with the recoil energy. On the other hand, C_A, the enhancement factor, depends on the nature of the interaction and may be dependent or independent of the spin. In the case of the spin-independent interaction, the enhancement factor is given by:

$$C_A^{SI} = \frac{1}{\pi G_F^2}[f_p Z + f_n(A-Z)]^2. \tag{4.8}$$

Assuming isospin invariance, i.e., the neutralino couples in the same way with neutrons and protons (f_p equals f_n), the cross section becomes proportional to the square of the number of nucleons:

$$C_A^{SI} \propto A^2 F(q^2). \tag{4.9}$$

Thus, for experiments sensitive to the spin-independent interaction, the most important factor is the mass number of the target nuclei. The enhancement factor of spin-dependent

interactions is given by:

$$C_A^{SD} = \frac{8}{\pi}(a_p\langle S_p\rangle + a_n\langle S_n\rangle)^2\frac{J+1}{J}, \tag{4.10}$$

where $\langle S_{p,n}\rangle$ represents the average value of the spin of all protons and neutrons of the target nucleus, J is the total spin of the nucleus, and $a_{(p,n)}$ are the coupling between the neutralino and the nucleons. The values of $\langle S_{p,n}\rangle$ for different nuclei are presented in Table 4.I.

Nucleus	Z	Uneven nucleon	J	$<S_p>$	$<S_n>$	C_A^p/C_p	C_A^n/C_n
^{1}H	1	p	1/2	0.5	0	1	0
^{19}F	9	p	1/2	0.441	-0.109	7.78×10^{-1}	4.75×10^{-2}
^{23}Na	11	p	3/2	0.248	0.020	1.37×10^{-1}	8.89×10^{-4}
^{27}Al	13	p	5/2	0.343	0.030	2.20×10^{-1}	1.68×10^{-3}
^{29}Si	14	n	1/2	-0.002	0.130	1.60×10^{-5}	6.76×10^{-2}
^{35}Cl	17	p	3/2	-0.083	0.004	1.53×10^{-2}	3.56×10^{-5}
^{39}K	19	p	3/2	-0.180	0.050	0.20×10^{-2}	5.56×10^{-3}
^{73}Ge	32	n	9/2	0.030	0.378	1.47×10^{-3}	2.33×10^{-1}
^{93}Nb	41	p	9/2	0.460	0.080	3.45×10^{-1}	1.04×10^{-2}
^{125}Te	52	n	1/2	0.001	0.287	4.00×10^{-6}	3.29×10^{-1}
^{127}I	53	p	5/2	0.309	0.075	1.78×10^{-1}	1.05×10^{-2}
^{129}Xe	54	n	1/2	0.0208	0.359	3.14×10^{-3}	5.16×10^{-1}
^{131}Xe	54	n	3/2	-0.009	-0.227	1.80×10^{-4}	1.15×10^{-1}

Table 4.I – Nuclear properties of nuclei relevant for spin-dependent dark matter searches [54].

According to Table 4.I, ^{93}Nb and ^{19}F are the most favorable nuclei for SD interactions with protons apart from hydrogen, while the SD-n interaction favors germanium and xenon. A much more detailed analysis of possible WIMP-nucleus interactions is based on Effective Field Theory (EFT) model and will be described in Chap. 12.

4.3 Expected WIMP signal

The purpose of direct detection experiments is to reduce and/or reject background events to isolate the rare events produced by the interaction of dark matter in a detector.

The WIMP signal depends on the event rate and on the energy spectrum following an elastic collision on a target nucleus. The general equation that describes the differential energy spectrum is:

$$\frac{dR}{dE_R} = \int_{E_{Rmin}}^{E_{Rmax}} \frac{1}{Er} dR(E), \tag{4.11}$$

where $r = 4\frac{(M_N M_\chi)}{(M_N+M_\chi)^2}$, $E = \frac{1}{2}M_\chi v^2$ is the kinematic energy of a dark matter particle, and $E_R = Er(1-\cos\theta)/2$ is the recoil energy of a nucleus, in the center of mass, after a collision with a dark matter particle ($0 \leq E_R \leq E$). For WIMP masses of $M_\chi = 10-1000$ GeV c^{-2}, the recoil energy corresponds to $E_R = 10-100$ keV.

Since E_{Rmin} and E_{Rmax} corresponds to the lowest and highest possible WIMP velocity, i.e., v_{min} and v_{max} the integral can be performed with respect to the velocity and eq. 4.11 becomes:

$$\frac{dR}{dE_R} = \frac{2}{rM_\chi} \int_{v_{min}}^{v_{max}} \frac{1}{v^2} dR(v), \tag{4.12}$$

where v_{min} is equal to $(2E_R/rM_\chi)^{1/2}$ and $v_{max} = v_{esc}$.

The second ingredient to calculate this integral is to know $dR(v)$ which is the event rate per unit mass on a target of atomic mass A as a function of the velocity for a cross section σ. The general equation that describes $dR(v)$ is:

$$dR = \frac{N_A}{A}\sigma v dn, \tag{4.13}$$

where dn is described by eq. 4.2 and N_A is Avogadro's number. Replacing dn in the above equation yields:

$$dR(v) = \frac{N_A}{A}\frac{\rho_\chi}{M_\chi}\frac{1}{k}\sigma v f(v, v_E) d^3 v. \tag{4.14}$$

By inserting eq. 4.14 into eq. 4.12, one obtains:

$$\frac{dR}{dE_R} = \frac{2}{rM_\chi}\frac{N_A}{A}\frac{\rho_\chi}{M_\chi}\frac{1}{k_1}\sigma\int_0^{2\pi} d\phi \int_{-1}^{+1} d(cos\theta)\int_{v_{min}}^{v_{esc}} vf(v,v_E)dv, \tag{4.15}$$

Evaluating the integrals yields the following results:

$$\frac{dR}{dE_R} = \frac{R_0}{E_0 r}\frac{k_0}{k_1}\left\{\frac{\sqrt{\pi}}{4}\frac{v_0}{v_E}\left[erf\left(\frac{v_{min}+v_E}{v_0}\right) - erf\left(\frac{v_{min}-v_E}{v_0}\right)\right] - e^{-v_{esc}^2/v_0^2}\right\}, \tag{4.16}$$

where E_0 is the dark matter kinetic energy for $v = v_0 = 230$. R_0 is defined as the event rate per unit mass for $v_E = 0$ and $v_{esc} = \infty$ and is equal to:

$$R_0 = \frac{2}{\sqrt{\pi}}\frac{N_A}{A}\frac{\rho_\chi}{M_\chi}\sigma v_0. \tag{4.17}$$

The other new terms in eq. 4.16, k_0, is the normalization factor for the same conditions as R_0. k_1 corresponds to the truncated velocity distribution due to v_{esc} and the ratio k_0/k_1 is equal to 0.9965 which means that the number of WIMPs with a velocity greater than the escape velocity is only 0.35%. Evaluating eq. 4.16 yields the number of detected counts per unit of time, energy and mass for a specified cross section.

The last step to predict the number of WIMP interactions within a detector is to integrate over the energy range accessible for the detector, as well as taking into account the detection efficiency in this energy range in order to obtain the observed rate of a dark matter detector (R_{obs}) with a detection efficiency $\varepsilon(E_R, M_\chi)$:

$$R_{obs} = \int_{E_{min}}^{E_{max}} \varepsilon(E_R, M_\chi)\frac{dR}{dE_R}dE_R \tag{4.18}$$

Note that the only variable that depends on the energy in eq. 4.16 is v_{min}. Fig. 4.4 shows the recoil spectrum for several WIMP masses for interactions with ^{19}F for a fixed 1 pb cross section obtained using eq. 4.16. The total the number of counts per unit of time and mass above threshold is analogous to integrating a curve in Fig. 4.4 and multiplying by the detection efficiency.

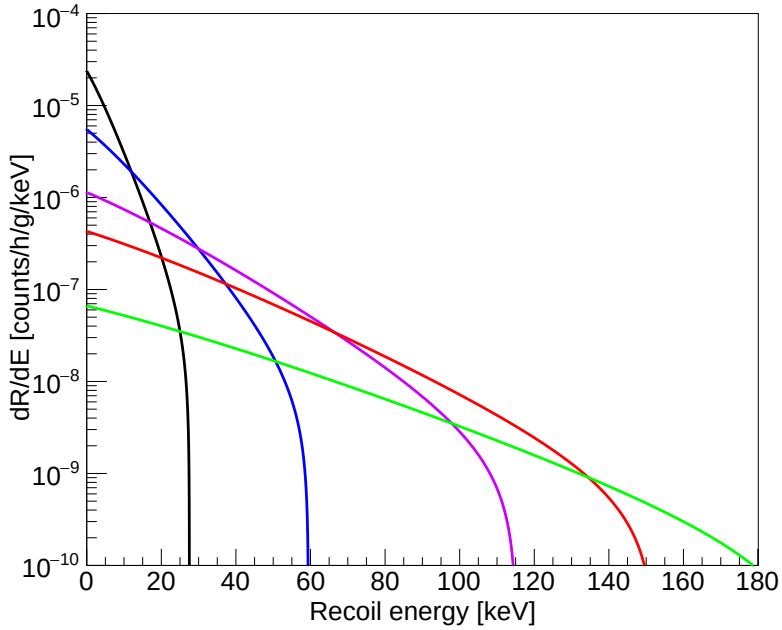

Figure 4.4 – Expected fluorine recoil spectrum (dE/dE_R) for different masses of dark matter for a 1 pb cross section: 10 GeV/c^2 (black), 20 GeV/c^2 (blue), 50 GeV/c^2 (violet), 100 GeV/c^2 (red), 500 GeV/c^2 (green).

When no WIMP candidate events are found, 90% C. L. limits are set on the WIMP-nucleon cross section for a given WIMP mass. The method to determine this limit depends on the background of the experiment as well as the characteristics of the detector.

If an experiment has a background that does not mimic the detector response to dark matter interaction, such as a flat background rate, the background rate can be subtracted to isolate the WIMP signal. In that case, a WIMP signal is fitted on the leftover signal and the cross section is extracted. The determination of the limit itself is performed with statistical tools that highly depends on the type of detector and background.

On the other hand, if no events are measured by a detector or if the background can be precisely predicted, the cross section limit is set by calculating the 90% C. L. Poisson limit. As an example, if no events are measured in a detector the 90% C. L. Poisson limit

is equal to 2.3 counts. By using eq. 4.16 and 4.18, the cross section that corresponds to $R_{obs} = 2.3$ is extracted for a given WIMP mass.

To compare different experiments, the results, in the absence of a signal, are presented in the form of exclusion curves. These curves show the cross section as a function of the mass of the WIMPs and delimit the excluded and allowed regions. An exclusion contour scheme is shown in 4.5.

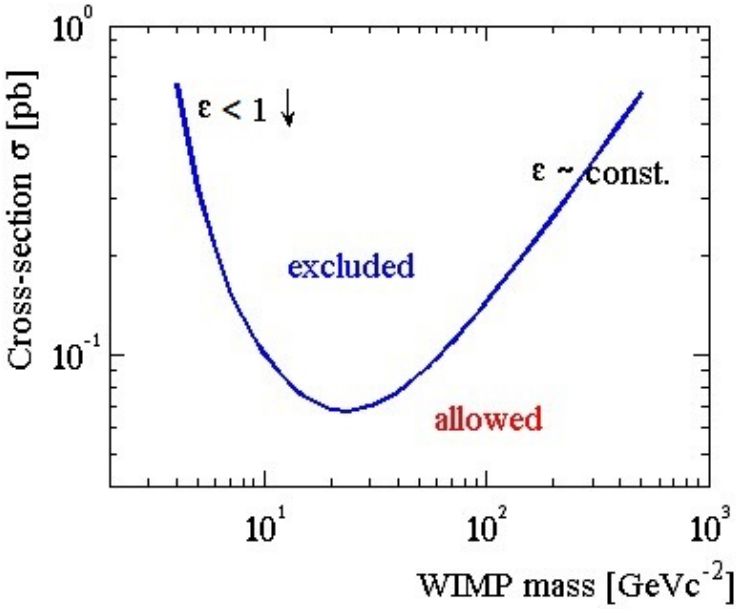

Figure 4.5 – Schematic of WIMP searches exclusion curves. The region above the blue curve correspondss to excluded parameter space, while the rest is still allowed. ε denotes the detection efficiencies of dark matter detectors. Typically, ε decreases for low mass WIMPs since they produce lower energy recoils as denoted in the figure ($\varepsilon < 1 \downarrow$), but ε stays constant for high mass WIMPs.

The detector efficiency, ε, as well as the recoil spectrum, play a significant role in the shape of the curve. According to Fig. 4.4, for WIMP masses smaller than the mass of the target nucleus, the recoil energies will be significantly diminished. Furthermore, detection efficiency typically decrease for energy recoils close to the energy threshold of a detector. On the other hand, for large WIMP masses, the efficiency is almost constant

since the detector will be sensitive to the whole recoil spectrum. However, if the WIMP mass increases, their abundance decreases, which decreases the WIMP interaction rate as can be seen in Fig. 4.4 which shows a decreasing absolute count rate for higher WIMP masses. Thus, the cross section limit decreases for higher WIMP masses.

4.4 Direct detection techniques

Many different types of detectors are currently aiming to detect dark matter. Three different quantities can be measured following an elastic WIMP scattering on a nucleus: scintillation, ionization, or phonons. Most experiments measure two of those quantities in order to be able to discriminate between neutrons and gammas. It is, however, easier to describe the current direct dark matter experiments as a function of the type of target they use which can either be liquid noble gas detectors, solid-state detectors, crystal detectors or superheated liquids. In this chapter, some example of the liquid noble gas, solid state and superheated liquid detectors will be described.

4.4.1 Liquid noble gas detectors

Dark matter experiments using noble gases can be separated into four types: Single phase Ar, dual-phase Ar, single phase Xe, and dual-phase Xe. When two phases are used, an electric field is applied, and a gaseous volume is added. In all cases, photomultipliers (PMTs) are used to capture scintillation light. When an electric field is applied, the charges are also collected. In the future, most liquid noble gas detectors are planning to use silicon photomultipliers (SiPMs) instead of PMTs to reduce their neutron background.

Scintillation is produced by a de-excitation of the singlet and triplet states whose lifetimes are different. In the case of argon and xenon, their ratios are respectively $\frac{7\text{ns}}{1.5\mu s}$ and $\frac{3\text{ns}}{27\text{ns}}$, respectively [55]. The percentage of production of each of these states is different for nuclear recoils and for electronic recoils. The electron recoil-neutron recoil discrimination (ER-NR) is therefore only possible in argon because the time difference

is too small in xenon.

By using two phases and an electric field, two scintillation signals are now produced. An initial signal (S1) due to scintillation at the interaction point and a second one (S2) when electrons are accelerated by the electric field and ionize the gas. The ratio between these two signals makes it possible to discriminate events produced by a nuclear recoil (NR) from those produced by an electromagnetic interaction (ER) which is crucial for Xe detectors due to the small time difference between the de-excitation of the singlet and triplet states. However for argon detectors, while the ER-NR discrimination power is decreased, a better position resolution of the events is gained [56].

Although the ER−NR discrimination is better in Ar, Ar detectors have the disadvantage of having an intrinsic background from the ^{39}Ar isotope that is produced due to cosmic ray activity. This disadvantage is countered by using argon with a reduced percentage of ^{39}Ar that is extracted from underground mines. Another disadvantage of argon is the blindness of PMTs to the Ar scintillation light. Therefore, a wavelength shifter needs to be applied and must stay in place during the lifetime of the experiment. The position of events is obtained and used to eliminate events near surfaces. Experiments using Ar and Xe, exploit a fiducial volume located in the center of the detector, while the rest of the volume acts as a "self-shielding".

An important source of background in these experiments are neutrons emitted by the PMTs. The DarkSide-50 experiment (46 kg LAr at LNGS) will be the first to incorporate a 4π neutron veto to reduce this kind of background. It consists of a boron-loaded liquid scintillator which is inside a 1000 tons water Cerenkov muon veto. This technique allows reducing the neutron background by a factor of 100 [55].

Experiments using LAr operate at higher energy thresholds than Xe based experiments. Due to the quenching effects, these detectors have a different threshold for electronic recoils and for nuclear recoils which are denoted as keVee and keVnr respectively.

As an example, the first results of DEAP3600 (3600 kg LAr at SNOLAB) were obtained with an energy window of $52-105$ keVnr [57], while the lowest energies achieved in Xe are 6.6 keVnr by XENON100 (100 kg LXe at LNGS) and around 3 keVnr for the LUX experiment [55][58][59]. An advantage of these types of detectors is that alpha particles do not produce any background because these particles have much higher energies than the region of interest of WIMP signals. Unfortunately, the energy threshold can hardly be decreased without losing most of the ER-NR discrimination. For example, DarkSide50 [60] did pursue this course and decreased their threshold to 13 keVnr, sacrificing ER$-$NR discrimination completely, but increased their sensitivity to WIMP masses down to 1.8 GeV/c^2.

4.4.2 Solid state detectors

All experiments using cryogenic solid state detectors such as EDELWEISS (4 kg of Ge, Modane) [61], CDMS (9 kg of Ge, Soudan)[62], and CRESST (5 kg of $CaWO_4$ at LNGS) [63] can distinguish between nuclear and electronic recoils. In order to do this, these experiments measure phonons and ionization for CDMS, heat, and ionization for EDELWEISS, while CRESST measures phonons and scintillation photons. The EDELWEISS and CDMS experiments use germanium detectors, while CRESST uses $CaWO_4$ crystals. As an example, the CDMS experiment rejects electronic recoils with a factor $> 10^4$ for events in the bulk of the crystals and up to a factor of $> 10^6$ for electron recoils and β-particle near the surface sensors [64].

Regarding detection thresholds, the latest results obtained by the CRESST experiment were obtained at an energy threshold of 307 eVnr [63], while EDELWEISS analyzed events with energies between 10 and 200 keV [61]. The CDMS experiment has released its latest results obtained with a recoil energy sensitivity of $10-100$ keV [62].

In the future, the CDMS experiment will be operated in SNOLAB and will be called SuperCDMS [65]. Two different types of detectors will be used that are denoted iZip and HV. The HV detector will run at a bias voltage of 100 V and will take advantage

of the Luke-Neganov effect to increase the phonon signal and hence reach lower energy thresholds but at the cost of losing ER−NR discrimination completely. On the other hand, the iZip detectors will exploit the ER-NR discrimination with an improved surface event rejection due to an improvement of the design of the detectors and will be sensitive to higher WIMP masses in comparison to the HV detectors.

4.4.3 Superheated liquids

To detect dark matter, superheated liquid detectors (SHL) characterize phase transitions produced when a particle deposits energy higher than an energy threshold E_{th}. The phase transitions produce bubbles that emit an acoustic wave that can be used to discriminate between alpha decays and nuclear recoil events. While solid-state detector and noble liquid detectors rely upon ER-NR discrimination for WIMP searches, superheated liquid detectors do not possess ER-NR discrimination and rely on the extremely low probability of 10^{-9} that an electron recoil produces a bubble which is lower than the CDMS experiment which is $\approx 10^{-6}$ [64]. There are currently two experiments that use this technique; PICO [2] and MOSCAB [66]. Since the PICASSO [1] and PICO are superheated liquid detectors, the detection principle will be described in details in Chap. 5.

4.5 Current limits

The results and the projections of the different direct detection dark matter experiments are usually given in the form of exclusion plots which show the limit on the WIMP cross section versus WIMP masses. The limits on the spin-dependent and spin-independent interaction are shown separately. The limits obtained by direct detection are also compared to indirect detection and dark matter production results from experiments at the LHC (ATLAS and CMS). Fig. 4.6 shows the current exclusion curves of the spin-independent sector while Fig. 4.7 shows the limits in the SD sector.

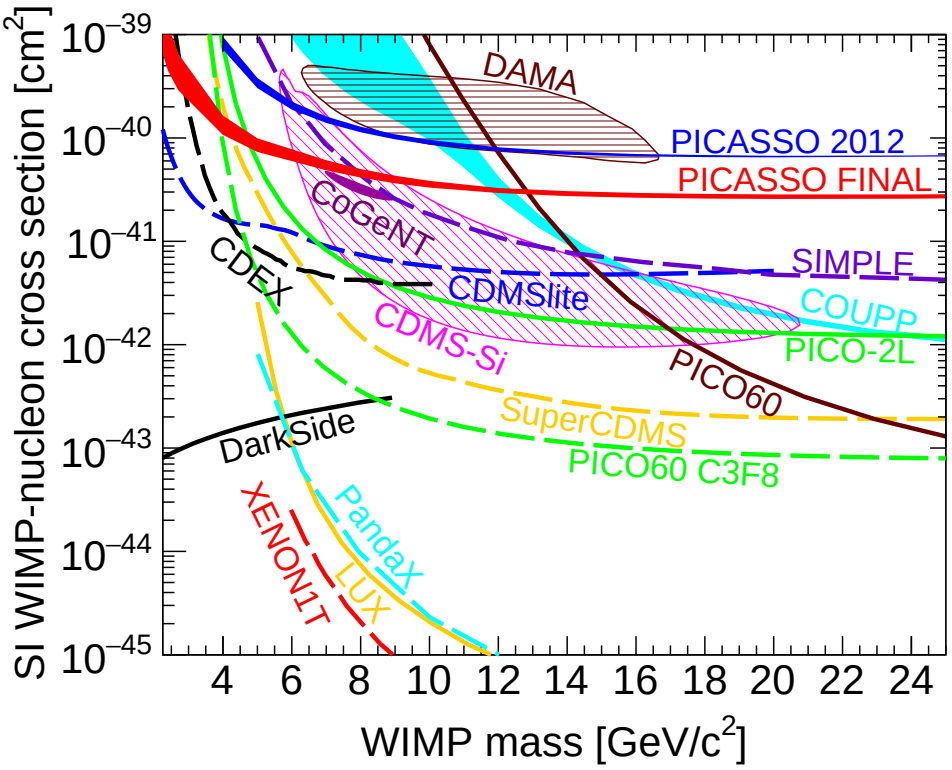

Figure 4.6 – Compilation of the WIMP-nucleon cross section limits in the spin-dependent proton sector. The results that are shown are only published results. The list of all the results and their corresponding references are: PICASSO 2012 (blue) [67], PICASSO FINAL (red) [1], COUPP (teal band) [68], SIMPLE (dashed purple) [69], PICO 2L run2 (green) [70], CDEX (dash black) [71] PICO60 CF_3I (brown, labeled PICO60) [72], PICO 60 C_3F_8 (ndash green) [73], DarkSide (black) [60], SuperCDMS (dashed orange) [74], PandaX (dashed teal) [75], LUX (orange) [76], XENON1T (dash red) [77]. There are also three contours which each represent the possible masses and cross sections that can explain the excess of events seen by the three experiments: DAMA (brown) [78], CoGeNT (magenta) [79] and CDMS-II Si (pink) [80].

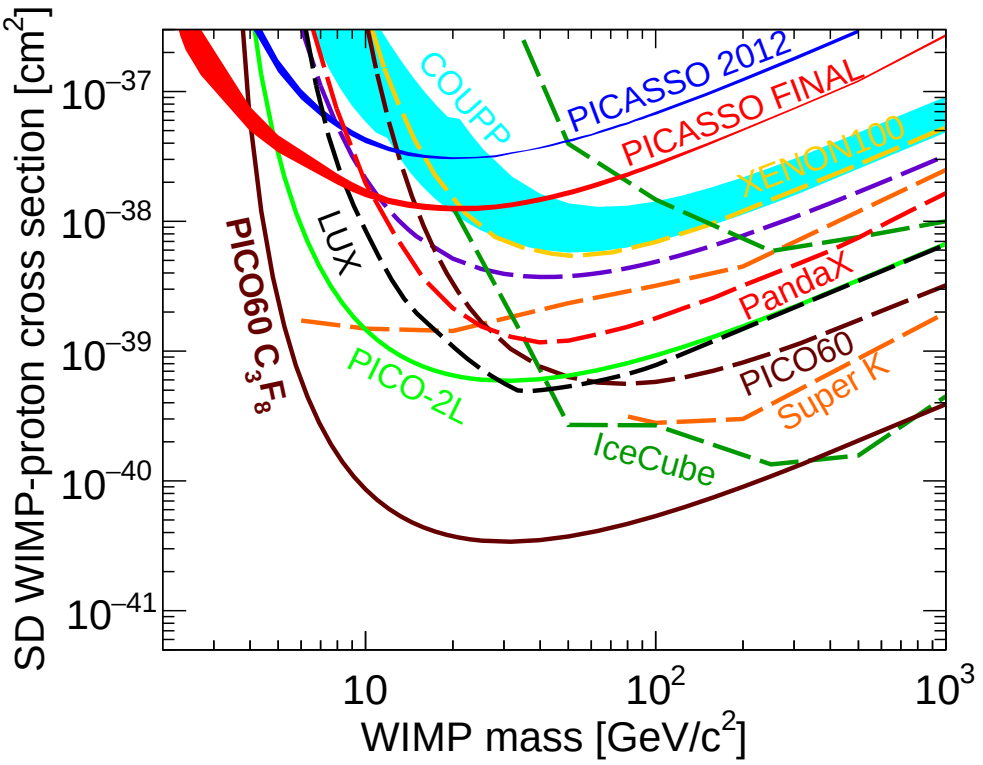

Figure 4.7 – Compilation of the WIMP-nucleon cross section limits in the spin-dependent proton sector. The results that are shown are only published results. The list of all the results and their corresponding references are: PICASSO 2012 (blue) [67], PICASSO FINAL (red) [1], COUPP (teal band) [68], XENON100 (orange) [81], SIMPLE (dashed purple) [69], PandaX (dashed red) [82], PICO 2L run2 (green) [70], LUX (dash black) [83] PICO60 CF_3I (dash brown, labeled PICO60) [72], PICO 60 C_3F_8 (brown) [73], IceCube (dash green) [84], SuperK (dash orange) [85]. The best limit for both indirect detection (IceCube and SuperK) corresponds to W channel, while the lowest corresponds to b quark channel.

Closed outlines are regions in which different experiments have measured an excess of events and claim it is due to a possible interaction of the dark matter with their detector.

4.6 Dark matter production

The search for WIMPs at the LHC [86] is carried out by the ATLAS [87] and CMS [88] detectors. Since WIMPs interact very weakly with matter, they do not deposit any energy in the detectors. If such events occur, much of the energy of the collision will not be reconstructed, which is commonly called "missing E_T". Events where a proton or an antiproton emits a gluon in the initial state before a collision are tagged and used for dark matter searches (gluon-bremsstrahlung). The gluons then disintegrate into a mono-jet of hadronic particles. This mono-jet is formed before the collision point and is easily identifiable. By hypothesis, WIMPs are always produced in pairs due to R-parity. The most important background, in this case, is the production of Z bosons which disintegrate into two neutrinos, which, like the WIMPs, do not interact with the detector and therefore produce a signal identical to a pair of WIMPs. The details of the signal analysis, background and systematic errors of the ATLAS experiment are presented in [89]. The analysis is based on the fact that the event rate of this type of signal, which is naturally produced by particles of the Standard Model, is very well known. If a surplus of events is measured, it can be interpreted as a signal produced by the production of dark matter particles.

To compare the results obtained by experiments of direct dark matter production with that of direct detection, it is necessary to translate them in terms of spin-independent and spin-dependent cross sections. To do this, an effective theory that models the known properties of dark matter is used. Using this theory, the different types of interaction are all surveyed. This effective theory considers only the first term of Taylor expansion of the SM-DM interaction propagator around momentum transfer Q_{tr} [89]:

$$\frac{1}{Q_{tr}^2 - M^2} = -\frac{1}{M^2}\left(1 + \frac{Q_{tr}^2}{M^2} + \mathscr{O}\left(\frac{Q_{tr}^4}{M^4}\right)\right) \approx -\frac{1}{M^2}, \tag{4.19}$$

where M is the mass of the mediator. This approximation is only valid if $Q_{tr} < M$, otherwise all the other terms in the expansion must be considered. Once this approximation

has been made, the parameter M is no longer used, but rather $\Lambda = M/\sqrt{g_\chi g_q}$ which parameterizes the energy scale of the effective theory. The terms g_χ and g_q are the coupling parameters of the mediators of the quark and dark matter fields, respectively. The parameters g are constrained by the perturbation theory which imposes $g_\chi g_q < (4\pi)^2$, while the constraint $Q_{tr} > 2m_\chi$ is imposed by the kinematics of the interaction. From these constraints, we obtain that:

$$\Lambda > \frac{Q_{tr}}{\sqrt{g_\chi g_q}} > \frac{Q_{tr}}{4\pi} > \frac{m_\chi}{2\pi}. \tag{4.20}$$

Finally, an effective Lagrangian describes the interaction:

$$L_{eff} = \sum c_i O_i, \tag{4.21}$$

where the c_i are the operator coefficients and the O_i are the operators. For example, if WIMPs are Dirac fermions, a possible interaction between quarks and WIMPs would be the $\bar{\chi}\chi\bar{q}q$ operator whose coefficient is m_q/Λ^3. The details of this effective theory, as well as the different operators and their respective coefficients, are presented in [89]. The effective theory is only valid for a certain range of Λ values for which the mass of the mediator is very large. It is, therefore, preferable to obtain predictions for simplified models which will be more accurate and valid for any mass of mediator. However, the effective theory approach is powerful because it represents all models simultaneously.

It is important to specify that the direct dark matter detection cross sections and those obtained by ATLAS or CMS are complementary. Indeed, as shown in Fig. 4.8, dark matter production experiments probe smaller cross-sections for large masses of mediators, while the limits of direct detection experiments dominate for small mediator masses [90].

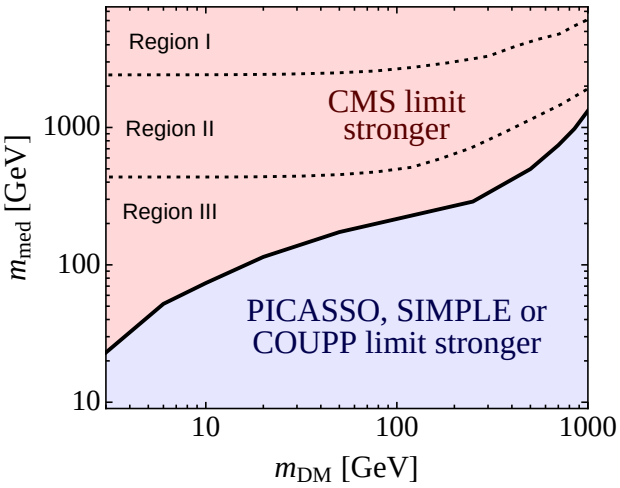

Figure 4.8 – The values of the mediator mass (m_{med}) and the mass of the dark matter particle (m_{DM}), for which the limit on the WIMP-proton cross sections are equal, are represented by the black line. The red region represents the limits where production experiments are better than direct detection experiments using superheated liquid detectors. The blue region represents the opposite [91].

4.7 Indirect detection

Indirect detection involves the measurement of WIMP annihilation products. Depending on the intrinsic nature of the neutralino, that is to say, if it is composed mainly of Wino, Zino or Higgsino, the most favorable channels of annihilation will be different. The possible channels are presented in Table 4.II.

Disintegration channels
ZH
W^+W^-
ZZ
HH
gg
$\gamma\gamma$
$f\bar{f}$

Table 4.II – Decay channels of the neutralino, where f is a fermion, $\bar{f}$ an anti-fermion and g is a gluon [92].

These particles subsequently disintegrate into Standard Model particles including gammas, antiprotons, positrons, and neutrinos. To gather information on the measured quantities of gamma rays, antiprotons, and positrons, the production of these particles by astronomical objects must be known very precisely especially in the case of gamma rays. Indeed, gamma rays observed by telescopes come from many different sources and their production mechanisms in the universe is not yet fully understood. Furthermore, to measure such signals, it is advantageous to probe regions of the space where the density of WIMPs is high. Since the center of our galaxy, of the Sun, and of Earth are dense regions, they generate more annihilation products.

When WIMPs annihilate, they can also create very high energy neutrinos. Furthermore, WIMPs lose momentum when they interact with baryonic matter by elastic collisions which means that their velocity can become lower than the escape velocity of the Earth or the Sun due to their gravitational potential. Thus WIMPs can get trapped in the center of the Sun and Earth and if WIMPs accumulate, their density increases and so does the number of decays. These decays could produce neutrinos emanating from the center of the Earth or of the Sun and could be detected. The experiences IceCube [93], and ANTARES [94] are experiments that actively seek this signal.

CHAPTER 5

SUPERHEATED LIQUID DARK MATTER DETECTORS

As shown in the previous chapter, several detector features are important for dark matter experiments. The electroweak strength ($10^{-39} - 10^{-50}$ cm^{-2}) of WIMP-nucleon interactions imposes the use of active targets scalable up to tonne scales. Experiments need a large exposure (kgd), i.e., a large active mass (kg), and a sufficiently large acquisition time (d) to optimize dark matter detection.

Another challenge is the small nuclear recoil energies which are expected in the range of $0.1 - 100$ keV for WIMP masses between $1 - 1000$ GeV/c^2. The PICASSO (Project In CAnada to Search for Supersymmetric Objects) and PICO experiments are both dark matter direct detection experiments that use superheated liquids to detect dark matter. PICO is the result of a merge between the PICASSO and the COUPP collaborations which occurred in 2014. The experiments use the bubble chamber technique with energy thresholds set by the operating conditions, i.e., temperature and pressure. The detectors can be operated at energy thresholds as low as a few keVs and events consist of a bubble formed by a heat spike following WIMP interaction in the liquid.

There are several specific backgrounds for this experimental technique which are discussed in Chap. 8. The active liquids used in both experiments are fluorinated hydrocarbons whose chemical compositions are C_4F_{10} and C_3F_8 for the PICASSO and PICO experiments, respectively. Those two freons are rich in ^{19}F and therefore provide enhanced sensitivity to SD interactions.

5.1 Bubble chambers

The bubble chamber was invented in 1952 by Donald A. Glaser which earned him the physics Nobel Prize in 1960 [95]. A bubble chamber consists of a large volume of

superheated liquid (e.g.: H, Freons, Ar, propane) placed inside a chamber made of either glass or metal. A superheated liquid is a metastable state that can undergo a phase transition to the vapor phase following the energy deposition of a particle. The bubbles produced along the path of a particle are recorded by a camera system and the kinematics of particles can be reconstructed from the photographic film.

The bubbles are not allowed to grow indefinitely and shortly after the passage of particles the pressure is raised to condensate the vapor to liquid. The operation of bubble chambers has rapidly evolved since its inception to adapt to different applications. Initially, Glaser developed the bubble chamber with the intention of detecting cosmic rays to replace the common cloud chamber detectors used at that time. However, triggering the cameras in coordination with the passage of cosmic rays was a difficult task. On the other hand, by placing the chamber in front of the beam of an accelerator, it can be activated in coincidence with the short beam spills. In this case, the chamber is recompressed after about 50 ms, and nucleations occurring due to irregularities in vessel walls are not important [96]. A magnetic field is applied to curve the path of incoming particles to identify their charge and to obtain their momentum. One of the best-known bubble chambers was Gargamelle a $12\,\mathrm{m}^3$ chamber filled with freon and operated at CERN between 1970 and 1979 at the PS and SPS neutrino beams [97]. The chamber is famous for its discovery of weak neutral currents at CERN in 1973.

Nowadays, this type of detector is no longer used in high energy physics, and wire chambers and semiconductor detectors have replaced it. In high energy physics, bubble chambers were operated at very high superheat to detect minimum ionizing particles (MIPs) while bubble chambers operated at low superheat are insensitive to MIPs, but fully sensitive to nuclear recoils. This characteristic lead this detection technique to a renaissance during the 90's in detectors for direct dark matter searches. In this application, the time during which the liquid is kept in the metastable state must be much longer, i.e., of the order of several minutes. Various experiment use the bubble chamber technique for dark matter searches such as PICASSO [1], COUPP [68], PICO [2], MOSCAB [66],

and SIMPLE [69].

Historically, the PICASSO experiment has pioneered the SHL technique in dark matter searches. The superheated liquid is in the form of a few millions of C_4F_{10} droplets of 200 μm in diameter that are suspended in a gel matrix. Once a droplet goes through a phase transition it stays gaseous until the whole detector is recompressed and therefore a detector can run continuously for several hours. In this case, there are no cameras, but the acoustic signals emitted during bubble formation are recorded by piezoelectric sensors installed at the acrylic detector walls [98].

COUPP and PICO detectors work exactly like traditional bubble chambers, but at reduced superheat. This type of detector uses synthetic silica jars to contain superheated C_3F_8 or CF_3I. Cameras take photographs of the bubbles and trigger a pressure system when a bubble is created. The cameras recognize bubbles when they reach a dimension of approximately 1 mm. A hydraulic pressure system compresses a bellows to recompress the SHL, while the temperature is controlled via a thermal bath in which the detector is immersed.

The Geyser detector is another version of a bubble chamber that is autoregulated by the usage of a thermal gradient. The superheated liquid and its saturated vapor are separated by a buffer liquid. Since the vapor is kept at a lower temperature than the liquid ($T_{vap} < T_{liq}$), the pressure applied onto the liquid is less than the vapor pressure of the liquid itself. Therefore, the liquid is in a superheated metastable state. When a phase transition occurs, vapor rises towards the top of the detector, passes through the buffer liquid and condensates after cooling and descends to rejoin the bulk liquid where it heats up and becomes superheated again. A schematic view of such a detector is shown in Fig. 5.1. PICASSO has developed several geyser prototypes at Université de Montréal (UdeM), and the MOSCAB collaboration has installed a 4L version at LNGS.

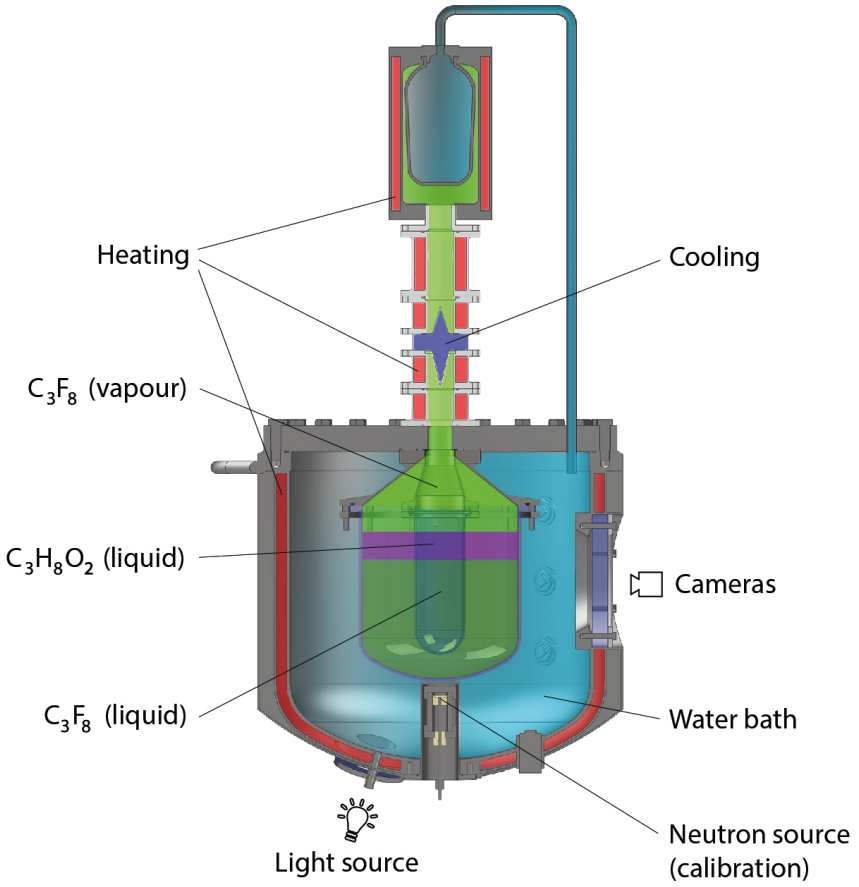

Figure 5.1 – Schematic view of the MOSCAB Geyser detector [66].

When a local phase transition occurs, it produces an acoustic emission that contains information on the nature of the incident particle. The theoretical characteristics of the acoustic emission depend on the growth mechanism of the bubbles. When bubble chambers were used in high energy accelerator physics, the theoretical aspects of bubble growth was important, because size and time evolution affected the quality and resolution of photographs. The theoretical description of bubble formation and bubble growth was developed in the ’60s and ’70s and are still relevant today in dark matter searches.

5.2 Superheated liquids

Fig. 5.2 shows a typical phase diagram where the dark orange area indicates the temperature and pressure region where a liquid is superheated, i.e., metastable liquid state. It is useful to introduce the thermodynamic potentials that describe the phase of a substance to describe the physics of the superheated state.

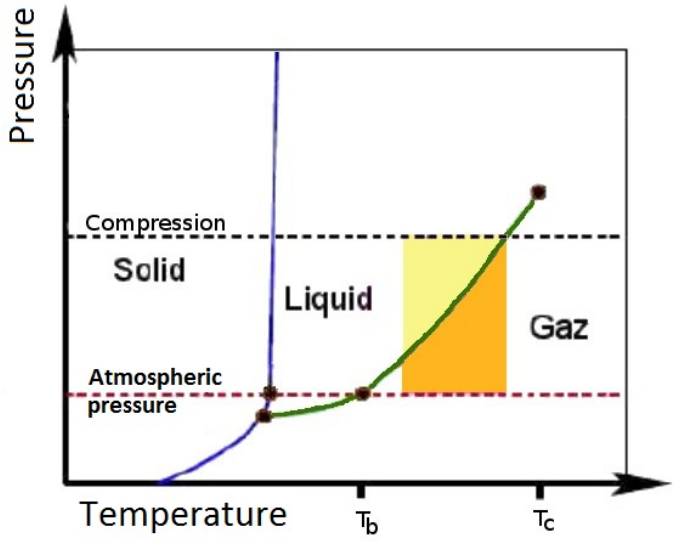

Figure 5.2 – Phase diagram indicating the region, in dark orange, of the superheated state and the stable liquid phase in yellow. The x-axis also shows the critical temperature T_c and the boiling temperature T_b .

The chemical potential of a substance must be calculated to determine the state of a substance held at constant pressure and temperature since the state with the lowest chemical potential is always the state that is favored by a substance. Therefore, the chemical potential denoted μ, is analogous to the gravitational potential. In the case of a phase transition, the chemical potential of a substance is defined as the energy that can be absorbed or released due to a change of the particle number from one phase to another. When chemical equilibrium is reached, e.g., in H_2O at the boiling point, both phases, i.e., the liquid and the gaseous phases coexist, because they both minimize the chemical potential. The first step to express the chemical potential μ_i of species i is to

consider the Gibbs free energy G:

$$G = U + PV - TS, \tag{5.1}$$

where U is the internal energy, S is the entropy, V is the volume, T is the temperature, and P is the pressure. The Gibbs free energy is the available energy at a constant temperature and pressure that may be used in a thermodynamic system. Replacing the expression for the internal energy U,

$$U = TS - PV + \sum_{i=1}^{n} \mu_i N_i, \tag{5.2}$$

in eq. 5.1, one gets:

$$G = \sum_{i=1}^{n} \mu_i N_i. \tag{5.3}$$

Consequently, for a substance containing only one species, the chemical potential is equal to the molar Gibbs free energy:

$$\mu = \frac{G}{N} = G_m. \tag{5.4}$$

Both quantities, the chemical potential, and molar Gibbs free energy are minimized when a system reaches chemical equilibrium at constant temperature and pressure.

One important information that is relevant in the context of superheated liquid dark matter detectors is how the chemical potential changes as a function of pressure and temperature. By definition, the Gibbs free energy differential eq. is

$$d\mu = dG = VdP - SdT + \mu dN. \tag{5.5}$$

If the substance is held at constant temperature ($dT = 0$) and the number of particles is

constant ($dN = 0$), and one considers the molar Gibbs free energy, one gets:

$$d\mu = dG_m = V_m dP, \tag{5.6}$$

where V_m is the molar volume, i.e., the volume of one mole of a substance. While this equation does not give any information regarding the absolute value of the Gibbs potential for the different phases, it indicates how it changes as a function of pressure. Knowing that the molar volume of the solid phase is smaller than that of the liquid phase, which in turn is smaller than that of the gaseous phase ($V_{m,s} < V_{m,l} < V_{m,g}$), the Gibbs free energy as a function of pressure can be schematically shown as in Fig. 5.3

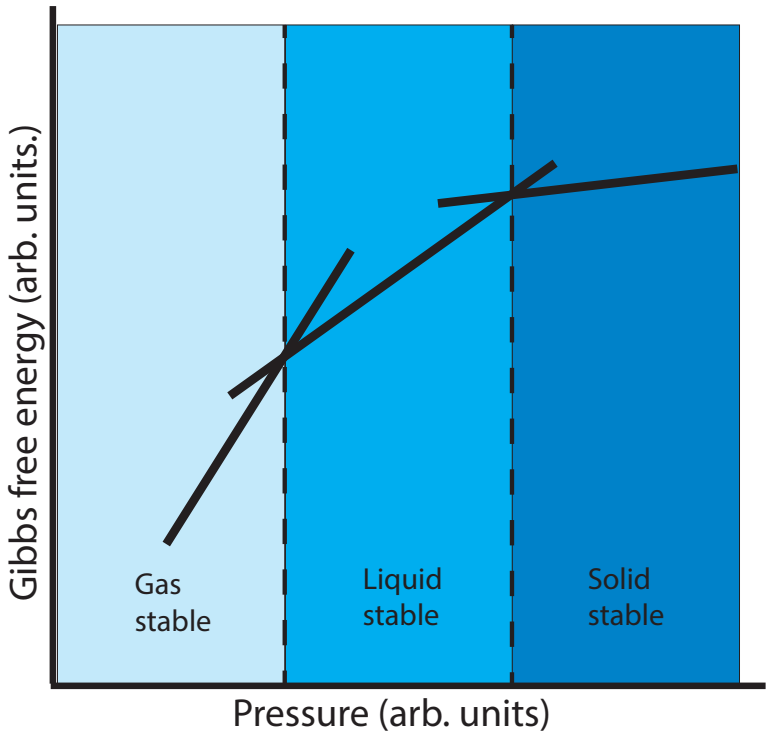

Figure 5.3 – Schematic view of the Gibbs free energy as a function of pressure. The gradient of each phase is given by the molar volume. A substance always rests in the state with the lowest possible Gibbs free energy. At a phase transition point, the Gibbs free energy of both states is equal as the schematic shows (crossing lines at phase transition points). While the molar volume of the solid and liquid states can be approximated as being constant, this is not the case for the gaseous phase as it is described in the text .

Taking the molar volume to be constant for the solid and liquid phase, the molar volume of an ideal gas is:

$$V_m = \frac{RT}{P}, \tag{5.7}$$

where R is the gas constant. The Gibbs free energy for an ideal gas as a function of pressure becomes:

$$d\mu = dG_m = V_m dP = RT\frac{dP}{P}. \tag{5.8}$$

Integrating this last equation yields:

$$\Delta G = RT ln\frac{P_f}{P_i}, \tag{5.9}$$

where P_f and P_i are the final and initial pressure of the system, respectively. A similar derivation can also be done at constant pressure to obtain the Gibbs free energy as a function of temperature:

$$d\mu = dG_m = -S_m dT. \tag{5.10}$$

In this case, the gradient is the negative of the entropy S_m. Thus, gases, which have large entropies, have the steepest gradient and solids have the smallest gradient. Experimentally, both the PICASSO and PICO experiments vary the pressure to reach the superheated state while keeping the temperature stable.

Now that the phase transition mechanism and its thermodynamic potential, i.e., the chemical potential and Gibbs free energy, have been described, superheated liquids can be defined. Consider a substance in the liquid state for which the pressure is decreased slowly. According to Fig. 5.3, the Gibbs free energy of the liquid and gaseous phases decrease until they reach equilibrium. If the pressure is lowered further, the Gibbs free energy of the gaseous phase will become smaller than that of the liquid phase. It is

described schematically by plotting the Gibbs free energy as a function of density for various pressures and is shown in Fig. 5.4

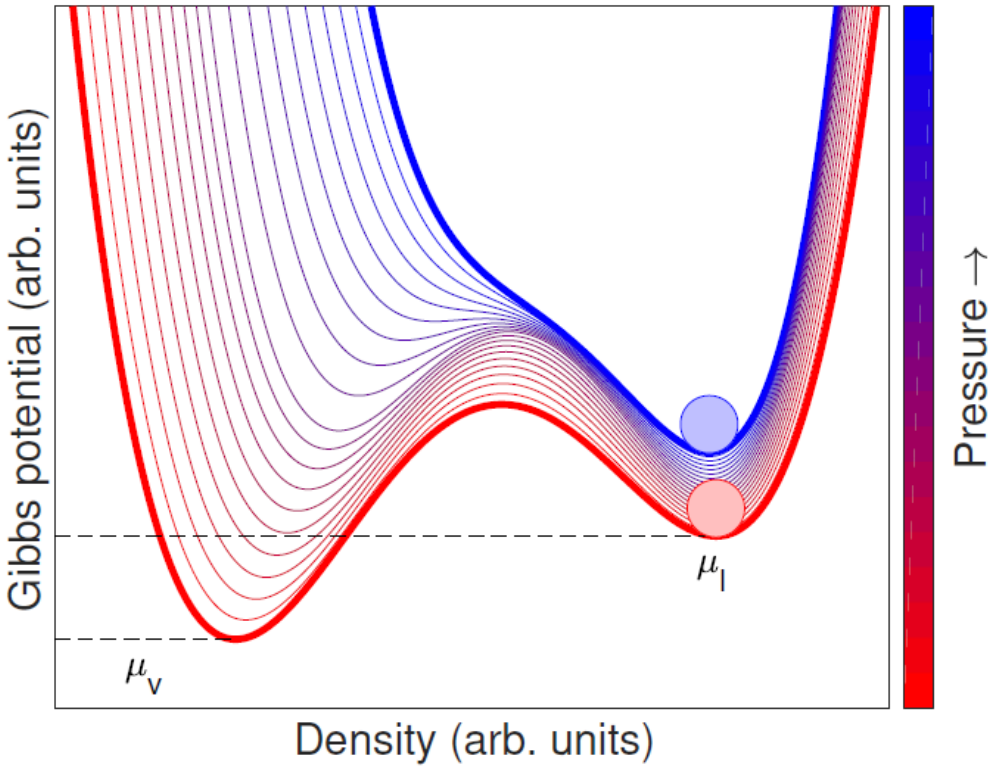

Figure 5.4 – Schematic view of the Gibbs free energy as a function of density and for various pressures. As the pressure is decreased (blue to red), the Gibbs free energy (μ_l and μ_v) for both phase, i.e. liquid and vapor, decreases, but that of the gas phase decreases more quickly than the liquid phase. Hence, the most stable state become the gaseous phase [99].

While both chemical potentials, μ_l and μ_v, decreases, μ_v decreases faster than μ_l when the pressure is lowered. If the pressure is decreased slowly, a potential barrier emerges, and thus the substance can get stuck in the liquid phase. When this happens, the liquid is in a metastable state called superheated state. This potential barrier can be overcome, e.g., by heating, and most importantly, if a particle passes through the metastable liquid, it could deposit enough energy to trigger a phase transition. The energy barrier or energy that a particle has to deposit can be calculated in the context of

the Seitz model which is described in the next section.

5.2.1 Critical radius

When a quantity of energy is deposited in a superheated liquid, a local phase transition is initiated by the heat spike thereby creating a protobubble, i.e., a spherical cavity of radius R filled with vapor and surrounded by superheated liquid. There is a critical radius, r_c, such that the protobubble is in static equilibrium with the surrounding liquid. If the radius of the protobubble is smaller than r_c, it collapses on itself whereas if the radius is larger than r_c, it carries out a macroscopic expansion. The following equation gives the critical radius [100]:

$$r_c = 2\sigma/(P_b - P_l), \tag{5.11}$$

where σ is the surface tension, P_b is the vapor pressure inside the protobubble and P_l is the superheated liquid pressure. P_l is a quantity controlled experimentally, however, this is not the case for P_b which must be approximated by using other measurable quantities. To show this, one considers the change in the Gibbs free energy of a superheated liquid and of a gaseous bubble at constant temperature T due to a pressure variation (eq. 5.6) as shown in Fig. 5.3. The change in the Gibbs free energy by going from P_l to P_v ($P_l < P_v$) in the liquid phase can be equivalent to that of going from P_b to P_v in the gaseous phase for a specific value of P_b, where P_v is the vapor pressure on the saturation curve, that is when $\mu_l = \mu_v$. Schematically, in Fig. 5.3, P_v corresponds to the point where the liquid and gaseous curves cross each other. Since the gradient in both phases differ, P_b cannot be equal to P_l. However, since P_v and P_l are measurable quantities and since the Gibbs free energy at the equilibrium vapor pressure, P_v, is equal for the gaseous and liquid phase, i.e.,

$$\mu_l(P_v, T) = \mu_v(P_v, T). \tag{5.12}$$

P_b can be expressed as a function of those two quantities, i.e., P_l and P_v. The fact that $\mu_l = \mu_v$ at P_v is very convenient since it reduces the number of unknown quantities in the following calculations.

The change in the Gibbs free energy, ΔG, when going from P_l to P_v in the liquid phase is:

$$\int_{P_l}^{P_v} V_{m,l} dP, \tag{5.13}$$

where $V_{m,l}$ is the molar volume in the liquid phase. The change in the Gibbs free energy in the gaseous phase is:

$$\int_{P_b}^{P_v} V_{m,v} dP. \tag{5.14}$$

Varying the pressure from P_l to P_v in liquid phase is equivalent to a change of pressure of P_b to P_v in the gaseous phase for a specific value of P_b that has to be expressed as a function of P_l and P_v:

$$\int_{P_l}^{P_v} V_{m,l} dP = \int_{P_b}^{P_v} V_{m,v} dP, \tag{5.15}$$

where P_v, P_l, $V_{m,l}$ and $V_{m,v}$ can all be measure experimentally and hence P_b can be calculated by evaluating the above integrals. Assuming an incompressible liquid and an ideal gas at constant isothermal compressibility ($V_{m,v} = \text{ct}$, $P = V_m RT$), one obtains:

$$V_{m,l}(P_v - P_l) = RT\, ln(\frac{P_v}{P_b}) = P_v V_{m,v} ln(\frac{P_v}{P_b}). \tag{5.16}$$

Knowing that the molar volume is given by:

$$V_{m,phase} = \frac{M}{\rho_{phase}}, \tag{5.17}$$

where ρ_{phase} is the density of the substance, M is the molar mass which is independent

of the state of a substance, V_m can be replaced by $1/\rho_{phase}$:

$$\frac{(P_v - P_l)}{\rho_l} = \frac{P_v}{\rho_v} ln\Big(\frac{P_v}{P_b}\Big), \tag{5.18}$$

and, P_b can be obtained as a function of known thermodynamic variables:

$$P_b = P_v e^{-\frac{\rho_v}{\rho_l}(1-\frac{P_l}{P_v})} \approx P_v - \frac{\rho_v}{\rho_l}(P_v - P_l). \tag{5.19}$$

While P_b is close to P_v, it is slightly lower. Eq. 5.19 can then be used to evaluate the critical radius r_c:

$$r_c = \frac{2\sigma}{P_v - P_l}\frac{\rho_l}{\rho_l - \rho_v} \approx \frac{2\sigma}{P_v - P_l}. \tag{5.20}$$

The bounds of the integrals of eq. 5.15 could have been different, but choosing a common bound, i.e., P_v, makes it possible to express P_b as a function of P_v and P_l only. This quantity is crucial to calculate the critical energy that must be deposited inside the critical radius to produce a phase transition in a superheated liquid. The critical radius of superheatead C_4F_{10} as a function of temperature at 1 (blue) and 1.2 bar (red) is shown in Fig. 5.5. The correspondence between temperature and critical energy is discussed in the next section and is shown in Fig. 5.6 for C_4F_{10}.

5.2.2 Seitz Model

The Seitz Model [101] describes the required conditions to induce a phase transition in a superheated liquid. It states that the energy supplied to the superheated liquid to generate a complete phase transition must be deposited inside the critical radius and larger a critical energy E_c.

$$E_{dep} = \frac{dE}{dx} r_c > E_c, \tag{5.21}$$

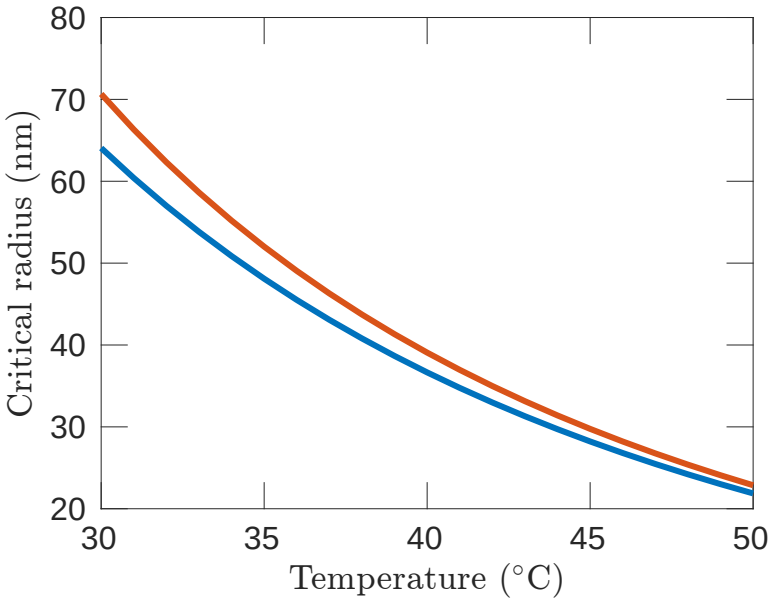

Figure 5.5 – Critical radius of C_4F_{10} as a function of temperature at a pressure of 1 bar (blue) and 1.2 bar (red) which correspond to the ambient pressure at SNOLAB .

where $\frac{dE}{dx}$ is the loss of energy E per unit path length dx of a particle. This model treats the deposition of energy as a "heat-spike" and the critical energy is given by the relation:

$$E_c = \frac{4\pi}{3} r_c^3 \rho_b (h_b - h_l) + 4\pi r_c^2 \left(\sigma - T\frac{d\sigma}{dT}\right) - \frac{4}{3}\pi r_c^3 (P_b - P_l) + W_{irr}, \tag{5.22}$$

where ρ_b is the density inside the bubble, i.e:

$$\rho_b \approx \rho_v \frac{P_b}{P_v}, \tag{5.23}$$

where h_b and h_l are the enthalpies of the states inside and outside the bubble, respectively. σ is the surface tension of the bubble, i.e., when $P_b - P_l \neq 0$, which is not the case in a superheated liquid.

The first term in eq. 5.22, represents the change in enthalpy, that is the change in internal energy in the fluid plus the work done by the expanding bubble against the liquid held at P_l which therefore includes the work done to produce the bubble itself. The

second term is the free energy of the surface, or the energy required to form the surface in the presence of a thermal reservoir. The heat drawn from the reservoir is the third term ($\frac{\partial\sigma}{\partial T} < 0$, so this term is also positive). The fourth term is the mechanical work required to create the bubble and is a negative term. The negative sign is explained by the fact that the first and second terms both count the energy to produce the bubble itself. This contribution has to be subtracted to avoid double counting.

In addition to those terms, there is also irreversible terms (W_{irr}) that include notably the emission of acoustic waves, effects due to the viscosity, energy lost to scintillation and energy lost due to diffusion of heat outside of the critical radius. The relative contribution of each term is shown in Table 5.I for C_4F_{10} which are also very similar for C_3F_8. The sum of each contribution does not sum up to E_c since the three listed terms are first-order terms: $Q_{0,w}, Q_{0,h}, (Q_{0,s} + Q_{0,ds})$. The second order terms must be taken into account to obtain E_c as explain in the following paragraphs.

Critical energy (Q)	$4\pi/3R_c^3\Delta_p$	$4\pi/3R_c^3\rho_v(h_b - h_l)$	$4\pi R_c^2(\sigma - Td\sigma/dT)$
1 keV	-0.05	0.43	0.57
10 keV	-0.5	5.85	4.49
100 keV	-4.38	71.71	32.37

Table 5.I – Normalized relative contribution of each Seitz energy terms at different threshold energies .

Each term in eq. 5.22 must be expressed differently in order to be calculable or directly approximated. The presence of a pressure difference of $P_b - P_v$ between the bubble and the liquid that surrounds it generates a spherical bubble. When surface tensions are measured, it is for a planar interface, i.e. on the saturation curve ($P_v = P_b$). To consider the surface tension of curved interfaces, the Tolman length (δ) must be taken into account, which by definition measures the difference between planar and curved interfaces. The Tolman length appears in the definition of the surface tension σ as follows:

$$\sigma = \sigma_0 + (P_b - P_v)\delta = \sigma_0\left(1 + 2\frac{\delta}{r_0}\right), \tag{5.24}$$

where σ_0 is the planar surface tension and r_0 is defined as followed:

$$r = r_0 + 2\frac{\delta}{r_0}, \tag{5.25}$$

where r_0 is the critical radius valid for a planar surface tension. Using those definitions, σ can be calculated using tabulated values of σ_0. The Tolman length is typically of the same order as the inter-molecular spacing, i.e a few angstroms, and it can be approximated to be constant. Terms involving the Tolman length are very small since r_0 is typically a fews tens of nanometers. Therefore, the critical energy Q can be written as an expansion series in orders of δ/r_0:

$$E_c = Q_0 + Q_1\frac{\delta}{r_0} + ... \tag{5.26}$$

Using this definition, Q_0 and Q_1 can be written as:

$$Q_0 = Q_{0,h} + Q_{0,s} + Q_{0,ds} + Q_{0,w}, \tag{5.27}$$

$$Q_1 = Q_{1,h} + Q_{1,s} + Q_{1,ds} + Q1_{,w}, \tag{5.28}$$

$$\tag{5.29}$$

where $Q_{0,h}$, $Q_{0,s}$, $Q_{0,ds}$, $Q_{0,w}$ correspond exactly to the terms in eq. 5.22 in the same order. The mathematical expressions of the Q_1,x terms are available in appendix A. They are small corrections to the first-order terms and their description is the same as the first-order terms.

The last term that has to be modified, to properly calculate the various terms above, is $h_b - h_l$. If $h_b = h_v$, the calculation of $h_v - h_l$ would be straightforward as it would be equal to ΔH_{vap}, that is the latent hear of vaporization which is the amount of energy (enthalpy) that must be added to a substance to transform a quantity of liquid to the gaseous phase and is usually expressed in J/kg. Since h_b is slightly lower than h_v, one

obtains:

$$h_b - h_l \approx \Delta H_{vap} + \frac{(P_v - P_l)}{\rho_l} T(\alpha_v - \alpha_l), \tag{5.30}$$

where ΔH_{vap} is the normal heat of vaporization of the fluid, that is $h_v - h_l$. The variable α is the thermal expansion coefficient that is given by

$$\alpha = 1/V(\partial V/\partial T)_P, \tag{5.31}$$

where V is the volume of the liquid. The most important approximations in this calculation are assuming that the α term is constant and that the fluid is incompressible. The term ΔH_{vap} is 100 to 1000 times larger than the correction term, i.e., the term containing the coefficients of thermal expansion.

All these thermodynamic parameters are compiled by NIST [102] from which the critical energy (E_c) and the critical radius (r_c) can be calculated. Since PICASSO detectors are operated at constant pressure and variable temperatures, the critical energy is shown as a function of temperature in Fig. 5.6. On the other hand, PICO detectors are operated at a constant temperature, and pressure varies and therefore the critical energy is plotted as a function of pressure in Fig.5.7.

5.3 Bubble growth

When the Seitz conditions are not fulfilled, the protobubble collapses on itself, while in the opposite case, it continues to grow. The dynamic of bubble growth can be then separated into two stages. The descriptions of each stage are described by the theoretical work of Rayleigh [103], and Plesset and Zwick [104] and are both based on approximated solutions of the Navier-Stokes equation.

The first bubble regime starts when a bubble reaches the critical radius r_c. In this stage, the bubble keeps growing by using the energy stored within itself. The force

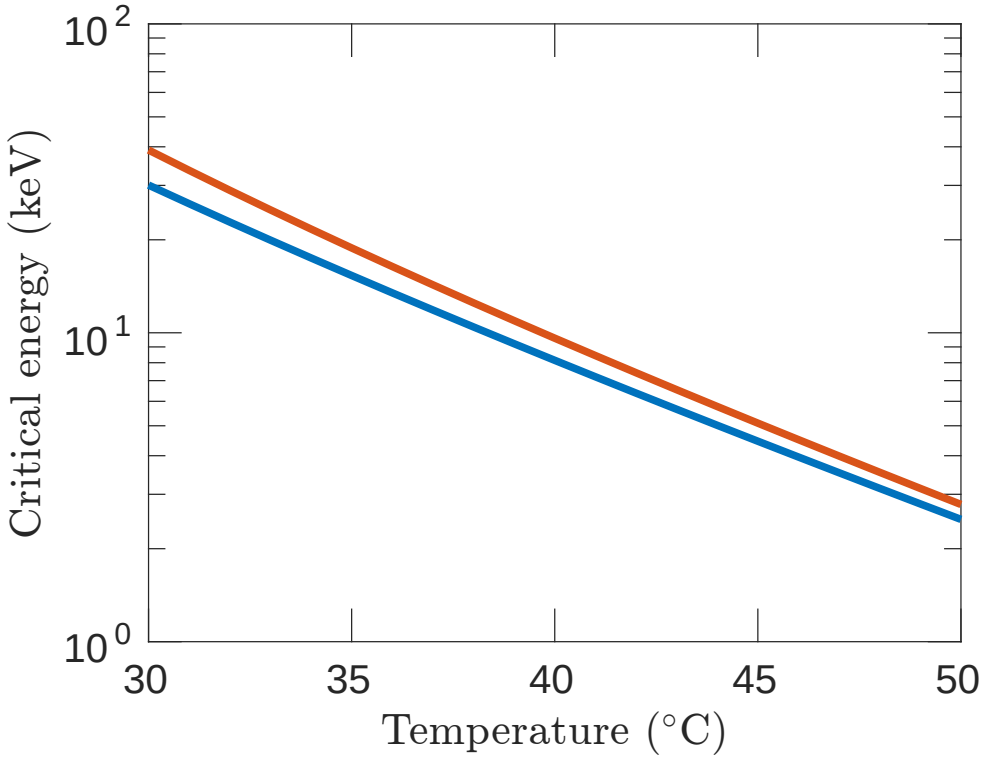

Figure 5.6 – Critical energy of C_4F_{10} as a function of temperature at a pressure of 1 bar (14.5 PSIA) (blue) and 1.2 bar (17.4 PSIA) (red) which correspond to the ambient pressure at SNOLAB .

acting against the growth of the bubble is the surface tension of the surrounding liquid which decreases as the bubble grows. It is described mathematically by the Rayleigh-Plesset equation. This regime is governed by the following eq. [103, 105]:

$$P_b = P_l + \frac{3}{2}\rho_l \dot{r}^2 + \rho_l r\ddot{r}, \tag{5.32}$$

where P_b is the pressure inside the bubble, P_l is the external pressure of the liquid, ρ_l is the density of the liquid and r is the radius of the bubble. The solution to this equation is given by

$$r_1(t) = \phi_1 t, \text{ with, } \phi_1 = \left(\frac{2}{3\rho_l}(P_b - P_l)\right)^{1/2}, \tag{5.33}$$

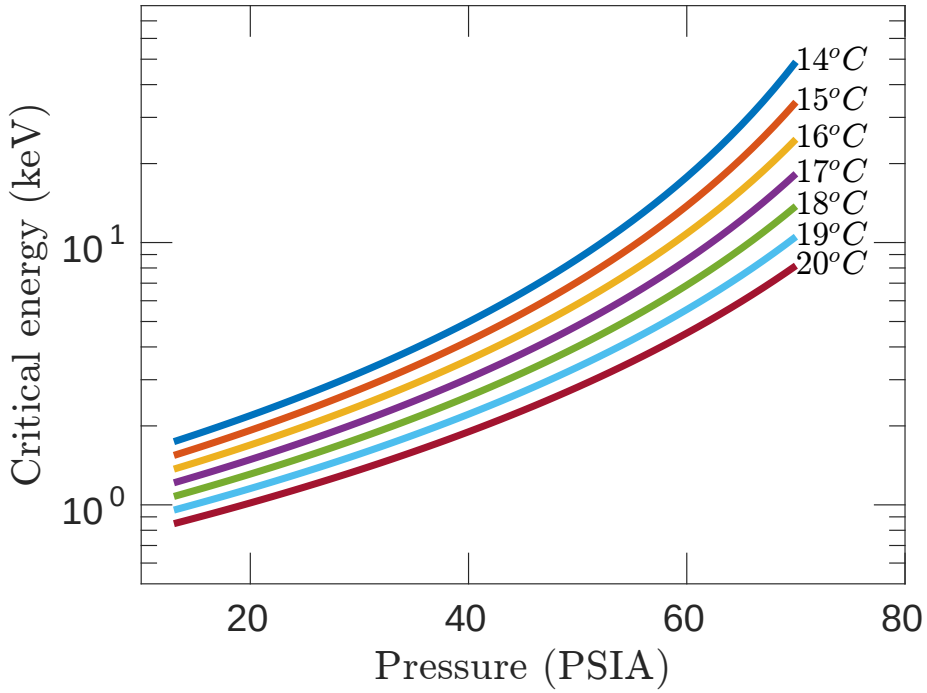

Figure 5.7 – Critical energy of C_3F_8 as a function of pressure for temperatures between 14 and 20°C .

where ϕ_1 is the rate of expansion of the inertial regime.

The second regime, known as the thermal growth regime, manifests itself when the energy in the immediate vicinity is no longer sufficient to fuel the phase transition. It is then required that the energy be provided by heat transfer from the region that surrounds the bubble. This regime is governed by the following expression [104]:

$$\frac{\partial T}{\partial t} + \frac{R^2\dot{R}}{r^2}\frac{\partial T}{\partial r} = D\left(\frac{\partial^2 T}{\partial r^2} + \frac{2}{r}\frac{\partial T}{\partial r}\right), \tag{5.34}$$

where r is the radius of the bubble, T is the temperature at a distance R from the center of the bubble and D is the thermal diffusivity. The solution of this equation is given

in [105]:

$$r_2(t) = \phi_2 t^{1/2} \text{ , with, } \phi_2 = Ja(12D/\pi)^{1/2}. \tag{5.35}$$

$$Ja = \frac{\rho_l C_l [T_l - T_{sat}(P_l)]}{\rho_v \Delta H_{vap}}, \tag{5.36}$$

where C_l is the specific heat capacity in the liquid phase, ρ_l the liquid density, T_l the temperature outside the droplet, $T_{sat}(P_l)$ is the saturation temperature at the external pressure, ρ_v is the vapour density of the droplet and ΔH_{vap} the enthalpy of evaporation. Ja is the so called Jakob number and is a dimensionless parameter. A typical bubble radius time evolution is shown in Fig. 5.9.

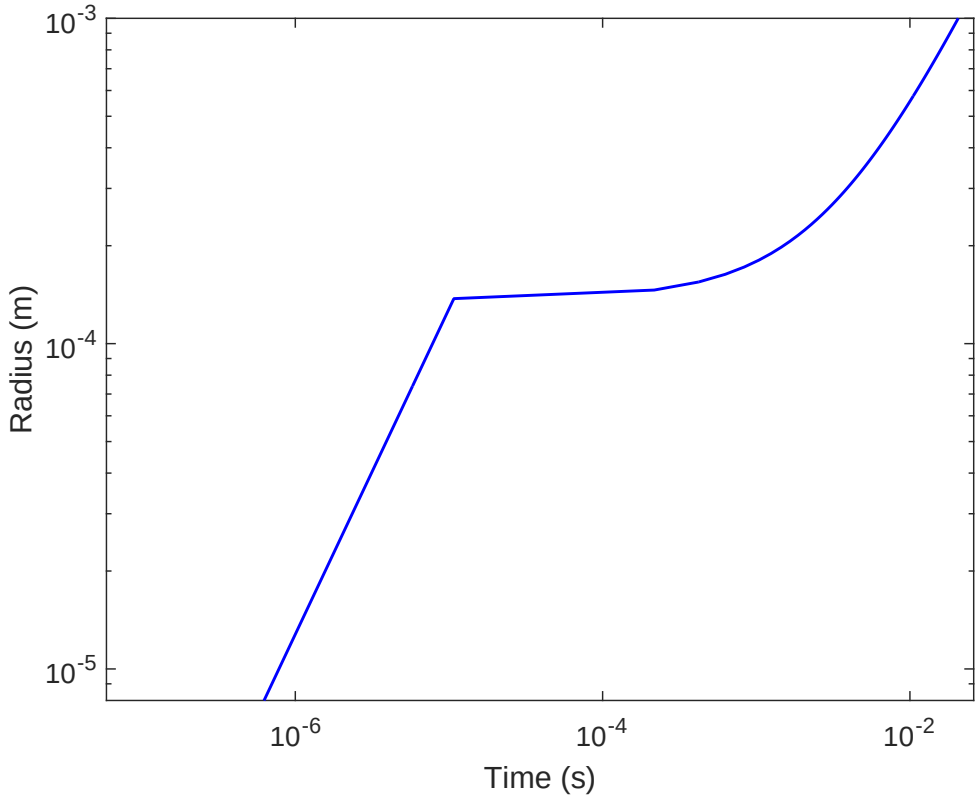

Figure 5.8 – Bubble radius time evolution. The linear time evolution corresponds to the inertial regime. The bubble growth evolves into the thermal regime at time t = τ which slows down the growth.

5.4 Acoustic emission

During the expansion of the bubble, an acoustic wave is emitted whose intensity is given by the following equation [106]:

$$I = \frac{\rho_l \ddot{V}^2}{4\pi C}, \tag{5.37}$$

where $\ddot{V}$ is the second derivative of the volume of the expanding bubble with respect to time and C is the speed of sound. It is then possible to obtain an expression for each regime by assuming that the expanding volume is a sphere. In this case, we get the

following expression for $\ddot{V}$:

$$\frac{4\pi\ddot{r}^3}{3} = \frac{4\pi}{3}(3r^2\ddot{r} + 6\dot{r}^2 r)^2. \tag{5.38}$$

Thus, the intensity for the inertial and thermal regime is given respectively by the following equations using r_1 and r_2 and where $\ddot{r}_1 = 0$ during the Rayleigh regime:

$$I_T = \frac{\pi\rho_l\phi_2^6}{C}\frac{1}{t}, \tag{5.39}$$

$$I_I = 16\pi\rho_l\phi_1^6 C t^2. \tag{5.40}$$

To calculate the total acoustic emission or the radius of a bubble, one needs to know the time required for the inertial regime to evolve into the thermal regime which happens when the bubble cools to the boiling point. A good approximation is to consider the time when the bubble radius in the inertial regime is equal in the thermal regime, that is when $r_2(t) = r_1(t)$ and solve for t which gives:

$$\tau = (\phi_2/\phi_1)^2, \tag{5.41}$$

where τ is the transfer time. This model assumes that there is a sharp transition between the inertial and thermal regime that occurs exactly at $t = \tau$ which is an approximation. A typical intensity versus time plot is shown in Fig. 5.9. The intensity behavior changes at $t = \tau$ and drops drastically.

Instead of finding an approximated solution to the Navier-Stokes equation as Rayleigh, Plesset and Zwick did, the equation can be solved numerically and is still today an area of active research. However, the results obtained by using the above equation are an excellent approximation when compared to numerical results [107].

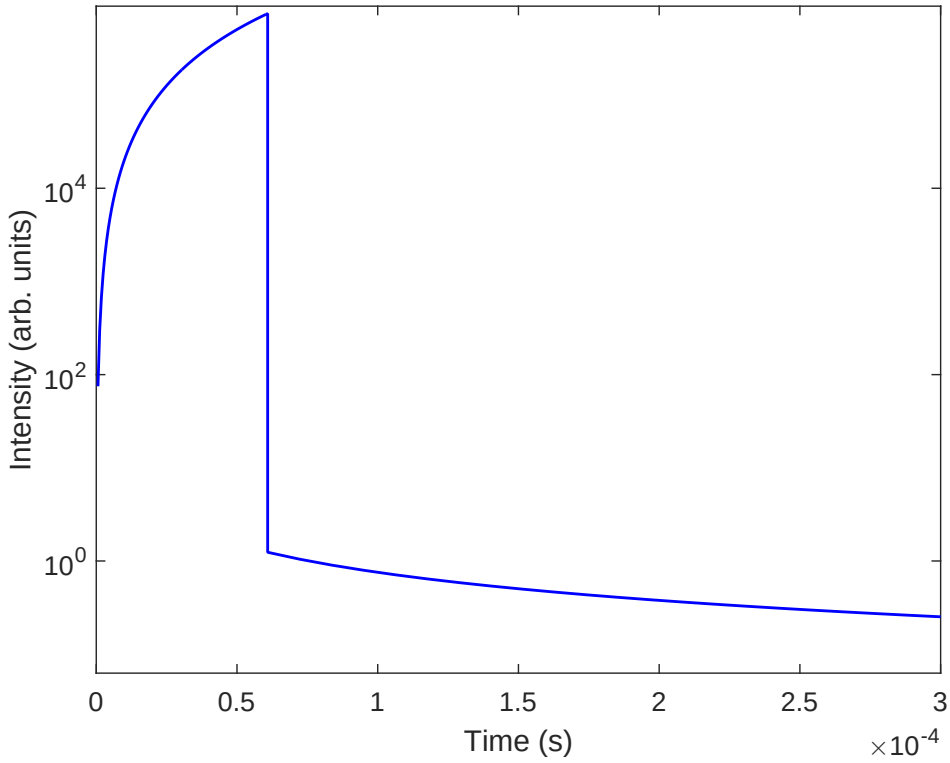

Figure 5.9 – Time evolution of the acoustic emission. The intensity rises quickly during the inertial regime and then becomes nearly negligible during the thermal regime. The inflection point corresponds to t = τ .

5.5 Acoustic response to different target fluids

The acoustic model presented in the previous section is valid for any SHL including freons. The PICASSO experiment had already compared the theoretical acoustic emission of this model to the amplitude of acoustic signals as a function of temperature as shown in Fig. 5.10 [108]. It is the first evidence that this model can predict acoustic emission characteristics of SHL bubble chamber detector.

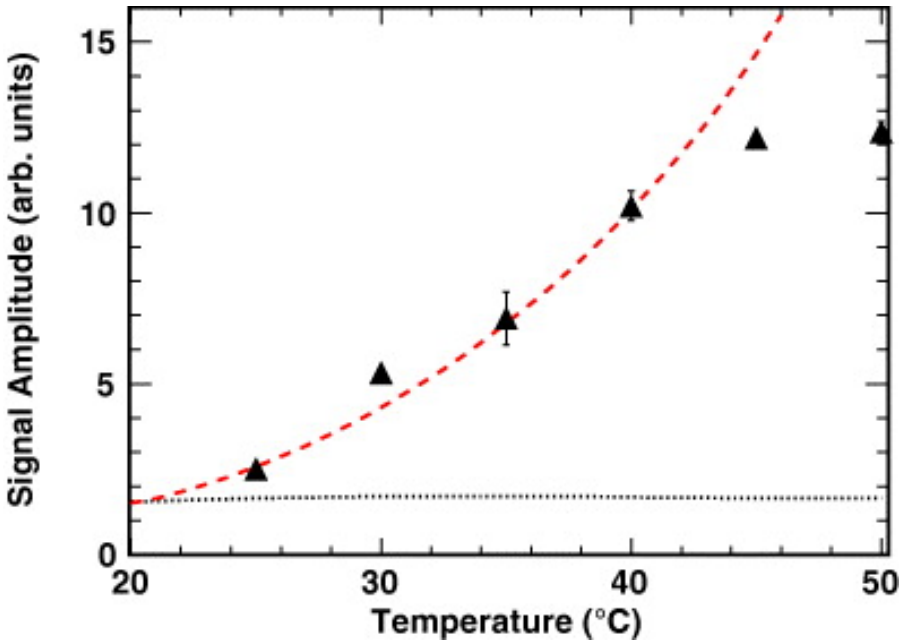

Figure 5.10 – PICASSO detector acoustic amplitude versus temperature at 1 bar compared to theoretical prediction. The red and black dotted lines represent the acoustic emission in the inertial regime and thermal regime respectively. The theoretical inertial regime replicates the experimental data [108].

The main goal of this section is to compare the theoretical acoustic emission of four different freons: $C_2H_2F_4$, C_2ClF_5, C_3F_8 and C_4F_{10}, where the first one is a freon that could be used for dark matter searches in the future, the second was used to perform a monoenergetic recoil calibration, the third is used for PICO WIMP searches, while PICASSO detectors are filled with the fourth one. Instead of considering the variation of the acoustic emission as a function of temperature at a fixed pressure as shown in Fig. 5.10, here the energy threshold is fixed at 2 keV, and pressure and temperature are varied correspondingly. Furthermore, the maximum radius of a bubble is set to 1 mm because this is approximately the size a bubble reaches before the PICO camera system triggers the compression system. Finally, the lowest operating pressure considered is 20 PSIA since PICO detectors are not stable at lower operating pressures.

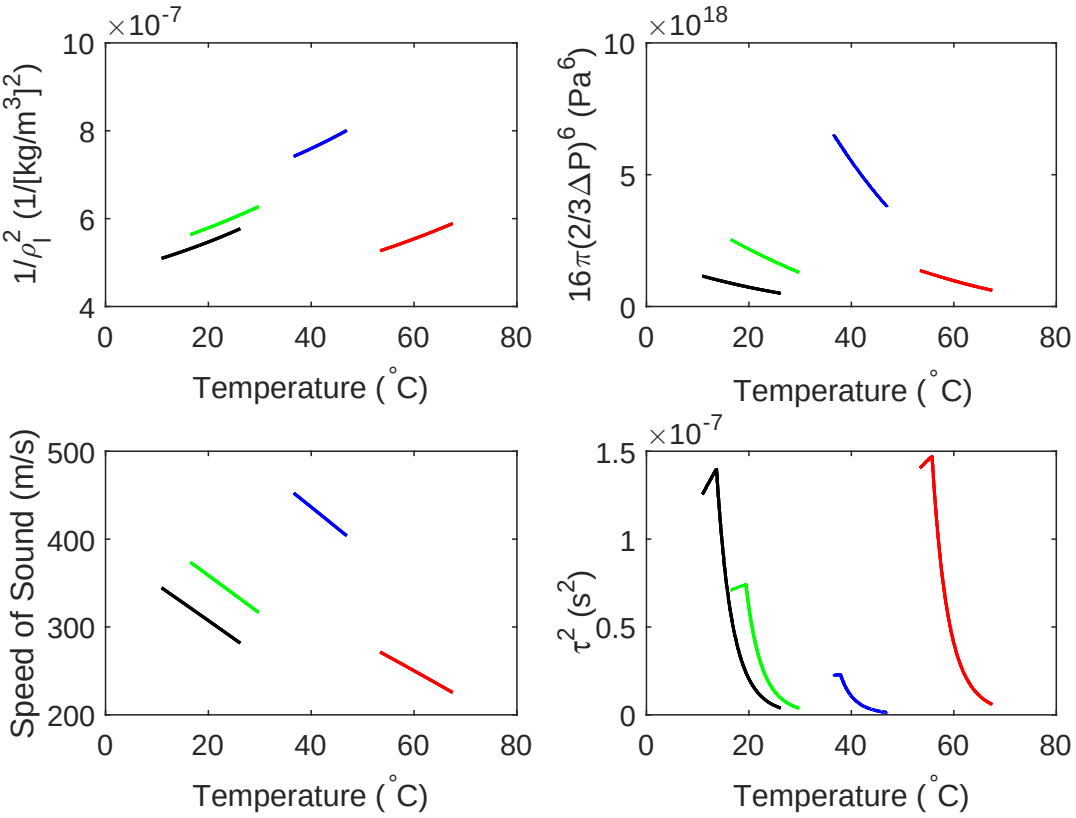

Figure 5.11 – Decomposition of the acoustic intensity of the inertial regime for four freons: C_4F_{10} (red) $C_2H_2F_4$ (blue), C_3F_8 (black) and C_2ClF_5 (green). Each subplot represent one of the quantities enclosed by square brackets in eq. 5.42.

For a fixed energy threshold and a given bubble radius, there are four competing terms which determine the acoustic intensity in the inertial regime (eq. 5.40) and are identified in the following equation within square brackets:

$$I_I = [16\pi(\frac{2}{3}\Delta_p)^6] \times [\frac{1}{\rho_l^2}] \times [C] \times [\tau^2], \tag{5.42}$$

where C is the speed of sound. Each term enclosed by square brackets in eq. 5.42 is shown in Fig. 5.11 as a function of temperature at a fixed 2 keV energy threshold. The objective of Fig. 5.11 is to highlight the tradeoff between decreasing the temperature to increasing the terms $16\pi(\frac{2}{3}\Delta_P)^6$ and C and decreasing the temperature to increase

the term $1/\rho_I^2$. Contrary to other terms, τ (bottom right Fig 5.11) behaves differently by having a maximum value, which means its maximum does not coincide with the other three terms. The acoustic intensity (I_I) as a function of operating temperatures at a constant 2 keV energy threshold is shown in Fig. 5.12.

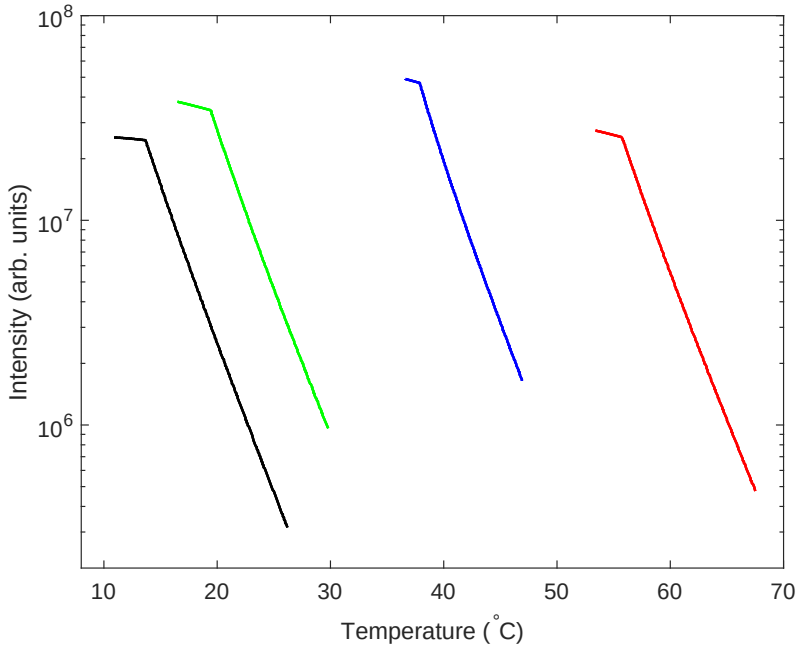

Figure 5.12 – Total acoustic intensity versus temperature at a constant 2 keV energy threshold for C_4F_{10} (red) $C_2H_2F_4$ (blue), C_3F_8 (black) and C_2ClF_5 (green). The shape of each freon mimics the shape of τ versus temperature shown in bottom right plot of Fig. 5.11.

The acoustic intensity always increases when the temperature decreases, but slows down when it crosses the maximum value of τ and for C_3F_8 (black), it almost becomes flat. Consequently, there is one optimal pressure and temperature set point for every freon that maximizes the acoustic intensity and it always corresponds to the lowest possible temperature for a give threshold energy. Moreover, it means there is a pressure and temperature window for which the acoustic intensity does not vary much. This feature adds some freedom regarding PICO detectors operation. For some detectors, it is challenging to reach 20 PSIA, but reaching 25 PSIA is not, and according to this model, it

would not decrease the acoustic intensity significantly.

To better grasp the difference between each freon, the maximum intensity for each freon is compiled in Table 5.II. Another interesting quantity is the intensity ratio between the different freons, and since the PICO experiment currently uses C_3F_8, the ratio is given as a function of this freon.

Freon	C_4F_{10}	$C_2H_2F_4$	C_3F_8	C_2ClF_5
$I_{max} \times 10^7 W$	2.7	4.9	2.5	3.8
I(Freons)/I(C_3F_8)	1.08	1.93	—	1.50

Table 5.II – Maximum total acoustic intensity of a 1 mm bubble of C_4F_{10}, $C_2H_2F_4$, C_3F_8 and C_2ClF_5. The last line indicates the ratio between the highest acoustic intensity of C_3F_8 and other freons, that is $\frac{I_{max}^{freon}}{I_{max}^{C_3F_8}}$.

The freon with the highest acoustic intensity are, in order from highest to lowest: $C_2H_2F_4$, C_2ClF_5, C_4F_{10}, C_3F_8. The acoustic intensity of C_4F_{10} and C_3F_8 are very similar with a ratio of 1.08. This means that the acoustic emissions of those two freons are $\sim$1.50 and $\sim$1.93 lower than C_2ClF_5 and $C_2H_2F_4$, respectively. Therefore, using the same piezoelectric acoustic sensors would not be a problem with $C_2H_2F_4$ or C_2ClF_5 since PICO acoustic sensors already perform well with C_3F_8.

While the amplitude of the acoustic emission of current PICO detectors is not problematic, there are worries regarding the PICO500 detector. Due to its much larger size, the acoustic sensors might be further away from the active liquid, which means the acoustic waves would have to travel through a lot more material before reaching the acoustic sensors. If the predictions of the acoustic model regarding the amplitude differences between each freon are correct, changing the freon might help to improve acoustic wave detection. A possible freon that could be used in the future is $C_2H_2F_4$, which has a higher SD sensitivity than C_3F_8, and is more sensitive to lower WIMP masses. Fortunately, the acoustic emission of $C_2H_2F_4$ is also greater than C_3F_8 by a factor ~ 2.

CHAPTER 6

THE PICASSO EXPERIMENT

The PICASSO experiment (Project In CAnada to Search for Supersymmetric Objects) was a project dedicated to direct dark matter detection using detectors filled with C_4F_{10} droplets trapped in a polymerized gel matrix. The underlying detector technology was similar to that of traditional bubble chambers used in high energy physics in the 70's and 80's. However, unlike bubble chambers, the detector modules contained millions of superheated droplets each acting as an independent tiny bubble chamber [109]. The acoustic emission following each phase transition was captured by nine piezoelectric sensors located on the periphery of the detector. The acoustic signals analysis served two purposes: event position determination and discrimination between bubble and electronic noise events. A schematic of a 4.5 L PICASSO detector module is shown in Fig. 6.1.

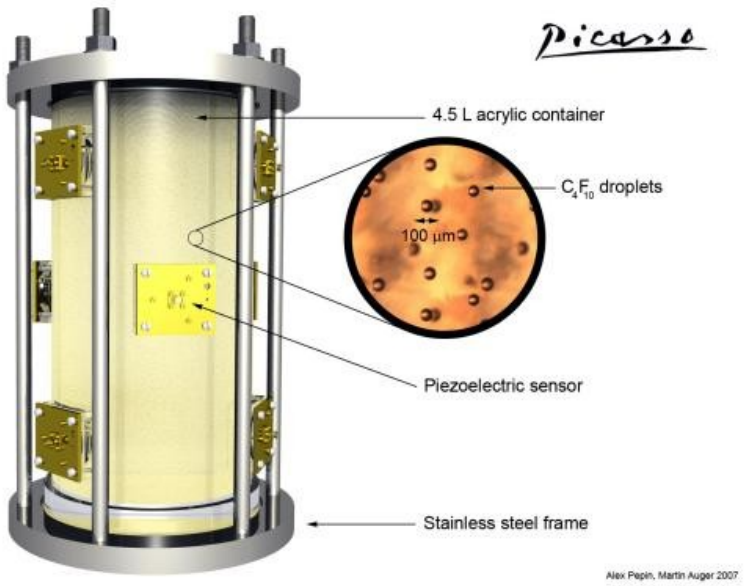

Figure 6.1 – Schematic view of a 4.5 L PICASSO detector module.

The acrylic container had a wall thickness of 1.25 cm, an inner radius of 7.00 cm and

a height of 32.50 cm. At the level of the piezoelectric sensors, the wall had a thickness of 0.7 cm [110]. Each end of the container was closed by a stainless steel disk and an o-ring. The dimensions of the detectors are shown in Fig. 6.2.

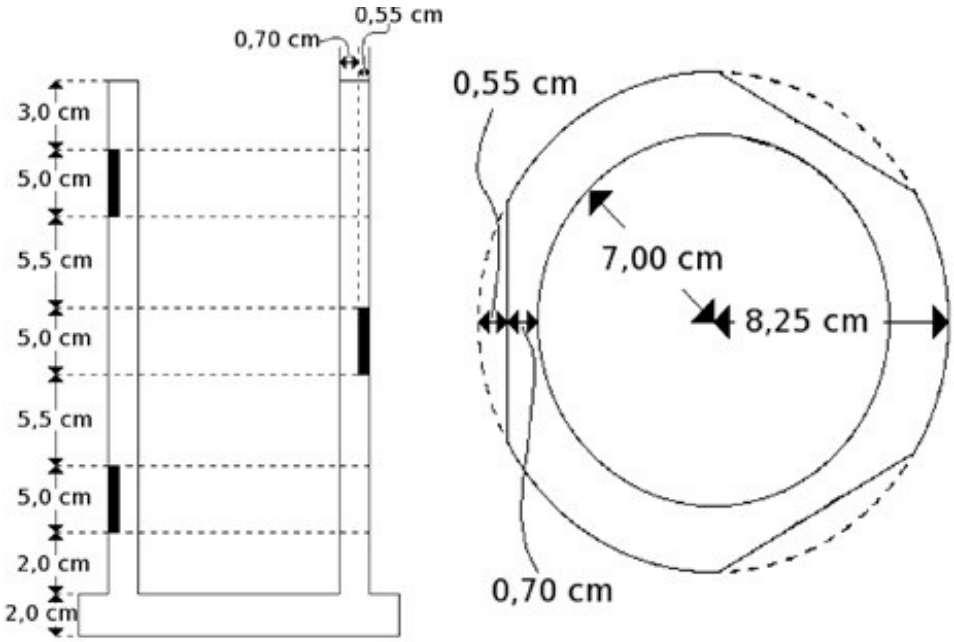

Figure 6.2 – A PICASSO detector module. The drawings show the dimensions of the containers as well as the position of the piezoelectric sensors [110].

The energy threshold of C_4F_{10} was controlled between 100 keV and 1 keV at atmospheric pressure by varying the detector temperature between 20 and 50°C. The different thermodynamic parameters of C_4F_{10} are presented in Table 6.I.

Critical temperature (T_c)	113.176° C
Critical pressure (P_c)	23.23 bar
Boiling point (T_b)	-2.089° C

Table 6.I – Thermodynamic parameters of C_4F_{10} [102].

The polymer gel that maintains the C_4F_{10} droplets was fabricated by mixing three different solutions. Their composition is shown in Table 6.II.

Ingredients	Relative quantity (%)
Main solution	98
UPW	68
Glycerin	18
Polyethylene glycol	8
Acrylamide	6
Bisacrylamide	0.2
Triton X-100	0.05
Polymerizing agent	1
UPW	97
Sodium persulfate	3
Catalyst	1
UPW	92
TEMED	8

Table 6.II – Ingredients for polymer gel fabrication. The table is split in three sections, one for each chemical solution.

The main solution was prepared directly in an empty acrylic container, while the other two solutions, the polymerizing agent and the catalyst solution were prepared separately. Since the boiling temperature of C_4F_{10} is -2.089°C, it is kept as cold as possible around -30 °C so that it does not evaporates. At this temperature, about $\sim$60 mL of liquid freon was added to the main solution. A magnetic stirrer was inserted in the container to disperse the freon uniformly in the main solution for 15 minutes. The size of the droplets depends on the rotational speed of the magnetic stirrer which has been adjusted to 250 rotations per minute to obtain an average droplet diameter of 200 microns. After this step, the two other solutions were added to polymerize the main solution and create the gel matrix. The detector was weighed before and after the addition of freon to obtain the injected freon mass. The mass of ^{19}F, which is the active mass used in the detector, typically ranges from 60 to 110 g.

6.1 Piezoelectric sensors

Each PICASSO module was equipped with nine piezoelectric sensors arranged in three layers on the perimeter of the detector. Each layer was 10.5 cm apart in height, and piezoelectric sensors subtended an angle of 120° with respect to one another as shown in Fig. 6.3.

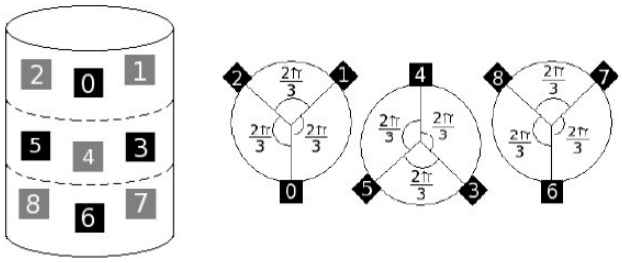

Figure 6.3 – Arrangement of the piezoelectric sensors in the PICASSO modules.

To optimize the acoustic transmission vacuum grease was added in-between the membrane of the piezoelectric sensor and the acrylic wall. Pictures of the piezoelectric sensors and the acrylic holder are shown in Fig. 6.4. The piezoelectric sensors were made of PZT (Lead zirconate titanate, Ferroperm), had a sensitivity of 27μ V$/\mu$bar, a diameter of 16.00 mm, and a thickness of 8.77 mm.

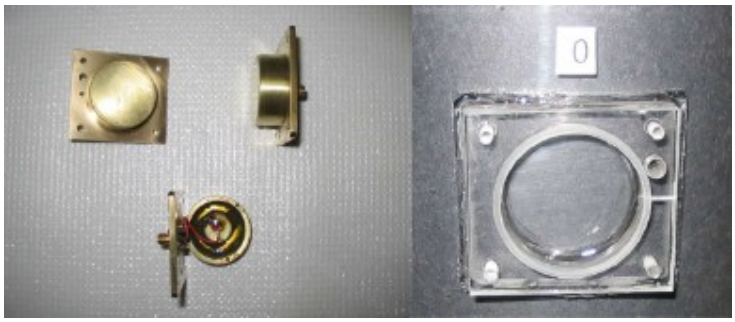

Figure 6.4 – Piezoelectric sensor (left) and acrylic holder (right) of PICASSO module [110].

6.2 Data taking at SNOLAB

The PICASSO detectors were installed at SNOLAB, Sudbury, Canada which is an underground laboratory that was initially build to host the SNO experiment [111]. SNOLAB is located in an active nickel mine at a depth of 2 km, the overlying rock served as an efficient shield against cosmic muons which produce muon-induced neutrons. SNOLAB is the second deepest underground laboratory in the world. Fig. 6.5 shows the muon flux as a function of water equivalent vertical depth of underground laboratories in the world.

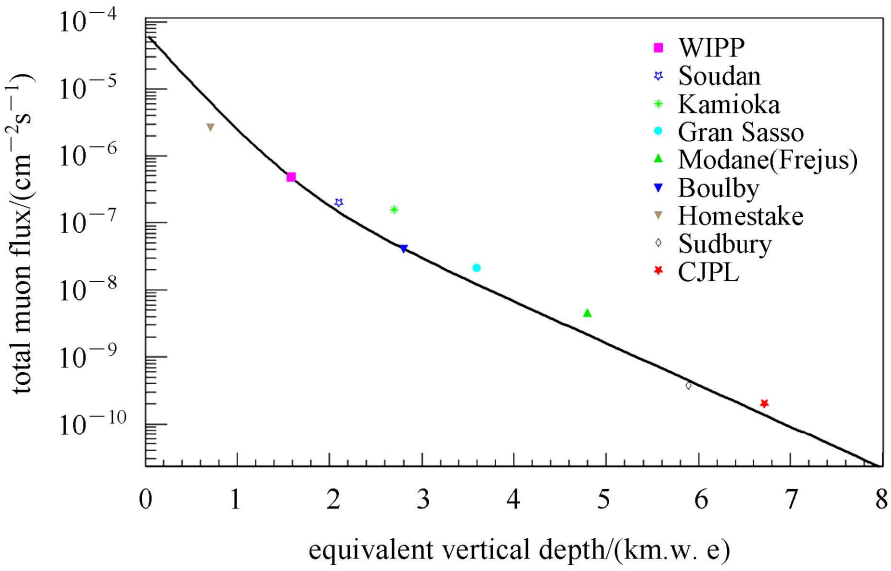

Figure 6.5 – Muon flux versus water equivalent vertical depth of the main underground laboratories in the world. The depth of each laboratory is calculated in water equivalent to account for the different rock densities unique to each underground laboratory [112].

Thirty-two detectors were placed in eight Temperature & Pressure Control System (TPCS) as shown in the left picture of Fig. 6.6. The role of a TPCS is to control the pressure and temperature with an accuracy of ± 0.1°C. The temperature is set in-between 30 and 50 °C to obtain different energy thresholds and is kept constant for a given data acquisition session. The pressure was set to atmospheric pressure for the expanded superheated state and was increased to 8 bars for the compressed stable liquid state.

TPCSs were surrounded by 50 cm cubic water tanks to shield the detectors from muon-induced neutrons which could mimic dark matter signals in the detector. At this depth, the cosmic muon flux is 0.29 μ/m^2/d [113]. Furthermore, there are also neutrons emitted by the surrounding rocks through (α, n) reactions and spontaneous fission (SF) due to the presence of uranium and thorium. Furthermore, 90% of these neutrons come from (α, n) reactions, and 10% from SF. The fast neutron flux in SNOLAB is $(4 \pm 2) \times 10^3$ n/m^2/d [114]. To verify that the water shield is sufficient to block those neutrons, Monte Carlo simulations have been carried out and have predicted a count rate of 0.14 counts/kg/d which is a factor ten smaller than the dark matter signal expected in PICASSO detectors [67]. The detector setup in SNOLAB is shown in Fig. 6.6.

Figure 6.6 – Left: One of the eight TPCS of the PICASSO experiment installed at SNOLAB. Each TPCS contains four PICASSO detectors. Right: PICASSO experiment setup in SNOLAB.

Data collection sessions were separated into two types; WIMP searches and neutron calibration. Calibration sessions were 6 hours long while WIMP runs lasted 40 hours. During a calibration session, a weak polyenergetic AmBe neutron source (68.71 ± 0.74 ns^{-1}) was placed inside a TPCS at the center of the four detectors at an equal distance from each of them. A total of $5.38 \pm$ 0.27 kgd of neutron calibrated data was amassed

over the entire temperature range (30 to 50 °C), and spread throughout the data taking period in order to follow temporal variations of the distribution of analysis variables. All data taking periods were followed by a compression period of 15 hours to reduced the gaseous freon droplets back to the liquid state. The number of events during a session was not allowed to exceed 3000 bubbles, otherwise, the gel matrix would have had a high probability of fracturing which would have permanently damage the detectors.

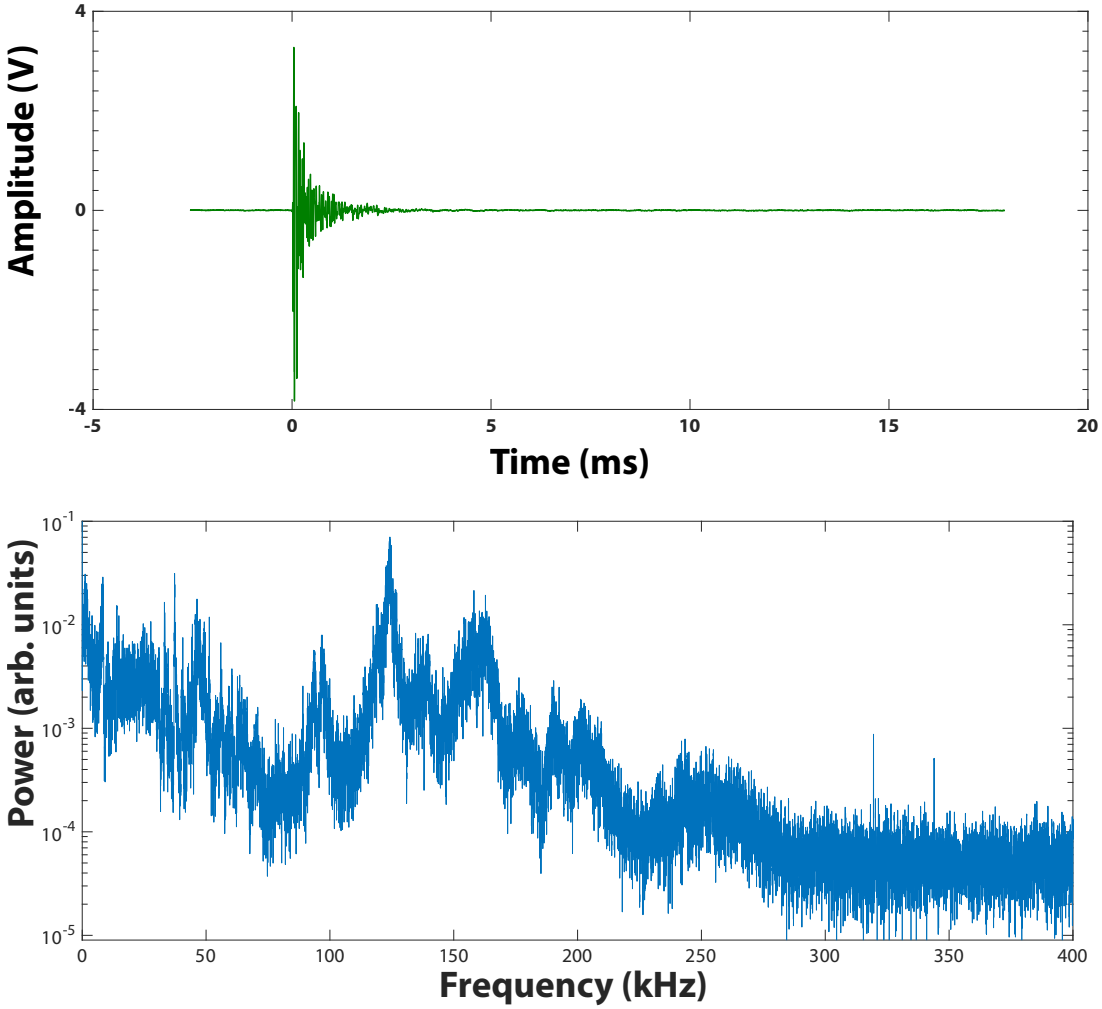

Figure 6.7 – Top: Signal induced by the acoustic emission of a bubble and recorded by the DAQ. Bottom: FFT of the above signal. The resonance of the piezoelectric sensor is located at $\approx$ 120 kHz.

6.3 Raw data processing

When an event occurred in a PICASSO detector, the amplitude of the acoustic emission from the vaporization of a droplet was measured by nine piezoelectric sensors and recorded by a data acquisition system (DAQ). The readout system generated sporadic electronic noise events which are discriminated in offline data analysis to isolate true bubble events.

6.4 Data acquisition system

The DAQ had an 800 kHz sampling frequency for a total duration of 40.96 ms, i.e., 16384 samples were taken at each 2.5 μs. Fig. 6.7 shows a typical signal produced by a neutron interaction in a PICASSO detector and its Fast Fourier Transform (FFT).

The acquisition system had a buffer of 1024 samples. Those samples are essential to determine t_0, the starting time of an event, which is different for each piezoelectric sensors and depends on the position of the event in the detector with respect to each sensor. Furthermore, those 1024 samples were used to evaluate the electronic noise of the DAQ and were used in the calculation of a variable (EVAR) which discriminates between electronic noise and bubble events. There were significant differences between these two types of events:

- Bubble events exhibit a sharp rise in amplitude of short duration at the beginning of the signal while electronic noise events had a constant amplitude throughout the 40.96 ms acquisition time window.

- The FFT spectrum of electronic noise events was concentrated in frequencies below 18 kHz, while bubble events had higher acoustic power at high frequencies as shown in Fig. 6.8.

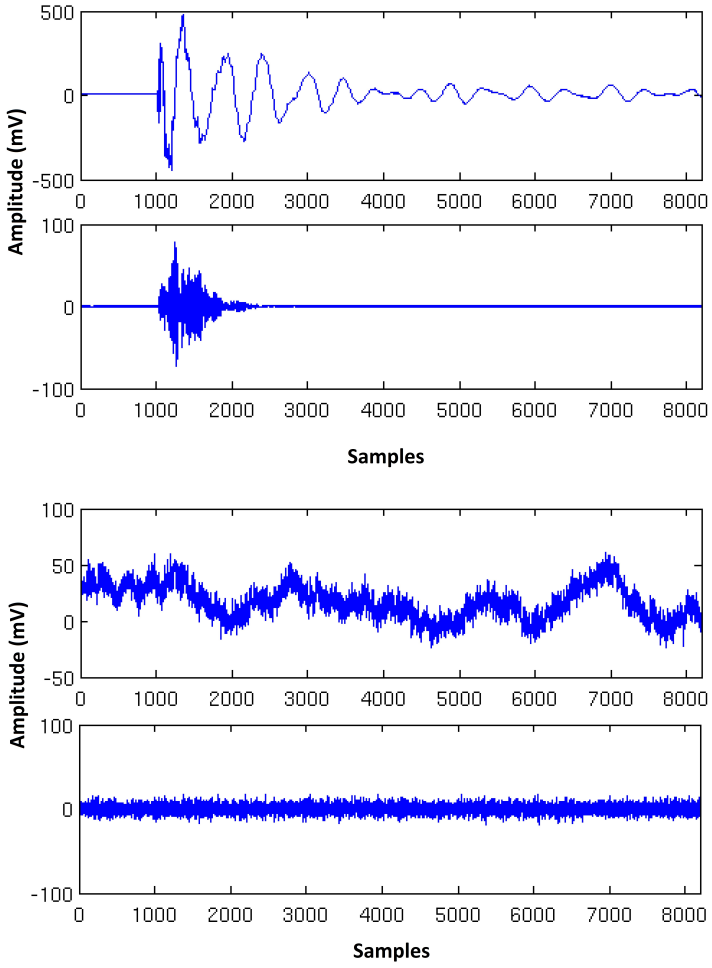

Figure 6.8 – The two top (bottom) figures represent the raw and 18 kHz high-pass filtered amplitudes of a bubble (electronic noise) event.

An analysis variable, EVAR, was constructed to discriminate these two types of events. The steps leading to the calculation of EVAR are shown in Fig. 6.9. First, a high pass 18 kHz filter is applied and significantly reduced the electronic noise amplitude such that their cumulative sum is linear. On the other hand, the cumulative sum of the amplitude of bubble events increases very abruptly and then follows a linear slope.

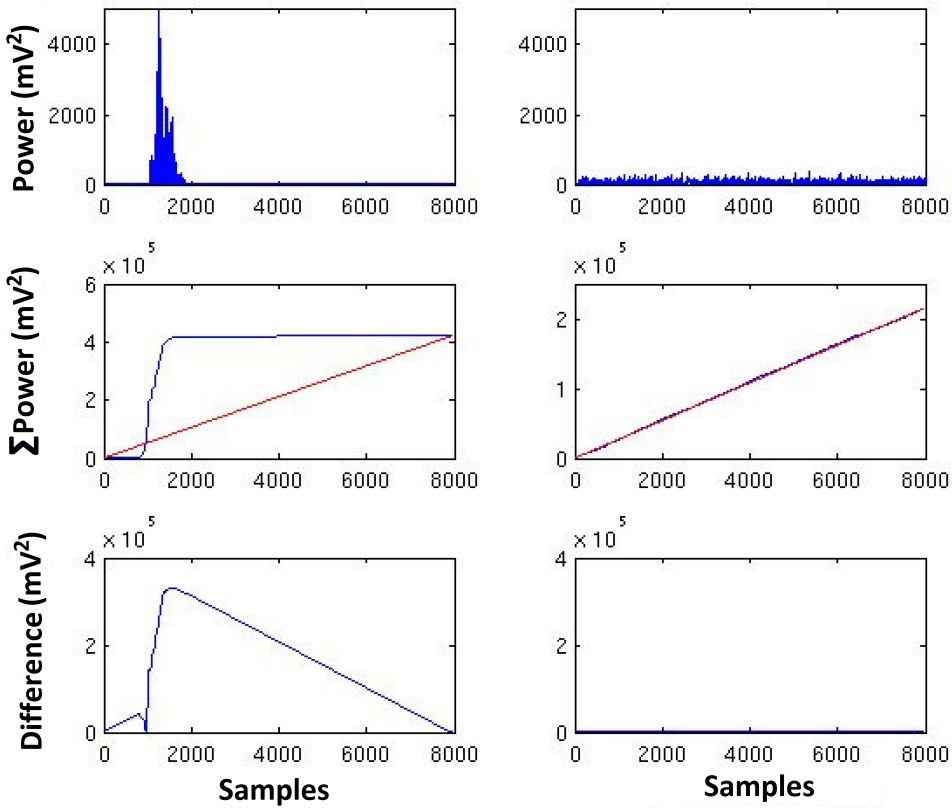

Figure 6.9 – Graphical representation of the different steps in the construction of the EVAR variable for a bubble event (left) and electronic noise event (right). Top row: squared signals. Middle row: cumulative sum and linear curve. Bottom row: linear curve subtraction

In order to increase the difference between the two types of signals, a linear curve with a gradient corresponding to the electronic noise events is subtracted. That way almost all the electronic noise contribution is eliminated. The final step to obtain EVAR is to calculate the natural logarithm of the differences. The raw amplitude and EVAR distributions of a neutron calibration run are shown in Fig. 6.10. There is no discrimination in raw amplitude distribution, but a clear bubble peak appears in the EVAR distribution.

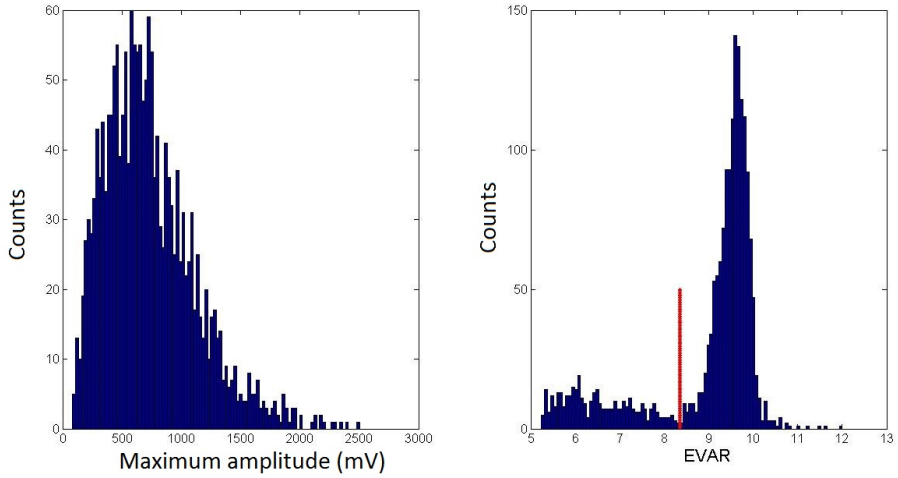

Figure 6.10 – Comparison between raw signal amplitude (left) and EVAR (right) distributions. There is no separation between bubble events and electronic noise events in the raw amplitude distribution, but a clear bubble peak is visible on the right side of the red line in the EVAR distribution.

In addition to the EVAR variable, four other analysis variables were developed to remove non-bubble events: RVAR, QVAR, TVAR, and WFLVAR. They are described in Chap. 9 along with the analysis of the final 2017 PICASSO result. EVAR removes efficiently electronic noise events with a constant amplitude which are the most common type of electronic background events. However, there are other electronic noise events with specific characteristics as well as so-called “mystery events”.

Another essential analysis tool used in the 2017 PICASSO analysis is the bubble event localization by acoustic triangulation which is detailed in Sect. 9.2. It was discovered that some detectors had distinct regions with a high concentration of bubble events that are attributed to high local alpha contamination and those regions could be removed by applying a fiducial cut.

CHAPTER 7

THE PICO EXPERIMENT

In contrast to the PICASSO experiment, the PICO experiment [2] uses a technique that is much more similar to traditional high-energy physics bubble chambers. The PICO chambers are scalable in size and use the alpha-neutron acoustic discrimination previously discovered by the PICASSO experiment [1] which makes it a background-free experiment (in principle). Since its inception, PICO has held the best dark matter SD WIMP-proton interaction limit in the world and has been improving this limit ever since. The first detector, PICO60, contained 36.8 kg of CF_3I as the active liquid during its first run and was followed by the PICO-2L detector which contained 2.90 kg of C_3F_8. During the second PICO60 run the chamber was filled with 52 kg of C_3F_8. Currently, the PICO collaboration is constructing PICO40L and designing its next detector, PICO500, which will contain $\sim$500L of active freon. The different versions of PICO detectors will be described in the following sections.

7.1 PICO detector working principle

Each PICO detector has the same set of components: a pressure vessel (PV) filled with hydraulic fluid (e.g., mineral oil or ethylene glycol), a hydraulic pressure system, cameras, piezoelectric sensors, and the superheated liquid (SHL). The detectors are immersed in a water shield whose role is to slow down high energy neutrons coming from the surrounding rocks. These high energy neutrons are produced either by spallation, by (α,n) reaction or by SF. Since the detector is held at a constant temperature of 15°C, it also acts as a thermal reservoir that helps stabilizing the detector temperature. The freon is enclosed by a fused silica jar connected to a set of bellows that rest inside the PV. Since they are submerged in the hydraulic fluid, the differential pressure on the fused silica jar is small, and thus allows the thickness of the jar to be small. A schematic view of a PICO detector is shown in Fig. 7.1.

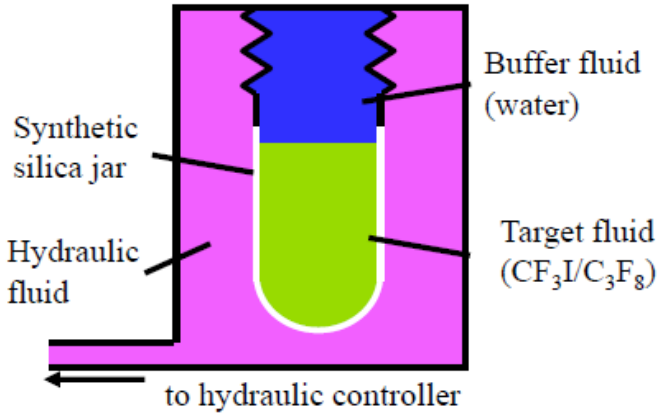

Figure 7.1 – Schematic view of a typical PICO detector.

The buffer liquid acts as a piston on the freon and must have a density lower than the freon, which is typically 1.4 g/cm^3 [102]. Linear alkylbenzene (LAB) and water are common buffer liquids used in PICO detectors. Detectors installed at SNOLAB have always used water, while the PICO 0.1 calibration chamber installed at UdeM uses LAB.

When a bubble appears, it is captured by the camera system which triggers the hydraulic pressure system to compress the freon back to the stable liquid phase. The acoustic emissions, camera images, and the pressure rise of each event are recorded and used in the offline data analysis.

Recently, the PICO collaboration has developed a new detector design called Right Side Up (RSU). Before, every PICO detector was built in the traditional normal design where the active liquid was covered by a lower density buffer liquid. Recently this concept was changed, and PICO40L will be the first detector build according to the RSU design.

7.1.1 RSU versus normal design

The CAD schematic renderings of Fig. 7.2 showing the PICO60 and PICO40L detectors highlight the main differences between the two detector designs.

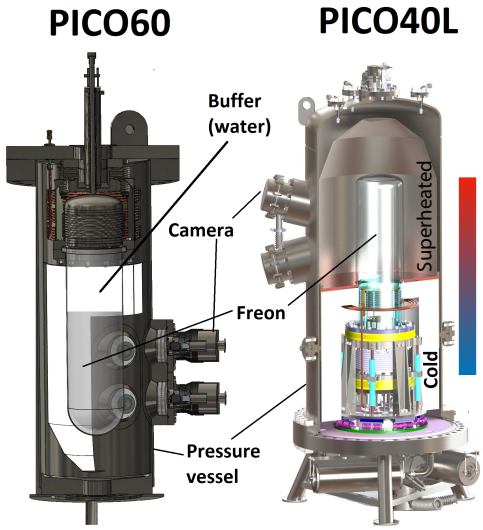

Figure 7.2 – PICO60 (left) and PICO40L (right) CAD drawings. The color band on the PICO40L figure highlight that temperature gradient inside the detector.

In the "normal" design, the bellows are above the SHL volume, and there is a buffer fluid that separates the freon from the SS bellows such that the SHL freon is not in contact with them which is vital otherwise spontaneous nucleations could occur due to the irregular surfaces of the SS bellows. However, tiny SS and glass fragments are generated throughout the life of the detector due to the friction after each compression cycle. When these particulates come in contact with the SHL and water, they create single bubble events with the same acoustic emission as WIMPs and are a direct background to dark matter searches. One solution consists of removing the buffer liquid and create a temperature gradient such that only cold stable liquid freon is in contact with the bellows. Inverting the orientation of the detector creates a natural thermal gradient as shown in Fig. 7.2. The top section is kept at 15°C, while the bottom section is at -25°C. An additional jar is also added to the design such that the smaller inner vessel (IV) can slide in the outer vessel (OV), and because their radial difference is small, there is only a small amount of freon in the cold region which reduces heat convection that naturally occurs.

7.1.2 Pressure vessel

In both configurations, the pressure vessel is a SS cylinder opened at one end and closed at the other one with a quasi-spherical cap. A flange is placed at the opened end and equipped with many plumbing ports to fill the detector with freon and to fill the pressure vessel with mineral oil. There are also electronic ports for the multiple wires of the piezoelectric sensors, the fast pressure transducers, and the temperature sensors.

The bellows are made of SS and submerged in the hydraulic fluid. When they are either compressed or decompressed, the pressure inside the active volume changes accordingly. They are attached to the jars by a set of SS or titanium flanges. The jars that contain the SHL liquid are made of synthetic silica jars due to their very smooth surface.

7.1.3 Pressure system

The pressure system consists of a hydraulic cart located outside of the water tank whose role is to control the pressure inside the active volume. It has a slow and fast compression system which are in charge of reaching and keeping the detector at the desired pressure during data taking periods. The fast compression system is used for compressing the detector when an event occurs and to keep the detector under pressure until it stabilizes. A schematic view of a typical PICO detector is the ”normal” design in shown in Fig. 7.1.

7.1.4 Read out systems

Every detector has at least two camera systems whose roles are to image bubbles to accomplish three things: trigger the compression system, determine the positions of the bubbles, and count the number of bubbles. When a bubble starts to increase in size, the camera will be able to see it when it reaches a diameter of approximately 1 mm, and when it does, it sends a signal to the pressure system which compresses the detector to 200 PSIA. Each camera possesses a focusing lens and a LED system that illuminates the active fluid with the help of a retro-reflective tape placed on the contour of the inside of

the pressure vessel. Bubble localization is performed during the post data analysis with the help of markers with known positions placed on the jar.

A fast pressure transducer records the pressure inside the bubble chamber and has three purposes. First, it records the pressure, which is essential for the calculation of the energy threshold of the detector. Secondly, it also acts as a backup system to the camera trigger system. If, somehow, the camera would not see a bubble, the next system that could identify it is the fast pressure transducer due to the increase in pressure when a bubble occurs. Finally, the fast pressure transducer can also be used to identify bubble events occurring at the wall of the jar since they have a characteristic faster pressure rise time compared to bulk bubble events. Usually, this fast pressure transducer is referenced as Dytran (name of the producer [115]).

There are multiple piezoelectric sensors, between 7 and 9, directly attached to the fused silica jar. Previously, in the PICO-2L and PICO CF_3I detectors, they were glued to the jar with epoxy, but after a certain amount of time, the epoxy would disintegrate due to continuous contact with the hydraulic fluid and the transducers would fall. Once this problem was identified, a spring belt was conceived to hold them and has been used ever since. A difference between the PICASSO and PICO piezoelectric sensor is the environment in which they need to be deployed. There is an added difficulty for PICO detector since they are constantly submerged in hydraulic fluid and consequently, the sensor casing has to be liquid tight. The signals acquired by the piezoelectric sensors are essential since they provide the alpha-neutron discrimination capability.

7.1.5 PICO detector operation

The PICO and PICASSO detector technologies differ mainly by the state of the active liquid. In PICASSO detectors, the freon is trapped inside millions of microscopic droplets that each act as an individual bubble chamber. On the other hand, in PICO detectors, the freon is contained within a single large volume of SHL. Therefore, after each event, the liquid must be recompressed as fast as possible otherwise the entire SHL

will undergo a complete phase transition with a rapid pressure rise that could break the detector. A typical detector cycle starts with the chamber in the compressed state at 200 PSIA and 15C°. The operating pressure is then lowered and is typically set between 25 and 35 PSIA. Once this pressure is reached, it is kept constant. If an event occurs or after 2000 seconds, the chamber is pressurized to 200 PSIA for 30 seconds and then is ready for another cycle. A schematic of the different phases of a cycle is shown in Fig. 7.3.

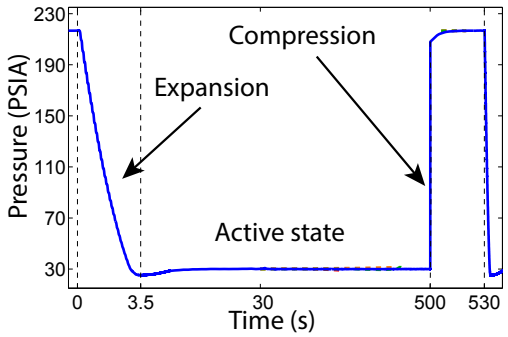

Figure 7.3 – Typical cycle of a PICO detector. The detector starts in a compressed state at 200 PSIA and followed by an expansion period of a few seconds to reach the desired pressure. When a bubble occurs, the pressure system increases the pressure to 200 PSIA, and the detector stays compressed for 30 seconds.

7.1.6 Background and simulations

Gamma calibrations are performed to determine the gamma nucleation probability at a fixed energy threshold. The latter is then used to predict the gamma background by performing GEANT4 simulations [116]. The neutron background is determined similarly, however, nuclear recoil efficiencies are determined via monoenergetic calibration at the UdeM accelerator facility. Again, neutron calibrations are replicated by a GEANT4 simulation which can then be used to predict the neutron background due to thorium and uranium contamination in the detector components and in the surrounding rock, as well as muon-induced neutrons. Furthermore, gamma and neutron bubble events produce the same acoustic emission as WIMPs, and thus their calibrations are used to define the acoustic region of interest to isolate WIMP events.

7.2 Data analysis

There are several physical quantities measured by a PICO detector, and each of them serves to isolate and characterize WIMP candidate bubble events. The temperature, bubble position, acoustic emission intensity, and the pressure variation are the four physical quantities that are exploited in the offline data analysis to achieve this goal.

The determination of the bubble position is essential for two reasons. First, it allows the implementation of a fiducial cut on the active volume, and secondly, it enters in the calculation of the acoustic power (AP) as a correction factor. A critical part of the analysis consists in applying an AP cut to discriminate between alphas and WIMPs which have distinctive AP as shown by several calibration measurements presented in Chap. 8. While alphas and WIMPs only produce single bubble events, neutrons can also produce multiple bubble events due to multiple scattering within the SHL. The multiplicity of events together with Monte Carlo simulation can be used to infer the neutron background.

The AP parameter has a radial and height dependence which are more pronounced for events near the wall of the jar or at the interface between the freon and the buffer liquid. Also, alpha events occurring in the bulk liquid will have a higher AP than a WIMP or a neutron event. However, if an alpha event occurs near the wall, its AP might be reduced and be identical to a WIMP candidate event and, therefore, every event near the wall and at the buffer-SHL interface must be removed using a fiducial cut that relies on the 3D position reconstruction of 2D camera images.

7.2.1 3D position reconstruction

Three distinct stages lead from the 2D camera images to the 3D bubble position reconstruction: image finding, optical simulation, and bubble matching. The image finding algorithm determines the center of each bubble by localizing the center of pixel clusters in the camera images using an entropy threshold algorithm. To reconstruct the 3D po-

sitions from the 2D images, each interface of the detector must be taken into account in the optical simulation (glass-air, glass-mineral oil, mineral oil-C_3F_8).

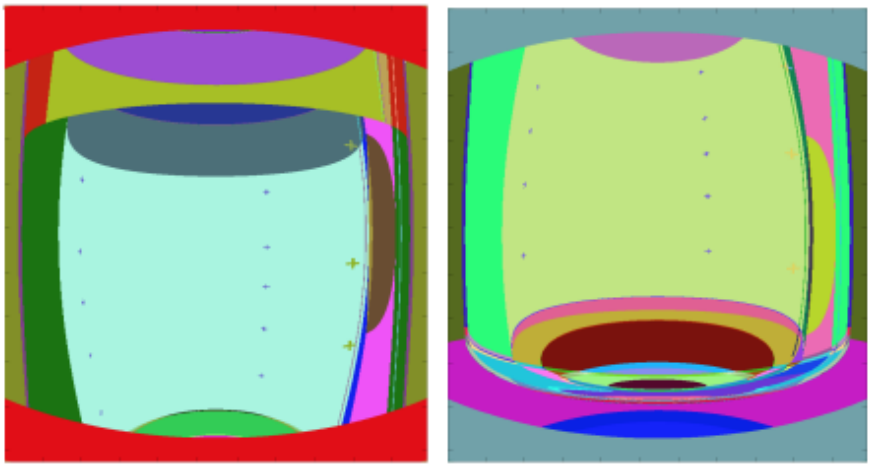

Figure 7.4 – PICO60 detector optical simulation of top (left) and bottom (right) cameras. Each color corresponds to a different sequence of interfaces. The small +'s are the fiducial markings on the jar.

As an example, the optical simulation of the PICO60 detector is shown in Fig. 7.4. It consists of propagating multiple rays in multiple directions from each pixel coordinate of each camera. A 3D position is reconstructed by finding the position of intercepting rays coming from two cameras. A lookup table can then be written such that the 3D position of ray A of pixel B of camera C intercepting ray A' of pixel B' of camera C' can be accessed quickly. The simulation is then verified and tuned using the known physical position of fiducial markings drawn on the physical jar. The main uncertainty of the simulation is due to the uncertainty in the indices of refraction. The lookup table is constructed by pinpointing the 3D position of the pixel coordinates of each bubble event determined by the image finding algorithm. Another significant output of the position reconstruction algorithm is the nearest distance from the wall (Dwall) which is used in the fast pressure transducer analysis.

7.2.2 Fast pressure transducer analysis

Following a bubble event, the pressure inside the freon volume rises sharply and depends directly on the distance between the bubble, the wall of the jar (Dwall), and on the number of bubbles. The pressure rise measured by the fast pressure transducer is used to construct the variable dytranC. This variable is obtained by fitting the pressure rise in between the start of an event (t_0) and the time of compression (t_{end}) with a 4^{th} degree polynomial function. It is then corrected for the different t_{end} and t_0 of each event, but also for the variation of the differential pressure between the inner and hydraulic volumes. The time since the detector fill is also used as a correction due to a continuous shift of the fast pressure transducer offset over time.

Compared to bulk events, wall events have a higher dytranC parameter while surface events have a lower dytranC, which is useful since wall and surface events can hardly be distinguished from bulk events with the optical system. In PICO2L, wall events had a distinctive tail trailing from their point of origin and therefore could be identified with the optical system, however, in PICO60, this feature is completely absent. To minimize the fiducial cut a dytranC cut is placed first to isolate wall and surface events before the Dwall cut is applied to remove them. The dytranC distribution versus height (Z) and versus Dwall of the PICO60 detector are shown in Fig. 7.5. A cut of dytranC > 1.3 and < 0.7 is defined to isolate wall and surface events, respectively.

The Dwall distribution of wall and surface events after applying the dytranC cut is then fitted to define a more precise Dwall cut which is set to 5σ beyond the mean value of the Gaussian fit. Wall events are further separated into four regions of the jar vessel: main cylinder, collar, hemisphere knuckle, and hemisphere dome. The main cylinder region corresponds to the vertical wall of the jar, and the collar region is the region near the buffer-freon interface. The hemisphere knuckle and dome are two distinct regions of the bottom cap of the jar with different curvatures. The Dwall distribution of each of those four regions is shown in Fig. 7.6

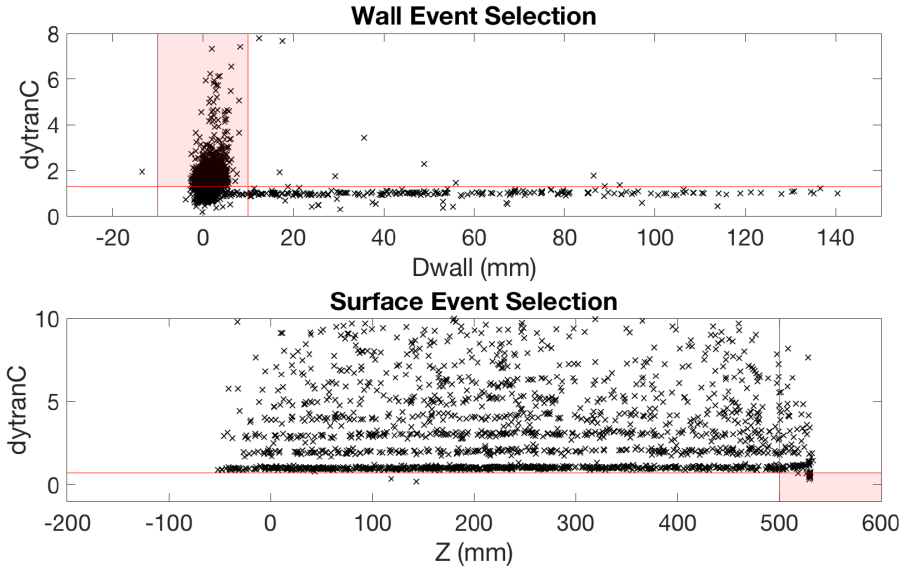

Figure 7.5 – dytranC versus Dwall (top) and Z (bottom). The dytranC>1.3 and abs(Dwall)<15 region corresponds to wall events and is shown in red in the top plot. dytranC < 0.7 and Z$>$ 500 cuts are used to isolate surface events and shown in red in the bottom plot.

7.2.3 Acoustic analysis

The acoustic power (AP) is an analysis variable, similar to EVAR in PICASSO, developed by the PICO collaboration to optimize the neutron-alpha acoustic discrimination by selecting specific frequency bands. It varies as a function of the distance between the bubble and the sensors and also changes as a function of the distance between the bubble and the wall of the jar. The AP parameter is the sum of each position corrected frequency window n of each sensor j and is given by the following equation:

$$AP = A(T)\sum_{j} G_j \left(\sum_{n} C_n(\vec{x}) \left(\sum_{f^n_{min}}^{f^n_{max}} f \times PSD^j_f \right) \right), \tag{7.1}$$

where $A(T), G_j, C_n(\vec{x})$ are all corrections factors, and f, f^n_{max}, f^n_{min} are the central frequency, the maximum and minimum frequency of a given frequency window, respectively. *PSD* stands for Power Spectral Density and thus PSD^j_f is the acoustic power of

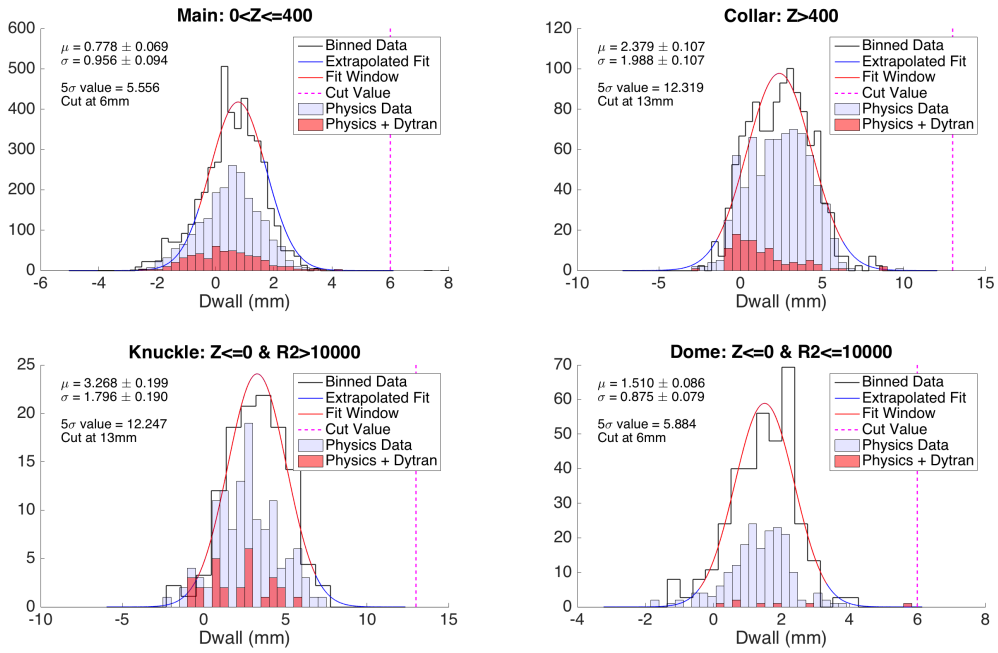

Figure 7.6 – Dwall event distributions of the cylinder region (top left, main), collar (top right), hemisphere knuckle (bottom left), and hemisphere dome (bottom right). A Gaussian fit is applied to each distribution to place a Dwall cut to the nearest mm beyond 5σ from the mean (dotted red line).

the signal band f^n_{min} to f^n_{max} of sensor j. $A(T)$ is a correction factor that accounts for the variation in acoustic emission due to temperature changes so that various acoustic data taken at different temperatures can be normalized to one another. G_j is a correction factor that accounts for the individual preamplifier gain of each sensor j. The parameter $C_n(\vec{x})$ is a correction factor proportional to the position of the bubble which varies for each of the different frequency band: 1.5-12 kHz, 12-35 kHz, 35-150 kHz, and 150-250 kHz. The Fig. 7.7 shows the spectral power density ($f \times PSD^2$) as a function of frequency for the average signal detected for alpha events (red), neutron events (dash blue), and electronic noise events (dash black). Also indicated are the four frequency bands.

The AP distribution of each type of events is obtained by performing calibration measurements and is shown in Fig. 7.8. When a WIMP run or a calibration run is taken, both neutron and alpha events can occur, however, in a neutron calibration run, there are

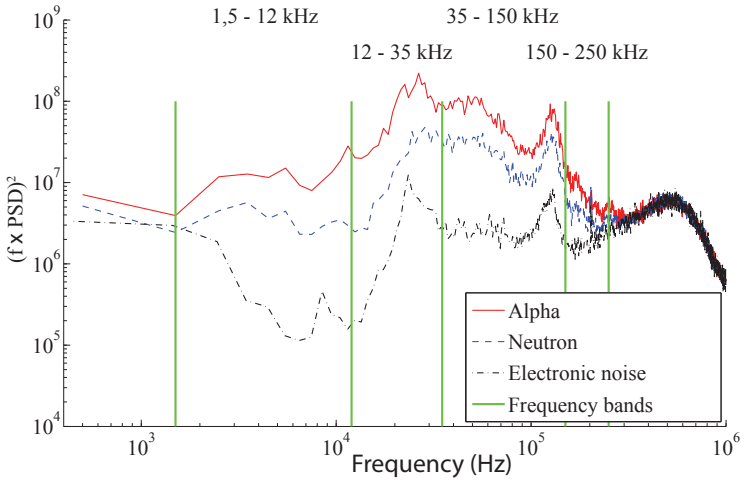

Figure 7.7 – Frequency power spectral density squared versus frequency for averaged signals detected for alpha events (red), neutron events (dash blue) and electronic noise events (dash black). The four frequency bands are identified by the green vertical lines.

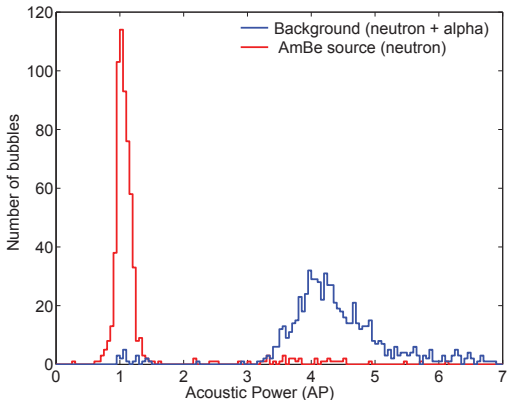

Figure 7.8 – Acoustic Power (AP) distribution for background runs in blue (alpha+neutrons) and for AmBe neutron calibration data in red.

a lot more neutron events than alpha events. Using AP as an acoustic variable yields two distinguishable acoustic peaks, one for neutron events and one for alpha events and thus AP is used to eliminate any alpha events in WIMP search data sessions. Unfortunately, gammas and neutrons can mimic WIMP signals in PICO detectors, and as such, they are an irreducible source of background that must be mitigated by shielding, material selection and by calibrating them precisely.

7.3 History of PICO detectors

The first detector operated by the PICO collaboration was the PICO60 detector filled with CF_3I (PICO60 CF_3I). Unfortunately, this detector was background limited and therefore triggered the idea to go back to a smaller detector, PICO2L, and fill it with C_3F_8 to verify if the same background was also present with this type of freon. The first WIMP searches with PICO2L, while resulting in the world leading limit in the SD WIMP-proton cross section, was initially limited due to an unknown background that was later attributed to the mixing of water, freon, and particulates. In order to remove this background with the PICO detector technology at that time, a very restrictive condition on the number of particulates of different sizes present in the SHL was imposed, and an elaborate cleaning procedure was introduced to remove them.

Cleaning the detector resulted in the complete removal of this water-particulate background in the second PICO2L WIMP search run. Consequently, the PICO60 detector was refilled with C_3F_8 following the same cleaning procedure and, again, no trace of the unknown background was seen. However, it is not guaranteed that every time a detector is assembled that its cleanliness will be sufficient to remove this problematic source of background and furthermore, it might be even more difficult to attain an increased level of purity required for a very large detector such as PICO500. Thus, with the knowledge acquired regarding the source of this background, the creation of the RSU design was launched.

The first detector to test the RSU design is PICO40L which is currently under construction at SNOLAB. It will be followed by PICO500 which is on drawing board at the moment and is expecting feedback information from PICO40L in order to improve the RSU design.

One of the goals of the PICO collaboration is to construct bubble chambers with jars made of materials other than fused silica, such as SS or acrylic. One explanation for

the boiling of the SHL seen on the surfaces of acrylic jars, such as the prototype Geyser detector at UdeM and at UAlberta, is the presence of imperfections on the surfaces. However, one hypothesis is that the boiling might be enhanced due to the presence of buffer liquid stuck in the interstices of the container, i.e., between the jar and the freon. Consequently, removing the buffer liquid, as in the RSU design and adding a coating might remove the need to have very smooth and costly jars made of synthetic silica. If this hypothesis is true, it opens up the possibility of using cheaper and less fragile materials like acrylic and SS.

7.3.1 PICO 60 (CF_3I)

The first published result of the PICO collaboration was obtained with the PICO60 detector filled with 36.8 kg of CF_3I [72]. During this run, a high number of low AP events near the WIMP signal region were detected with the unfortunate consequence of yielding worse limits than expected for a background-free experiment. It was decided to discontinue the use of CF_3I since the cause of this unknown background was most probably due to the presence of iodine. On the other hand, and as will be described in section 12, physic wise, iodine has interesting characteristics such as having high coupling to novel WIMP-nucleon interactions, i.e., other than SD and SI interactions. Furthermore, the use of iodine allowed the PICO collaboration to be a competitive experiment in the SI WIMP-nucleon interaction sector while still being the world most sensitive experiment in the SD sector.

7.3.2 PICO 2L

The main goal of this chamber was to verify if the same unknown background present in CF_3I was also present in C_3F_8 [70]. Two distinct runs were performed with this detector. During the first run, an incident during the filling of the chamber introduced an unknown number of particulates inside the chamber which produced a similar background as the one seen in CF_3I. The main hypothesis that explains this background is the presence of particulates, such as quartz or stainless steel, merging with water droplets

which release enough energy to produce phase transitions with an acoustic power within the WIMP signal region. For this reason, this background is called water-particulate background.

In the second run, this background was completely removed after a thorough cleaning was performed, leading to the first evidence of a link between the number of particulates and the number of events. During the same time, a small test chamber was assembled to study the relation between the number of particulates and the number of water-particulate events. These studies only showed that there was a relation between the presence or the absence of water-particulate events and the cleanliness of the jars, but one could not quantify the count rate dependence versus the number of particulates introduced in the chamber.

When the first PICO-2L result was published, it yielded the best SD limit even in the presence of the water-particulate background, which was due to an in-depth analysis of the single bubble events that showed that the events were not consistent with a dark matter signal due to the non-uniform time distribution of the events. Consequently, an additional cut was applied to remove those single non-WIMP bubble events.

During the second PICO-2L run, additional precautions were applied when drying the freon container so that as few particulates as possible could enter, but no measures were taken to mitigate the production of SS particulates coming from the SS bellows. Those precautions paid off as no event in the water-particulate background region was seen during this second run, and only one single nuclear-recoil event was observed which was consistent with the predicted neutron background rate. This result surpassed the first PICO-2L run and yielded the world best limit in the SD-p limit for WIMP masses in the range between 5 and 40 GeV/c^2. For masses above 40 GeV/c^2, the best limit was still held by PICO60 CF_3I result due to higher iodine coupling with heavy WIMPs. Another important discovery made using this freon was the gamma bubble nucleation efficiency dependence on the number of electrons of a nucleus which was highlighted by the higher

gamma sensitivity of CF_3I compared to C_3F_8.

The second PICO-2L WIMP search run was critical to the future of the experiment because it showed that it was imperative to be extremely careful with particulate contamination. Since PICO60 is a bigger detector, even better cleaning was crucial for the success of the experiment.

7.3.3 PICO60 (C_3F_8)

The danger of the particulate contamination was fully known before filling the PICO60 detector with C_3F_8. Therefore, the quartz jar was thoroughly cleaned with ultrapure water and water samples were collected until a pre-specified standard was met. The cleaning setup of the PICO60 quartz jar is shown in the left image of Fig. 7.9. The tolerated number of particulate of different sizes per liters of collected water and the result of the last collected water sample before the filling is shown in the right image of Fig. 7.9. The targeted standard is shown in red and was achieved as shown by the black experimental data points.

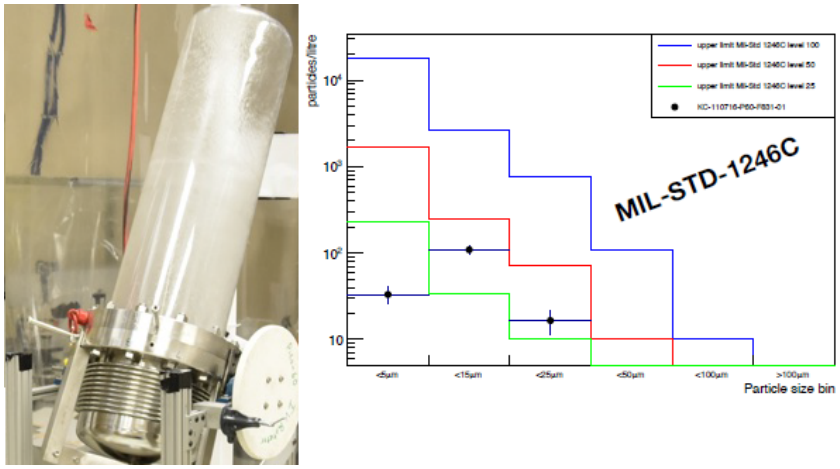

Figure 7.9 – Left: Picture of the device used to clean the PICO60 jar by rinsing the jar with UPW and soap (called "dishwasher"). Right: Particulates per liter versus particulate sizes for three different standards. The targeted standard (MIL-STD-1246C) is shown in red and was achieved.

There were two WIMP searches carried out with this detector, the first at a thermodynamic threshold of 3.29 keV and a second at 2.45 keV. The limits of these two independent searches were recently combined and published in [2], which is still to this day the best SD WIMP-proton cross section limit in the world for WIMP masses above 4 GeV/c^2. PICO60 was decommissioned during summer 2017, and thus marked the end of the non-RSU PICO detector design. Regardless of the detector design, the cleaning procedure that was adopted and developed for this detector will also be applied for the future detectors.

7.3.4 PICO40L

PICO40L is currently under construction at SNOLAB. Since this detector is relevant for the PICO40L neutron background study that will be presented in Chap. 13, the main characteristics of the detector are described here. The CAD drawings of PICO40L was previously shown in Fig. 7.2.

PICO40L has two quartz jars attached to the SS bellows which encloses the active freon. Each jar is attached to the bellows with a set of three flanges made of titanium as to match the hardness of the quartz jar flanges in order to prevent them from flaking. Four cameras are used to provide 3D bubble reconstruction, and each camera has an individual red LED ring that illuminates the chamber using a reflective tape stuck on the inside of the PV as well as on two conical parts that hang from the top of the PV.

The PV holds mineral oil that acts as the hydraulic fluid, and the space inside of the PV is divided into two sections: a cold and a hot region. A chiller is attached to the bottom of the PV and keeps the bottom region at $-25°$C while the hot region is heated with several heating coils and copper heating plates. Inside the IV, a copper heating plate was added to heat the cold mineral oil making sure that the temperature of the freon nearby the IV is kept at 15°C. Since this hot oil can mix with nearby cold oil, a thermal tower that consists of multiple plastic layers is inserted inside the IV to limit the convection.

One of the new technical aspects of this detector that was not present in any previous PICO detector design is the understanding of the thermal flow. There are multiple resistance temperature detectors (RTDs) that were placed inside the PV to monitor the temperature and to understand and control the thermal gradient.

The PV rests inside a cylindrical water tank that acts as a shield to block neutrons coming from the norite rock of the underground laboratory. The water is held at 15°C and is used as a thermal reservoir to improve the temperature stability of the hot region of the detector.

The primary goal of this detector is to prove the feasibility of the RSU design, while also improving SD limits by increasing the total exposure amassed which will be possible due to the expected reduced neutron background. The latter reduction should be guaranteed by the large diameter of the PV which was increased from 24 inches for PICO60 to 36 inches for PICO40L. Consequently, this detector should be able to acquire a higher amount of exposure before being background limited. The current plan is to acquire one year of exposure with 55.75 kg of C_3F_8 which amounts to 20349 kg-day. The PICO60 C_3F_8 detector acquired 1167 kg-day of exposure after all cuts at 3.29 keV. Therefore, the PICO40L should be able to improve the PICO60 C_3F_8 result by a factor $\approx$17, if the neutron background is 1 event/year or lower.

The PICO40L detector has many engineering challenges, and one of the most important is undoubtedly the thermal control of the hot and cold part of the detector which will be carefully studied to inform the design of the future PICO500 detector.

CHAPTER 8

CALIBRATION AND BACKGROUND OF PICO AND PICASSO DETECTORS

WIMPs interact via elastic scattering with the SHL generate fluorine/carbon recoils which produce single bubble events with a characteristic acoustic emission. The detector response to any Standard Model particles, susceptible of creating single bubble events with the same acoustic emission as WIMPs and present in sufficient amount in the detector environment, must be characterized by performing calibrations. For SHL detectors, these particles are neutrons, gammas, and alpha decays occurring inside the SHL. Each of these particles is a possible background source for dark matter detection, and thus the number of bubbles, the acoustic emission intensity, the count rate, and its energy dependence must all be characterized precisely in order to discriminate them and/or reduce their count rate. Furthermore, since both WIMPs and neutrons produce atomic recoils, neutrons are used to define the detection efficiency of fluorine/carbon recoils at different energy thresholds which translate directly into a determination of the WIMP detection efficiency of SHL detectors.

Most of PICASSO and PICO calibration efforts were done at the Laboratoire René J.A. Lévesque at the University of Montreal using the 6 MV Pelletron tandem. By exploiting the nuclear reaction X(p, n)Y on ^{51}V and ^{7}Li targets, monoenergetic neutrons are produced to calibrate the neutron response of SHL bubble chamber detectors or other dark matter experiments. Monoenergetic and polyenergetic neutron sources, as well as multiple gamma sources, were also used to calibrate detectors. In the early days of the PICASSO experiment, considerable effort has been put in understanding the detector's behavior to alpha decays, and thus multiple innovative alpha calibrations were performed such as spiking the detectors with radioactive solutions.

8.1 Neutron interactions with freons

Neutrons interact predominantly by elastic scattering with carbon or fluorine atoms of the freon ($\sigma_{el} \approx \sigma_{total}$). The energy spectrum of the recoiling nuclei is given by:

$$E_R = \frac{2A}{[A+1]^2}(1 - cos\theta)E_n, \tag{8.1}$$

where A is the atomic mass of the recoiling nuclei, θ is the neutron scattering angle in the center of mass frame, and E_n is the incident neutron energy. If the diffusion is isotropic, the energy spectrum is a boxlike spectrum. Since SHL detectors are energy threshold detectors, their count rate increases when their energy threshold is decreased as shown in Fig. 8.1.

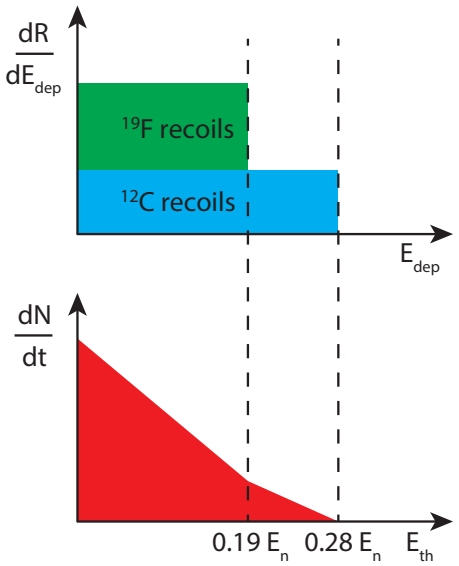

Figure 8.1 – Top: Theoretical energy spectrum of nuclear recoils for isotropic scattering in the CM frame. Bottom: the count rate that is measured with a threshold detector.

There are resonances in the (^{19}F, n) elastic cross section for which the diffusion is anisotropic and therefore the recoil spectrum deviates from the simple box shape shown here [117]. The (^{19}F, n) and (^{12}C, n) weighted elastic cross sections for C_4F_{10} are shown in Fig. 8.2.

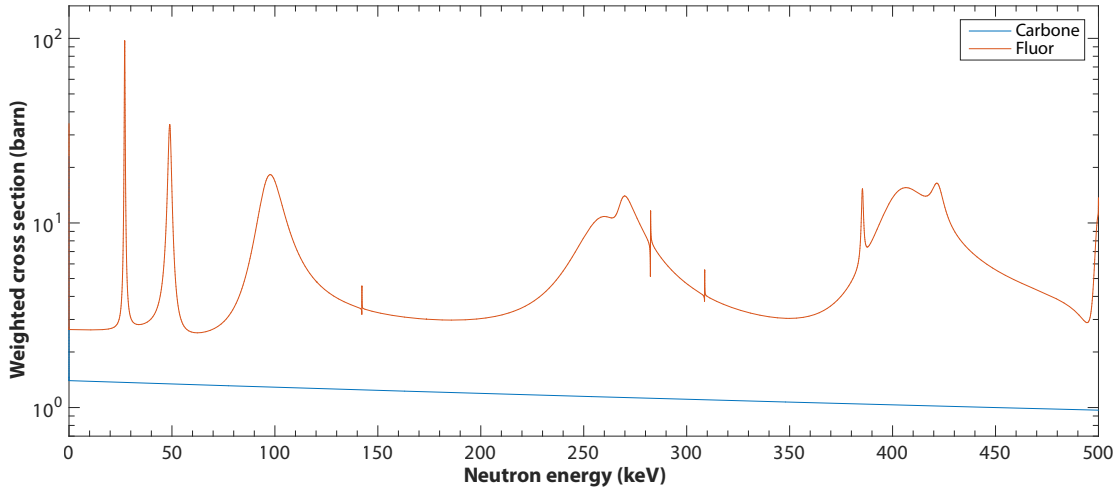

Figure 8.2 – Weighted elastic cross section of (F/C, n) for C_4F_{10} as a function of neutron energies for the energy range used during detector calibration.

Another important aspect of fluorine and carbon interactions is the mass difference between them, which impacts the maximum energy that a neutron can transfer due to the term $\frac{2A}{[A+1]^2}$ in eq. 8.1. The highest carbon and fluorine recoils following an elastic neutron scatter is 0.28 E_n (E^c_{max}) and 0.19 E_n (E^f_{max}) as specified in Fig. 8.1. Due to their mass difference, they also have different stopping power (dE/dx), as shown in Fig. 8.3 and consequently, fluorine has a smaller range than carbon in C_4F_{10} as shown in Fig. 8.4. Since the Seitz model states that the critical energy must be deposited within the critical radius, fluorine and carbon ranges must be compared to the critical radius to inform the bubble efficiency of these recoils. As an example during the last PICO60 C_3F_8 WIMP search run, the critical energy was 3.29 keV, at 13.9 °C and 30.2 PSIA which corresponds to a critical radius of 23.9 nm, while the mean range of fluorine and carbon are 15.4 nm and 20.7 nm, respectively. Consequently, fluorine recoils have a higher bubble efficiency than carbon recoils.

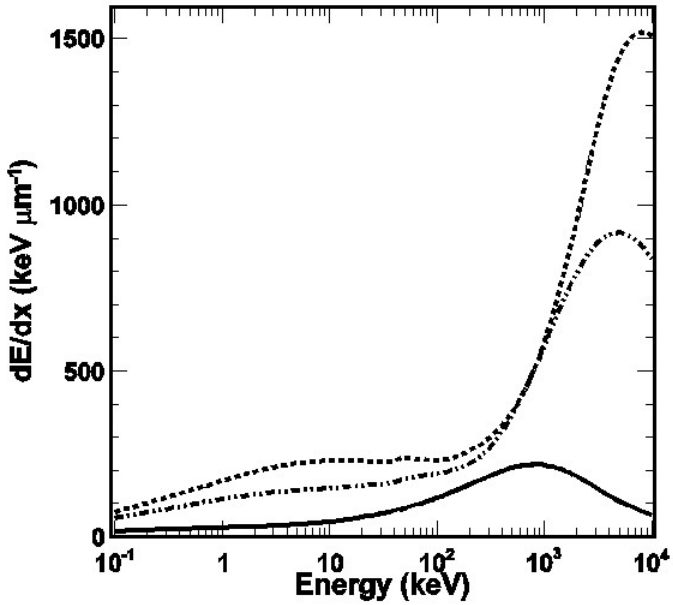

Figure 8.3 – Stopping power (dE/dx), calculated with SRIM [118], in units of keV/μm as a function of incident energy for fluorine (dotted), carbon (dash-dotted) and for α particle (continuous line) in C_4F_{10}. Below 500 keV, fluorine has a higher dE/dx than the other two particles.

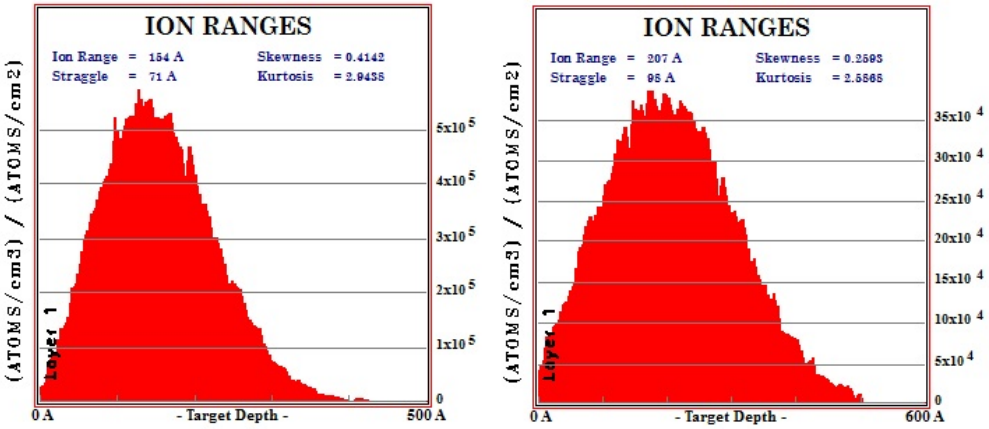

Figure 8.4 – Simulated range distribution of 3.29 keV fluorine and carbon ions with SRIM. This energy corresponds to the most recent energy threshold used with the PICO60 C_3F_8 detector. The range distribution of fluorine is smaller than carbon which plays a role in bubble formation.

8.2 6 MV Pelletron Tandem accelerator

The accelerator located at the Laboratoire René J.A. Lévesque of the University of Montreal is a 6 MV Pelletron Tandem [119]. Fig. 8.5 shows a schematic view of a typical tandem accelerator.

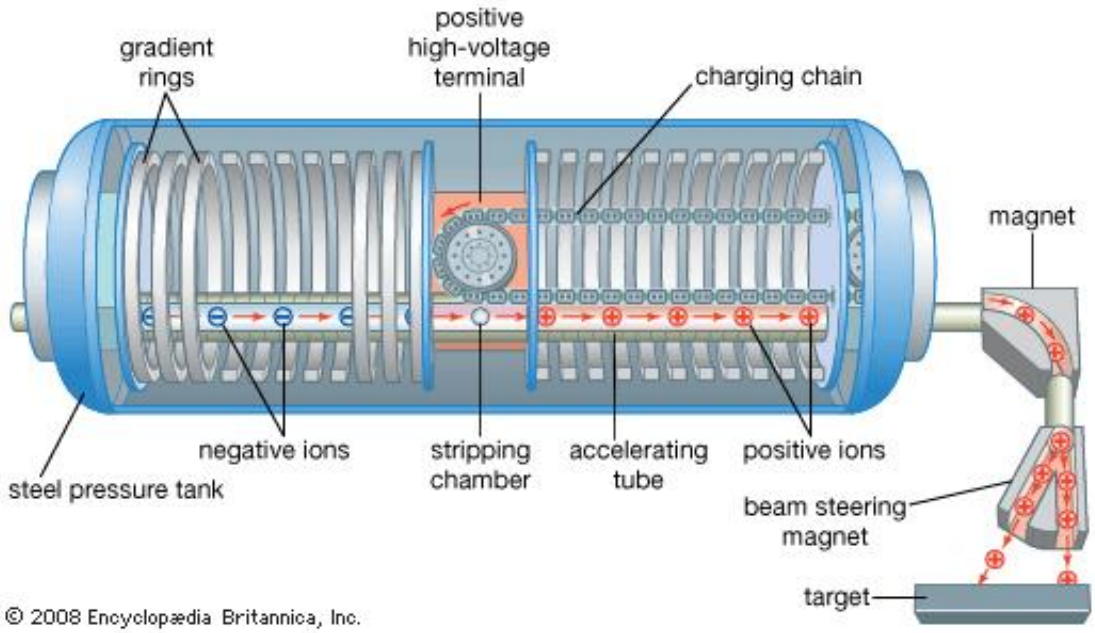

Figure 8.5 – Schematic of the internals of a tandem accelerator [120].

Negative ions are accelerated by a positive high-voltage terminal that has a maximum potential of 6 MV. The voltage gradually decreases along the beam pipe and creates a uniform electric field. The high-voltage terminal is held at a high voltage by two Pelletron systems which work similarly to a Van de Graaff system, but the belt is replaced by a SS chain and the links are made of nylon. A schematic view of the Pelletron charging system is shown in Fig. 8.6.

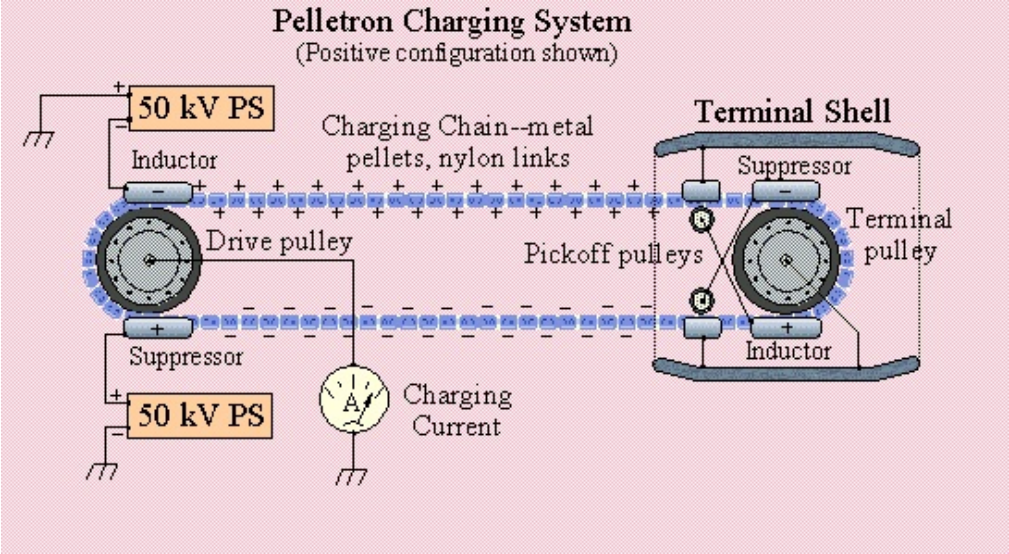

Figure 8.6 – Schematic of the Pelletron charging system. This system is installed in the Montreal Tandem accelerator [120].

A high voltage tension generator induces charges on the SS chains, and those charges are transported and transferred to the high-voltage terminal by induction. The voltage generator controls the voltage on the high-voltage terminal by changing the speed of the chains, which changes the energy of the accelerated ions.

When negative ions reach the center of the tandem, they pass through a low-pressure O^2 gas jet that removes electrons from them, and they become positive ions. They are then repelled by the positive high-voltage terminal and accelerated a second time.

8.3 Monoenergetic neutron production

Two (p,n) reactions are used to produce monoenergetic neutron beams: monoenergetic neutrons with energies in between 100 keV and 4 MeV are obtained with a lithium target via the reaction $^{7}\mathrm{Li}(p,n)^{7}\mathrm{Be}$, while for lower neutron energies, a vanadium target is used to produce neutrons via the reaction $^{51}\mathrm{V}(p,n)^{51}\mathrm{Cr}$.

The vanadium reaction has multiple resonances for the (p,n) reaction and the yield of each of them, as a function of proton energy, is shown in Fig. 8.7 [121]. When the proton energy is increased, the energy of the neutron increases proportionally, the proton energy required to exploit each resonance is presented in Table 8.I.

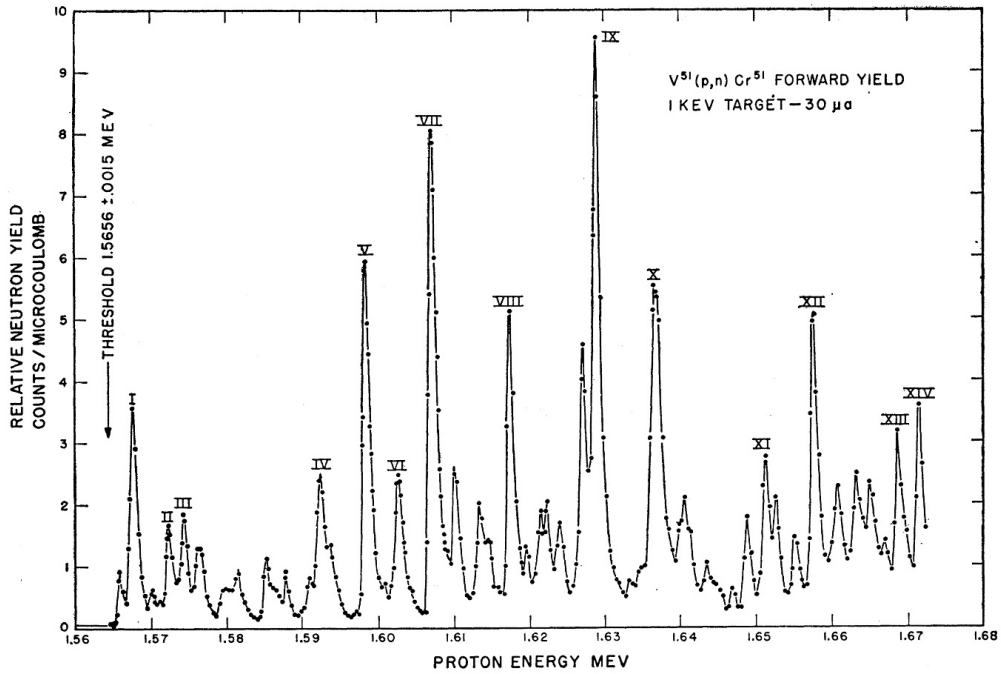

Figure 8.7 – Neutron yield of the ^{51}V$(p,n)^{51}$Cr reaction as a function of incident proton energy. Resonances allow an excellent definition of neutron energies [121].

By carefully setting the proton energy, the precision of the neutron energy can be as low as 0.1 keV. In order to set the proton energy to be precisely on the peak of a resonance, an ^{3}He counter is placed directly nearby the vanadium target. By changing the proton energy, the neutron count rate changes and reaches a maximum when directly on a resonance.

Resonances	E_p (MeV)	E_n at 0° (keV)
I	1.568	4.8
II	1.573	11.3
III	1.575	13.6
IV	1.592	34
V	1.598	40
VI	1.603	45
VII	1.607	50
VIII	1.617	61
IX	1.629	74
X	1.637	82
XI	1.651	97
XII	1.658	104
XIII	1.669	116
XIV	1.672	119

Table 8.I – Proton (E_p) and neutron (E_n) energy of $^{51}\mathrm{V}(p,n)^{51}\mathrm{Cr}$ resonances.

For PICASSO calibration purposes, 4.5 L detectors were replaced by a smaller detector to reduce interactions between neutrons and other materials such as the gel matrix which is almost entirely composed of water and modifies the neutron energy spectrum. The latest PICASSO calibration detector is shown in Fig. 8.8.

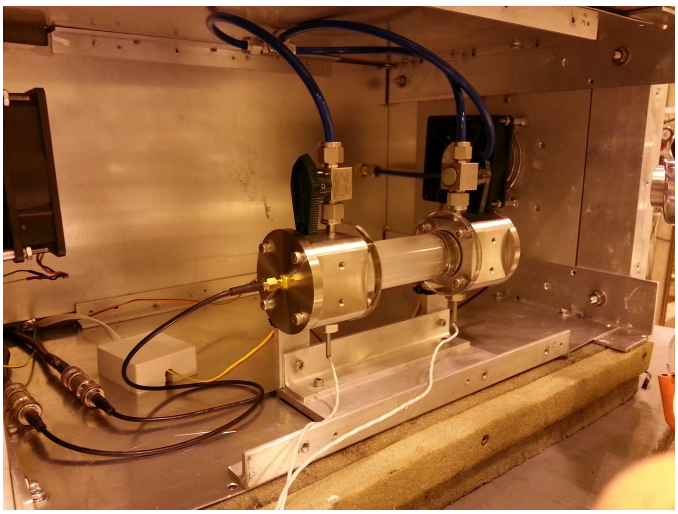

Figure 8.8 – The latest version of the PICASSO calibration detector had two temperature probes as well as two piezoelectric sensors at each end cap.

Any material in between the incident neutrons and the detector will modify the neutron energy spectrum as shown in Fig. 8.9 for PICASSO detectors. Consequently, the PICASSO detectors that were developed for calibration purposes are kept small to minimize this effect, however, their active mass must be sufficiently large so that the threshold behavior of C_4F_{10} for multiple neutron energies can be measured in a reasonable timescale.

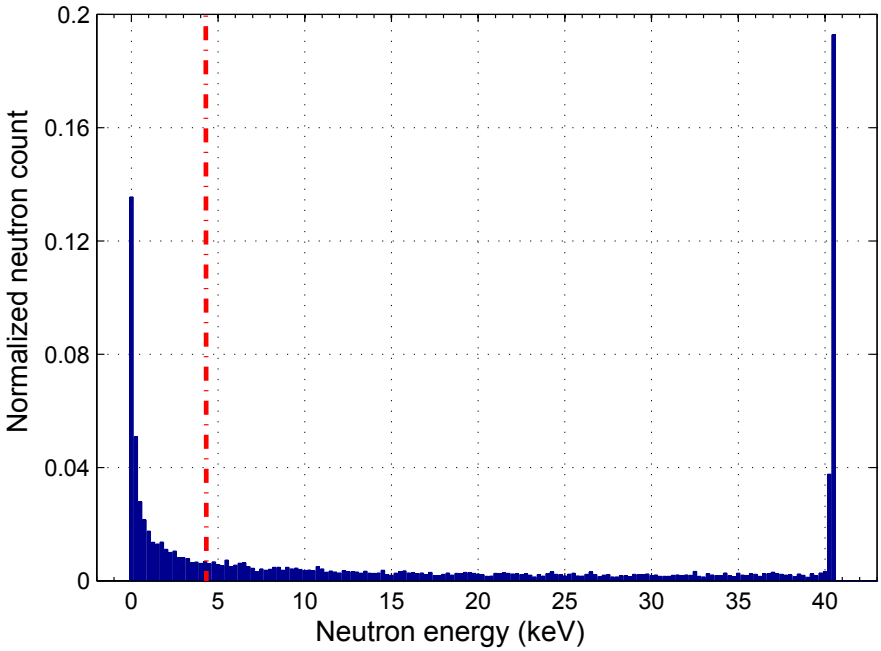

Figure 8.9 – Energy spectrum of simulated 40 keV neutrons just before interacting with the C_4F_{10} droplets. The red band represents the energy threshold that is determined by the operating temperature of the PICASSO detector.

For PICO calibration purposes, a dedicated chamber, named PICO 0.1, was built and contains 30 ml of active liquid. This detector sits inside a water bath with only 1 mm of water in between the neutron beam and the active volume. The chamber is shown in Fig. 8.10.

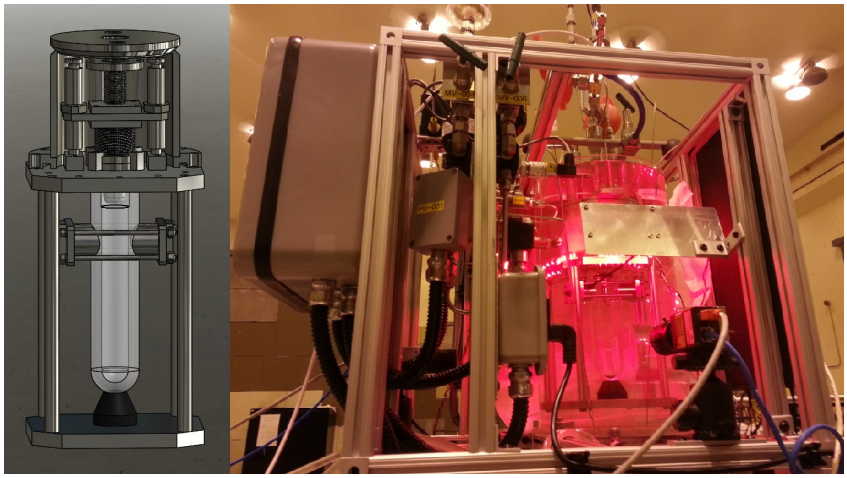

Figure 8.10 – Left: CAD drawing showing the bellows, piezoelectric sensors and the glass jar of the PICO 0.1 detector. Right: Picture of the PICO 0.1 chamber at UdeM inside the thermal water bath.

8.4 Neutron calibration measurements

The calibration measurement of both PICASSO and PICO are the same, i.e, they both measure the detector response at various energy threshold for several monoenergetic neutron energies. However, the data interpretation and data analysis is quite distinct, and they are therefore described in separate sections.

8.4.1 PICASSO neutron calibrations

PICASSO neutron calibrations use monoenergetic neutrons to measure count rates at different energy thresholds by varying the temperature of the detector at atmospheric pressure (1 bar). The goal is to determine the threshold temperature (T_{th}), which is the lowest temperature with an observable count rate, and then to compare it with the theoretical critical temperature predicted by the Seitz model for several neutron energies. The count rate curves obtained for various monoenergetic neutron energies are shown in Fig. 8.11 and on each curve a fit is performed to determine T_{th}.

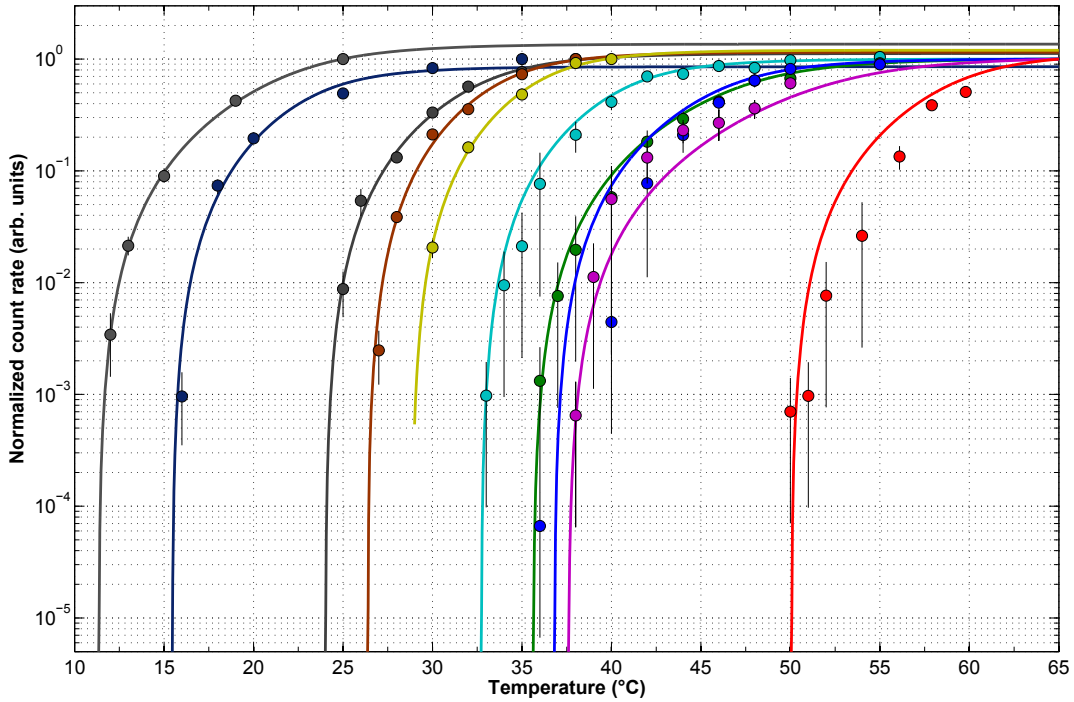

Figure 8.11 – Normalized responses of the monoenergetic neutron beam detector for different incident energies, from left to right: 4 MeV, 2 MeV, 400 keV, 300 keV, 200 keV, 97 keV, 61 keV, 50 keV, 40 keV and 4.8 keV. The five lowest energies were obtained with the resonances of the ^{51}V (p,n) ^{51}Cr reaction and the higher energies with the ^{7}Li (p, n) ^{7}Be reaction.

T_{th} can correspond to either the maximum fluorine or carbon recoil energy (E^{f}_{max}, and E^{c}_{max}). Even though $E^{c}_{max} > E^{f}_{max}$ ($0.28E_n$ for carbon versus $0.19E_n$ for fluorine), fluorine has a higher stopping power, a lower range distribution and higher neutron cross section than carbon as shown in Fig. 8.3, 8.4, and 8.2, respectively, which all increase its bubble formation efficiency. Furthermore, there are two monoenergetic neutron energies, 97 keV and 50 keV, that are exactly on neutron-fluorine cross section resonances which considerably enhances the fluorine cross section compared to carbon. Therefore, for those two energies, there is no ambiguity regarding which atom sets the experimental energy threshold. Once a sufficient amount of temperature thresholds are determined, an empirical mathematical relation between the energy threshold and T_{th} is formulated and compared to the Seitz model. The result is shown in Fig. 8.12.

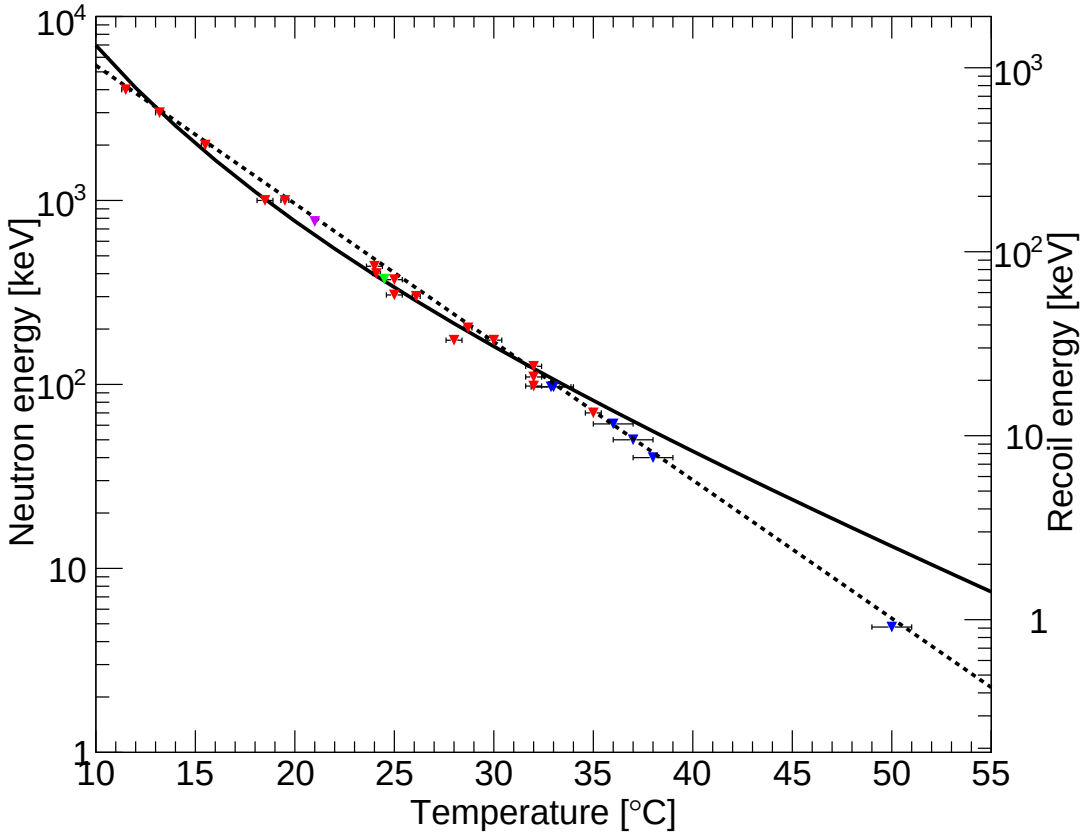

Figure 8.12 – Energy threshold as a function of C_4F_{10} temperature. The red and blue triangles shows the different neutron energies produced (left y-axis) with a vanadium target and a lithium target respectively and their corresponding fluorine recoil energy (right y-axis) and their measured critical temperature (x-axis). The black dashed line shows the Seitz threshold energy as a function of the temperature at 1 bar, while the black dashed line shows the fit to the data. The ^{210}Pb data point (purple triangle) and ^{241}Am data point (green triangle) have an energy threshold of 144.1 keV and 71 kev respectively. The details of these alpha calibrations are presented in section 8.7. The energy of the lithium and vanadium data points are, from left to right: 4 MeV, 2 MeV, 400 keV, 300 keV, 200 keV, 97 keV, 61 keV, 50 keV, 40 keV and 4.8 keV.

The important information that is extracted from Fig. 8.12 is the experimental fit of the relation between recoil energy and threshold temperature. This is particularly true for lower recoil energies since the experimental measurements start to disagree with the

Seitz model. The equation that fits the experimental data is:

$$E_{th} = 0.19 \times 0.00927 \frac{(T_c - T_{op})^3}{(P_{vap} - P_{op})^2}, \tag{8.2}$$

where T_c is the critical temperature of C_4F_{10} and is equal to 72.45°C, T_{op} and P_{op} are the operating temperature and pressure, respectively, and P_{vap} is the vapor pressure of the freon at T_{op} and P_{op}. This equation is used to determine the energy threshold for any given operating temperature at atmospheric pressure of PICASSO detectors. However, it does not say anything about the detection efficiency when the energy deposited is higher than E_{th}. This information is obtained using the experimental data shown in Fig. 8.11. The standard approach of the PICASSO experiment is to perform a fit on each curve, where the experimental fit is given by the following equation:

$$P(E_R, E_{R_{th}}(T)) = 1 - exp\left(\alpha(T)\left(1 - \frac{E_R}{E_{R_{th}}(T)}\right)\right), \tag{8.3}$$

where E_R is the energy deposited, and α is a free parameter that is fit for each neutron calibration curves. The detection efficiency increases faster for high α values and slows down for lower values of α as shown in Fig. 8.13. For neutron energies ranging from 5 to 100 keV, the α parameter varies between 1 and 10. Low energy thresholds favor smaller α which means that there is a slower efficiency increase. In the final PICASSO analysis, the value of $\alpha = 5 \pm^{7.5}_{1.0}$ was used to determine the cross section limit of the WIMP-nucleon interaction.

8.5 PICO neutron calibrations

While the PICO analysis of the neutron calibration data and its interpretation is different from the PICASSO approach, the experimental measurements are the same as PICASSO. However, detector stability prevented any calibration with 4.8 keV neutrons produced with the vanadium target. Hence an additional calibration was done using a SbBe source that produces 22 keV monoenergetic neutrons. Furthermore, for the first

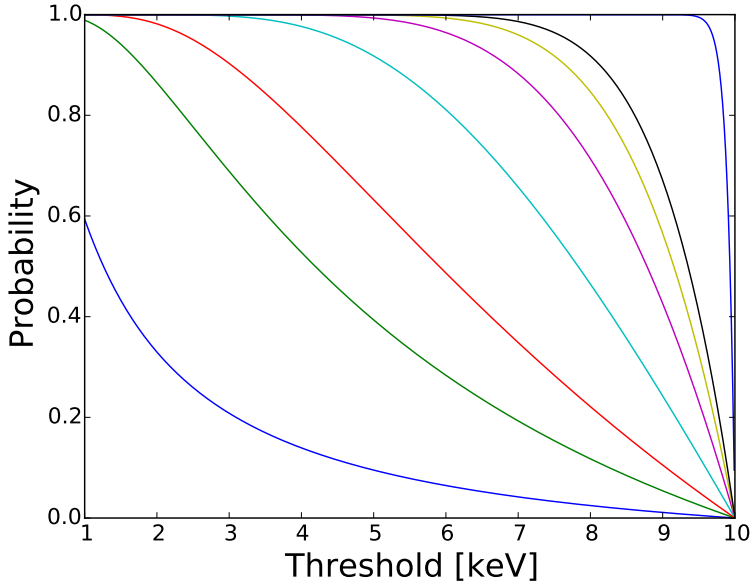

Figure 8.13 – Nucleation probability function used in PICASSO to fit the calibration data. Each curve shows the probability variation for different α parameters as a function of the energy threshold for a fixed energy recoil. The α parameter used in this plot have the following values: [0.1,0.5,1,2.5,5,7.5,10,100]. For a higher value of α, the probability reaches 1 faster.

time other freons were also calibrated with neutrons by filling the PICO 0.1 detector with C_2ClF_5, and $C_2H_2F_4$.

8.5.1 The C_3F_8 neutron beam calibrations

One of the advantages of PICASSO detectors over PICO detectors is their higher stability at a low energy threshold. Since a PICASSO detector has millions of droplets, each acting as an individual bubble chamber, even if there is a non-negligible background, the detectors can still be operated. On the other hand, for a PICO detector, every time there is a bubble, the detector must be re-compressed. In order to do a 4.8 keV neutron calibration with the PICO 0.1 detector, the energy threshold must be lowered to 1.34 keV and 0.91 keV to see the monoenergetic carbon and fluorine recoils, respectively. To measure a partial count rate curve, one needs to vary the detector threshold

between $\sim 0.5 - 1.34$ keV. At those energy thresholds, the environment background was too high and no calibration could be performed.

Neutron calibration measurements with PICO 0.1 were performed for 40, 50, 61 and 97 keV. The result of the 61 keV measurements is shown in Fig. 8.14, on which also appears the same measurement done with a PICASSO detector containing C_4F_{10}, and the usual response curve with the α parameter used for PICASSO calibration purposes. Due to their close carbon to fluorine atomic ratio, C_4F_{10} and C_3F_8 count rate curves agree well with one another.

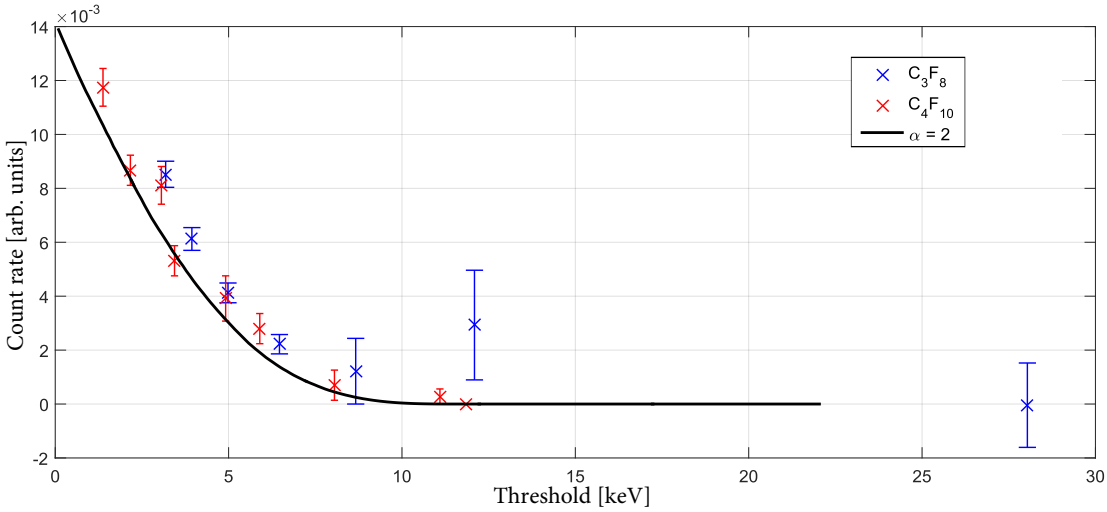

Figure 8.14 – Event rate for 61 keV neutrons measured by PICASSO and PICO. Both data sets were normalized to one another to highlight the similarity of both measurements. The black curve is a fit using the response function from eq. 8.3 with $\alpha = 2$.

8.5.2 C_3F_8 SbBe neutron calibration

To compensate for the inconclusive 4.8 keV monoenergetic neutron beam calibration, a 22.8 keV SbBe neutron calibration source was used to study the detector response to low energy recoils. A SbBe photoneutron source is a two-component source which contains a gamma active ^{124}Sb, and a ^{9}Be conversion target. The ^{124}Sb source was obtained by inserting encapsulated powder of natural Sb (42.6% of ^{123}Sb) inside

the Slowpoke research nuclear reactor of the Polytechnique Montreal. Through neutron thermal captures, ^{123}Sb becomes ^{124}Sb which has a half-life of 60.20 days and decays via beta decay to ^{124}Te accompanied by gamma ray emissions [122]. These gammas can then knock out a neutron from ^{9}Be which has the lowest Q value for neutron emission (1.665 MeV). There are two gamma rays emitted by ^{124}Sb that have energies above this Q value: 1691 and 2091 keV with branching ratios of 0.484 and 0.057 respectively. The complete reaction is described by the following relation:

$$^{124}Sb \rightarrow ^{124}Te + \beta^{-} + \gamma \tag{8.4}$$

$$\gamma + ^{9}Be \rightarrow ^{8}Be + n \tag{8.5}$$

The 1691 keV gammas produce 22.8 keV neutrons, while 2091 keV produce 378 keV neutrons, both with a similar branching ratio as their parent gamma ray.

This calibration is harder to perform because the source emits both neutrons and gammas. Since the detector becomes gamma sensitive at low threshold (< 3 keV), the gamma response is measured by removing the beryllium disk and is then subtracted from the SbBe response of the detector. Throughout the measurements, two 1-inch thick lead disks were inserted in front of the SbBe source to attenuate the gamma flux. The calibration curve obtained for this measurement is shown in Fig. 8.15.

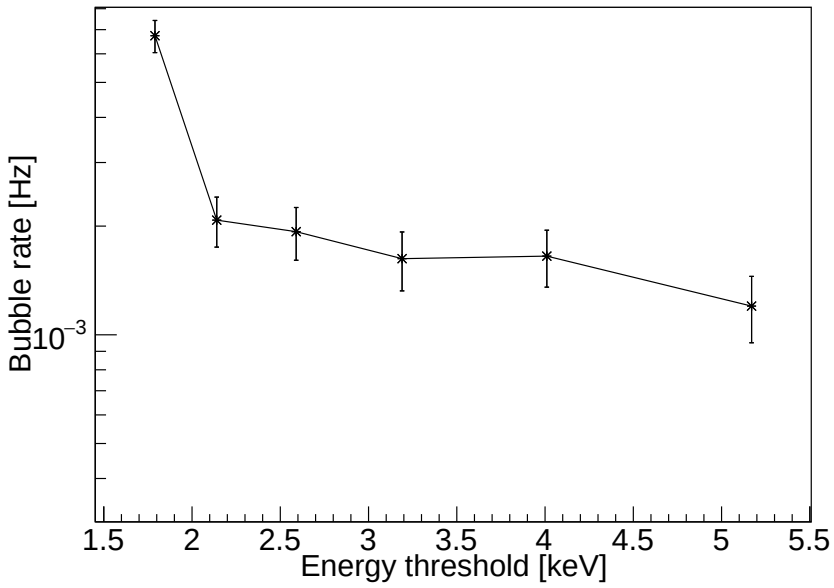

Figure 8.15 – Bubble rate as a function of the Seitz threshold measured with the PICO 0.1 detector with a SbBe source that produces 22.8 keV neutrons. The error bars on the y-axis are due to the statistical uncertainty. The sharp increase of count rate at 1.8 keV is due to gamma produced by Sb.

The 1.8 keV data point has a higher rate than the other points due to the gamma produced by the Sb source and is therefore not used in the neutron efficiency analysis. Consequently, the data point at 2.14 keV is the lowest energy calibration ever performed for neutron calibration purposes with a PICO detector. It was crucial for the new PICO neutron calibration paper in order to describe the bubble efficiency at 2.45 keV, which corresponds to the energy threshold of the second PICO60 C_3F_8 WIMP search.

8.6 Calibration data analysis

The PICO collaboration has developed a Markov Chain Monte Carlo (MCMC) approach to extract the carbon and fluorine efficiency curves from the neutron calibrations. The goal of this approach is to determine the detection efficiency for a fixed energy threshold as a function of recoil energies. The calibration data set used to extract the bubble efficiency at 2.45 keV and 3.29 keV is shown in Table 8.II. These two thresholds were chosen to match the energy threshold of the latest PICO 60 C_3F_8 WIMP searches.

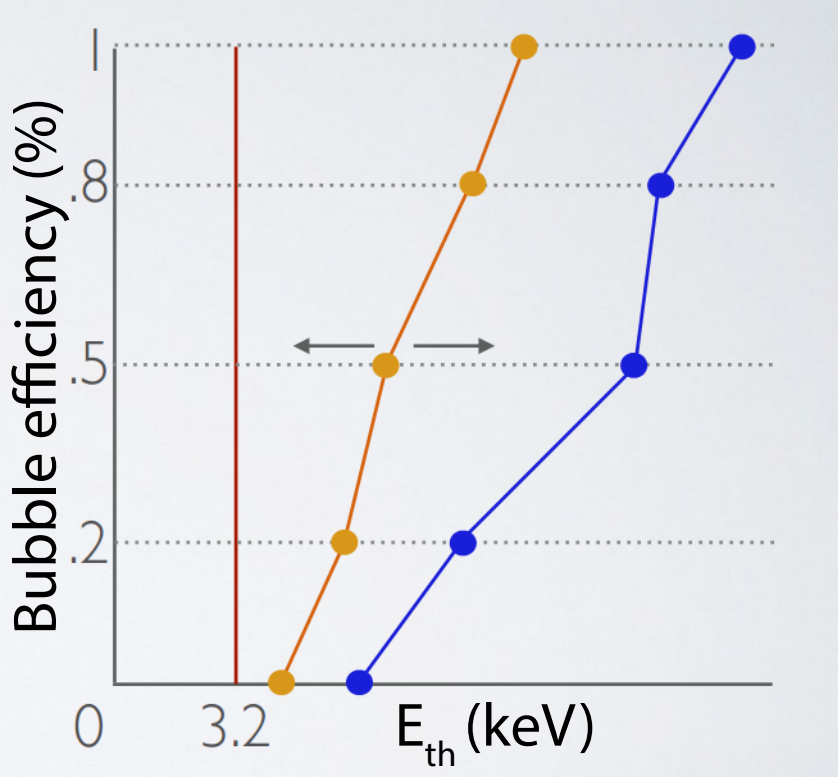

Figure 8.16 – Bubble efficiency of fluorine (yellow) and carbon (blue) for 5 different probability nodes [0,0.2,0.5,0.8,1]. While the probability node are fixed, their correspoding threshold must be determined by the MCMC.

The efficiency curves are obtained separately for carbon and fluorine recoils using the MCMC technique which can be explained as follows: for each recoil species (fluorine and carbon), there are 5 probability nodes: [0,0.2,0.5,0.8,1] that the MCMC must

determine as shown in Fig. 8.16, and for each node, there are two fenceposts, i.e., two threshold energies, 2.45 keV and 3.29 keV. There are also 14 nuisance parameters that provide the systematic errors to the MCMC as well as some additional constraints. The most important constraints are the assumptions that the detection efficiency must be equal to zero for energy depositions that are lower than the Seitz threshold, and that the efficiency must be monotonically increasing.

For each calibration data set, a GEANT4 [116] or MCNPX-Polimi Monte Carlo simulation [123] is performed to provide recoil spectra, and for each of them the likelihood of a given efficiency curve convoluted with the simulated recoil spectra is calculated. The recoil spectra, efficiency curve, and nuisance parameters are inputs to a maximum likelihood calculator that gets called by the MCMC, which then varies the 10 probability nodes to obtain the chi-square space of the efficiency curves. Furthermore, there are recoil spectra for 1, 2 and more than 2 bubble events for the PICO 0.1 dataset and up to 7 in multiplicity for the PICO2L dataset. The multiplicity of each data set is shown in Fig. 8.17.

Dataset	Detector	Thresholds (keV)	Multiplicity
97keV Beam	PICO0.1-2013	3.2	1,2,3+
61keV Beam	PICO0.1-2013	3.1	1,2,3+
97keV Beam	PICO0.1-2014	3.0, 3.6	1,2,3+
61keV Beam	PICO0.1-2014	2.9, 3.6	1,2,3+
50keV Beam	PICO0.1-2014	2.5, 3.5	1,2,3+
SbBe	PICO0.1	2.1, 2.6, 3.2	2,3+
AmBe	PICO2L	3.2	1,2,3,4,5,6,7+

Table 8.II – Neutron calibration data sets used to determine nuclear bubble formation efficiency at 2.45 keV and 3.29 keV. The threshold values listed here correspond to data point that were taken at those specific value in order to determine, using an MCMC approach, the bubble efficiency at 2.45 keV and 3.29 keV.

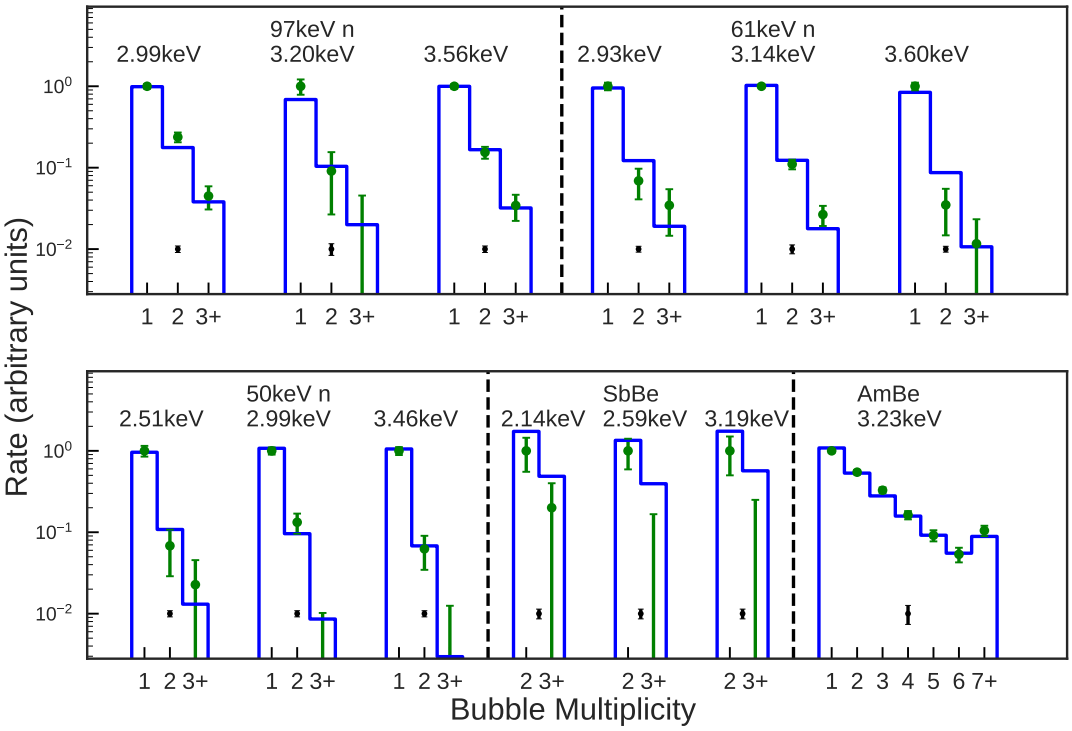

Figure 8.17 – Comparison between the bubble rate multiplicity of GEANT4 simulations and the experimental data taken with the PICO 0.1 detector. The green points are the experimental data points while the blue histograms are the result of the GEANT4 simulations convoluted with the best bubble efficiency curves found with the MCMC.

A log-likelihood (LL) is then constructed from the Poisson log-likelihood for observed event counts plus a Gaussian penalty for nuisance parameters:

$$LL = \sum_{i=exp} \sum_{j=nbub} \left(-\nu_{i,j} + k_{i,j} + k_{i,j} \log\left(\frac{\nu_{i,j}}{k_{i,j}}\right)\right) + \sum_{l=nuisance} -\frac{s_l^2}{2}, \tag{8.6}$$

where $k_{i,j}$ are the number of bubbles with multiplicity j observed in experiment i, $\nu_{i,j}$ are the expected number of bubbles given a set of efficiency curves and nuisance parameters, and s_i is the number of standard deviation the nuisance parameter l is away from its nominal value. An experiment i, in this context, is any dataset listed in Table 8.II and

each calibrated energy threshold of a given dataset is also an experiment. The goodness of fit χ^2 is define as

$$\chi^2 = -2 \cdot LL. \tag{8.7}$$

The resulting bubble efficiency curves are the ones shown in Fig. 8.18.

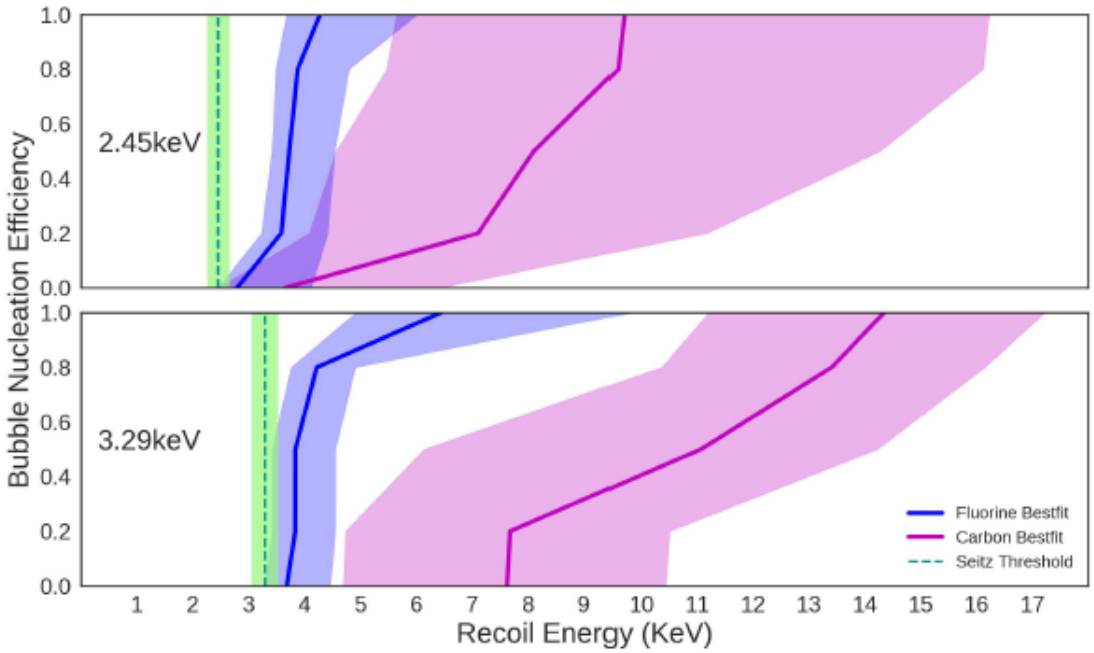

Figure 8.18 – Bubble efficiency as a function of recoil energy in keV. The green band shows the operating Seitz threshold, while the blue and purple bands show the detection efficiency of fluorine and carbon recoils respectively. The top (bottom) plot shows the bubble efficiency for a 2.45 (3.29) keV threshold.

The uncertainty on each curve, but especially on the carbon curve (purple), is much larger at 2.45 keV than at 3.29 keV, since fewer calibration data were available. In the near future, the PICO 0.1 detector will be refilled with C_3F_8 and will be calibrated with 4.8 keV neutrons once again. By improving the cleanliness of the detector and the pressure system stability, it might be possible successfully to calibrate the detector at this neutron energy.

8.6.1 C_2ClF_5 (R-115) calibration measurements

As discussed in the previous sections, monoenergetic neutrons are used to calibrate SHL detectors, and from these measurements, the bubble efficiency of carbon and fluorine recoils at a fixed energy threshold are extracted with a complex data analysis method. Ideally, if possible, the bubble efficiency at a fixed energy threshold for various recoil energies would be measured. This measurement would be possible if the energy of the recoils would be measured by, for example, determining the energy of the recoiling neutrons with a backscatter arrangement. On the other hand, a monoenergetic recoil source can also be used to study the bubble formation mechanisms by measuring its count rate as a function of the energy threshold. This type of measurement had already been performed with PICASSO detectors by using recoils of daughter nuclei in alpha decays, but those measurements involved high energy monoenergetic recoils typically around 100 keV. Another similar measurement was performed by filling PICO 0.1 with C_2ClF_5, and by using the reaction $^{35}Cl(n_{th}, p)^{35}S$ which produces 17 keV monoenergetic sulfur recoils and a 550 keV proton. To perform the measurement, a 1-inch paraffin disk was placed in front of a SbBe source to slow down and thermalize the 22.8 keV neutrons. The thermodynamic properties of C_2ClF_5 are similar to those of C_3F_8 as shown in Table 8.III.

Freons	C_2ClF_5	C_3F_8
T_c (°C)	80.0	71.87
T_b (°C)	-38.94	-36.79
Density at 15°C (g/ml)	1.3388	1.3795

Table 8.III – Thermodynamic properties of C_2ClF_5 and C_3F_8.

Thus studying this new freon can inform the bubble formation mechanism of superheated freons. The count rate as a function of the Seitz energy threshold of this measurement is shown in Fig. 8.19.

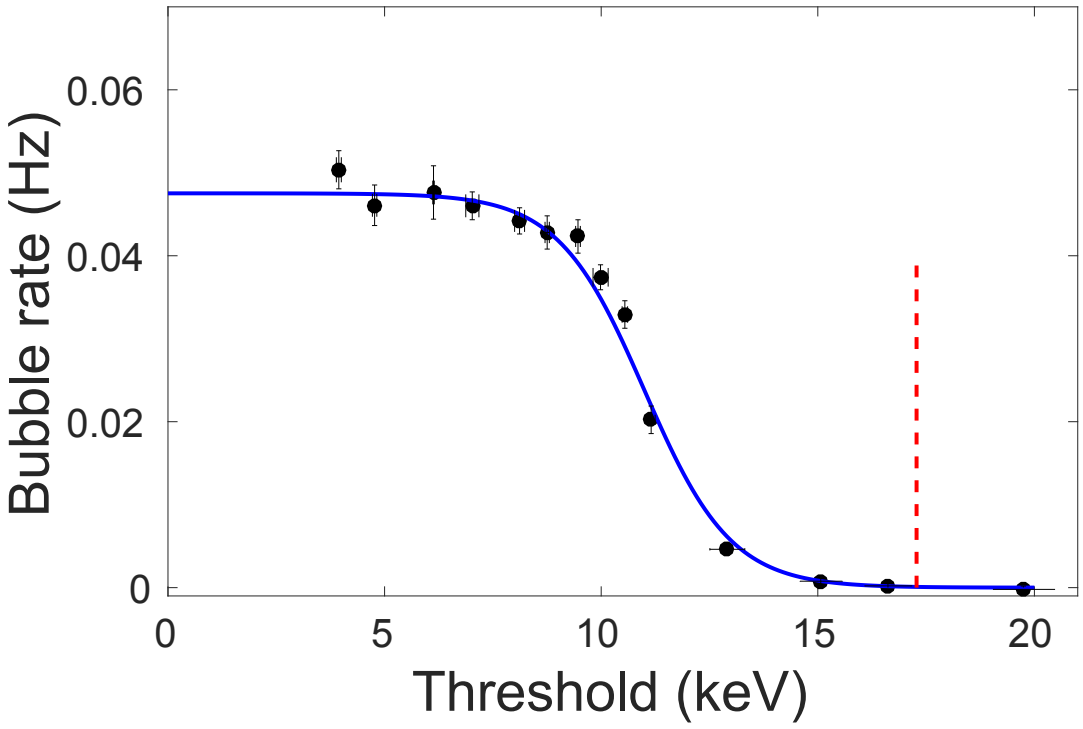

Figure 8.19 – ^{35}S 17 keV monoenergetic recoil calibration with the PICO 0.1 detector filled with C_2ClF_5. The dashed red line indicates the Seitz energy threshold of 17 keV while the blue curve shows a sigmoid fit. The uncertainty on the bubble rate is purely statistical while the uncertainty on the energy threshold is due to pressure and temperature uncertainties.

Since the lowest energy threshold point is at ~ 4 keV, 1.691 MeV gammas produced by the ^{124}Sb source do not generate any events in addition to thermal neutron capture events. A measurement without the beryllium disk was performed and confirmed this hypothesis.

This measurement provides insight for models whose goal is to describe the bubble production mechanism. While the MCMC approach used by PICO collaboration, presented in Sect. 8.6, does provide WIMP bubble efficiency curves at a fixed threshold, it does not explain any of the physics involved in the nucleation process.

An alternative model was developed by the PICO group in Montreal to describe, from a macroscopic point of view, the efficiency of bubble formation by nuclear recoils. This model is described in the section following the description of alpha calibration measurements since those also include monoenergetic recoils from the daughter nuclei of alpha decays, and provide additional input to this alternative model.

8.7 Alpha calibrations with PICASSO detectors

The main background of the PICASSO experiment comes from the incorporation of ^{222}Rn inside the detector during the fabrication process due to its high solubility in freons. During alpha decays, both the recoil of the daughter nucleus and the alpha particle can deposit enough energy to create bubbles. One of the most significant discoveries of PICASSO was the observation that alpha decays had louder acoustic signals than neutron and WIMP interactions [98]. This allowed full alpha-neutron discrimination in PICO and partial alpha-neutron discrimination in PICASSO. The following equation gives a good approximation of the recoil energy of a daughter nucleus:

$$E_R = \frac{m_\alpha}{m_R} E_\alpha, \tag{8.8}$$

where m_α is the mass of the alpha particle, m_R is the mass of the daughter nucleus, and E_α is the energy of the alpha particle. Typical alpha energies range from 5 to 7 MeV. The recoil energy of the daughter nucleus is between 90 - 160 keV. Alpha particles have a total energy much higher than the energy threshold, but have a low dE/dx and thus deposit their energy along a track much longer than the critical radius. Consequently, they do not always produce bubbles as it is highlighted by the alpha calibrations described in the next sections. However, the dE/dx of alpha particles increases significantly at the end of their path due to their Bragg peak. This feature increases the alpha bubble formation efficiency considerably, and directly impacts their bubble formation threshold.

8.7.1 ^{214}Am alpha decays outside of droplets

A dedicated 1.5 L (1/3) PICASSO detector was built to perform a ^{241}Am alpha decay calibration. During its fabrication, ^{241}AmCl was added to the main solution before polymerization and generated an activity of 6.4 Bq. Since ^{241}AmCl is hydrophilic and C_4F_{10} is hydrophobic, the ^{241}AmCl solution does not enter inside the droplets and stays in the gel. The result of the measurement is shown in Fig. 8.20 and the decay chain of ^{241}Am is shown in Table 8.IV.

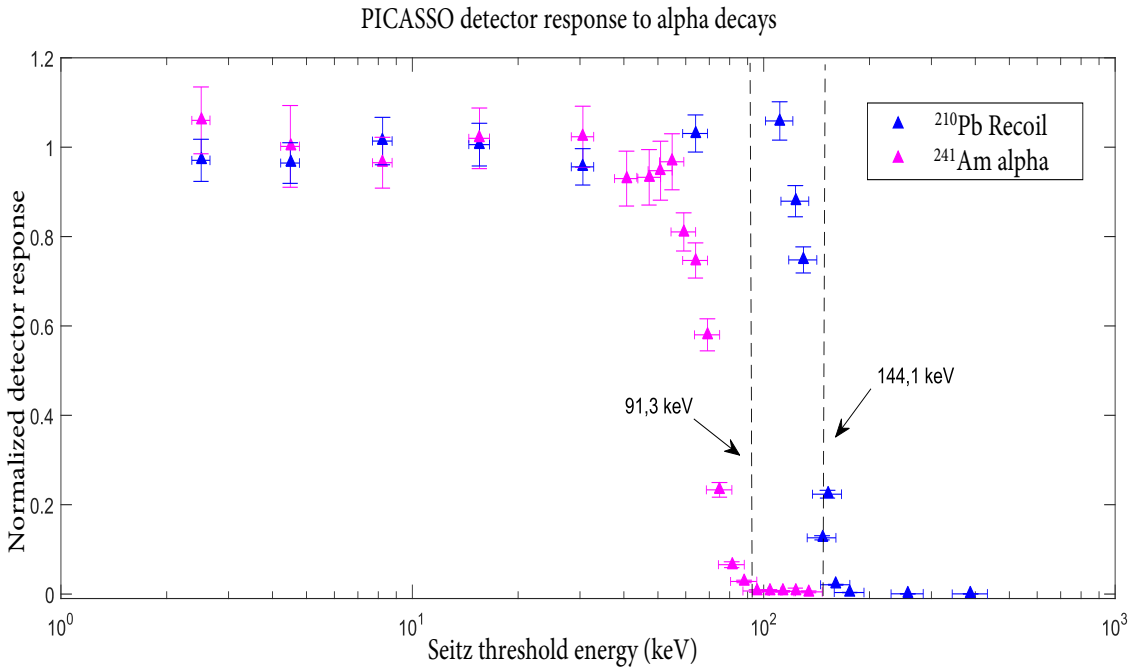

Figure 8.20 – PICASSO detectors response to alpha decays. The pink curve shows the detector response to the ^{241}Am decay chain. ^{241}Am is located outside of the droplets, and therefore only alphas can travel inside the droplets. The blue curve shows the detector response to 144.1 keV recoils produced by the recoils of the daughter nucleus of the ^{214}Po alpha decay.

Nucleus	Decay mode	Half-life	Alpha energy	Daughter nucleus recoil energy
^{241}Am	α	432.6 y	5.490 MeV	91.30 keV ^{237}Np
^{237}Np	α	2.14x10^{6} y	4.788 MeV	80.97 keV ^{223}Pa

Table 8.IV – ^{241}Am decay chain [124].

The energy of neptunium recoils is 91.3 keV, however, the data shows that the count rate starts to increase only at a lower energy threshold of 71 keV which confirms that only alpha particles at their Bragg peak produce bubbles.

8.7.2 ^{222}Rn background and ^{226}RaCl calibration

^{226}Ra has a long decay chain that contains multiple alpha decays which are listed in Table 8.V.

Nucleus	Decay mode	Half-life	Alpha energy	Daughter nucleus
^{226}Ra	α	1602 y	4.871	80.8 keV ^{222}Rn
^{222}Rn	α	3.8235 d	5.590	102.5 keV ^{218}Po
^{218}Po	α 99.98%	3.10 min	6.115	^{214}Pb
	β 0.02%		2.883	
^{218}At	α 99.90 %	1.5 s	6.874	^{214}Bi
	β^- 0.10%		2.883	^{218}Rn
^{218}Rn	α	35ms	7.263	^{214}Po
^{214}Pb	β^-	26.8 min	1.024	^{214}Bi
^{214}Bi	β 99.98%	19.9 min	3.272	^{214}Po
	α 0.02%		5.617	^{210}Ti
^{214}Po	α	0.1643 ms	7.883	144.1 keV ^{210}Pb
^{210}Ti	β^-	1.30 min	5.484	^{210}Pb
^{210}Pb	β^-	22.3 y	0.064	^{210}Bi
^{210}Bi	β^-99.99987%	5.013 d	1.426	^{210}Po
	α 0.00013%		5.982	^{206}Ti
^{210}Po	α	138.376 d	5.407	^{206}Pb
^{206}Ti	β^-	4.199 min	1.533	^{206}Pb
^{206}Pb	-	stable	-	-

Table 8.V – ^{226}Ra decay chain [125]. The main alpha decay chain is shown in red.

To get a better understanding of this alpha background, a ^{226}RaCl solution was injected on the top of the detector. The ^{226}Ra can decay into ^{222}Rn which then diffuses inside freon droplets. The initial activity was ≈ 10 Bq. The highest monoenergetic recoil of the decay chain comes from the ^{214}Po decay that produces 144.1 keV ^{210}Pb recoils. The experimental count rate is shown in Fig. 8.20 and corresponds precisely to this value and therefore confirms that the alpha decay happens directly inside the droplets.

Additional information regarding the alpha response of SHL can be extracted by studying the acoustic emission as a function of threshold. As the threshold is lowered, alpha particles start producing bubbles as well, and thus increases the acoustic emission. This effect is shown in Fig. 8.21 which displays the acoustic variable EVAR (Sect. 6.4) for three different thresholds. At $E_c = 105.2$ keV (left), only a single acoustic peak due to 144.1 keV ^{210}Pb recoils shows up. At $E_c = 57.9$ keV (middle), the lower EVAR peak is due to the single bubble produced by recoils of daughter nuclei, while the higher EVAR peak is produced by the combination of both the bubbles induced by alpha particles and the bubble produced by daughter nuclei. However, alpha bubble efficiency is less than 100% at this threshold. At $E_c = 5.1$ keV (right), the alpha efficiency is 100%, and hence there is only one EVAR peak. For this analysis, the EVAR variable was corrected to account for the temperature dependence of the acoustic emission in Fig. 8.21

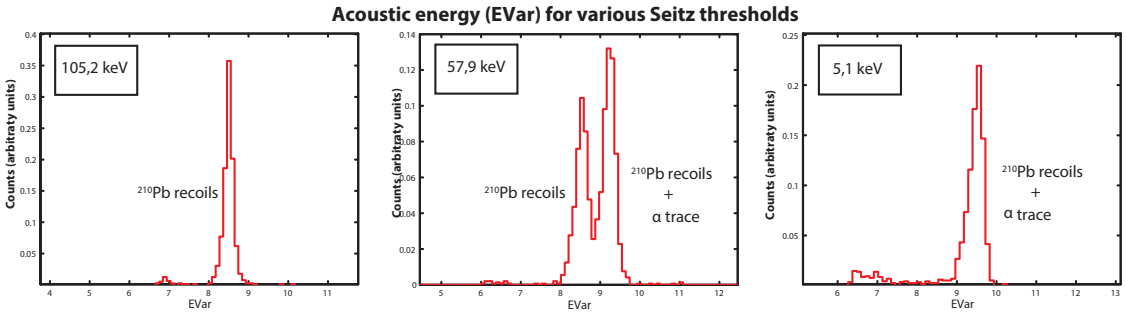

Figure 8.21 – EVar distribution for three different energy thresholds; from left to right: 105.2 keV, 57.9 keV, and 5.1 keV. A second EVAR peak appears due to additional bubbles produce by alpha particles.

The ratio between the count rates of each acoustic peak as a function of the energy threshold is shown in Fig. 8.22. The second acoustic peak (^{210}Pb + alpha) is a direct measurement of the alpha detection efficiency. It is only at ∼80 keV that alpha particles by themselves start to produce bubbles along their track which is in agreement with the ^{214}Am calibration.

These alpha calibration measurements proved to be essential in PICASSO and the SHL technique in general. The possibility of having total alpha discrimination offers the prospect of a larger increase in dark matter detection sensitivity. In PICASSO, however, the discrimination capabilities, unfortunately, could never be fully exploited. A typical neutron-alpha EVAR distribution is shown in Fig. 8.23.

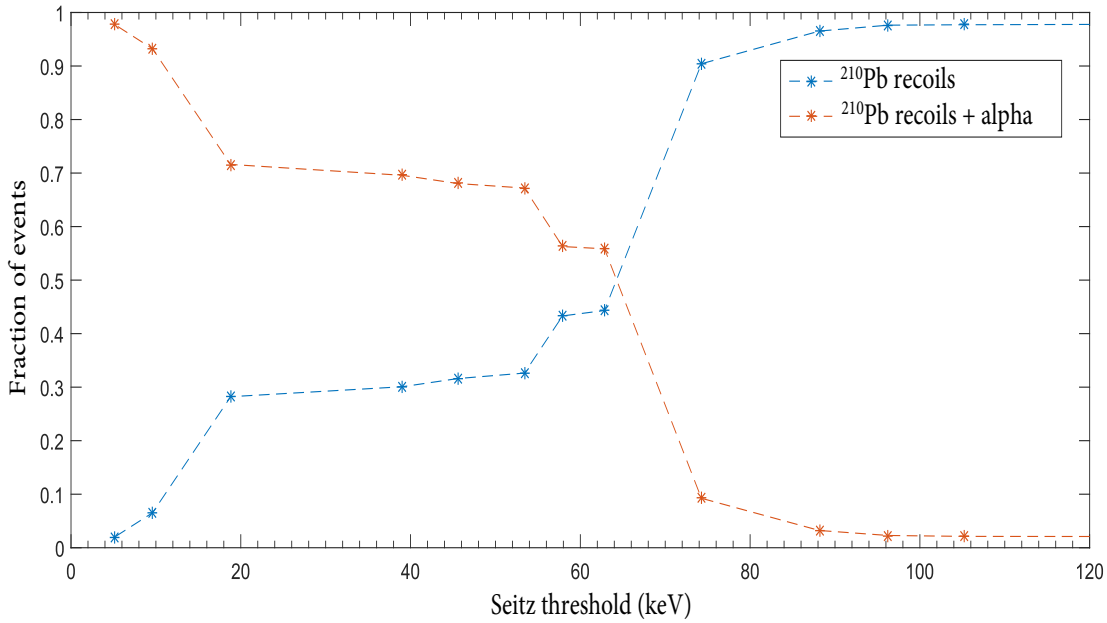

Figure 8.22 – Acoustic peak ratio between ^{210}Pb + alpha (red) and ^{210}Pb recoils (blue) as a function of Seitz threshold. As the threshold decreases the count rate of the second acoustic peak increases and tends toward 100%.

These alpha calibrations also highlighted the fact that the alpha contamination produces a constant background as a function of the energy threshold. Once the threshold

is lower than 144.1 keV, the recoil of the daughter nucleus will always produce a bubble regardless of the alpha particle, and thus the count rate is stable. Therefore, if dark matter interacts with the detector, the count rate should increase as the energy threshold is decreased while if there is no dark matter interaction, the count rate will stay at a constant plateau as a function of the energy threshold. This observation was key for WIMP searches with PICASSO.

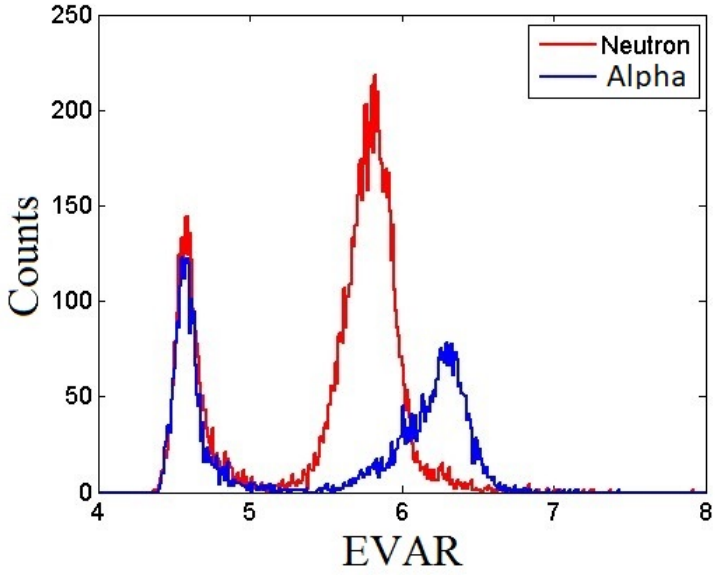

Figure 8.23 – EVAR count distribution for neutron (red) and alpha decay events (blue). There is an overlap between the neutron peak and alpha peak.

8.7.3 Alpha acoustic spectroscopy in PICO

Alpha decays in the radon decay chain can be identified in a PICO detector by examining the time difference between individual alpha events and by comparing it to the half-life of each decay. The main decay chain of radon is shown in red in Table 8.V. The fourth alpha decay has a much longer half-life than the other three decays and thus cannot be tagged. Using the time difference between each decay, the frequency spectrum of AP for the first three decays is isolated and shown in Fig. 8.24. A higher energy alpha will produce more bubbles along its track and generate a higher acoustic signal. The first

and second alpha decay have similar energies (5.6 & 6.1 MeV) and form a single wide acoustic peak, while the third alpha decay of 7.9 MeV forms a single higher AP peak.

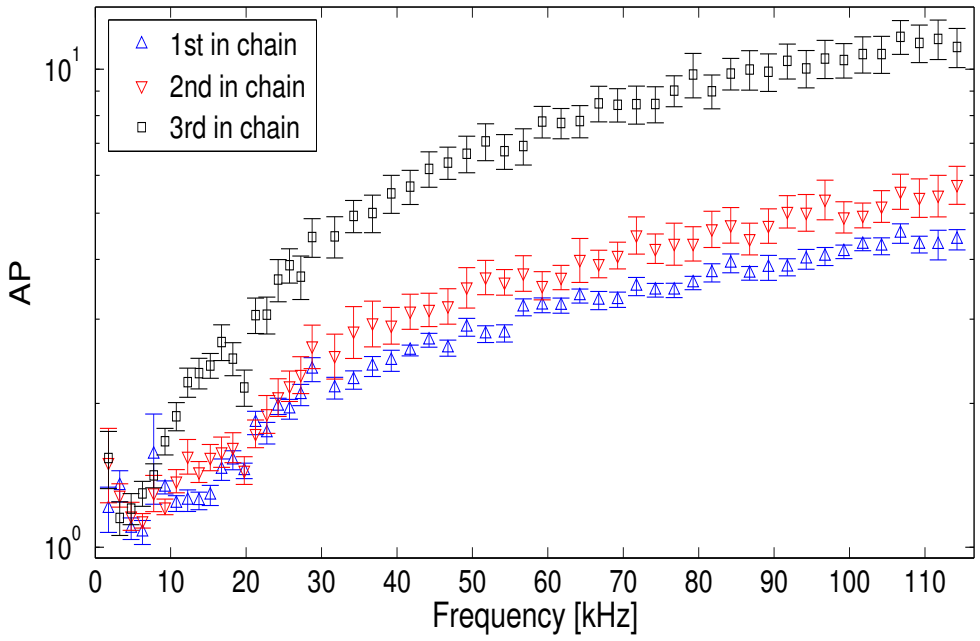

Figure 8.24 – AP frequency spectrum of the first three alpha decays in the ^{226}Rn decay chain: 5.6 MeV (blue), 6.1 MeV (red) and 7.9 MeV (black). It highlights the dependence of AP on the energy of alpha particles.

To highlight this characteristic and to demonstrate that alpha events are louder than neutron events, Fig. 8.25 shows the AP distribution of the PICO 2L detector during an AmBe calibration as well as during a WIMP search run. The AmBe source produces only polyenergetic neutrons, but the length of the calibration is long enough for alpha decay to occurs, however during a WIMP search run, there are almost exclusively alpha events. There is an unambiguous separation in AP between the black peak on the left at AP equals 0 (neutron peak) and the two red peaks on the right (alpha). The left alpha peak corresponds to the two first alpha decays in the radon decay chain, and the right peak corresponds to the third decay with the largest energy and smallest range (7.9 MeV α + 144.1 keV ^{210}Pb). During dark matter searches and in every PICO detector, an AP cut is applied which is able to remove $\sim$100% of alpha events, while retaining $\sim$ 99%

of the WIMP signal region. The AP cut is delimited by the two dotted blue lines.

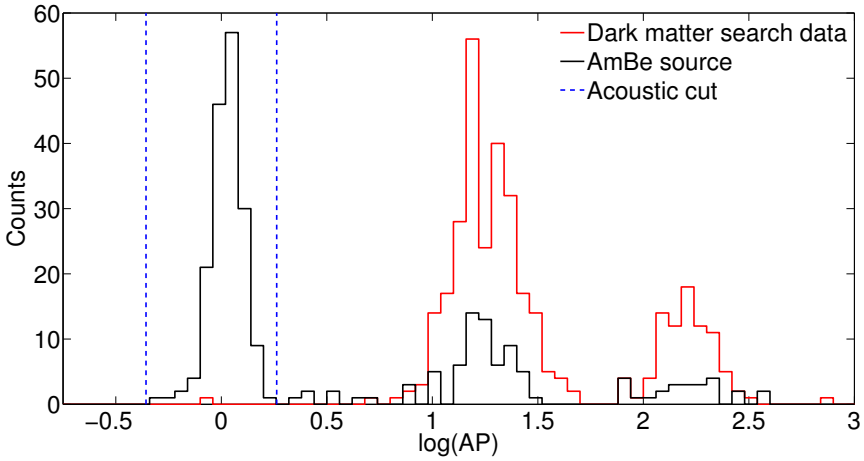

Figure 8.25 – AP distribution of the PICO 2L detector for two data taking sessions. The AmBe (black) calibration contains both neutron and alpha events, while the dark matter search (red) contains mostly alpha events. The dotted blue line indicates the AP cut defined to reject alpha events while maintaining WIMP sensitivity.

8.8 The phenomenological sigmoid model

Instead of assuming a particular microscopic model of the bubble production mechanism, one can also pursue a phenomenological approach, and try to build a global model that is capable to reproduce the data, and might have predictive capabilities. This is the path that was pursued by the PICO UdeM group and is in some way an improvement of the alpha parameterization (eq. 8.3) that was used to fit the neutron calibration measurements of the PICASSO detector response. Since the detector response looks similar to a sigmoid function, a heavyside function folded with a Gaussian was investigated. The probability function of this so-called Gaussian Blurred Step (GBS) is a function with two free parameters, and is expression is given in eq. 8.9.

$$P(E,E_{th}) = 0.5 \times \left[\left(erf\left(\frac{E - E_{th}}{\sqrt{2}\sigma} \right) \left(\frac{0 - E_{th}}{\sqrt{2}\sigma} \right) \right], \tag{8.9}$$

where $E_{th} = E_S + \Delta E$, $\Delta E = 1.81 \times ln(E_S) + 0.93$, $\sigma = 0.12 \times E_{th}$, and E_S is the Seitz threshold.

The free parameters are σ which describe the width of the response, i.e., the transition region between the beginning of the response and the plateau, and the energy shift ΔE, which is the energy difference between the Seitz threshold and the 50% inflection point of the transition curve to the plateau. To determine the value of those two parameters, the 17 keV ^{35}S and 144.1 keV ^{210}Pb monoenergetic recoil measurements were used. One distinctive feature between those two measurements is their ΔE, which is larger for 144.1 keV recoils than for 17 keV recoils as shown in Fig. 8.26.

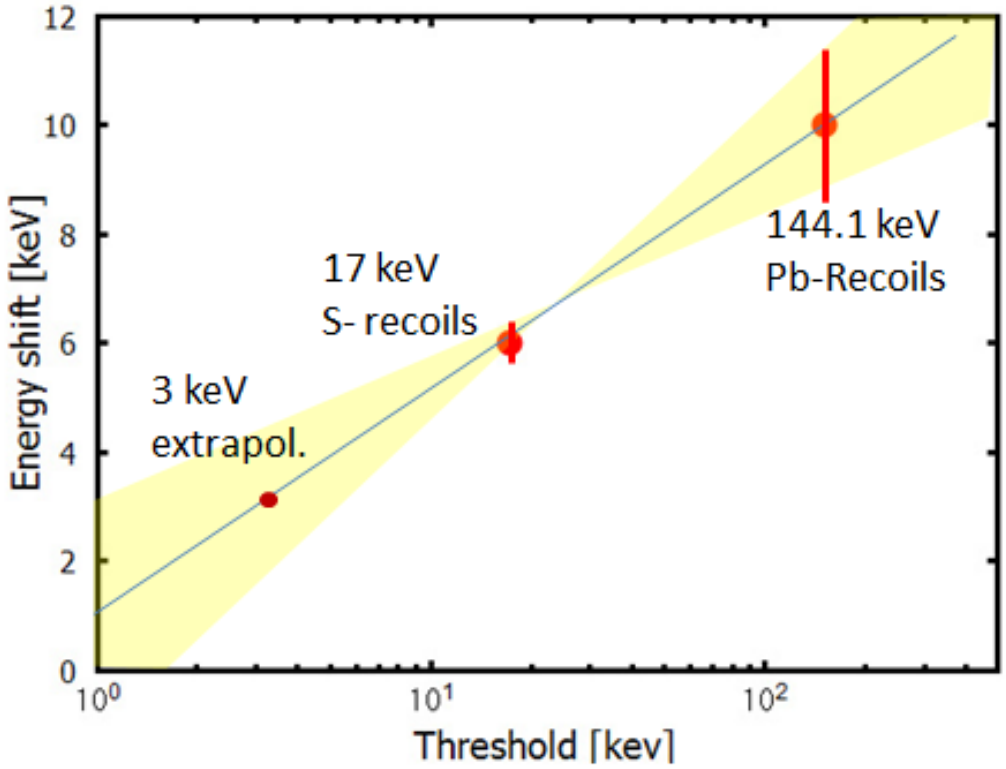

Figure 8.26 – Energy shift (ΔE) as a function of Seitz energy thresholds obtained with 17 keV and 144.1 keV calibrations. This way, within the given errors (yellow), ΔE can be extrapolated to the lower PICO operating thresholds.

To test this model, the probability function $P(E, E_{th})$ is multiplied by the theoretical

count rate which is calculated using the (n, F/C) elastic scattering cross sections. This model can then also be applied to the measured count rate of several monoenergetic neutron calibrations done both with C_3F_8 and C_4F_{10}. The result of this comparison is shown in Fig. 8.27 for 61 keV monoenergetic neutrons for both C_3F_8 (PICO) and C_4F_{10} (PICASSO). In both cases, this model reproduces well the experimental count rate curves. Hence, with only two fitted data points to extract σ and ΔE, this model is able to emulate a complex calibration curve in a large range of neutron energies.

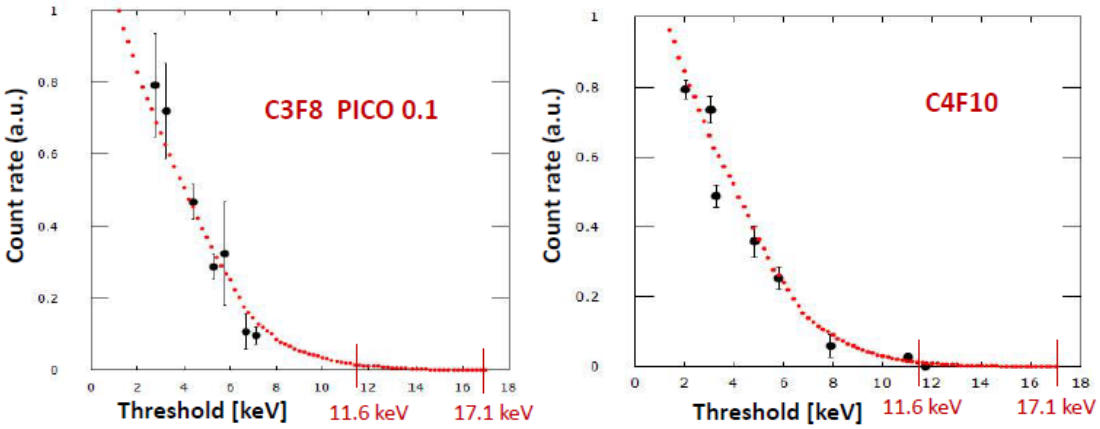

Figure 8.27 – GBS model comparison of 61 keV monoenergetic neutrons. The theoretical curve was normalized to the experimental data. The GBS model shows very good agreement both in C_3F_8 (left, PICO) and C_4F_{10} (right, PICASSO), and also at other neutron energies.

8.9 Gamma background and calibration

One of the essential characteristics of superheated liquid bubble chambers is their intrinsic low gamma sensitivity. The main interaction process between gammas and the active target is Compton scattering. Along the path of a gamma ray, multiple Compton electrons will produce delta rays with a maximum energy of about 1 keV and an energy spectrum decreasing exponentially as a function of energy. Therefore, 1 keV delta rays are very rare, and consequently, SHL bubble chambers only become sensitive to gammas at low energy thresholds in the keV range. The probability of multiple delta rays

combining their energy to produce a small bubble since it is suppressed by the second Seitz criterion which states that the energy must be deposited within a critical radius of a few nanometers. Over the years, many gamma calibrations were performed by the COUPP, PICASSO and PICO collaborations, and the sum of the results are compiled in Fig. 8.28. The nucleation probability of C_3F_8 at 3.3 keV is equal to $\sim 10^{-10}$.

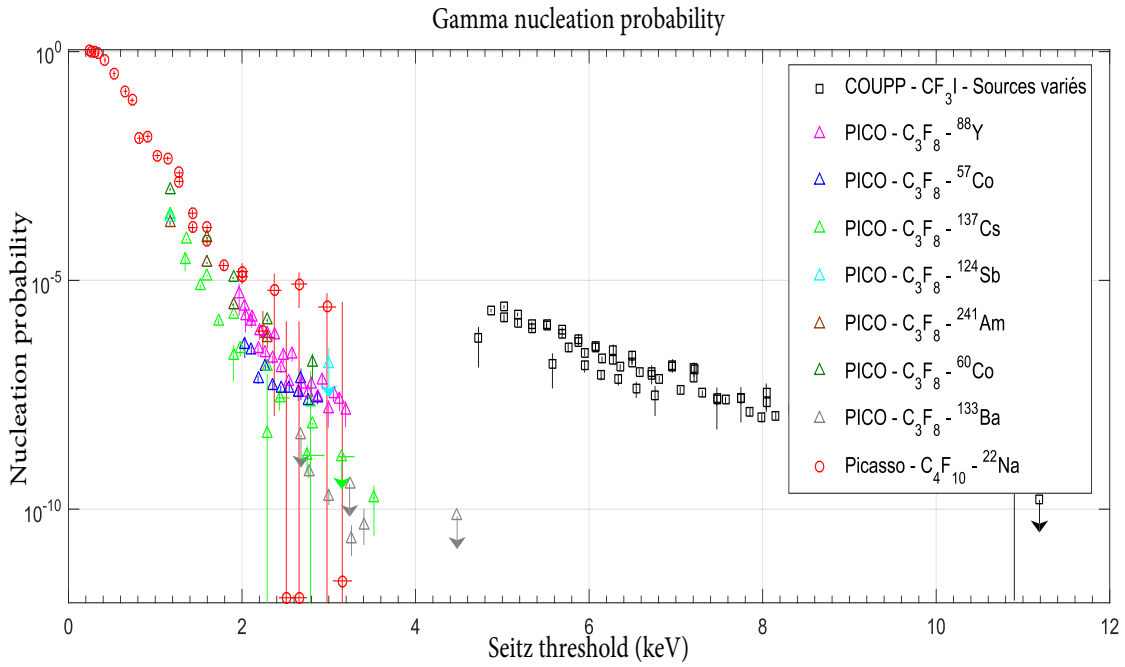

Figure 8.28 – Gamma nucleation probability of several gamma calibrations performed by COUPP, PICASSO, and PICO. The nucleation probability of C_3F_8 at 3.3 keV is equal to $\sim 10^{-10}$. Decreasing the Seitz energy threshold increases the gamma nucleation probability exponentially.

This contrasts with the gamma nucleation probability of CF_3I, which starts to be important at a higher threshold than C_3F_8. This limits the detection capabilities of low WIMP masses with CF_3I. The main hypothesis, that explains the higher gamma sensitivity of CF_3I, is the presence of iodine which carries more electrons that can be ionized than for C_3F_8. This difference between CF_3I and C_3F_8 suggest that $C_2H_2F_4$, another interesting detector fluid, could have an even smaller gamma nucleation probability. If

this hypothesis turns out to be true, a detector filled with $C_2H_2F_4$ could be operated at an even lower threshold and become sensitive to even smaller WIMP masses than C_3F_8. Furthermore, some CF_3I contamination was detected in PICO2L and PICO60 after the PICO CF_3I program ended and this is considered to be the cause of the disagreement and data scattering between several calibration measurements shown in Fig. 8.28. The CF_3I contamination level in C_3F_8 detectors was measured latter precisely and its addition in GEANT4 simulations showed that it indeed increases the nucleation probability and fully explains the anomalies in some of the gamma calibration measurements. A complete review of the PICO gamma calibrations is underway which also includes the implementation of an improved gamma nucleation model (to be submitted).

It is important to note that PICASSO has also performed several gamma calibrations with different gamma sources, and each result showed the same nucleation probability regardless of the energy of the gamma sources. The impact of the gamma background in both experiments is entirely different. In the case of PICASSO, the main and irreducible background was due to alpha contamination in the detector and the gamma background at the achieved level of sensitivity was not significant in the range of 1 - 30 keV energy threshold during WIMP searches.

In PICO, with full alpha discrimination, a much higher level of sensitivity (10^{-3} with respect to PICASSO) was achieved and therefore at low energy threshold, i.e., below 3 keV, the gamma sensitivity becomes an important issue. The current way to address this problem is to directly measure the gamma response at the same energy threshold as WIMP searches are conducted with gamma sources and populate Fig. 8.28. This approach, however, cannot provide any knowledge regarding the production rate of gammas due to radioactive contamination of the components of the detector. The number of gammas that interact with the freon during a given WIMP run must, therefore, be predicted by a complete GEANT4 simulation. The experimental nucleation probability extracted from the gamma calibrations can then be used to predict the number of gamma events that will occur inside the detector.

8.10 Complete response of PICASSO detectors

The PICASSO detector response to different type of particle interactions is summarized in Fig. 8.29. It shows the detector response to gammas measured with a ^{22}Na source as well as the two alpha calibration measurements previously shown in Fig. 8.7. In addition, the response to fast neutrons from a calibrated AcBe source which are also used to monitor the mass of C_4F_{10} in PICASSO detectors is shown, as well as the response to a hypothetical WIMP of 10 GeV/c^2 mass.

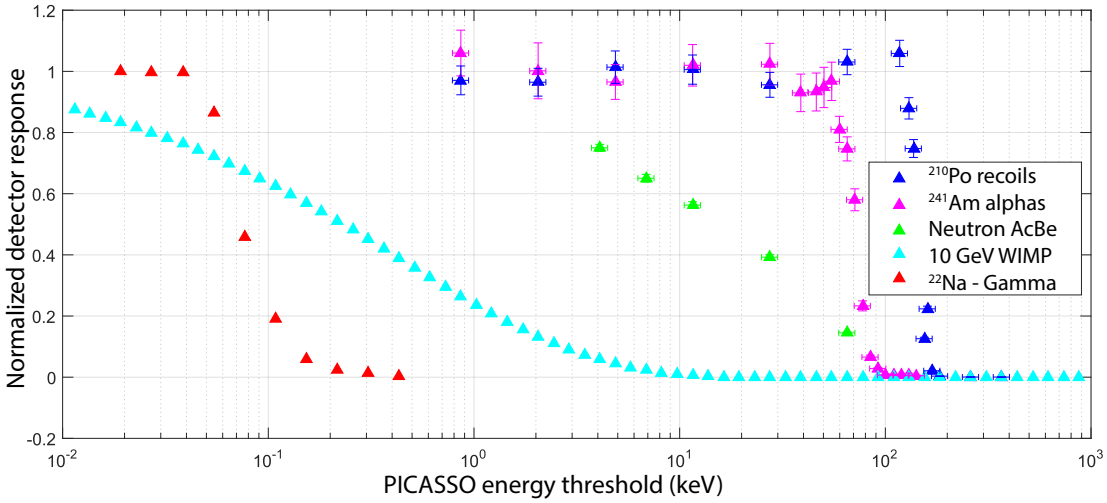

Figure 8.29 – Normalized PICASSO detector response to various calibration sources as well as the response to a theoretical 10 GeV/c^2 WIMP as a function of the calibrated threshold energy determined with neutron calibration measurements.

8.11 Neutrino floor

Solar and atmospheric neutrinos can interact with dark matter detectors via coherent scattering and produce the same footprint as dark matter. Furthermore, there is a WIMP-nucleon cross section beyond which detectors become equally sensitive to dark matter and to coherent scattering neutrinos. Consequently, solar and atmospheric neutrinos are a future source of background commonly named the neutrino floor due to the impossibility to discover dark matter past a certain WIMP-nucleon cross section. The event rate of this

background depends on the energy of the neutrinos and their flux, as well as on the mass of the target and on the elastic scattering cross section.

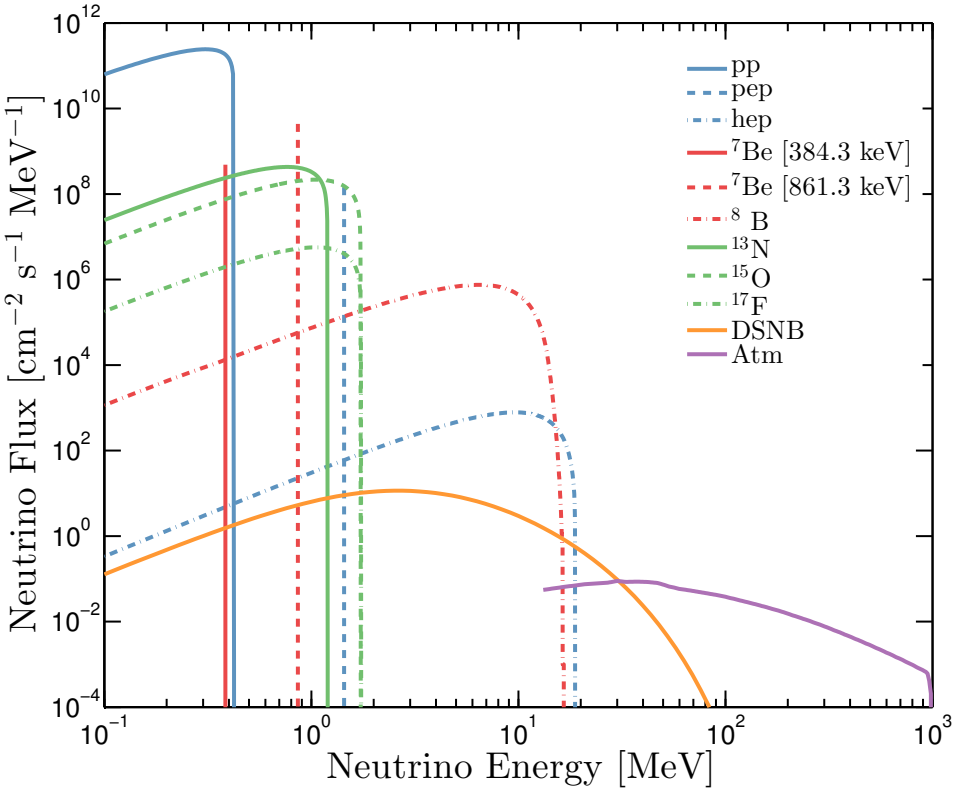

Figure 8.30 – Neutrino flux energy spectrum [126]. There are three sources: solar, diffuse supernova background (DSNB) and atmospheric. Dark matter detectors are most sensitive to atmospheric and ^{8}B neutrinos, i.e., high energy neutrinos.

The cross section of coherent neutrino-nucleon scattering depends essentially on the number of neutrons in the target nucleus, and consequently, every target used for direct dark matter searches has its distinct spectrum, and its unique neutrino floor. The cross section is given by the following equation [126]:

$$\frac{d\sigma(E_\nu, E_R)}{dE_R} = \frac{G_f^2}{4\pi} Q_w^2 m_N \left(1 - \frac{m_N E_R}{2E_\nu^2}\right) F^2(E_R), \tag{8.10}$$

where $F^2(E_R)$ is the nuclear form factor of the target nucleus mass m_N at energy recoil

E_r, E_ν is the neutrino energy, Q_w is the weak nuclear hypercharge and is given by:

$$Q_w = N - (1 - 4sin^2\theta_w)Z, \tag{8.11}$$

where N is the number of neutrons, Z the number of protons, and θ_w is the weak mixing angle. Since $4sin^2\theta_w \approx 1$, $Q_w \approx 1$, the ν-nucleus cross section becomes directly proportional to the number of neutrons of the nucleus. Fig. 8.30 shows the neutrino flux from several neutrino sources and Fig. 8.31 shows the event rate for a dark matter detector filled with Xe [127].

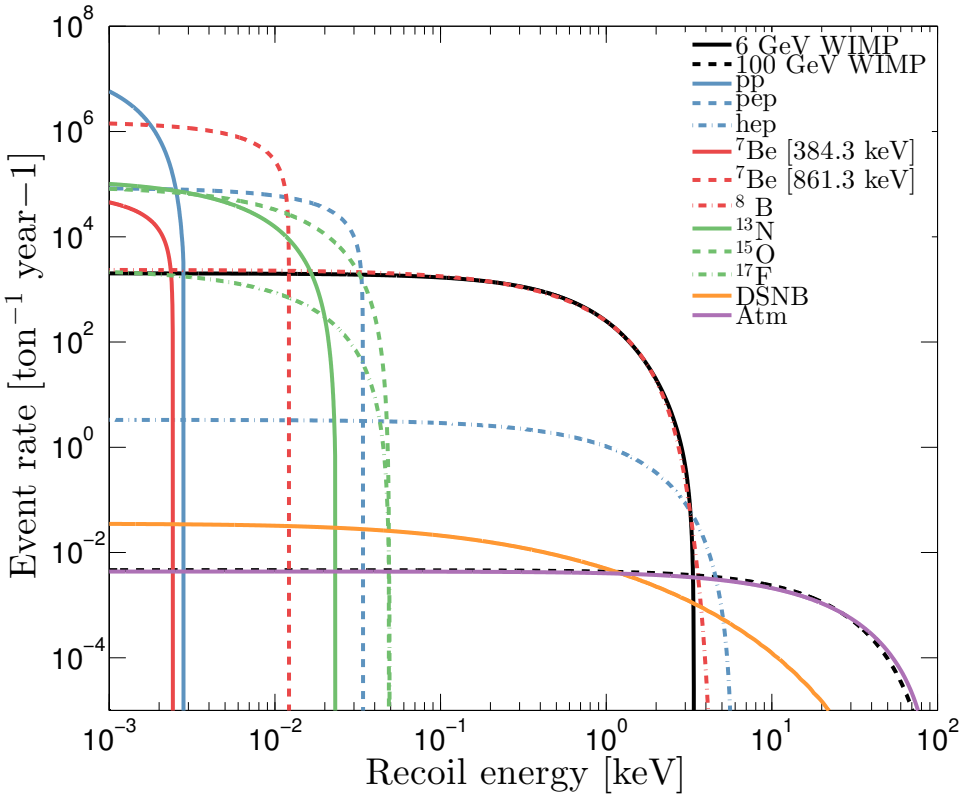

Figure 8.31 – ν-Xe elastic scattering event rate as a function of recoil energy deposited for the same type of neutrinos shown in Fig. 8.30. A 6 GeV/c^2 and a 100 GeV/c^2 WIMP with cross sections of 5×10^{-45} cm^2 and 2.5×10^{-49}cm^2 respectively are added to highlight the possibility of producing the same signal as ^{8}B and atmospheric neutrino-induced recoils respectively [127].

As can be seen in Fig. 8.31, neutrino interactions can produce the same number of events and the same recoil spectrum as WIMP interactions which makes it an irreducible background for direct dark matter searches.

To go beyond this neutrino floor, a dark matter detector has to be sensitive to the direction of the incoming particles. Since the solar system is heading roughly towards the Cygnus constellation, WIMP events pointing back to this constellation could be distinguished from tracks that do not point back to it. Therefore, a directional dark matter detector would reduce this background. In addition, by tracking the position of the Sun with respect to the detector, neutrinos coming from the Sun could also be discarded. As for atmospheric neutrinos, knowing their angular distribution, they can also be discriminated in a similar manner. The neutrino floor depends on the active target of the dark matter detector which means that some experiments can be sensitive to lower WIMP cross sections than others before being confronted by this background. A comparison of the neutrino floor of different targets will be presented in Chap. 12, and it can be shown that this neutrino floor is several orders of magnitude lower in cross section for fluorine loaded detector compared to e.g., Xe (see Fig. 12.5).

Due to this neutrino floor, experiments exploiting the directionality of dark matter signals have emerged. Different detector techniques are used: pressurized gas Time Projection Chambers (TPCs), nuclear emulsions, columnar recombination in high-pressure gaseous Xenon TPCs, and solid-state detectors. The most common type of detector and also the most advanced technique for dark matter searches are TPCs. Some of the most advanced experiments are DRIFT [128], MIMAC [129], and NEWAGE [130]. A newcomer is an emulsion based detector name NEWSdm [131]. There are many other experiences in this field, and a review of directional dark matter detection is presented in [132].

CHAPTER 9

PICASSO RESULTS

The PICASSO collaboration has published three dark matter search results in the last decade; in 2009 [133], 2012 [67], and a final one in 2017 [1]. This chapter describes the general features of the 2012 and 2017 results, their scientific impacts and the differences between them. In the following, a complete section is dedicated to the description of the 2017 analysis, and the published paper is also attached at the end of this document.

The main difficulty of this experiment is its irreducible alpha background, however, it was shown that the alpha response is constant over the range of energies used during WIMP searches. Since only the WIMP count rate increases at low thresholds, an increased rate can only be attributed to the presence of WIMP interactions in the detector. Thus, the alpha background can be subtracted from the total count rate, and the WIMP cross section that best matches the left-over signal is extracted to set WIMP-nucleon cross section limits with the Feldman-Cousins statistical method [134]. Furthermore, if all 32 PICASSO detectors showed an increasing rate as a function of decreasing energy threshold, a WIMP discovery could be claimed.

Both, the 2012 and 2017 results were background limited due to alpha contamination coming from the presence of radon inside the detector. Throughout the lifetime of the experiment, the radon contamination level of the detectors was significantly decreased by improving the fabrication process. In the last paper, the best detector had an alpha rate of $\sim$8 counts/kg/d compared to $\sim$70 counts/kg/d for the detector with the highest contamination. The introduction of a fiducial cut, a cut that discards high alpha rate regions in the detector using acoustic localization, lowered the alpha rate drastically.

In the 2012 PICASSO run only 10 out of the 32 detectors were used in the analysis which was due to the presence of so-called ”mystery events”. In addition to the alpha

background, this unknown background appeared only at low energy thresholds and had characteristics incompatible with WIMP interactions or any other known particle interactions. Several studies were done to understand the nature of these "mystery events", but none gave very conclusive results. These events were typically concentrated along the edges of the detector, i.e., near the detector acrylic wall and at the top and bottom of the acrylic container. The primary hypothesis describing the origin of these events is shear and stress effects near the gel matrix interfaces. The solution to this problem was the introduction of a fiducial cut and to implement a new analysis variable named WFLVAR. Removing the volume near the detector walls in the analysis resulted in regaining a constant count rate as a function of energy threshold compatible with the alpha background, and the possibility to use data at 50°C (1 keV) for the first time. For the first time, all 32 detectors could be included in the analysis.

At this point, PICASSO had reached its maximum potential. The only way to improve the sensitivity of the experiment would have been to significantly increase its active mass, but since it is not possible to increase the loading of the detector or to increase their size due to the gel characteristics, the only way forward would have been to increase the number of detector modules. In addition, the droplet detector technology is also background limited due to the incapacity of fully discriminating between alpha and WIMPs events. Also, this implies that the sensitivity grows much slower than a background-free experiment, i.e., with the square root of the exposure. Still, the main advantages of this technology were its low energy threshold and fast deployment capacity. If dark matter candidates had a higher WIMP-nucleon cross section in the SD sector, PICASSO could have been the first to see it. The significant achievement of the last PICASSO analysis is not the scientific result itself, even though it stills hold the best limits for WIMP masses between 2-5 GeV/c^2, but the full exploitation of the potential of the droplet technique by adding, notably, a fiducial cut. The following sections describe the final PICASSO analysis in detail.

9.1 PICASSO Final Result

The final result of the PICASSO experiment was published in March 2017 with 3.0 kg of C_4F_{10} and a total exposure of 231.4 kgd amassed between March 2012 and January 2014 [1]. A new element in this analysis was the use of acoustic localization to remove detector regions with high alpha contamination as well as the so-called "mystery events". The methodology used to determine the fiducial cuts is presented in this section. Another important aspect of this analysis was the determination of the cut values of the analysis variables and their efficiency. Finally, the procedures to quantify the systematic errors are described.

9.1.1 Analysis variables

In addition to the acoustic energy variable EVAR that was previously described in Chap. 6, four additional analysis variables were introduced to remove "mystery events" and other types of electronic noise events as well as a quality cut named Burst Cut.

- RVAR: This is a signal rise time variable which was derived from the standard deviation of the amplitude in the first 100 μs after t_0. It removes events with a characteristic slow rise time such as "mystery events" and a class of electronic noise events.

- QVAR: The event shape/quality variable consists of calculating the ratio of signal power during the first and second 10 ms of the signals. Bubble events have a very high QVAR value since the acoustic power during the second 10 ms is much smaller than during the first 10 ms. Events with unusual shapes such as long, ringing signals, have low QVAR and are cut out.

- TVAR: The event time variable TVAR removes repeating events due to delayed signals and electronic glitches that have a high acoustic power at later times in the signal. It is derived from the mean time of the signal squared.

- WFLVAR: is a wavelet-based frequency and time variable. It calculates ratios of parts of the decomposed continuous wavelet signal of acoustic traces. It replaced

the analysis variable named FVAR that was used in the 2012 analysis that consisted of calculating the ratios of the energy of two different frequency regions of the FFT. Both variables were designed to remove "mystery events".

- Burst cut: This cut is a quality cut which removes any triggers that occurred within 10.0 seconds of each other. During data analysis bursts of triggers following bubble events were identified which were clearly afterpulses and not particle induced events. The rate of these events was sufficiently low such that it did not affect the detector deadtime.

The event rate after the application of each cut at 30 °C and 50 °C is shown in Table 9.I. RVAR, QVAR, and TVAR are grouped together since their impact on the event rate is small compared to EVAR and WFLVAR.

	30 °C	50 °C
Triggers/kgd	241.5 ± 8.4	5385.9 ± 32.1
After Burst cut	26.9 ± 3.8	700.4 ± 49.2
After EVAR	19.2 ± 2.6	32.62 ± 3.4
After RVAR, QVAR, TVAR	19.1 ± 2.6	31.2 ± 2.7
After WFLVAR	18.3 ± 2.5	30.1 ± 2.7
After fid. cut	9.7 ± 3.1	8.6 ± 2.4

Table 9.I – Count rate of a PICASSO detector (# 153) at 30 °C and 50 °C after applying each of the analysis cuts.

9.2 Fiducialization

The first step to locate a bubble with the 9 piezoelectric sensors of a PICASSO detector module is to determine the time at which the signal of each sensor begins (t_0). Time differences between the t_0's of each sensor are used to determine the localization of an event with a triangulation algorithm. There are several ways to obtain t_0, and in the final analysis, two methods were combined to improve the localization accuracy.

In one of the methods, t_0 is equal to the time sample at which two different time averages of the signal start diverging: one averaged over 10 μs, and the other averaged over 45 μs. This method is illustrated graphically in Fig. 9.1. The other method is based on finding the separation between the cumulative time-weighted average amplitude and a uniform time integral, which is more thoroughly described in [110].

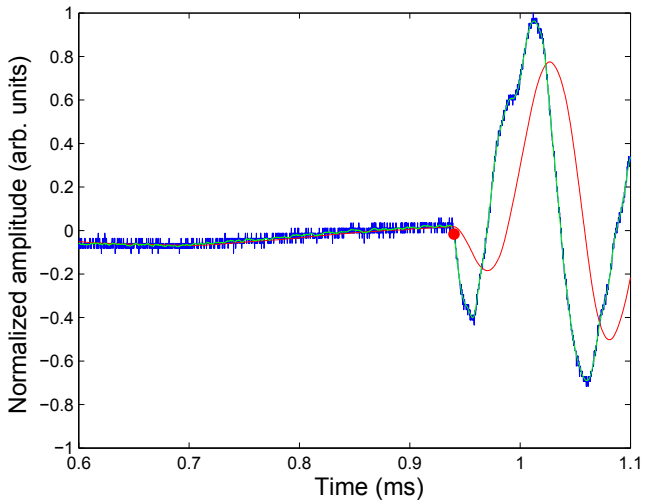

Figure 9.1 – Graphical representation of the t_0 finding method based on the difference between time signal averages of 10 μs (green) and 45 μs (red). The raw signal is shown in blue, and the red dot represents t_0.

The event position is determined by the χ^2 minimization of the function:

$$\chi^2 = \sum_{i=0}^{n-1} \left(\frac{(t_{0,i} - t_R) - \frac{d_i}{v}}{\sigma_i} \right)^2, \tag{9.1}$$

where $t_{0,i}$ is the t_0 of sensors i, t_R is the detector clock time at which the signal was emitted, d_i is the distance between the event and sensor i, σ_i is the uncertainty on $t_{0,i}$, and v is the speed of sound in the medium [110]. The distance d_i is given by

$$d_i = \sqrt{(x_R - x_i)^2 + (y_R - y_i)^2 + (z_R - z_i)^2)}. \tag{9.2}$$

The speed of sound and the position of each piezoelectric sensor (x_i, y_i, z_i) are required inputs to determine the position of each event. Using the Minuit library [135], the parameters t_R, x_R, y_R, and z_R that minimize eq. 9.1 are extracted. Furthermore, the algorithm can remove up to three piezoelectric sensors if their t_0 does not match with the other sensors and it does so by calculating the fit quality χ^2 with and without each sensor. If one sensor drastically worsens the fit quality, it is removed. Before the localization was incorporated into the main PICASSO analysis, extensive in-situ measurements were performed at UdeM to test the feasibility and performance of the technique. In these tests, the speed of sound was measured in order to be used in the localization algorithm as an input instead of a free parameter. The position uncertainty varies from ± 0.8 cm in the center of the detector and up to ± 2 cm.

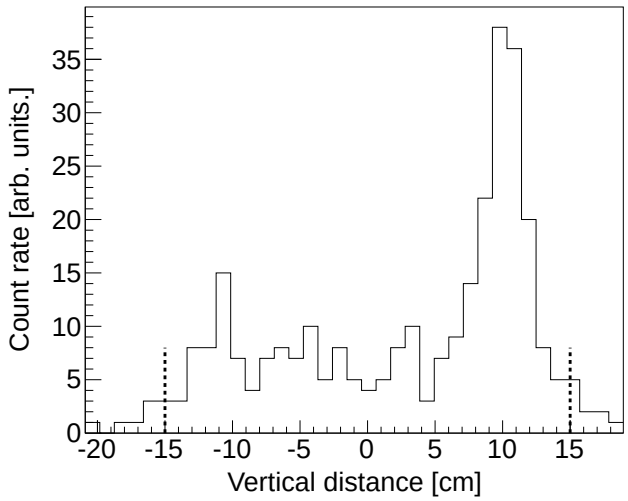

Figure 9.2 – Vertical distribution of localized bubble events in detector 145 during WIMP run searches. The distribution should be flat as a function of the vertical distance, but an apparent excess of events his present at the top of the detector. The dotted line represents the physical limit of the detector, and thus several events are reconstructed slightly outside of the detector. In this case, a fiducial cut of z = 6 cm was applied to remove the excess of events at the top of the detector.

By using the bubble event localization technique, the profile of the height distribution of the bubble events can be analyzed as shown in Fig. 9.2. A noticeable feature is

the higher number of events at the top of several detectors. Since the droplet distribution of a detector is uniform, the height distribution of bubble events should also be uniform. Thus, the excess of events at the top of the detector shown in Fig. 9.2 is attributed to a high level of local alpha contamination and are removed by a fiducial cut.

Moreover, it was found that using an identical fiducial volume for every detector resulted in regaining a completely flat rate as a function of energy threshold and confirmed that ”mystery events” could be removed with a fiducial cut. The identical fiducial volume consists of removing any events located beyond 5 cm from the center of the detector (5 cm radial cut) cut and a height cut that removes events that are more than 8 cm away from the center ($\pm$ 8 cm). This volume is used as a benchmark volume, but by using such a drastic fiducial cut, the total exposure of the 32 detectors was similar to the one of the 10 detectors used in the 2012 analysis. The considerable count rate variability of several detectors when the radial cut was relaxed supported the hypothesis that ”mystery events” were located near the detector wall. Since the number and position of "mystery events" varied from one detector to another, a different fiducial cut was applied to each detector. Determining a unique fiducial cut for every detector imposes the need to set strict conditions to avoid any biased fiducial cuts that could generate a perfectly flat detector response regardless of the presence of a WIMP signal or not.

When no fiducial cuts are applied, the vast majority of detectors have a rising count rate for decreasing energy thresholds and thus the count rate of the benchmark volume might diverge from the flat rate response if it is overrelaxed. Consequently, a criterion that defines if it is the case or not had to be determined in order to increase the total fiducial mass by relaxing the benchmark volume, while still maintaining a count rate that behaves similarly to the benchmark volume count rate. Since both the benchmark and relaxed fiducial volume have different absolute count rates, they must be normalized in order to compare the behavior of their count rate curves. To do so, their respective count rate at 30°C is subtracted from all other temperature rate points, which is allowed since the rate at this temperature is unaffected by ”mystery events”. A criterion was

defined as follows: if the 1σ uncertainties of the normalized count rate in the fiducial volume and in the benchmark volume agreed with one another, then the fiducial volume was allowed to be relaxed as long as it respected this condition. However, detector regions with high alpha contamination had to be treated separately by forcing fiducial cuts to exclude these regions. The fiducial mass is computed by comparing GEANT4 Monte Carlo simulations and polyenergetic neutron calibrations. This criterion creates a long trial and error process until the fiducial cut of each detector is determined as shown in Fig. 9.3.

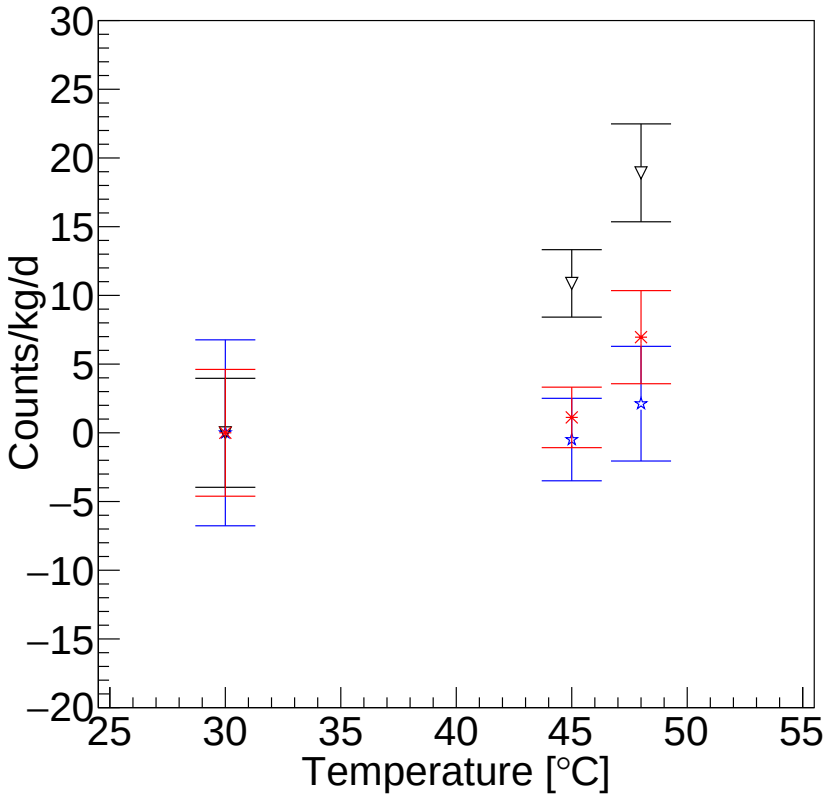

Figure 9.3 – The count rate (counts/kg/d) of detector #159 for several fiducial cuts. The count rate without a fiducial cut is shown in black, while the count rate for the benchmark volume (R= 5 cm, Z= $\pm$8 cm) is in blue and the final fiducial cut is in red. The error bars are 1σ and only statistical. The count rate of of a fiducial volume must agree with the count rate inside the benchmark volume within 1σ at all temperatures.

As can be seen from Fig. 9.3, the count rate obtained without any fiducial cut (black) does not agree with the count rate of the benchmark volume (blue) at 45°C and 50°C. The 1σ error bars of the fiducial volume count rate (red) overlap those of the benchmark volume count rate for all temperature. In this particular case, the final fiducial cut is R= 5.5 cm without any Z cut and contains 61% of the total detector volume. The fiducial mass determination using these cuts is presented later.

9.3 Systematic errors

Several systematic errors were identified in the experimental setup. Each of them is listed below and detailed in this section.

Systematic error	
Fiducial mass determination	5%
Temperature stability	1%
Atmospheric pressure variation	<1%
Hydrostatic pressure gradient	<1%
Active mass determination	5%

Table 9.II – List of systematic errors and their contribution to the total uncertainty on the cross section.

9.3.1 Determination of total active mass and systematic uncertainties

The active mass is determined by weighing the detector before and after the addition of the freon during the fabrication process and is known with a precision of 1%. The polymerization process that traps freon inside the detector is not instantaneous, and potential losses can occur due to freon diffusion into the gel matrix and surface leakage. A total systematic error of 5% on the active mass is attributed due to this potential effect. Active mass losses can also occur throughout the life of a detector and is thus monitored by periodic AmBe calibrations at SNOLAB and compared to a GEANT4 simulation as shown in Fig. 9.4. The count rate is directly proportional to the active mass which is extracted by fitting the simulated curve to the experimental calibration curve. However,

directly weighing the active mass is more precise than this method which was only used to monitor the active mass throughout WIMP searches, and confirmed that no loss occurred. The total content of C_4F_{10} in the setup was determined to be 2.97 $\pm$ 0.15 kg, corresponding to 2.37 ± 0.12 kg of ^{19}F.

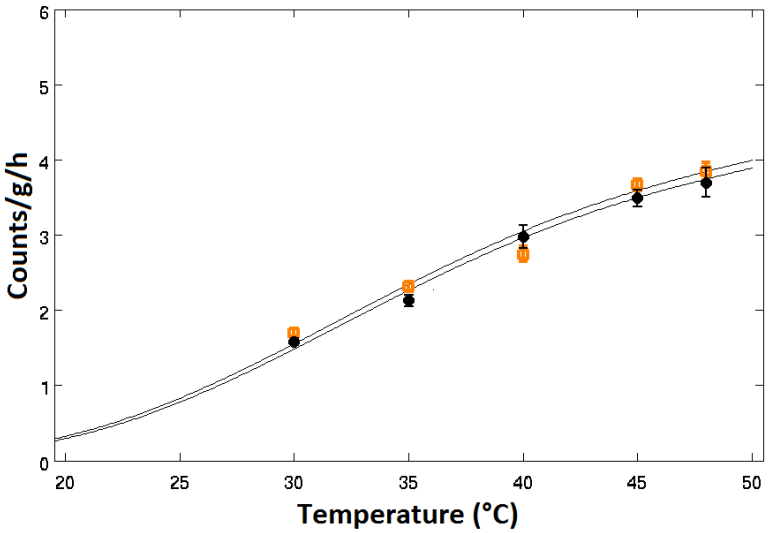

Figure 9.4 – Count rate versus temperature of AmBe calibration data with WFLVAR cut (black) and without WFLVAR cut (orange). GEANT4 simulated response fitted to each data set is shown as a continuous black line.

9.3.2 Fiducial mass uncertainty

The fiducial mass is determined using AmBe neutron calibrations at SNOLAB. The percentage of mass inside the fiducial volume is obtained by calculating the ratio of events at 30°C before and after the fiducial cut is applied. The fabrication process (Chap. 6) produces an almost uniform droplet distribution in the detector. However, the distribution of events during a calibration depends on the neutron flux profile and the source position. A GEANT4 Monte Carlo simulation was performed to determine the expected event height distribution for a given source location. The results of this simulation are then fitted by a polynomial curve $F(z)$ as shown in Fig. 9.5. This polynomial fitted curve $F(z)$ was then used to extract the actual droplet distribution of a detector. To take into account the effect of the source position, the measured event distribution $D(r,z)$

is divided by the fitted simulated curve $F(z)$. The fiducial volume fraction $\varepsilon_{fid.vol.}$ is obtained by calculating the ratio of the integral of the event distribution before and after applying the fiducial cut:

$$\varepsilon_{fid.vol.} = \frac{\int_{fid.vol.} \frac{D(r,z)^{30^\circ C}}{F(z)}\, dz}{\int_{det.vol.} \frac{D(r,z)^{30^\circ C}}{F(z)}\, dz}, \tag{9.3}$$

The integral is taken over the fiducial cut (fid. vol.) and for the entire volume (det. vol.), respectively.

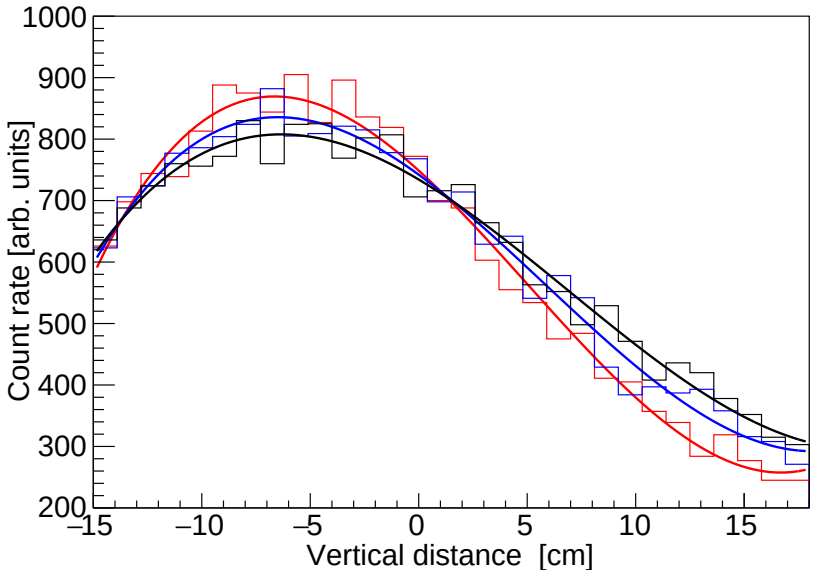

Figure 9.5 – Vertical event distribution in a PICASSO 4.5 L detector during neutron calibration for three different source distances. The various histograms show the bubble height distribution while the solid lines are the fits to the data $F(z)$. The known position of the neutron source in the mine is 14.75 cm between the center of a detector and the source, and the resulting distribution is shown by the blue curve. This distance can vary between 16 cm and 12.2 cm and the corresponding distribution are shown in black and red, respectively. If not corrected, this effect changes the fiducial mass by 3%.

An additional systematic error is introduced by the uncertainty in the position of the source in the setup. Within its uncertainty range, i.e., from 12.2 cm to 16 cm, the event distribution changes as can be seen by the colored curves on Fig. 9.5. This variation of the source position affects the fitted distribution curve $F(z)$ (eq. 9.3) and introduces a systematic error of approximately 3% on the fiducial mass which is detector dependent due to the individual intrinsic droplet distribution of each detector. The total mass of ^{19}F after fiducial cuts amounts to 1.41 ± 0.11 kg and corresponds to 59.5% of the total fluorine mass.

9.3.3 Determination of the cut efficiency and systematic errors

Cut values and their respective efficiency were determined by analyzing a series of calibration runs. Initially, the cuts of each calibration period were combined and the difference between individual cuts and the combined cut was treated as a systematic uncertainty. If the cut values fluctuate very little, it results in small systematic uncertainties which saves an enormous amount of work considering there are 32 detectors, 5 analysis variables, and at least 3 series of calibration. However, if there are significant shifts, considerable systematic errors might be introduced, which was indeed the case for some of the variables, such as EVAR shown in Fig. 9.6.

To circumvent this issue and to introduce no bias in the analysis, each WIMP run was assigned to the closest calibration period, and the variation of the cut value and the efficiency from neighboring calibrations were treated as a systematic uncertainty. The resulting cut efficiency of all 5 cut variables was determined using a correlation matrix. This correlation matrix was determined using the neutron calibration data and then used as an input to a pseudo-Monte Carlo simulation. For each detector and each temperature, the number of simulated events that passed all the cut variables was used to determine the total efficiency for a given calibration period which was typically in the range of $80-90\%$.

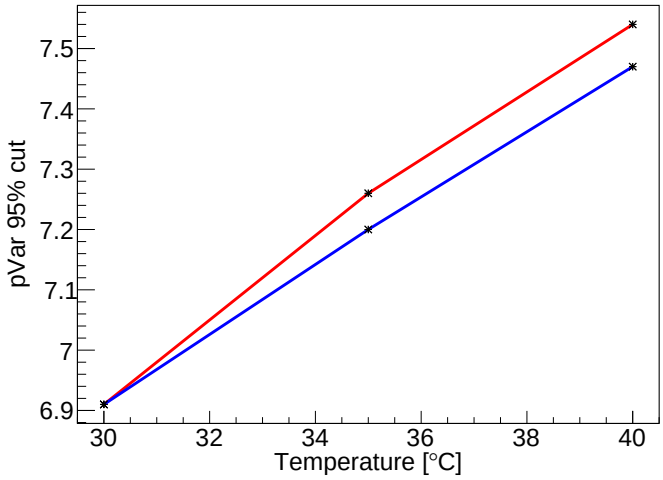

Figure 9.6 – 95% acceptance cut for the variable EVAR as a function of temperature for two distinct calibration periods of detector 157. The blue and red curves show very similar cut values at 30°C, but then drift away at 35°C and 40°C.

It was estimated that the uncertainty on the cut efficiency was 5% for all 5 analysis variables by considering the impact of the different cut values of each calibration period on WIMP runs. Since calibration periods were only taken sporadically and WIMP runs were performed throughout the data taking period, the distributions of various variables differ from one another. This effect was even more critical for WIMP runs that were taken approximately between two calibrations periods. The resulting 5% systematic uncertainty is also much smaller than the systematic uncertainty of the initial method that combined the cut values.

9.3.4 Temperature and pressure systematic error

Since the operating pressure and temperature affect the energy threshold, an uncertainty in the pressure determination translates to an equivalent temperature variation. The main uncertainty of this kind are (1) a 1°C uncertainty due to the temperature stability of the TPCSs, (2) a 3% uncertainty due to atmospheric pressure changes, and (3) a less than 1% uncertainty due to the hydrostatic pressure gradient in each detector modules. All three uncertainties introduce a systematic error on the energy threshold and a

corresponding uncertainty in the rate plot of each detector, which translates into an error on the WIMP cross section limit. The most important error of this kind is the temperature stability error ($\pm 1°$C) which results in a 1% uncertainty on the cross section limit. The contribution of the other two uncertainties is less than 1%.

9.4 Limit setting methodology

When no WIMP signal is detected, a 90% C. L. limit on the WIMP-nucleon cross section is calculated. The first step to set these limits is to calculate the recoil spectrum produced by WIMP-nucleon elastic scattering (sect. 4.3). It also requires to know the detection efficiency of the PICASSO detectors which is described by the α parameter and eq. 8.3. The number of WIMP events per kgd (R_{obs}) as a function of energy threshold, which is directly proportional to WIMP-fluorine cross section, is then fitted to each individual detector as shown in Fig. 9.7.

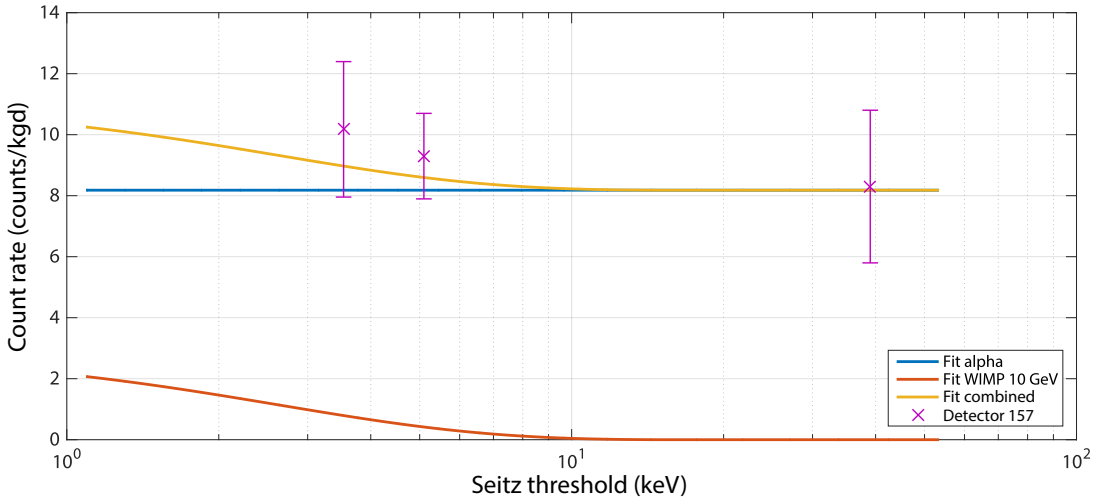

Figure 9.7 – Count rate of detector #157 as a function of the Seitz energy threshold after all cuts including the fiducial cut. The purple data points show the experimental count rate while the blue curve is the alpha rate fit. A 10 GeV/c^2 WIMP is fitted to the data (red) onto which the flat alpha rate is added to produce the orange curve. The maximum cross section of a WIMP hypothesis compatible with the data is then extracted from the fit.

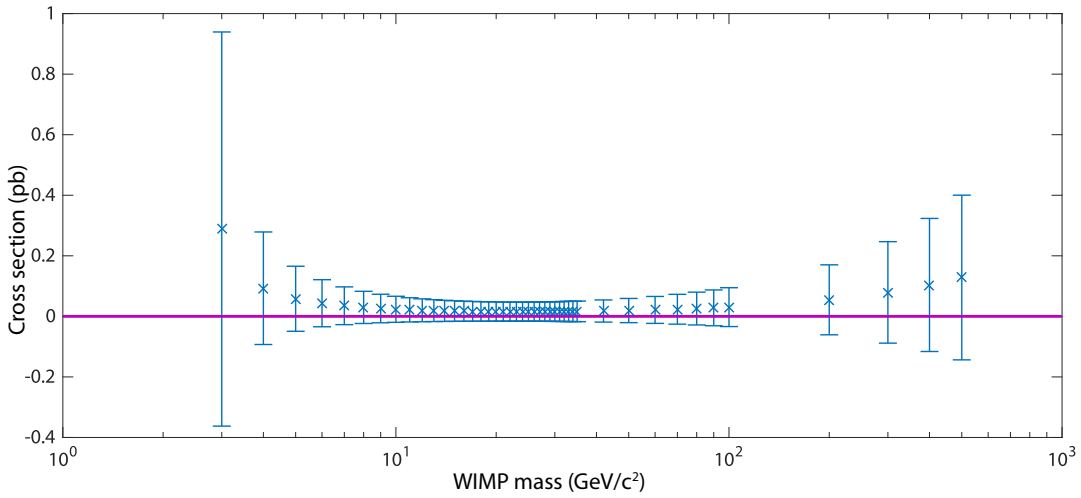

Figure 9.8 – Cross section (picobarn) as a function of the WIMP mass for detector 157. Each data point represents the best WIMP fit for a given WIMP mass. A positive cross section indicates that the count rate increases as a function of the threshold while a decreasing count rate would have yielded a negative cross section, i.e., nonphysical cross section.

Two free parameters are fitted: the WIMP cross section, and the alpha background. This fit is performed for WIMP masses between 2 and 5000 GeV/c^2. The error on the cross section corresponds to the fit uncertainty which is due to the statistical uncertainty on the count rate and the systematic uncertainties. Once this step is done, the cross section as a function of the WIMP mass is obtained as it is shown in Fig. 9.8.

The WIMP-fluorine cross section is determined individually for each of the 32 PICASSO modules and then combined. The WIMP-fluorine spin-dependent cross section is related to the WIMP-proton spin-dependent (SDp) cross section by the following equation:

$$\sigma_p^{SD} = \sigma_F \left(\frac{\mu_p}{\mu_F}\right)^2 \frac{C_p^{SD}}{C_{p(F)}^{SD}}, \tag{9.4}$$

where the term $C_p^{SD}/C_{p(F)}^{SD}$ corresponds to the ratio between the spin-dependent proton

enhancement factor of proton and fluorine. This term is equal to 1.285, and is calculated using the tabulated values of $< S_p >$ of Table 4.I and via eq. 4.7. The terms μ_p and μ_F are the WIMP-proton and WIMP-fluorine reduced masses, respectively. A similar calculation allows the translation of σ_F^I to σ_p^I. Once the combined cross section is obtained, the 90% C. L. limit is calculated using the Feldman-Cousins method.

9.4.1 Feldman-Cousins limit setting

Every PICASSO WIMP search relied on the Feldman-Cousins statistical approach to set limits on the WIMP-nucleon cross section. The detail of the method is presented in [134]. It is based on the ratio between the cross section (σ) and the Gaussian uncertainty on the cross section ($\Delta\sigma$) to obtain upper confidence limits for a null result which in this case is the absence of a WIMP signal. If the ratio is higher than 3.0 than the limit is simply the cross section + $1.6446\Delta\sigma$. On the other hand, if the ratio is < -3.0, then this method cannot be used. For PICASSO results, a negative value means a decreasing rate as a function of temperature. If the ratio is between -3.0 and 3.0, the 90% C. L. limit on the cross section is given by:

$$\sigma_{limit}(90\%\text{ C. L}) = \mu \times \Delta\sigma + 1.6446\Delta\sigma, \tag{9.5}$$

where $\Delta\sigma$ is the uncertainty on the cross section and μ is a 9-degree polynomial equation that depends on the ratio $\sigma/\Delta\sigma$ and is a parameterization of the values taken in [134]. The values of μ are shown in Fig. 9.9, and can either be negative or positive. If σ is negative, μ takes values between -1.38 and 0, while for $\sigma > 0$, μ is between 0 and 3. In other words, if the cross section is negative, then there was no WIMP interaction seen in the detector, so a "bonus" is gained for the limit setting, and if the cross section is positive, it yields a "penalty" on the limit.

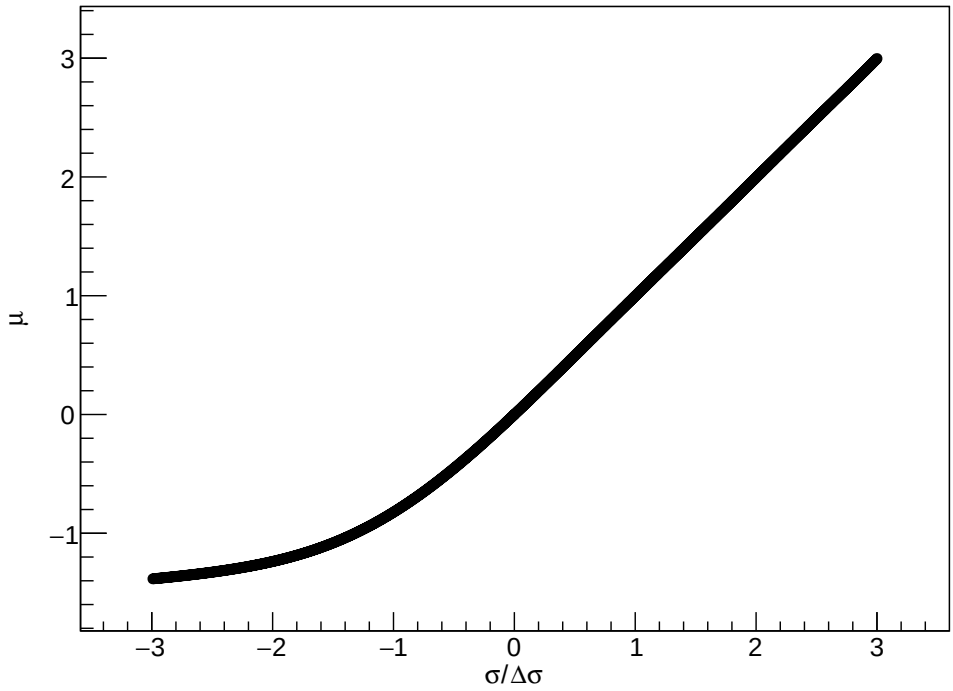

Figure 9.9 – Feldman Cousins statistical analysis used for PICASSO WIMP searches. The ratio between the cross section and its error ($\sigma/\Delta\sigma$) yields different μ values. For a negative value of σ, μ is negative while for positive σ, μ is positive.

9.5 PICASSO results

The 2012 PICASSO analysis used 10 detectors for a total active mass of 0.72 kg of ^{19}F and full exposure of 114 kg-day. The detectors were operated at an energy threshold of 1.7 keV (48°C) and were sensitive to WIMP masses as low as 4 GeV/c^2. No dark matter signal was identified, and the best exclusion limit obtained in the SDp sector was $\sigma_p^{SD} = 0.032$ pb (90% C. L.) for a WIMP mass of 20 GeV/c^2. The exclusion plot is shown in Fig. 9.10. At the time of publication, the PICASSO limit was the best SDp limit in the world for WIMP masses below 30 GeV/c^2 and in particular, it ruled out completely the DAMA/LIBRA allowed contours [78].

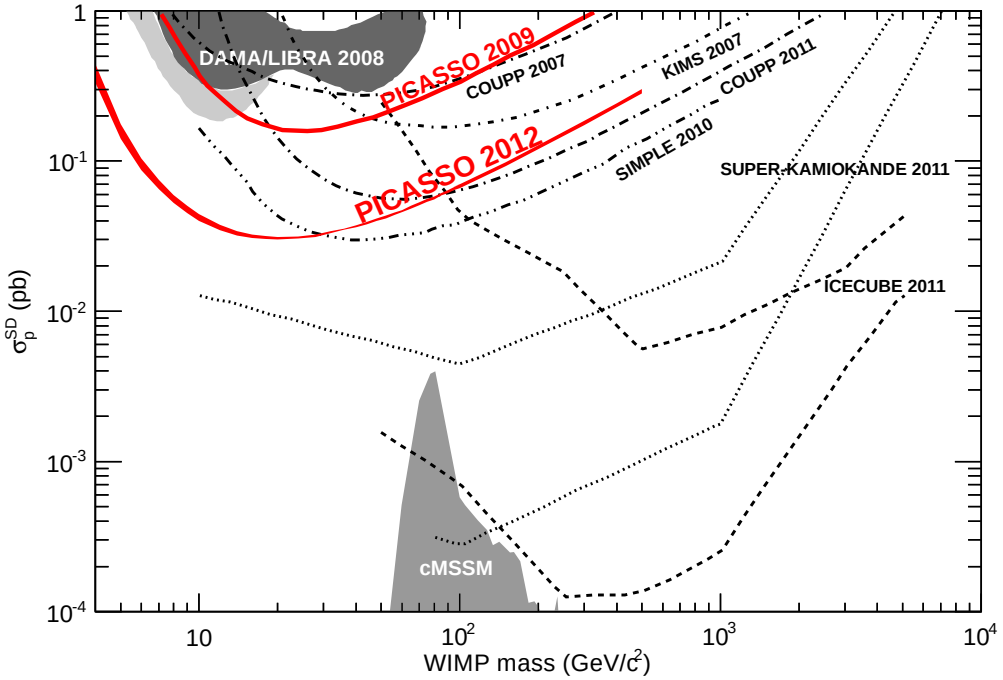

Figure 9.10 – Compilation of SD WIMP-proton cross section limits at the time of publication (2012) [67].

The final PICASSO result, published in 2017, was not the best exclusion limits in the SDp sector at the time, as the newly formed PICO collaboration now held this claim, but it was still a great improvement compared to the 2012 analysis mainly due to the addition of more detectors and more sophisticated analysis cuts. The normalized weighted combined rates of the 10 detectors used in 2012 analysis and the 32 detectors of the 2017 analysis are shown in Fig. 9.11 along with the signal of a hypothetical 15 GeV/c^2 WIMP with a SDp cross section of 3.2×10^{-2} pb and an α parameter equal to 5. In the following, every cross section quoted, or shown in plots, always corresponds to a 68% C. L. and with $\alpha = 5$. The normalization was performed by subtracting the average count rate at 30°C & 35°C from the individual temperature data points at lower energy.

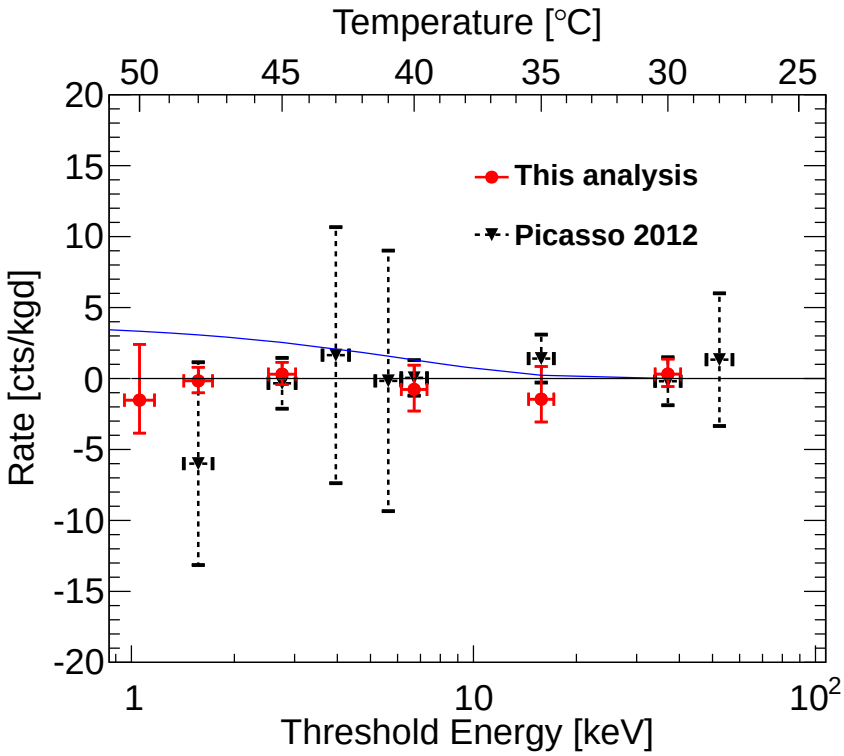

Figure 9.11 – Normalized combined weighted average rate versus energy threshold and temperature of 2012 (black) and 2017 (red) datasets. The rate curve of a hypothetical 15 GeV/c^2 WIMP is shown is blue.

Since the errors bars are dominated by the statistical uncertainty, they reflect the time spent at each temperature. This figure highlights the significant increase in exposure of the 2017 analysis at 48°C compared to the 2012 dataset, and more importantly, it displays the impressive flatness of the detector response of the entire setup down to keV thresholds. The two x-axes illustrate the relation between temperature and energy threshold which was determined with monoenergetic neutron calibrations (sect. 8.4.1) at atmospheric pressure (1 bar). To take into account the higher mine pressure of 1.2 bar, calibration measurements were performed at 1 bar and 1.2 bar and showed that a pressure increase of 0.2 bar is equivalent to a 2°C temperature decrease. Consequently, the relation between temperature and energy threshold described by eq. 8.2 was modified by decreasing the operating temperature by 2°C. Moreover, it is the first time that WIMP searches were successfully performed at 50°C which is equivalent to an energy threshold

of $\sim$1 keV and is still, to this day, the lowest achieved energy threshold for dark matter searches using SHL detectors.

The WIMP-fluorine cross section of each detector was determined following the procedure described in sect. 9.4 for WIMP masses between 2 and 5000 GeV/c^2. A compilation of the SD WIMP-fluorine cross sections versus detector number, which follows the time of fabrication, is shown in Fig. 9.12 for a WIMP mass of 10 GeV/c^2.

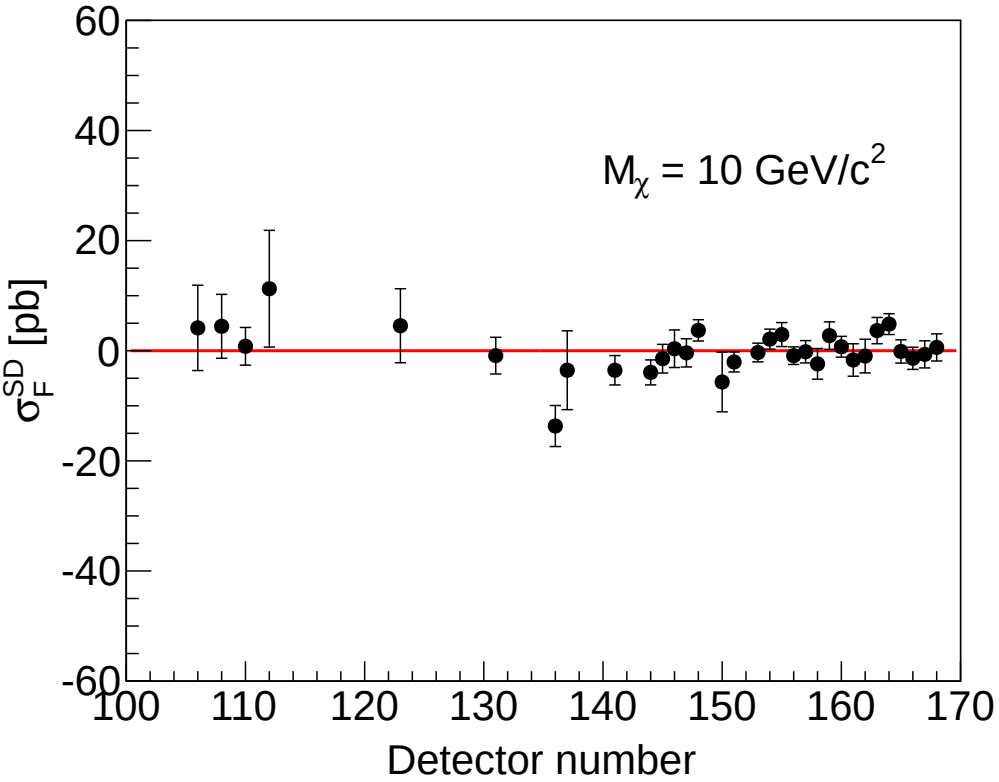

Figure 9.12 – Summary of the performance of all 32 detectors in term of SD WIMP-fluorine cross section. The error bars are dominated by statistical uncertainty which comes from the alpha background and decreases as a function of detector number.

Since the errors bars on the cross section of most detectors agree with $\sigma_F^{SD} = 0$ (red line), it confirms that no WIMP interactions have occurred in the detector modules, as otherwise, a global positive cross section would have been measured across all detectors. The diminishing error bars as a function of detector number also highlights the decreased

alpha background rate of the most recent detectors.

The total fluorine mass was 3.0 kg with a total exposure of 231.4 kg-day. The combined cross section of all 32 detector modules yielded a maximum sensitivity of $\sigma_F = 0.083 \pm 0.448 \pm 0.039$ pb for 10 GeV/c^2 WIMPs. This fluorine cross section can then be converted to $\sigma_p = (1.39 \pm 8.46 \pm 0.072) \times 10^{-3}$ pb using eq. 9.4.

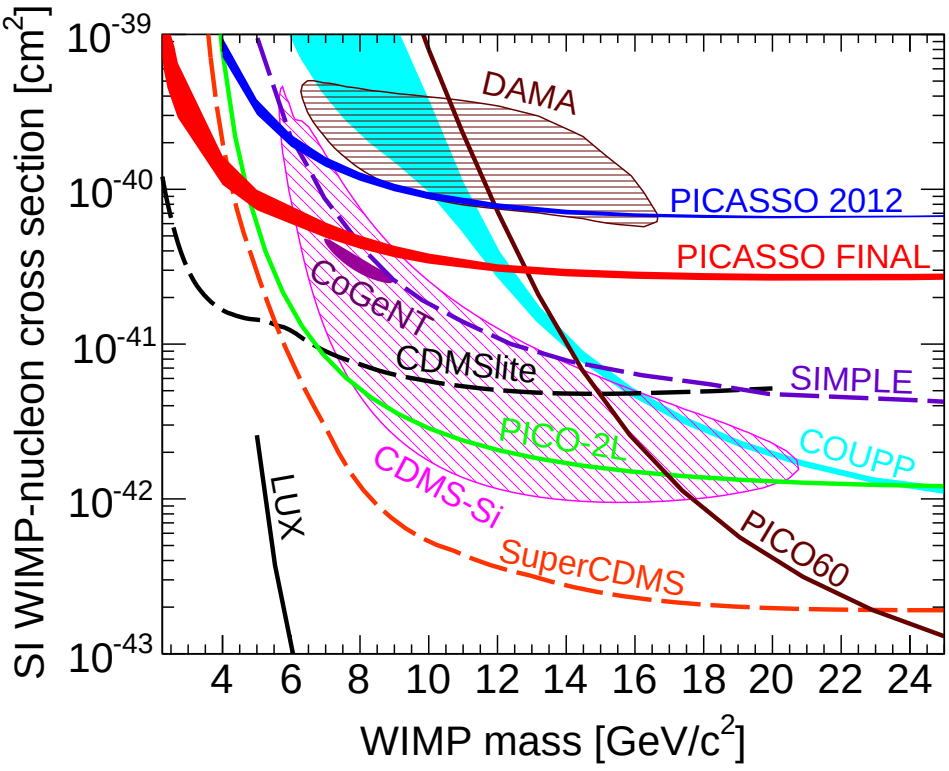

Figure 9.13 – Upper limits at 90% C.L. on SI-WIMP proton interactions. The final PICASSO limit is shown as a full red line along with other direct detection experiments: PICASSO 2012 (blue), PICO-2L (green [70]), PICO60 (brown [72]), COUPP-4 (light blue [136]), SIMPLE (dashed purple [69]), CDMSlite (dashed black [137], SuperCDMS (dashed orange [74]), and LUX (black [138]). The closed countours are the allowed regions of DAMA (brown [78], CoGeNT (magenta [79], and CDMS-II SI (pink [80].

Since no signal consistent with dark matter was observed, a limit on the SD WIMP-proton interaction of $\sigma_p^{SD} = 1.53 \times 10^{-2}$ pb (90% C. L.) for a WIMP mass of 20 GeV/c^2 was set, which is an improvement by a factor 2.4 compared to the 2012 result. A com-

bined exposure of 345.4 kgd was obtained by the combination of the 2012 and 2017 results which slightly improved this cross section limit to $\sigma_p^{SD} = 1.32 \times 10^{-2}$ pb (90% C. L.), and yielded a spin-independent limit of $\sigma^{SI} = 2.8 \times 10^{-5}$ pb (90% C. L.) for 20 GeV/c^2 WIMPs. Due to the 1 keV threshold, this result still holds the best world limit for the SD proton interactions for WIMPs of 2-5 GeV/c^2. The limit obtained in the SI and SDp sector at the time of publication is shown in Fig. 9.13 and Fig. 9.14, respectively. The widening of the limit at low WIMP masses reflects the uncertainty on the α parameter which varies within the interval $1 < \alpha < 7.5$.

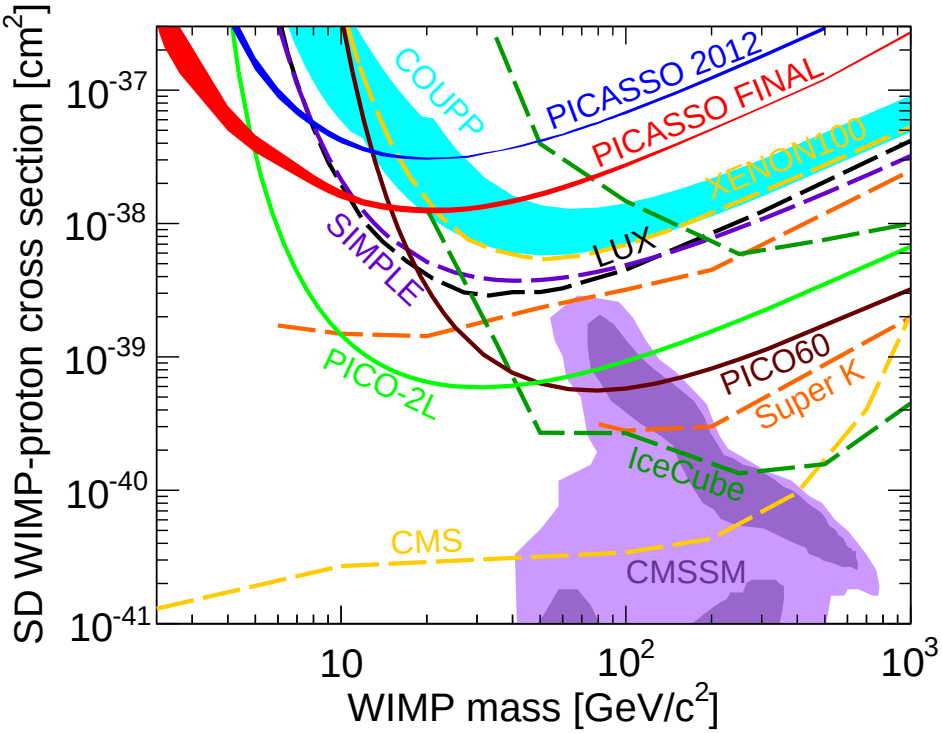

Figure 9.14 – Upper limits at 90% C.L. on SD-WIMP proton interactions. The final PICASSO limit is shown as a full red line along with other direct detection experiments: PICO-2L (green [70]), PICO60 (brown [72]), COUPP-4 (light blue [136]), SIMPLE (dashed purple [69]), XENON100 (dashed light orange [139]) and LUX (dashed black [138]). Indirect searches are represented by Ice-Cube (dashed dark green [140]), SuperK (dashed orange [141, 142]) with comparable limits by ANTARES, Baikal and Baksan [94, 143, 144]. Limits from accelerator searches by CMS are shown in dashed light orange [145]. Comparable limits are set by ATLAS [146]. The purple region represents predictions in the framework of the CMSSM [147].

9.6 Lessons learn from the final PICASSO result

At the time of publication of the final PICASSO result, the result did not push the detection limit of dark matter to uncharted cross sections except for WIMP masses between $\sim 2 - 5\,\mathrm{GeV/c^2}$ for SD WIMP-proton interactions. The main innovation in this analysis was the addition of the localization technique that significantly improved the physics reach of the experiment by removing mystery events and reducing the alpha background drastically. Moreover, the removal of mystery events allowed the inclusion of WIMP runs taken at 50°C (1 keV) for the first time. Another substantial improvement, shown in Fig. 9.15, is the one order of magnitude decrease in the alpha background rate, which is due to the refinement of the detector fabrication technique.

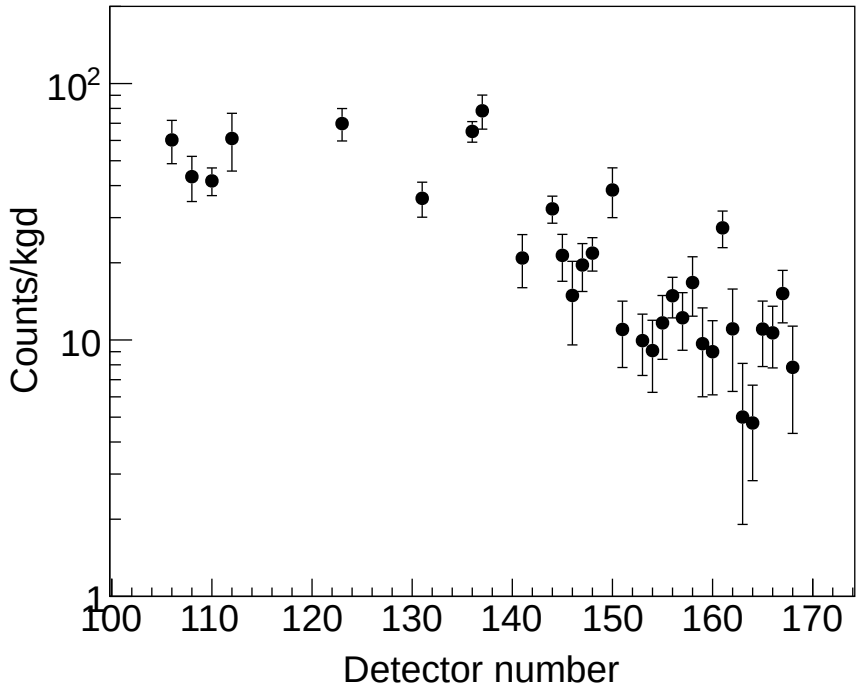

Figure 9.15 – Alpha background rate as a function of detector numbers which follows the time of fabrication. There is one order of magnitude decrease in the rate between the oldest and newest detector used in the analysis. The alpha background rate is the first source of uncertainty in this WIMP search.

It could be argued that some systematic uncertainties could have been improved, e.g, the calibration source position uncertainty (3%) could have been easily reduced. Furthermore, additional calibration data would have enhanced the stability of certain analysis variables. Finally, having 32 detectors with an alpha background lower than 10 counts/kg/d as it is the case for the latest generation of detectors would have also yielded a better sensitivity. However, even with these improvements, it would not have been possible to compete with the next generation of PICO detectors with a larger active mass and full alpha discrimination capabilities. On the other hand, due to its superior stability at thresholds as low as 1 keV, PICASSO could maintain to this date the best limit for small WIMP masses below 5 GeV/c^2.

CHAPTER 10

PICO RESULTS

Since the merger of the PICASSO and COUPP collaborations, the PICO collaboration has published an important number of dark matter search results with different detectors operating at SNOLAB. The latest result was obtained with PICO60 filled with 52.2 ± 0.5 kg of C_3F_8. A blind analysis was performed after 1167 kg-day of efficiency-corrected exposure between November 2016 and January 2017. The WIMP search dataset was taken at 30.2 ± 0.3 PSIA and 13.9 ± 0.1 °C which corresponds to a thermodynamic energy threshold of 3.29 ± 0.09 keV.

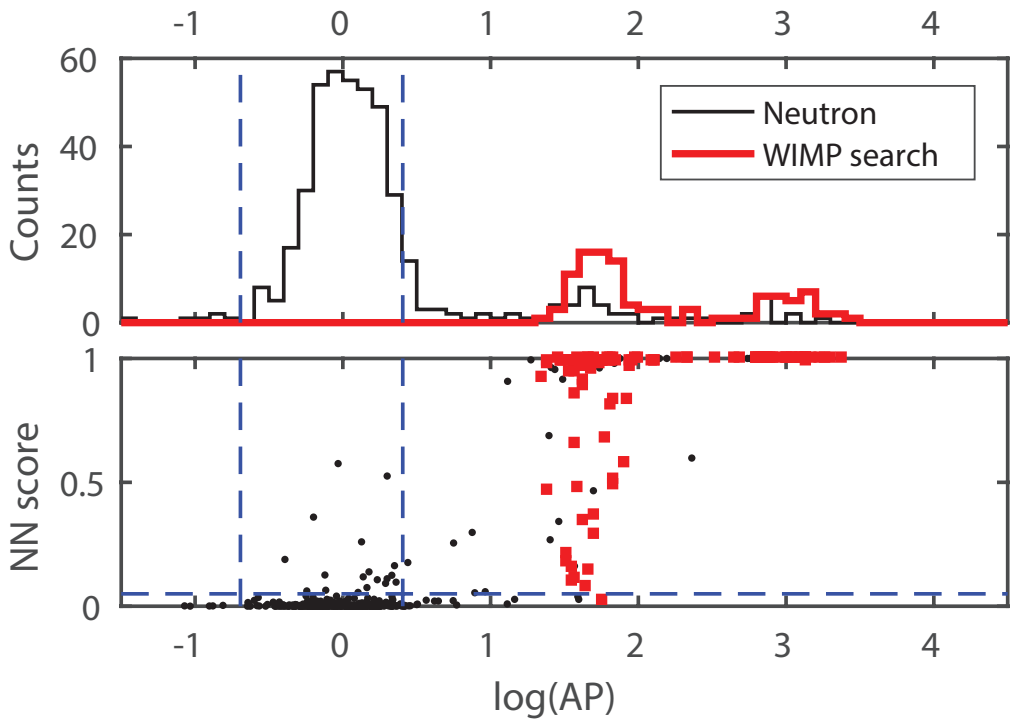

Figure 10.1 – Top: Acoustic power (AP) distribution of neutron calibrations (black) and WIMP search data (red). Bottom: Neural network (NN) score versus log(AP) and the corresponding NN score cut of > 0.05 of the same dataset. The AP cuts of 0.5 and 1.5 are displayed in dashed blue in both plots.

In addition to the usual AP cut performed to isolate WIMP type events, a neural network (NN) was trained to distinguish pure alpha events (NN =1) from pure nuclear or electron recoil events (NN =0) by using neutron and gamma calibrations and an unblinded commissioning run. The main analysis was blinded by hiding the AP variable and NN score throughout the data taking period. Single bulk bubble events with AP between 0.5 and 1.5 and with a NN score lower than 0.05 were accepted with a combined cut efficiency of $88.5 \pm 1.6\%$ as shown in Fig. 10.1 for the neutron calibration and WIMP search datasets.

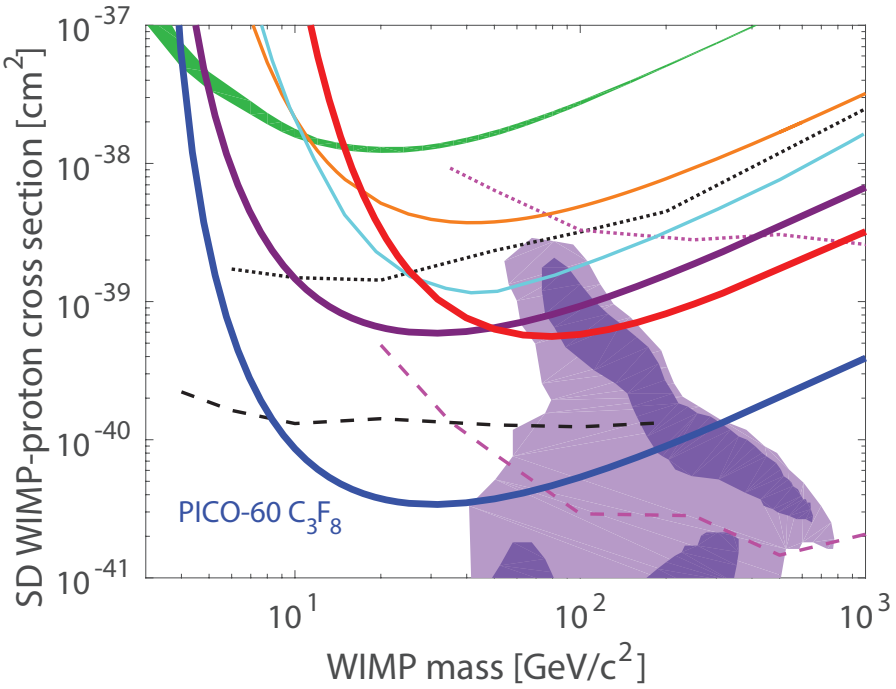

Figure 10.2 – The 90% C.L. limit on the SD WIMP-proton cross section from PICO-60 C3F8 plotted in thick blue [73], along with limits from PICO-60 CF3I (thick red) [72], PICO-2L (thick purple) [70], PICASSO (green band) [1], SIMPLE (orange) [69], PandaX-II (cyan) [82], IceCube (dashed and dotted pink) [93], and SuperK (dashed and dotted black) [141, 142]. The indirect limits from IceCube and SuperK assume annihilation to τ leptons (dashed) and b quarks (dotted). The purple region represents the parameter space of the constrained minimal supersymmetric model of [147]. Additional limits, not shown for clarity, are set by LUX [138] and XENON100 [81] (comparable to PandaX-II) and by ANTARES [148, 149] (comparable to IceCube).

During this data-taking period, a neutron background of 0.25 ± 0.09 (0.96 ± 0.34) single (multiple) bubbles events were predicted by GEANT4 simulations. In addition to this background, a gamma nucleation efficiency of $(1.80 \pm 0.38) \times 10^{-10}$ was extracted from gamma calibrations and GEANT4 simulations. According to Monte Carlo simulations of the external gamma flux, 0.026 ± 0.007 events were predicted. Finally, the background from coherent scattering of ^{8}B neutrinos was estimated to be 0.055 ± 0.007 events.

Before unblinding, by using the optical system, 106 single and 3 multiple events were found. After unblinding the acoustic data, none of the 106 single bulk bubble events were identified as WIMP candidate events since none was within the defined AP and NN cuts for nuclear recoil events as shown in Fig. 10.1. This deviation from the predicted number of single (0.331) and multiple (0.96) bubble events is attributed to a statistical fluctuation of the neutron background.

The calculated Poisson upper limits at the 90% C.L. for the SD WIMP-proton and spin-independent WIMP-nucleon elastic scattering cross sections, as a function of WIMP mass, are shown in Fig. 10.2 and Fig. 10.3, respectively. These limits, corresponding to an upper limit on the spin-dependent WIMP-proton cross section of 3.4×10^{-41} cm^2 for a 30 GeV/c^2 WIMP, are currently the world-leading constraints in the WIMP-proton spin-dependent sector and indicate an improved sensitivity to dark matter by a factor of 17, compared to previously reported PICO results [2].

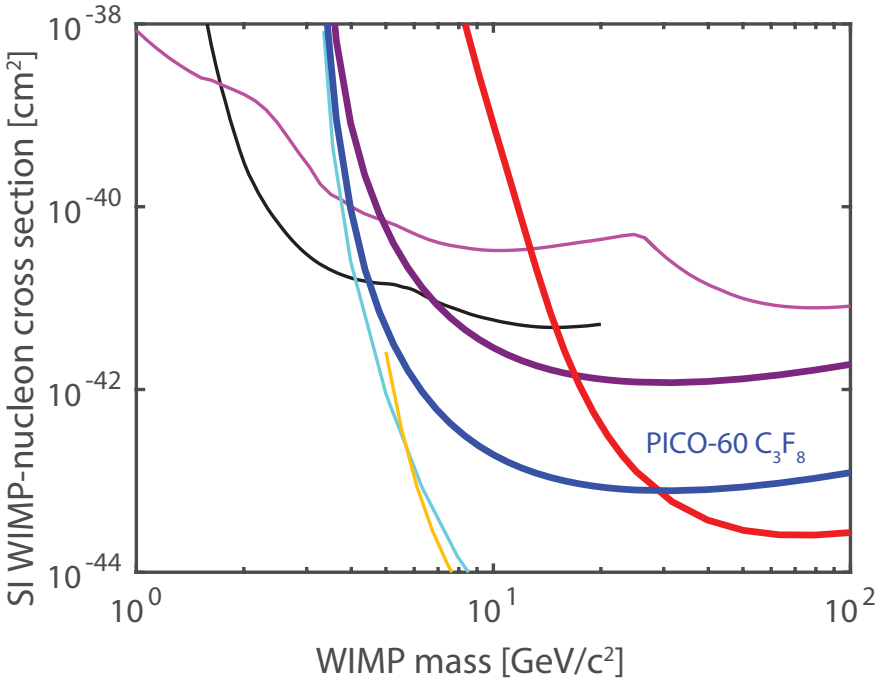

Figure 10.3 – The 90% C.L. limit on the SI WIMP-nucleon cross section from PICO-60 C_3F_8 plotted in thick blue, along with limits from PICO-60 CF3I (thick red) [72], PICO-2L (thick purple) [70], LUX (yellow) [76], PandaX-II (cyan) [75], CRESST-II (magenta) [63], and CDMS-lite (black) [150]. Additional limits, not shown for clarity, are set by PICASSO [1], XENON100 [81], DarkSide-50 [56], SuperCDMS [74], CDMSII [62], and Edelweiss-III [151].

Since its beginning, PICO has always produced the best published limit on the WIMP-nucleon cross section in the SDp sector. With the upcoming PICO40L and PICO500 detectors, this experiment will continue to lead the way in the search for dark matter in the SDp sector. Fig. 10.4 shows a summary plot of all the PICO limits published over the years as well as the projections for PICO40L and PICO500. The PICO40L projected limit shown in Fig. 10.4 assumes one year of running at a 3.2 keV energy threshold while the PICO500 prediction assumes 1/4 year of running at 3 keV and 1/2 year at 10 keV. The motivation for using 2 different thresholds in PICO500 is the presence of the neutrino background which depends on the energy threshold as described in sect. 8.11.

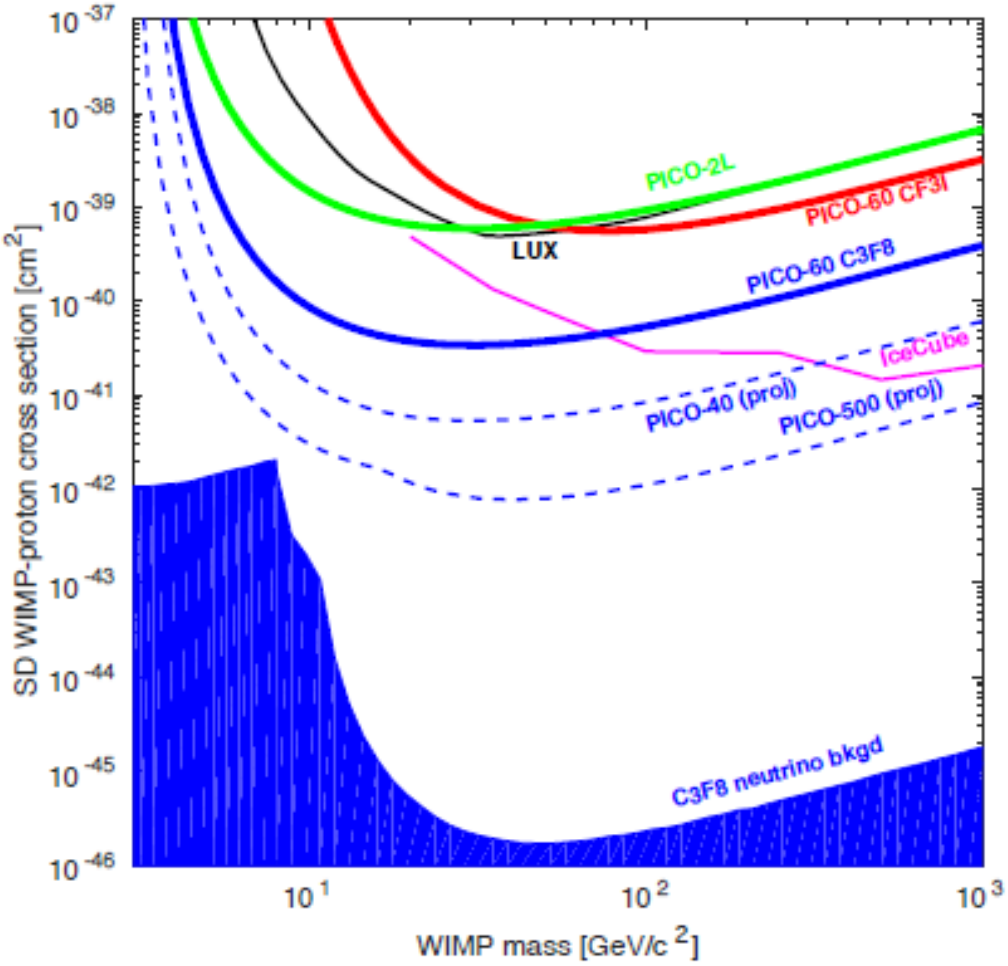

Figure 10.4 – SDp limit for various PICO detectors as well as IceCube [93] and LUX [138]. The PICO40L prediction assumes one year of running at a 3.2 keV energy threshold. The PICO500 prediction assumes 1/4 year of running at 3 keV and 1/2 year at 10 keV.

If the energy threshold is increased, the detector is no longer sensitive to ^{8}B solar neutrinos but is still sensitive to atmospheric neutrinos. Fortunately, the abundance of the latter one is smaller compared to ^{8}B neutrinos, which explains the sharp decrease of this background for WIMP masses higher than above 10 GeV/c^2. While the ^{8}B neutrinos are a limiting background to WIMP searches, they also have never been measured to this day through elastic scattering, and PICO500 could be the first to detect them.

CHAPTER 11

PICO40L NEUTRON BACKGROUND SIMULATION

In anticipation of the next dark matter search with PICO40L, the neutron background produced by thorium and uranium impurities that are present inside every detector component must be predicted. The work presented in this chapter has been designed to predict the single and multiple event rates generated due to fast neutrons emitted by these impurities: ^{235}U, ^{238}U and ^{232}Th. These contaminants are found at the ppb and ppt level inside the detector components of PICO40L and the neutron background they induced are simulated using GEANT4 [116] (GEometry ANd Tracking).

To accomplish this goal, a code package was developed with the purpose to write GEANT4 geometries by using the McCAD [152] software that translates CAD (Computer-Aided Design) drawings into GDML [153] (Geometry Description Markup Language) format which is directly usable in GEANT4. This approach makes it possible to produce complex geometries containing many components without performing any geometrical approximations unlike with other methods such as CADMesh [154]. There are two additional indirect advantages to this method; the first is the possibility of translating CAD files into MCNP files. The second advantage is the ability to use this code package to perform GEANT4 simulations throughout the design progress of PICO500.

The prediction of the neutron background due to the presence of the above mentioned contaminants is a common simulation that has been performed for every PICO detector. The novelties of these PICO40L neutron background simulations are a higher number of detector components in the geometry itself and the simulation of a higher number of detector components as well. Both these improvements increased the accuracy of the prediction of this neutron background and it was only possible due to development of this code packages which reduced the time it takes to construct GEANT4 geometries from a few months down to only a few days. To increase the time it takes to perform

these simulations, GEANT4 was run in multi-threaded mode on a 28 cores computer such that simulating 10^8 neutrons took typically 30 minutes.

Increasing the diameter of the pressure vessel (PV) is one of the significant improvements of PICO40L compared to PICO60 from a neutron background perspective since it reduces the neutron and gamma background by moving away several radioactive components from the active volume.

Four quantities are needed to predict the number of single and multiple event rates: the neutron spectrum, the neutron yield (neutron/ppb/sec/g), the leakage probability, and the contamination level. The neutron spectrum and the neutron yield are calculated using the SOURCES4C code [155] while the leakage probability, i.e., the number of single and multiple bubble events divided by the number of simulated neutrons is an output of the GEANT4 simulations. Lastly, the contamination level of the three isotopes serving as input to the simulations are measured by either High Purity Germanium counters (HPGe) or by Inductively Coupled Plasma Mass Spectrometry (ICP-MS)

11.1 Prediction of the single and multiple events

By convention, the number of single and multiple events in PICO detector are always given for one year and is obtained by using the following equation:

$$\text{Bubbles/year} = \text{Leakage probability} \times \text{Neutron yield} \times \text{Mass} \times 1\ \text{Year} \times \text{ppb level}, \tag{11.1}$$

where the neutron yield is in units of neutrons/ppb/sec/g and has an uncertainty of $\approx 20\%$ mostly due to cross section uncertainties, and calculation approximations. Since the ppb level is measured experimentally, it has also an uncertainty associated with it. The leakage probability has a statistical uncertainty, but it is small due to the high number of simulated events for each detector components which is either 10^6 or 10^8 neutrons for each component and each isotope.

11.2 Neutron spectrum and yield

Three contaminants, ^{235}U, ^{238}U and ^{232}Th, are present in every material, and each possesses their distinctive decay chain. These isotopes can produce fast neutrons through three different processes:

- Spontaneous fission (SF),
- Delayed neutron emission,
- (α,n) reactions.

Each process has a distinct energy spectrum and yield. Furthermore, the yield and spectrum of the neutrons produced via (α,n) reactions highly depend on the cross section between the α particle and the nucleus it interacts with as well as the energy threshold of the process for a given nucleus. To put this in perspective, Fig. 11.1 shows the neutron yield as a function of the energy for two detector materials: camera (50% Al, 18% H, 17% C, 14% O) and stainless steel, but also for two different processes: SF and (α,n) reaction.

Both materials share the same SF yield because this process only depends on the contaminant which is the same for both materials, i.e., ^{238}U in this particular case. Furthermore, there is an order of magnitude difference between the yield of stainless steel (SS) and the camera material for (α,n) reactions. There is also one order of magnitude decrease in yield near ~ 4 MeV for SS that is not present for the camera material. The SS yield is dominated by SF, while the camera material is dominated by neutron produced via (α,n) reactions. The main reason for those differences is the presence of aluminum in the camera. Typically, the neutron production through (α,n) reactions increases for elements with a small mass number, and it also increases the production of higher energy neutrons as can be seen in Fig. 11.1. It is therefore desirable to avoid any material containing elements that have a small mass number as much as possible.

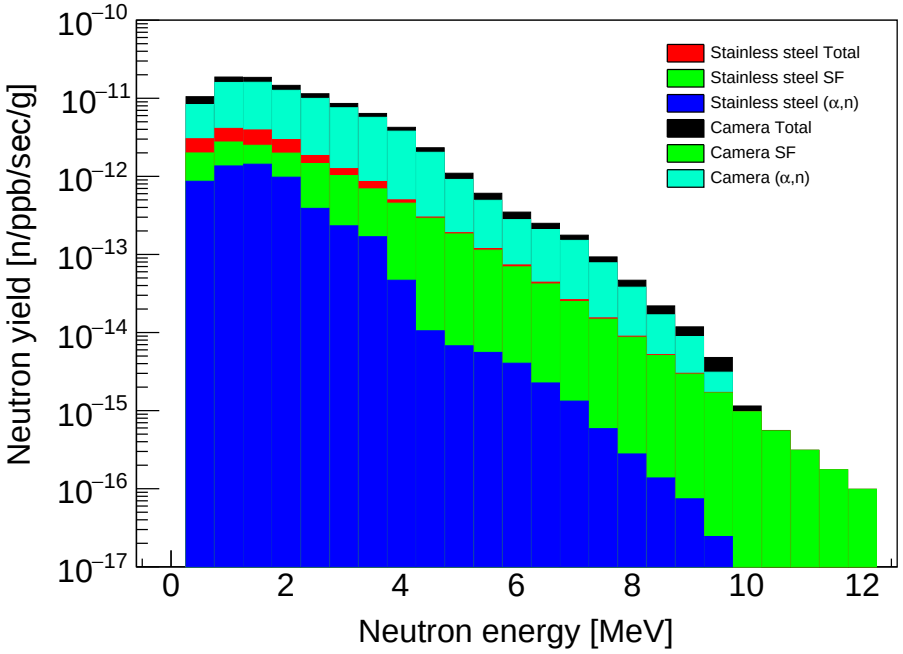

Figure 11.1 – Histogram of the neutron yield (n/ppb/sec/g) of ^{238}U as a function of the neutron energy for two different materials: camera (50%Al, 18%H, %17C, %14O), SS and for two different processes: SF and (α,n). The neutron yield produced by (α,n) reactions for the camera material is about one order of magnitude higher than for SS which is mainly due to the presence of aluminum.

11.3 Contamination level

Samples of each detector components are measured with an HPGe counter at SNOLAB for contamination levels down to a few tens of ppb, and ICP-MS is used for parts with ppt contamination levels, such as the quartz vessel and the hydraulic fluid (mineral oil).

In addition to the three main isotopes, the ^{238}U decay chain is separated into two decay chains due to the radon absorption propensity of certain material such as plastic. The first section emcompases ^{238}U to ^{226}Ra while the second decay chain, goes from ^{222}Rn to ^{210}Tl.

Due to the chemical affinities of ^{222}Rn with certain materials, radon can be absorbed and thus a material can have a higher concentration of ^{222}Rn than ^{238}U. If a component has such a feature, two simulations have to be performed which will impact the single and multiple bubble rates of this particular component.

11.4 GEANT4 simulations

GEANT4 is a free software package for Monte Carlo simulations of particle-matter interactions. It is developed by CERN and uses C++ object-oriented programming language that allows users to construct stand-alone applications. Version 4.10.02 was used in all simulations that were done in this work. Starting from the Underground Physics example of GEANT4, a C_3F_8 volume is designated as a sensitive detector volume. Using a sensitive volume has the advantage of facilitating the collection of physical quantities from the specified sensitive detector such as the energy and the position of the interaction points. This example also contains every physical process essential to the low energy interactions of fermions and hadrons, but also of the high energy muons that can produce muon-induced neutrons through the interaction of muons with the rock that surrounds the detector or the detector components.

11.4.1 GDML

The Geometry Description Markup Language (GDML) [153] is an application-independent geometry description format based on XML (eXtensible Markup Language) which both GEANT4 and ROOT can read. This geometry description offers multiple improvements over the standard GEANT4 geometry. It is effective due to its simplicity to edit and update existing geometries. It is also modular, i.e., each part is independent of the others. Therefore, without recompiling the application, the user can decide to use only a specific section of a detector geometry if some sections are irrelevant for a given simulation in order to decrease the simulation time. More importantly, since it is application independent, softwares such as McCAD, can be used to translate CAD drawings of the detector directly into GDML format that can then be used in GEANT4.

11.4.2 McCAD

McCAD is a geometry conversion tool developed at the Karlsruhe Institute of Technology (KIT) that converts CAD drawings into Monte Carlo software geometries [152]. It can convert STEP files, which is an ISO standard for CAD drawings, into GDML or MCNP format. Unfortunately, there are certain limitations to this software. There are primitive solids that cannot be translated such as toruses and cones. It is still currently in development so it is possible that in the future it will become more versatile and able to convert more complex geometries that contain multiple different primitive solids. While this software converts components, it does not convert assembly files which hold the information regarding the position and rotation of the components of a CAD drawing, and thus a separate Python code was written to extract this information. Another reason to use McCAD is the capability of decomposing CAD drawings, i.e., it can recognize that a sphere and a cylinder that are merged to form a complex geometrical part, which means that there is no approximation during the translation. If required, it can use an approximation method to translate STEP files into GDML or MCNP format. In this work, none of the detector components were translated using approximations. In the case where components could not be translated into GDML by McCAD, they were written directly into GDML format so that no approximations were present in the whole geometry.

11.5 From CAD files to Geant4

Starting with STEP files and a code package written in C++, Bash, and Python, the McCAD software may be used to obtain ready to use GDML files that can be directly implemented in GEANT4 to build a geometry.

A block diagram that shows the steps to obtain all the required files for a GEANT4 geometry is shown in Fig. 11.2.

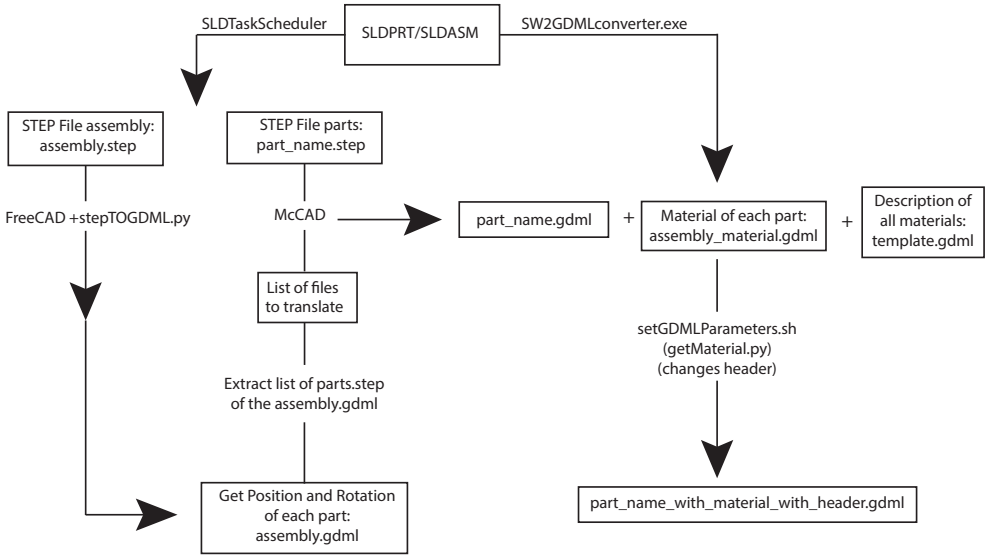

Figure 11.2 – Block diagram showing each step required to produce GDML assembly files and GDML component files that are ready to use for GEANT4.

The first step to achieve this goal is to translate CAD files into STEP files which can then be read by McCAD that can then translate the STEP files into GDML format. While McCAD does translate STEP files of components, it does not provide the positions and rotations of where those components rest inside the detector. The information regarding the location of each part is inside the STEP assembly file. This assembly file is read by a software called FreeCAD [156] and then a Python code has to be executed to extract the position and rotation of each detector component. There are various ways of describing rotations in three-dimensional space, and the CAD software and the GEANT4 descriptions are not compatible. Thus, the rotation angles in unit quaternions are extracted and then transformed in Euler angles that correspond to the GDML convention which is x-y-z, meaning that the first rotation is around the x-axis and so on.

The CAD software used within the PICO collaboration is Solidworks [157]. In this software, one can specify the material of each component, and consequently, a Visual Studio code that can extract this information was written whose output is then added to the GDML component files using a Python code (get_material.py, see Fig. 11.2).

11.6 PICO40L GDML Geometry

The PICO40L detector geometry was already presented in Chap. 7. This section will present relevant dimensions from the simulation point of view. The PICO40L GDML geometry that was written to simulate and predict the neutron background coming from thorium and uranium contamination includes a total of 48 components. Three different views of the detector are shown in Fig. 11.3.

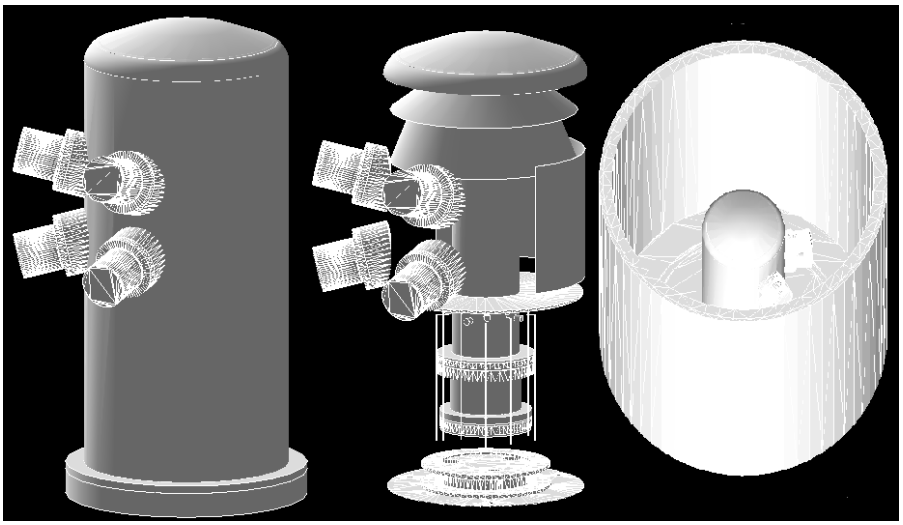

Figure 11.3 – Left: View of the PICO40L PV which includes the camera ports. Middle: View of the PICO40L detector without the mineral oil and the plastic shield. Right: PICO40L detector inside the water bath. The three retroreflector components can be seen and are made of two conical parts and a 180° hollow cylinder. The central cylinders are the IV, OV, and bellows. The bellows are in between the bellows flanges near the bottom of the central cylinder. The piezoelectric sensors and their cable are also shown.

For simulation purposes, the detector sits in a 50 cm thick hollow concrete cube of 5 x 5 x 7 m^3. The detector's neutron and thermal shield consists of a water tank of $\sim$1.8 m diameter and 3.8 m in height made of two SS cylinder that surrounds a polyethylene sheet that provides heat insulation. The water tank is filled with water up to a height of 3.3 meters. The PV has a 90 cm diameter (36 inches) and rests inside the water tank. It contains mineral oil and the detector itself. There is a distance of $\sim$100 cm between the PV and the inner SS wall of the water tank. The oil acts as the hydraulic fluid as well as

a neutron shield that blocks fast neutrons that are produced from the surrounding rocks of the mine as well as neutrons produced by thorium and uranium contamination. There is a distance of $\sim$30 cm between the inner wall of the PV and the OV.

There are four camera systems, and each of them includes a camera, a lens, and a LED ring. A retroreflector is required to reflect the LED light so that the camera can see the bubbles that are produced during an event. The retroreflector is stuck on two conical parts as well as on the inside of the PV (see Fig. 11.3). The IV and the OV have a diameter of 27.2 and 30 cm respectively. There are 66.72 kg of C_3F_8 enclosed by the jars, but only 55.75 kg will be in a superheated state at a temperature of 15°C since only the freon in the upper part of the detector will be superheated.

There is a heating device enclosed between two copper disks inside of the PV that surrounds the OV as well as another one inside the IV jar. They both separate the PV volume in two sections. The top section, where the active volume is located will be held at 15°C while the bottom section will be held at -25°C. Just below the heating device inside the IV, there are 12 piezoelectric sensors. Each sensor is made of a PZT crystal, a PCB (Printed Circuit Board), a cable and a copper housing. There is a plastic shield that surrounds the bottom section that provides thermal insulation to keep both sections at a stable temperature by limiting thermal convection.

11.7 Important components for simulation

Five criteria can make a detector component relevant regarding background contribution: distance from the active volume, mass, contamination level, neutron yield, and high energy spectrum. Most of the time, components need to meet more than one of these five criteria to produce a relevant background in the detector. Furthermore, for components that are far from the active volume the only way for neutrons to reach the active volume is to pass through the mineral oil, which is an excellent neutron moderator and therefore only high energy neutrons are of concern in this situation. The most im-

portant contributors to the neutron background are classified as a function of these five criteria in Table 11.I

Component	Close	Mass	ppb level	Neutron yield	Energy
IV and OV	✓				
LEDs			✓	✓	✓
Lenses			✓	✓	
Camera			✓	✓	✓
Retro reflector			✓		
Mineral oil	✓	✓			✓
Plastic castle	✓	✓			✓
Titanium flanges	✓	✓		✓	
Bellows	✓	✓			
PV		✓			
Copper heating disks	✓	✓			
Piezo PZT	✓		✓	✓	✓
Piezo PCB	✓		✓	✓	✓
Piezo Copper	✓		✓	✓	✓
Piezo Cable	✓		✓	✓	✓

Table 11.I – Characteristics of each components that are important neutron background contributors. This table is strictly for qualitative description purposes.

Since the quartz vessels (IV and OV) and the mineral oil are extremely close to the active volume, the contamination level must be very low and had to be measured by ICP-MS.

The SS bellows, their flanges, as well as the titanium flanges that connect the IV and OV to the bellows, also had to be simulated due to being relatively massive and close to the active volume.

The cameras, lenses, and LEDs all have a high contamination level, neutron yield, and high energy spectrum except the lenses that do not have a high energy spectrum. The LEDs are a concern due to the high neutron yield of the Kapton PCB on which they

are attached. The cameras have a relatively high contamination level of a few hundred ppb, a high neutron yield due to the aluminum casing (Z = 13), and a PCB that contains oxygen (Z = 8).

Another important contributor to the PICO60 neutron background was the retroreflector. However, the retroreflector contamination level highly depends on the batch, and luckily the current batch used for PICO40L has a much lower contamination level. As an example, the contamination level of ^{232}Th is 663.08 ± 17.22 ppb and 35.26 ± 10.41 ppb for the PICO60 and PICO40L detectors respectively. One of the difficulties in predicting the neutron background contribution of the retroreflector is due to its partially unknown material composition. It is assumed to be SS in the simulations, but if this assumption is wrong, it could highly affect the neutron yield in a similar way to the cameras and lenses.

The piezoelectric sensors are the only component that meet four out of five of the criteria, and thus their number and closeness to the active volume must be carefully controlled.

11.7.1 Radon emanation

Plastic components tend to absorb radon which can then be released within the detector when they degas. The radon can then dissolve uniformly within the oil and increase the neutron background via (α, n) reactions. There are several plastic components inside the detector, the largest being the plastic thermal shield, and in order to minimize the amount of radon absorbed by it, it was assembled and stored inside a radon-free room. The other important plastic components are the multiple o-rings and gasket seals. The gaskets have a higher mass than the o-rings and can, therefore, emanate a greater amount of radon. To quantify the radon emanation of all gaskets and o-rings, they have to be placed inside a radon emanation chamber. As of now, the amount of radon that is expected inside the oil due to radon emanation has not been estimated. Simulation can still be performed, but only the number of single and multiple events per year per ppb of radon is available and is reported in Table 11.IV.

11.8 Verification steps

Several ways have been developed to verify the GEANT4 simulations. There are several steps throughout a simulation that can go wrong without preventing the simulation from finishing.

An important step is to define the neutron energy and the starting position of the neutrons. There are two steps to properly simulate the position of the neutrons. The first is to randomly generate a position inside a cylinder, sphere or a cube. The position of the center of the chosen geometrical object is set by the user as well as the different dimensions to specify the object (radius, height). The second is to verify that the random position (x, y, z) is confined within the desired component of the detector. One problem that can occur is when the user enters a slightly wrong specification for the geometrical object in such a way that only a small portion of the specified volume overlaps the detector component. If this happens, the simulation will work, and there won't be any errors, but the full component volume will not be taken into account in the simulation.

To ensure that this type of error does not occur, an output file containing the energy and position of the initial neutrons was added. The initial energy of the neutrons was simply checked to make sure that the random generator was effectively generating the energy spectrum given as an input. More importantly, a code was written to visualize the position of the simulated neutrons to make sure that they encompass the desired component completely. Fig. 11.4 shows, as an example, the initial neutron positions during the simulation of the piezoelectric sensors and confirms that there are effectively 12 sensors that are situated at their known position.

Another problem that can arise is the overlap of two or more detector parts which can be tested in multiple ways. The first is to use a GDML visualizer that lists every overlap between any component. Also, during a given simulation, if there is an overlap and if a particle happens to pass through an overlap, a warning message will be displayed, and then the overlapping components can be identified and the geometry can be corrected.

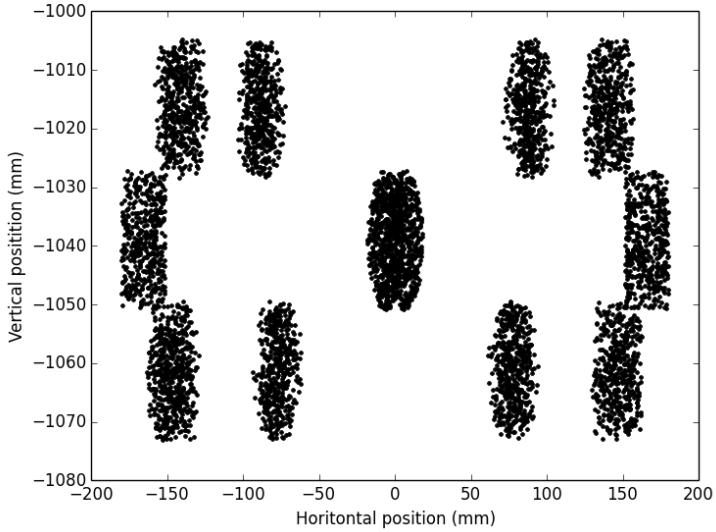

Figure 11.4 – 2D plot of the initial positions of the simulated neutrons for the piezoelectric sensors. There are three stacks of piezoelectric sensors, and on each stack, there are four sensors.

Finally, in GEANT4, one can also use a geantino as an incident particle which passes through the geometry in a straight line without interacting and again with this method one can identify overlapping components. All these methods were used to verify that no overlap remained in the PICO40L GEANT4 geometry. An important advantage of using a code to extract the position and the rotation of each detector component is that if there are no overlaps in the CAD drawings, it means there are none in the GEANT4 geometry because a code is in charge of writing the position of each component and not a user.

11.9 Analysis

To calculate the single and multiple event rate due to contamination of ^{235}U, ^{238}U and ^{232}Th, a simulation for each of them has to be done since they all have a different neutron spectrum. The basic quantities that are not required for simulations are presented in Table .VI and are the ppb level, the neutron yield, the volume, the density and the number of simulated events. If a component has a density equal to one in this table,

it means that the component was weighed. Furthermore, if a component has a density and a volume both equal to one, which is only the case for the PZT crystals of the piezoelectric sensors, it is because there are two different types of PZT crystals, and each has a different massand contamination level and thus its ppb level is, in fact, its g$\times$ppsb in the particular case.

Once this information is collected, and the simulations are done, the next step is to calculate the single and multiple rates per year for every component and every contaminant. Since the result of those calculations are an intermediate calculation, they are shown in Appendix A. The same quantities are shown in a more condensed way in Table 11.II by summing the contribution of the three isotopes.

An important parameter that is extracted from the results in Table 11.II is the single to multiple events ratio which is $34.75\times10^{-4}/13.30\times10^{-4} = 2.61$ which means that 28% of neutron interactions produce only one bubble in the detector. This detector characteristic is essential since it provides a way to predict the neutron background in dark matter searches. Indeed, a dark matter interaction would only produce single bubble events due to its very low cross-section, which means that any multiple bubble event is not a background for dark matter searches.

In addition to giving the predicted number of single and multiple bubble event rate per year, Table 11.II also shows the leakage probability which is a very useful quantity when comparing different simulations of the same detector since it only depends on the simulation and the neutron spectrum, but not on the ppb level, the mass, or the neutron yield.

Another interesting fact is obtained by comparing the leakage probability of the Kapton PCBs and the lenses. Even though they are almost exactly in the same position, there is a factor of 10 between them which this is only due to the higher neutron energy spectrum of the Kapton PCBs. This highlights the need to avoid any material containing elements that have a small mass number.

Component	Leakage prob. S(M) x 10^{-4}	Singles/year $\times 10^{-4}$	Multiples/year $\times 10^{-4}$
Kapton	0.67(1.79)	76.07±19.00	203.38±50.98
Lens	0.06(0.18)	25.24±4.24	72.73±12.17
Camera	0.07(0.19)	19.70±2.27	53.03±6.08
Top Reflector	0.09(0.22)	0.10±0.02	0.26±0.05
Bot Reflector	0.47(1.23)	0.68±0.21	1.80±0.56
PV Reflector	0.23(0.67)	1.40±0.28	4.08±0.83
Reflector	0.26(0.70)	2.19±0.35	6.14±1.00
Oil	42.44(105.35)	0.11±0.02	0.29±0.05
Plastic shielding	1.54(3.29)	283.04±52.50	606.10±112.20
Titanium flange Top-Top	0.41(0.85)	9.13±10.80	18.95±22.40
Titanium flange Top-Bot	0.27(0.57)	6.14±7.23	12.99±15.25
Titanium flange Top-Mid	0.22(0.46)	6.97±8.30	14.53±16.96
Titanium flange Bottom-Top	0.00(0.01)	0.08±0.08	0.18±0.21
Titanium flange Bottom-Bot	0.00(0.00)	0.03±0.03	0.07±0.08
Titanium flange Bottom-Mid	0.00(0.00)	0.05±0.07	0.11±0.13
Titanium total	0.15(0.32)	22.40±15.42	46.82±31.97
Bellows	0.05(0.09)	1.95±0.42	3.64±0.78
Bellows top flange	0.09(0.20)	69.83±15.11	145.07±31.13
Bellows bottom flange	0.00(0.01)	1.80±0.45	3.71±0.86
DishHead	0.00(0.01)	1.43±0.34	3.23±0.71
PV	0.06(0.17)	356.90±71.37	991.04±194.85
Inner heating top copper plate	136.69(372.85)	0.00±0.00	0.01±0.00
Inner heating bottom copper plate	146.41(385.08)	0.00±0.00	0.01±0.00
Outer thermal control copper disk	13.36(26.40)	0.02±0.01	0.04±0.01
Copper Plates	98.82(261.44)	0.03±0.01	0.06±0.01
Piezo Copper	18.44(35.34)	0.00±0.00	0.00±0.00
Piezo PCB	53.56(111.09)	2.60±29.53	5.40±60.96
Piezo PZT	46.07(97.68)	15.42±23.40	32.91±49.90
Piezo Cable Vert	0.83(1.63)	8.77±2.67	17.56±5.32
Piezo Cable Horz	12.88(27.45)	8.16±2.55	17.33±5.43
Sum piezo components	26.35(54.64)	34.95±37.86	73.19±79.15
Piezo 84 Copper	18.43(35.36)	0.00±0.00	0.00±0.00
Piezo 84 PCB	53.54(111.10)	10.41±4.59	21.59±9.50
Piezo 84 PZT	46.06(97.67)	5.44±2.52	11.59±5.39
Piezo 84 Cable Vert	0.83(1.63)	16.96±5.86	33.58±11.74
Piezo 84 Cable Horz	12.86(27.45)	16.41±5.22	35.02±11.12
Sum Piezo 84 components	26.35(54.64)	49.21±9.44	101.78±19.52
IV	125.74(278.54)	0.00±0.00	0.00±0.00
OV	728.90(1856.40)	0.01±0.00	0.02±0.01
Total	13.30(34.75)	895.65±100.67	2208.47±248.19

Table 11.II – Leakage probability and single and multiple events rate per year for every simulated components of PICO40L with GEANT4.

11.10 Design improvements

Minor modifications of the detector design could reduce this neutron background and should be applied to the PICO500 design. First, the detector components with the highest predicted bubble events per year are, in order: the PV, plastic shielding, Kapton PCB, top bellows flange, lenses, cameras, piezoelectric sensors, and titanium flanges. The top bellows flange, piezoelectric sensors, and titanium flanges are three components that would find their leakage probability drastically reduced by moving them a few centimeters further away from the active volume which is something that could be done by having a longer IV and OV. It is already planned that the PICO500 PV will be much bigger than the PICO40L PV which is desirable since the PICO40L PV is the most important contributor to the neutron background and a bigger PV would also move the camera system away from the active volume, thus reducing the neutron background even more. However, there is a distance above which not much is gained by moving these components away from the active volume since it will become near impossible for the highest energy neutron to pass through the mineral oil that acts as a neutron shielding.

To reduce the background contribution of piezoelectric sensors, they would need to be moved further away from the detector. However, due to the dampening of the acoustic signal, there is a maximum distance above which the alpha discrimination capabilities would be lost.

Since the contamination level of the oil and quartz vessels must be lower than 1 ppb, they were both measured by ICP-MS. Initially, the oil was measured at SNOLAB with an HPGe and yielded a contamination level of 2.40 ± 2.32 ppb, 1.31 ± 2.08 ppb and < 0.10 ppb for ^{238}U, ^{235}U and ^{232}Th respectively. On the other hand, the ICP-MS measurement found that the same oil contained < 4.1 ppt ^{238}U and < 4.0 ppt ^{232}Th which means that the HPGe detectors are not sensitive enough.

Table 11.II shows that the single bubble rate of the plastic shielding is a factor $\sim$2500 higher than that of the oil even though the plastic shield is further away from the active volume and that they share the same composition (CH_2). The only difference between them is the much higher contamination level of the plastic shield which is < 0.94 ppb, < 1.27 ppb, and < 0.12 ppb for ^{238}U and ^{232}Th, respectively. This implies that the contamination level of the plastic shield is approximately 10^6 times higher than that of the oil. Since the contamination level for all three isotopes is an upper limit, it points to the possibility that the contamination level is, in fact, much lower, and that an ICP-MS measurement is required.

Increasing the distance between a radioactive component and the active liquid has two effects. First, it decreases the solid angle of the component with respect to the active volume. Secondly, it increased the amount of oil between a component and the active volume. This second effect implies that the mineral oil volume that acts as a neutron shield can shield against higher energy neutrons. Consequently, in PICO40L, the mineral oil blocks almost all of the low energy high yield neutrons, which means that only the low yield high energy neutrons can reach the active volume. Both these effects explain why the PICO40L neutron background drastically decrease with respect to PICO60. Furthermore, as can be seen in Fig. 11.1, neutrons with energies above 10 MeV are only produced by SF reactions. Consequently, for a specific amount of shielding, the necessity of choosing materials without low mass number elements disappears, because (α, n) reactions do not induce any neutrons with energies above 10 MeV.

11.11 Piezo electric sensors

Regardless of the position of the sensors, a detailed look at each piezoelectric sensor component shows that some of them have a higher bubble rate per year than others which is the case for the PZT crystals and the cables. However, the result of the PZT and PCB are still compatible with zero due to the uncertainty on the PZT and PCB contamination

levels. As an example, the ppb level of ^{238}U for the PCB is 35.64 $\pm$ 770.774 which makes it hard to conclude anything due to the large uncertainty.

Component	Contaminant	g×ppb	Δ g×ppb
PZT	^{238}U	743	1156
PZT	^{235}U	823	675
PZT	^{232}Th	66	38
PCB	^{238}U	41	899
PCB	^{235}U	534	889
PCB	^{232}Th	91	129
Housing	^{238}U	0.032	0.006
Housing	^{235}U	0.032	0.006
Housing	^{232}Th	0.004	0.001
Cables	^{238}U	11928	111
Cables	^{235}U	11928	111
Cables	^{232}Th	2120	18
Sum	^{238}U	12713	1469
Sum	^{235}U	13286	1122
Sum	^{232}Th	2278	136
Sum	Sum	28278	2727
Piezo	^{238}U	24201	13754
Piezo	^{235}U	33700	3424
Piezo	^{232}Th	34338	1702
Piezo	Sum	92241	14276

Table 11.III – Comparison of the g×ppb values between the sum of each piezoelectric sensor components and the resulting measurement when fully assembled sensors were counted (PICO-84). A strong disagreement exist between the two result highlighted in red.

In addition to this problem, the contamination level of 14 fully assembled piezoelectric sensors was measured with an HPGe detector and yielded a much higher ppb level than the ppb level of the individual piezoelectric sensor components. This measurement will be referred to as PICO-84 (SNOLAB measurement numbering). The important quantity used to compare both measurements is the g×ppb values which is shown in Table 11.III for each sensor component and for each contaminant.

The result shown in Table 11.III is re-normalized to 14 sensors since there were 14 fully assembled sensors for the PICO-84 measurement. The red rows show the numbers that have to be compared, and that should agree with one another. Those numbers are not the ones used for the prediction of the single and multiple bubble rates since the simulations contain not 14, but 12 piezoelectric sensors. This calculation is used to compare the g×ppb of the several measurements made with an HPGe at SNOLAB.

The measurement for the full piezoelectric assembly is a factor ∼3 higher in terms of g×ppb than the sum of each piezoelectric component. The two measurements should match approximately, and since this is not the case, it opens the possibility of an introduction of outside contamination during the assembly process of the sensors. Since the full piezoelectric assembly will be put inside the detector, the contamination level measured for the 14 fully assembled units should be taken into account when predicting the neutron background. However, the neutron yield and neutron spectrum is different for every piezoelectric sensor component. Thus each component has to be simulated separately to have a precise neutron background prediction. The single and multiple neutron rates that are shown in Table 11.II use the individual contamination level of each component.

Component	Contaminant	Leak. prob. S (M)×10^{-4}	Singles/year/ppb	Multiples/year/ppb
Oil	^{235}U	43.7 (106)	0.065	0.16
Oil	^{238}U	38.9 (100)	2.2	5.7
Oil	^{232}Th	44.7 (109)	0.51	1.28
Oil	^{226}Ra	43.8 (107)	0.98	2.4
Oil	^{210}Po	51.1 (122)	0.11	0.25

Table 11.IV – Single (S) and multiple (M) rate per year per ppb of ^{235}U, ^{238}U, ^{232}Th, ^{226}Ra and ^{210}Po inside the PICO40L mineral oil as well as the leakage probability for single and multiple bubble events.

11.12 Additional oil contamination

Another source of background is the level of radon inside the oil that emanates from the plastic shield, the o-rings, and gaskets that then dissolves into the oil and can then produce neutron through (α,n) reaction on ^{13}C. Another possibility is the presence of ^{210}Po out of equilibrium with the uranium decay chain. Even though the precise contributions of these two process are unknown, the simulations can still yield the number of single and multiple events per year per ppb of those two contaminants. Those results are presented in Table 11.IV.

Calculations show that the contamination level in ppb of ^{210}Po and ^{226}Ra required to produce the same single and multiple events per year as ^{238}U in the oil is 20 and 2.2, respectively. Therefore, it should be kept in mind that it might be mandatory for PICO500 to measure the amount of ^{210}Po in the oil.

11.13 Conclusion and comparison to PICO60

Several differences between the PICO60 and PICO40L detectors drastically decreased the neutron background produced by ^{238}U, ^{235}U and ^{232}Th contamination in PICO40L. Various factors helped reduce this background such as the increased diameter of the PV which has decreased not only the contribution of the PV, but also the contribution of the cameras, the lenses, the LEDs and the retroreflector. The much lower contamination level of the retroreflector also helped in the reduction of the neutron background. As a comparison and summary, Table 11.V shows the single and multiple events predictions of PICO60 and PICO40L.

Detector	Single/ year	Multiple/year
PICO60	4.62±2.15	13.19±5.17
PICO40L	0.09±0.01	0.22±0.03

Table 11.V – Comparison of single and multiples neutron background rate due to ^{238}U, ^{235}U and ^{232}Th contamination in the detector component of both PICO60 and PICO40L detectors.

The much lower neutron background will allow PICO40L to accumulate more data than PICO60 before becoming background limited. After ~ 79 days, one single bubble event would be produced in the PICO60 detector and it would, therefore, be background limited at that moment. On the other hand, PICO40L could run for 4055 days, or ~ 11 years before reaching one single bubble event. However, those numbers are only valid for this particular neutron background. It does not include external neutrons sources such as muon-induced neutrons, nor radon in the water of the water tank or the water in the cooling pipes. Therefore, other neutron background simulations must be performed to obtain a final prediction for the total neutron background of PICO40L. Although the goal of this work was to predict the neutron background produced due to uranium and thorium contamination of the detector components, the same geometry can be used to predict other types of background such as external neutrons and gammas due to the presence of ^{40}K, ^{137}Cs, and ^{60}Co inside detector components. Ultimately, in order to validate any predictions regarding any background rates, GEANT4 simulations must be verified by comparing the simulated count rate to the experimental count rate measured using a calibrated source. However, this cannot be done at the moment since PICO40L is still under construction, but the introduction of a source inside the current state of the simulation and the calculation of simulated rates is straightforward.

To conclude, developing and using this new code package reduced the time it takes to generate GEANT4 geometries from a few months down to only a few days. This new method led to the production of a more precise and complete GEANT4 geometry of PICO40L by removing the presence of approximated geometrical volumes and by increasing the number of detector components and simulated components in comparison to the PICO60 GEANT4 simulations.

CHAPTER 12

EFFECTIVE FIELD THEORY OF DARK MATTER

In Chap. 4, the standard SI and SD WIMP-nucleon interactions and the traditional way of presenting direct dark matter detection limits were described in detail. However, this approach describes only a subset of all possible WIMP-nucleon interactions. Recently, a well-described effective field theory (EFT) of dark matter direct detection was proposed by [158–160] which describes all possible types of WIMP-nucleon interactions. It was written such that quantities with a direct connection to experimental observables can be easily obtained. In this context, just like the traditional limit setting, one can put limits on the different interactions and also highlight the complementarity of different experiments.

12.1 The EFT approach

The reason why an effective field theory approach is very convenient to describe WIMP-nucleon interactions is because it intrinsically makes as few assumptions as possible regarding the details of the interaction. It focuses on the low energy scale of the interactions for which direct detection experiments are sensitive and makes the theoretical calculations much easier. By definition, an EFT is only valid for energies lower than a cut-off energy Λ_{UV}. Therefore, one must fix Λ_{UV} such that it is above the momentum transfers $q = \sqrt{2m_T E_R}$ relevant for a direct detection experiment. The maximum recoil energy E_R is given by the escape velocity of dark matter in our galaxy which is $v_{\rm esc} \sim 2 \times 10^{-3}$c and becomes $E_R = \frac{1}{2}\mu_T v_{\rm esc}^2$, with $\mu_T = \frac{m_T m_\chi}{m_T + m_\chi}$. Typical target masses are $m_T \sim 100$ GeV/c^2 which yields:

$$q_{\rm max} \sim 200 \text{ MeV/c}. \tag{12.1}$$

Predictions of this theory are valid only if the momentum transfer is less than 200 MeV/c. The consequence of this cut-off energy is that high energy and heavy particle contribu-

tions can be neglected, and thus the theory concentrates on describing the low energy behavior of the interaction. Starting with the WIMP-nucleon elastic scattering Lagrangian

$$\mathscr{L}_{\text{int}} = \sum_{\tau=n,p} \sum_i c_i^{(\tau)} \mathscr{O}_i \chi^+ \chi^- N^+ N^-, \tag{12.2}$$

where χ and N are the non-relativistic fields of dark matter and nucleon respectively, $\mathscr{O}_i$ are the EFT operators, c_i^τ's are the isospin couplings of the corresponding EFT operator, and τ is the isospin. The EFT operators $\mathscr{O}_i$ are a combination of four basic hermitian operators which are:

$$i\vec{q}, \quad \vec{v}^\perp \equiv \vec{v} + \frac{\vec{q}}{2\mu_N}, \quad \vec{S}_\chi, \quad \vec{S}_N, \tag{12.3}$$

where $\vec{S}_N$, $\vec{S}_\chi$ are the nucleon and WIMP spins respectively and $\vec{v}$ is the velocity of the incoming dark matter particle in the nucleon rest frame. Furthermore, $\vec{v}^\perp$ is split in two components: $\vec{v}^\perp = \vec{v}_T^\perp + \vec{v}_N^\perp$

- $\vec{v}_T^\perp$ acts on the center-of-mass velocity of the atomic nucleus as a whole
- $\vec{v}_N^\perp$ acts on the relative distances of the nucleons within the nucleus.

The next step is to build all possible operators, $\mathscr{O}_i$, which are a combination of the 4 hermitian operators listed in eq. 12.3, and listed in Table 12.I.

$\mathscr{O}_1 = 1_\chi 1_N$	$\mathscr{O}_3 = i\vec{S}_N \cdot \left[\frac{\vec{q}}{m_N} \times \vec{v}^\perp\right]$
$\mathscr{O}_4 = \vec{S}_\chi \cdot \vec{S}_N$	$\mathscr{O}_5 = i\vec{S}_\chi \cdot \left[\frac{\vec{q}}{m_N} \times \vec{v}^\perp\right]$
$\mathscr{O}_6 = \left[\vec{S}_\chi \cdot \frac{\vec{q}}{m_N}\right]\left[\vec{S}_N \cdot \frac{\vec{q}}{m_N}\right]$	$\mathscr{O}_7 = \vec{S}_N \cdot \vec{v}^\perp$
$\mathscr{O}_8 = \vec{S}_\chi \cdot \vec{v}^\perp$	$\mathscr{O}_9 = i\vec{S}_\chi \cdot \left[\vec{S}_N \times \frac{\vec{q}}{m_N}\right]$
$\mathscr{O}_{10} = i\vec{S}_N \cdot \frac{\vec{q}}{m_N}$	$\mathscr{O}_{11} = i\vec{S}_\chi \cdot \frac{\vec{q}}{m_N}$
$\mathscr{O}_{12} = \vec{S}_\chi \cdot \left[\vec{S}_N \times \vec{v}^\perp\right]$	$\mathscr{O}_{13} = i\left[\vec{S}_\chi \cdot \vec{v}^\perp\right]\left[\vec{S}_N \cdot \frac{\vec{q}}{m_N}\right]$
$\mathscr{O}_{14} = i\left[\vec{S}_\chi \cdot \frac{\vec{q}}{m_N}\right]\left[\vec{S}_N \cdot \vec{v}^\perp\right]$	$\mathscr{O}_{15} = -\left[\vec{S}_\chi \cdot \frac{\vec{q}}{m_N}\right]\left[\left(\vec{S}_N \times \vec{v}^\perp\right) \cdot \frac{\vec{q}}{m_N}\right]$

Table 12.I – List of EFT operators.

These operators depend explicitly on the relative speed between the WIMPs and the nucleons $\vec{v}^{\perp}$, on the momentum transfer $\vec{q}$ as well as on the spin of the WIMP and the nucleon $\vec{S}_{\chi}, \vec{S}_{N}$. It is important to note that without $\vec{v}^{\perp}$ and $\vec{q}$, the only EFT operators left are $\mathscr{O}_1$ and $\mathscr{O}_4$ which are the standard SI and SD interactions, respectively. Thus, all the new WIMP-nucleon interactions are introduced by the addition of $\vec{v}^{\perp}$ and $\vec{q}$. As will be shown later, altogether, these 14 operators will generate six types of interactions.

The next step is to use these operators to calculate the WIMP interaction with the entire nucleus. Taking a top to bottom approach, experimentalists need to be able to calculate the recoil spectrum as discussed in Chap.4:

$$\frac{dR}{dE_R} = N_A \frac{\rho_{\chi}}{m_{\chi}} \int_{v_{min}} d^3v \, f(v) \, v \, \frac{d\sigma}{dE_R}, \tag{12.4}$$

where N_A is the Avogadro number, ρ_{χ} and m_{χ} are the dark matter density and mass, respectively, $f(v)$ is the halo velocity distribution and $v_{min} = \sqrt{\frac{m_T E_R c^2}{2\mu_T^2}}$. All the new content of this approach lies in the cross section term:

$$\frac{d\sigma}{dE_R} = \frac{m_T}{2\pi v^2} P_{tot}(v^2, q^2) \tag{12.5}$$

$$\text{with } P_{tot} = \frac{1}{2j_{\chi}+1} \frac{1}{2j_N+1} \sum_{spins} |\mathscr{M}|^2_{\text{nucleus}-\text{HO/EFT}} \tag{12.6}$$

$$\text{and } \mathscr{M}_{\text{nucleus-HO/EFT}} = \sum_{\tau=0,1} \langle j_{\chi}, M_{\chi}; j_N, M_N | \left[\sum_{i=1}^{15} c_i^{\tau} \mathscr{O}_i t^{\tau}(i) \right] | j_{\chi}, M_{\chi}; j_N, M_N \rangle, \tag{12.7}$$

where HO stands for harmonic oscillator since the nuclear response of the interactions is calculated using the harmonic oscillator shell model [161], j and M are the main and second total angular momentum quantum number, respectively, τ is the isospin, the c_i^{τ}'s

are the isospin couplings, and t^τ are the isospin operators:

$$t^{\tau=0} = \begin{pmatrix} 1 & 0 \\ 0 & 1 \end{pmatrix}, \; t^{\tau=1} = \begin{pmatrix} 1 & 0 \\ 0 & -1 \end{pmatrix}. \tag{12.8}$$

The matrix element $\mathscr{M}_{\text{nucleus-HO/EFT}}$ of eq. 12.7 was calculated in [160] and yields:

$$\begin{aligned} &\tfrac{1}{2j_\chi+1}\tfrac{1}{2j_N+1}\textstyle\sum_{\text{spins}}|\mathscr{M}|^2_{\text{nucleus-HO/EFT}} = \tfrac{4\pi}{2j_N+1}\textstyle\sum_{\tau=0,1}\sum_{\tau'=0,1} \\ &\left\{\left[R_M^{\tau\tau'}(\vec{v}_T^{\perp 2},\tfrac{\vec{q}^{\,2}}{m_N^2})\, W_M^{\tau\tau'}(y) + R_{\Sigma''}^{\tau\tau'}(\vec{v}_T^{\perp 2},\tfrac{\vec{q}^{\,2}}{m_N^2})\, W_{\Sigma''}^{\tau\tau'}(y) + \right.\right. \\ &\left.R_{\Sigma'}^{\tau\tau'}(\vec{v}_T^{\perp 2},\tfrac{\vec{q}^{\,2}}{m_N^2}) W_{\Sigma'}^{\tau\tau'}(y)\right] + \tfrac{\vec{q}^{\,2}}{m_N^2}\left[R_{\Phi''}^{\tau\tau'}(\vec{v}_T^{\perp 2},\tfrac{\vec{q}^{\,2}}{m_N^2})\, W_{\Phi''}^{\tau\tau'}(y) + \right. \\ &R_{\Phi''M}^{\tau\tau'}(\vec{v}_T^{\perp 2},\tfrac{\vec{q}^{\,2}}{m_N^2})\, W_{\Phi''M}^{\tau\tau'}(y) + R_{\tilde{\Phi}'}^{\tau\tau'}(\vec{v}_T^{\perp 2},\tfrac{\vec{q}^{\,2}}{m_N^2}) W_{\tilde{\Phi}'}^{\tau\tau'}(y) + \\ &\left.\left.R_{\Delta}^{\tau\tau'}(\vec{v}_T^{\perp 2},\tfrac{\vec{q}^{\,2}}{m_N^2})\, W_{\Delta}^{\tau\tau'}(y) + R_{\Delta\Sigma'}^{\tau\tau'}(\vec{v}_T^{\perp 2},\tfrac{\vec{q}^{\,2}}{m_N^2})\, W_{\Delta\Sigma'}^{\tau\tau'}(y)\right]\right\}, \end{aligned} \tag{12.9}$$

where $R_k^{\tau\tau'}(\vec{v}_T^{\perp 2},\frac{\vec{q}^{\,2}}{m_N^2})$ and $W_k^{\tau\tau'}(y)$ are respectively the eight WIMP and nuclear response functions, where $k = M,\Delta,\Sigma',\Sigma'',\tilde{\Phi}',\Phi''$ denotes the six different possible types of interactions. There are five terms which depend explicitly on $\frac{\vec{q}^2}{m_N^2} \sim 1\times 10^{-3}$, two interference terms (blue), three describe new interactions (red), while the terms in black are the standard SI and SD interactions. Together, the 14 operators ($\mathscr{O}_i$) contribute to the following interactions:

- M: Standard SI response,
- Δ: Interaction involving angular momentum of a nucleon (ℓ),
- Σ': Interaction involving $\vec{S}_N|_{\text{transverse}}$ of the nucleon spin with respect to $\vec{q}$,
- Σ'': Interaction involving $\vec{S}_N|_{\text{longitudinal}}$ of the nucleon spin with respect to $\vec{q}$,
- Φ'': Spin-orbit interaction ($\vec{L}\cdot\vec{S}$),
- $\tilde{\Phi}'$: Also $\vec{L}\cdot\vec{S}$ dependent interaction, but with CP-violation.

The nuclear response functions are given by the following matrix element

$$W_k^{\tau\tau'}(y) = \langle j_N || \, k_{J;\tau}(q) \, || j_N \rangle \langle j_N || \, k_{J;\tau'}(q) \, || j_N \rangle, \tag{12.10}$$

where $||$ denotes a nuclear matrix element reduced in angular momentum. The calculation of those parameters depends on the target nucleus involved in the WIMP-nucleon interaction. The WIMP response function $R_k^{\tau\tau'}(\vec{v}_T^{\perp 2}, \frac{\vec{q}^{\,2}}{m_N^2})$ are listed in eq. 12.11. The first thing to note is the presence of the terms $\vec{v}_T^{\perp 2} \sim 1 \times 10^{-3}$ and $\frac{\vec{q}^2}{m_N^2} \sim 1 \times 10^{-6}$ in front of certain coefficients that decrease the coupling strength substantively.

$$\begin{aligned}
R_M^{\tau\tau'}(\vec{v}_T^{\perp 2}, \frac{\vec{q}^2}{m_N^2}) &= c_1^\tau c_1^{\tau'} + \frac{j_\chi(j_\chi+1)}{3}\left[\frac{\vec{q}^2}{m_N^2}\vec{v}_T^{\perp 2} c_5^\tau c_5^{\tau'} + \vec{v}_T^{\perp 2} c_8^\tau c_8^{\tau'} + \frac{\vec{q}^2}{m_N^2} c_{11}^\tau c_{11}^{\tau'}\right] \\
R_{\Phi''}^{\tau\tau'}(\vec{v}_T^{\perp 2}, \frac{\vec{q}^2}{m_N^2}) &= \frac{\vec{q}^2}{4m_N^2} c_3^\tau c_3^{\tau'} + \frac{j_\chi(j_\chi+1)}{12}\left(c_{12}^\tau - \frac{\vec{q}^2}{m_N^2} c_{15}^\tau\right)\left(c_{12}^{\tau'} - \frac{\vec{q}^2}{m_N^2} c_{15}^{\tau'}\right) \\
R_{\Phi''M}^{\tau\tau'}(\vec{v}_T^{\perp 2}, \frac{\vec{q}^2}{m_N^2}) &= c_3^\tau c_1^{\tau'} + \frac{j_\chi(j_\chi+1)}{3}\left(c_{12}^\tau - \frac{\vec{q}^2}{m_N^2} c_{15}^\tau\right) c_{11}^{\tau'} \\
R_{\tilde{\Phi}'}^{\tau\tau'}(\vec{v}_T^{\perp 2}, \frac{\vec{q}^2}{m_N^2}) &= \frac{j_\chi(j_\chi+1)}{12}\left[c_{12}^\tau c_{12}^{\tau'} + \frac{\vec{q}^2}{m_N^2} c_{13}^\tau c_{13}^{\tau'}\right] \\
R_{\Sigma''}^{\tau\tau'}(\vec{v}_T^{\perp 2}, \frac{\vec{q}^2}{m_N^2}) &= \frac{\vec{q}^2}{4m_N^2} c_{10}^\tau c_{10}^{\tau'} + \frac{j_\chi(j_\chi+1)}{12}\left[c_4^\tau c_4^{\tau'} + \right. \\
&\quad \left. \frac{\vec{q}^2}{m_N^2}(c_4^\tau c_6^{\tau'} + c_6^\tau c_4^{\tau'}) + \frac{\vec{q}^4}{m_N^4} c_6^\tau c_6^{\tau'} + \vec{v}_T^{\perp 2} c_{12}^\tau c_{12}^{\tau'} + \frac{\vec{q}^2}{m_N^2}\vec{v}_T^{\perp 2} c_{13}^\tau c_{13}^{\tau'}\right] \\
R_{\Sigma'}^{\tau\tau'}(\vec{v}_T^{\perp 2}, \frac{\vec{q}^2}{m_N^2}) &= \frac{1}{8}\left[\frac{\vec{q}^2}{m_N^2}\vec{v}_T^{\perp 2} c_3^\tau c_3^{\tau'} + \vec{v}_T^{\perp 2} c_7^\tau c_7^{\tau'}\right] + \frac{j_\chi(j_\chi+1)}{12}\left[c_4^\tau c_4^{\tau'} + \right. \\
&\quad \left. \frac{\vec{q}^2}{m_N^2} c_9^\tau c_9^{\tau'} + \frac{\vec{v}_T^{\perp 2}}{2}\left(c_{12}^\tau - \frac{\vec{q}^2}{m_N^2} c_{15}^\tau\right)\left(c_{12}^{\tau'} - \frac{\vec{q}^2}{m_N^2} c_{15}^{\tau\prime}\right) + \frac{\vec{q}^2}{2m_N^2}\vec{v}_T^{\perp 2} c_{14}^\tau c_{14}^{\tau'}\right] \\
R_\Delta^{\tau\tau'}(\vec{v}_T^{\perp 2}, \frac{\vec{q}^2}{m_N^2}) &= \frac{j_\chi(j_\chi+1)}{3}\left[\frac{\vec{q}^2}{m_N^2} c_5^\tau c_5^{\tau'} + c_8^\tau c_8^{\tau'}\right] \\
R_{\Delta\Sigma'}^{\tau\tau'}(\vec{v}_T^{\perp 2}, \frac{\vec{q}^2}{m_N^2}) &= \frac{j_\chi(j_\chi+1)}{3}\left[c_5^\tau c_4^{\tau'} - c_8^\tau c_9^{\tau'}\right].
\end{aligned} \tag{12.11}$$

Furthermore, there are multiple EFT operators for a given interaction. Taking again M as an example, eq. 12.11 shows that the EFT operators $\mathcal{O}_1$, $\mathcal{O}_5$, $\mathcal{O}_8$ and $\mathcal{O}_{11}$ contribute.

This is due to the fact that a given EFT operator couples to several interactions. As an example, $\mathcal{O}_5$ couples to M and Δ. In the traditional approach, the SD response was given by a single coupling, in this context, it is given by two terms, Σ' and Σ'' which are dominated by $\mathcal{O}_4$. A particular combination of the two interactions yields the usual SD response. One of the crucial points concerning this calculation of the cross section is that all the free parameters of the EFT, the c_i^τ's, are contained within the WIMP response function $R_k^{\tau\tau'}(\vec{v}_T^{\perp 2}, \frac{\vec{q}^{\,2}}{m_N^2})$ and none in the nuclear response function. More precisely, the c_i^τs can be expressed as a function of the proton and neutron couplings

$$c_i^0 = \frac{1}{2}(c_i^p + c_i^n) \text{ and } c_i^1 = \frac{1}{2}(c_i^p - c_i^n), \tag{12.12}$$

where $c_i^0 \equiv$ isoscalar, $c_i^1 \equiv$ isovector. Thus,

$$c_i^p = c_i^0 + c_i^1, \tag{12.13}$$

$$c_i^n = c_i^0 - c_i^1. \tag{12.14}$$

For a pure proton or neutron coupling, one must have $c_i^0 = c_i^1$ and $c_i^0 = -c_i^1$ respectively. This will become useful later for describing limits which depend on different combination of isospin couplings such as: $c_i^0 = c_i \cdot \cos(\theta)$ and $c_i^1 = c_i \cdot \sin(\theta)$.

A Mathematica Package for experimental analysis was released by [160] and translated into Matlab by [162]. The latter was used and modified for the analysis presented in the following sections.

12.2 Transition probabilities

The first step in understanding all the new interactions of the EFT approach is to calculate the transition probability for each type of interaction for different targets, i.e., to calculate P_{tot} (eq. 12.6), for different cases. Such calculations were done for the six different interactions, for six different targets (Xe, I, Ge, Si, Na, F), for two WIMPs masses (4 and 100 GeV/c^2) and for both pure proton and neutron couplings.

In order to calculate the transition probabilities, the recoil energies are integrated from 1 keV up to the maximum recoil energy following a WIMP interaction with a given target:

$$E_{\max} = E_{\text{recoil}}[v_{\chi,max}, \mu(\mathrm{T})], \tag{12.15}$$

where $v_{\chi,max}$ is $v_{Earth} + v_{Esc}$.

To highlight which target has the best coupling for a specific interaction, the plots that are shown in Fig. 12.1 are normalized via a color code with respect to the most responsive target for a given interaction, in other words, it shows which target is the best for a given interaction.

This approach produces the same similar known couplings for the traditional SI and SD interaction. Fig. 12.1 shows that the M_p and M_n couplings are favored by heavy targets such as Xe and I. The proton SD interactions Σ'_p and Σ''_p favor ^{19}F just like the traditional interaction. Furthermore, the only effect of changing the WIMP mass is an increase of the couplings for heavy targets due to kinematics.

One of the new interactions, Φ''_p, is of the spin-orbit type and its relative strength can be evaluated as follows:

$$(\vec{L}\cdot\vec{S}) \propto (\ell+1)\, n_+(\ell) - \ell\, n_-(\ell), \tag{12.16}$$

where $n_\pm$ is the number of nucleons in the $j = \ell \pm \frac{1}{2}$ sublevel. Thus, having a disparity in the number of nucleons for a given ℓ produces a stronger coupling. By using a simple nuclear shell model, it is possible to explain why the most responsive target for this interaction is iodine in the proton sector. With the help of Fig. 12.2, it can be seen that the proportionality factors for Xe, I and Ge are 34, 38 and 32, respectively. The reason

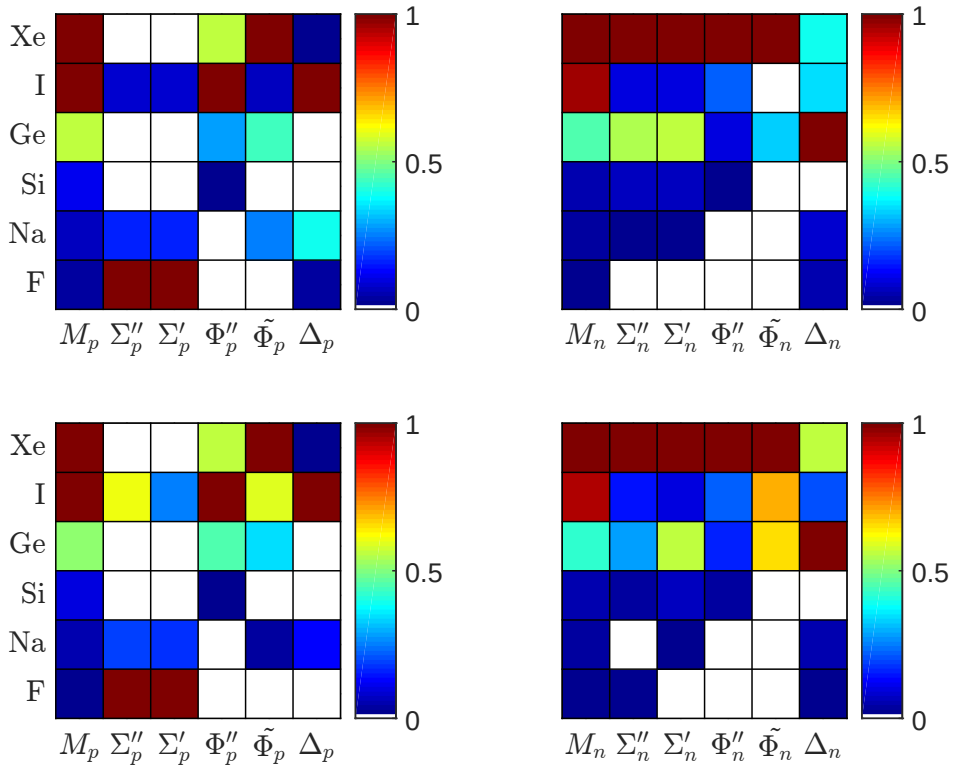

Figure 12.1 – Transition probabilities for a 4 GeV/c^2 (top) and 100 GeV/c^2 (bottom) WIMP for the six possible interactions mentioned in the text. The probabilities are obtained by integrating from 1 keV up to the maximum recoil energy (see eq. 12.15). The left (right)-hand side plot shows the transition probabilities for a pure proton (neutron) coupling. All plots are normalized to 1 with respect to the most responsive target for a given interaction.

why the value for I is larger than in Xe is that the $1g_{7/2}$ orbital in Xe has 1 more proton than iodine. This result can be confirmed by looking at the Φ''_p column in Fig. 12.1. A similar, but somewhat longer reasoning applies to the neutron sector.

It is also interesting to identify the strongest type of interaction for a given target. This is displayed in Fig. 12.3 where the respective entries are normalized with respect to the most responsive interaction for a given target. The calculations were done in the same way as for Fig. 12.1, but only this time the *M* response was removed in order to enhance the differences in strength between the remaining interaction.

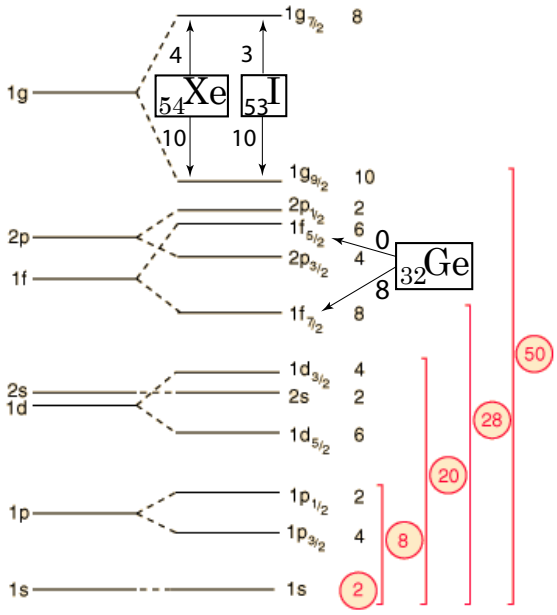

Figure 12.2 – Schematic view of the nuclear shell model for the proton content. The number of protons in each level for Ge, I and Xe is specified and enters in the estimate of the strength of the spin-orbit coupling.

The Fig. 12.3 shows that Xe, I, Ge and Si all have a strong couplings to Φ''_p of similar magnitude as Σ' and Σ'' interactions. For some of the targets, Φ''_p is even the dominating response. As expected, fluorine is favored by Σ'_p and Σ''_p. It is a significant advantage to use a target that is sensitive to multiple interactions because it improves the chances to detect a WIMP, especially since the nature of the WIMP-nucleon interaction is still unknown. On the other hand, it might also turn out to be very difficult to constrain this model because the WIMP interaction seen, for example, by a Xe loaded detector can be due to either the M, Φ'' or Σ'. However, in the case of a ^{19}F loaded detector, there is little doubt that a WIMP signal will be due to the SD interactions because the strength of the next to leading interaction, Δ, is a factor $\sim 10^{-3}$ smaller.

Finally, it is interesting to compare transition probabilities which are normalized with respect to M_n which is shown in Fig. 12.4. This approach is motivated by the observa-

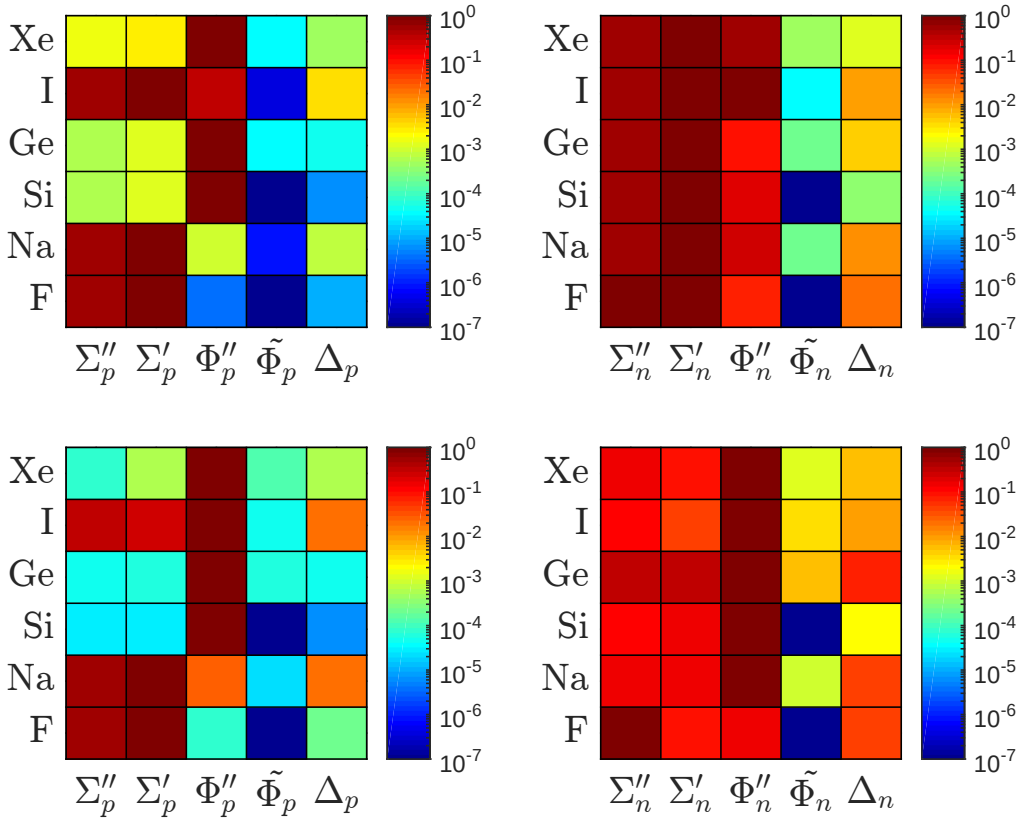

Figure 12.3 – Transition probabilities for a 4 GeV/c^2 (top row) and 100 GeV/c^2 WIMPs (bottom row) WIMP for the five subdominant interactions (without M). The probabilities are obtained by integrating from 1 keV up to the maximum recoil energy (see eq. 12.15). The left (right)-hand side plot shows the transition probability from a pure proton (neutron) coupling. All plots are normalized to 1 with respect to the most responsive interaction for a given target (horizontally normalized).

tion that the coherent neutrino scattering cross section is proportional to the number of neutrons squared. Therefore, once the neutrino floor is reached, WIMP-nucleon interactions will be outnumbered by solar or atmospheric neutrinos. Consequently, interactions weaker than M_n will be even more difficult to be probed. As an example, ^{19}F, as shown in Fig. 12.4, has a Σ'_p transition probability which is smaller by a factor of $\sim 10^{-3}$ than M_n, and for the other targets the situation is even worse. There is only ^{23}Na which has $\Sigma'_p/M_n \sim 10^{-4}$ that is comparable to fluorine. The maximum transition probabilities that

could be reached with a Xe, I, Ge, or Si target is in between 10^{-6} to 10^{-7} times smaller than the transition probability related to M_n. The presence of the neutrino floor implies that experiments using ^{19}F as a target fluid will be able to probe SD cross sections at a level which is $\sim 10^{-3}$ to $\sim 10^{-4}$ smaller than for any other targets. For example, Fig. 12.4 shows that the ^{19}F sensitivity to the Σ'_p interaction is a factor $\sim 10^3$ higher than that of Xe.

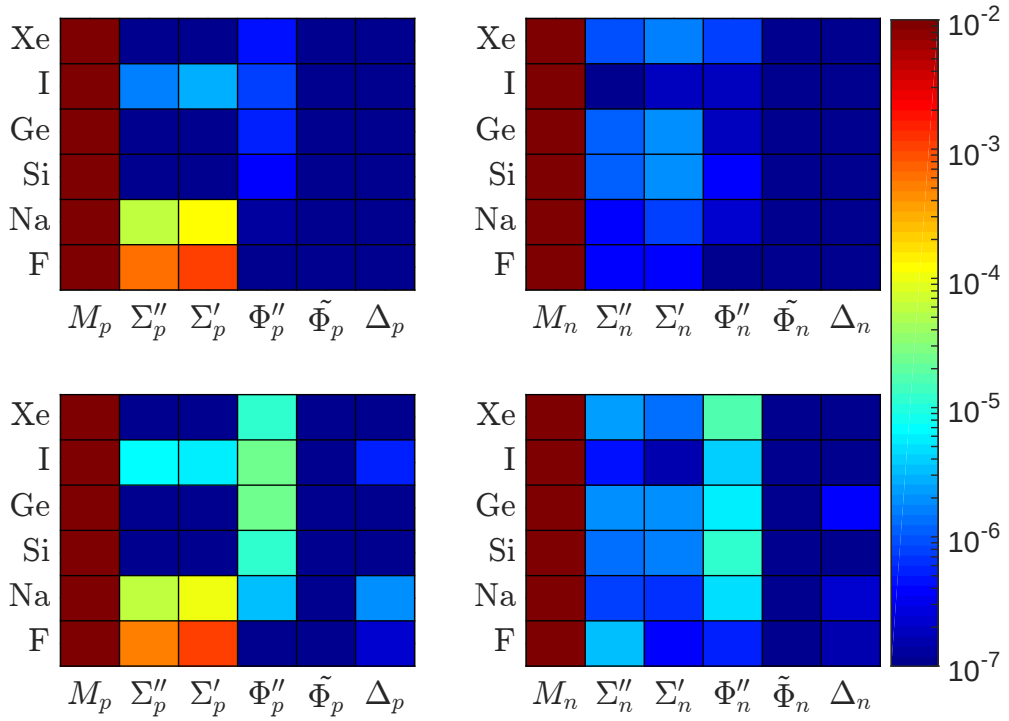

Figure 12.4 – Transition probabilities for a 4 GeV/c^2 (top) and a 100 GeV/c^2 (bottom) WIMP for the six possible interactions. The probabilities are obtained by integrating from 1 keV up to the maximum recoil energy (see eq. 12.15). The left (right)-hand side plot shows the transition probability for a pure proton (neutron) coupling. All plots are normalized to 1 with respect to the M_n.

While Fig. 12.4 illustrates the calculations in the EFT context, Fig. 12.5 shows the neutrino floor for C_3F_8 and Xe as well as the projected sensitivities for the SD-n/p sector for the future PICO40L, PICO500 and LZ (Xe) experiments.

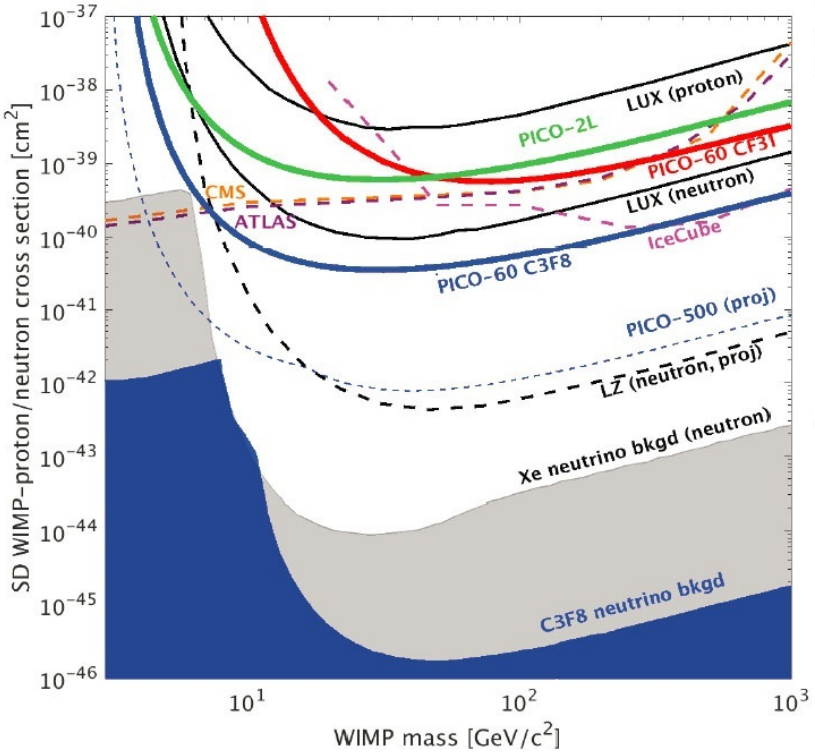

Figure 12.5 – Projected sensitivity of current and future Xe (LUX & LZ) and fluorine based experiment (PICO) in the spin-dependent neutron and proton sector. The corresponding neutrino floor of each active target is shown in gray (Xe) and blue (C_3F_8).

The neutrino floor for a WIMP mass of 100 GeV/c^2 for Xe is equal to $\sim 2 \times 10^{-46}$ cm^2 which is a factor $\sim 10^3$ higher than for ^{19}F which was predicted within the EFT context. The same procedure is applicable to the other novel types of interactions introduced by EFT. If dark matter couples not only to spin-independent interaction but to other novel interactions such as the spin-orbit interaction, it might be impossible to probe this coupling due to the presence of the neutrino floor. Also, depending on the coupling strength of the spin-dependent interaction, it is possible that the SD-p coupling could be measured by an experiment that uses fluorine as a target, while the SD-n coupling might not be accessible by an experiment that uses Xe as a target due to its elevated neutrino floor, and thus operating various experiments using different targets is crucial for the discovery of dark matter.

12.3 Recoil spectra and limit setting

Now that the transition probabilities have been described in detail, the next step is to derive the nuclear recoil spectrum following the various kind of WIMP interactions. The results are shown in Fig. 12.6 for 20 GeV/c^2 WIMPs scattering on ^{19}F, involving five EFT operators: $\mathcal{O}_1$, $\mathcal{O}_3$, $\mathcal{O}_4$, $\mathcal{O}_8$, $\mathcal{O}_{11}$.

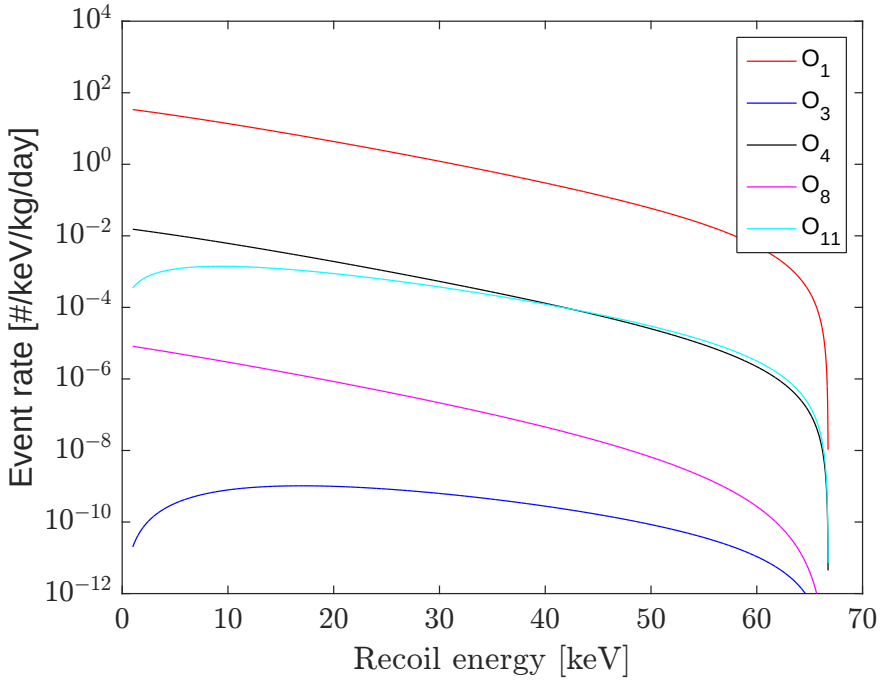

Figure 12.6 – Recoil spectra for WIMP-^{19}F interactions for a 20 GeV/c^2 WIMP, and for the 5 EFT operators: $\mathcal{O}_1$, $\mathcal{O}_3$, $\mathcal{O}_4$, $\mathcal{O}_8$, $\mathcal{O}_{11}$. The spectrum at low recoil energies is suppressed for some of the EFT operators by the factor $\frac{\vec{q}^2}{m_N^2}$ in their expression.

A procedure can be performed to yield a simplified mathematical expression that approximates the strength of each EFT operator $\mathcal{O}$ and allows a better comparison between each of them. First, to do so, each nuclear response is simplified: $W_M \sim K_N^2$, $W_{\Phi''} \sim (L_N \cdot S_N)^2$, $W_{\Sigma''} \& W_{\Sigma'} \sim S_N^2, W_\Delta \sim L_N^2$, where K_N is the coherence factor, defined as (A - Z), Z for N = (n, p), and L_N is the angular momentum. Second, the terms in front of the c_i's, i.e., $\frac{\vec{q}^2}{m_N^2}$ and $\vec{v}_T^{\perp 2}$ in eq. 12.11 and the term $\frac{\vec{q}^2}{m_N^2}$ in front of the various

interactions in eq. 12.9 are extracted. The results are labeled $(\mathscr{L}^2_{int})_{\mathscr{O}}$ and given below:

$$\begin{aligned}
(\mathscr{L}^2_{int})_{\mathscr{O}_3} &\approx \frac{\vec{q}^2}{m_N^2}\left[\frac{\vec{q}^2}{4m_N^2}(L_N\cdot S_N)^2+\frac{\vec{v}_T^{\perp 2}}{8}S_N^2\right],\\
(\mathscr{L}^2_{int})_{\mathscr{O}_4} &\approx S_N^2,\\
(\mathscr{L}^2_{int})_{\mathscr{O}_5} &\approx \frac{\vec{q}^2}{m_N^2}\left[\frac{\vec{q}^2}{m_N^2}(L_N)^2+\vec{v}_T^{\perp 2}K_N^2\right],\\
(\mathscr{L}^2_{int})\mathscr{O}_8 &\approx \frac{\vec{q}^2}{m_N^2}L_N^2+\vec{v}_T^{\perp 2}K_N^2,\\
(\mathscr{L}^2_{int})_{\mathscr{O}_{11}} &\approx \frac{\vec{q}^2}{m_N^2}K_N^2.
\end{aligned} \tag{12.17}$$

These approximations help to understand why the operators $\mathscr{O}_3$ and $\mathscr{O}_{11}$ lead to spectra that decrease for very low recoil energy. The reason being that their terms have a factor $\frac{\vec{q}^2}{m_N^2}$ in their expression. While $\mathscr{O}_8$ also has such a term ($\frac{\vec{q}^2}{m_N^2}L_N^2$), the dominant term is $\vec{v}_T^{\perp 2}K_N^2$ which explains why the spectrum does not decrease at low recoil energies.

In this EFT context, it is interesting to look at one of the novel interactions, i.e., the spin-orbit Φ'' or the angular momentum interactions Δ. Since most targets studied here have a non-zero response to the Δ interaction, limits on $\mathscr{O}_5$, which couples to both M and Δ, were calculated for four experiments: PICO60 loaded with C_3F_8 [73], a projection of PICO60 detector assuming the same detection efficiency and exposure but filled with CF_3I, LUX (LXe) [83] and SuperCDMS (Ge) [162].

To better understand the EFT operator $\mathscr{O}_5$, the recoil spectrum of each target of the experiments listed above is shown in Fig. 12.7 for an isoscalar coupling with contributions from the M (full line) and Δ interactions (dotted line) displayed separately. It is interesting to note that the iodine Δ response is about one order of magnitude stronger than in Xe which means that for the same exposure, Iodine should produce better limits since I and Xe have almost identical M responses.

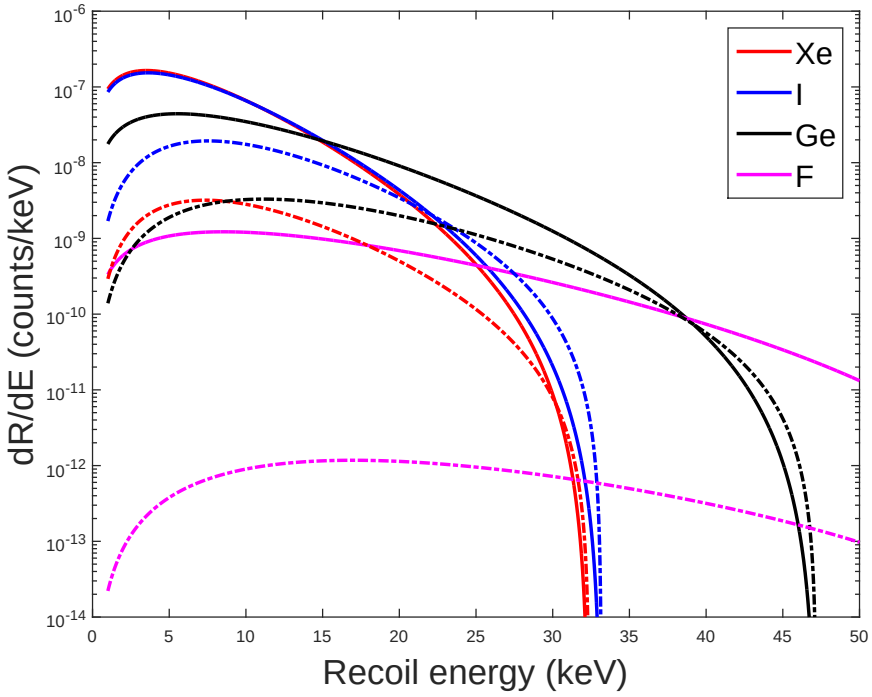

Figure 12.7 – Recoil spectrum for Xe (red), I (blue), Ge (black) and ^{19}F (magenta) for a 20 GeV/c^2 WIMP and for the EFT operator $\mathcal{O}_5$. The solid lines correspond to the M type interaction and the dotted line to Δ. The plot highlights differences in strengths of the two interactions M and Δ for the EFT operator $\mathcal{O}_5$.

The limits obtained are shown in Fig. 12.8 for the case of a pure isoscalar coupling, i.e., equal coupling to proton and neutron. Contrary to traditional limit plots, the results are plotted against $(c_5^0)^2 \cdot m_{weak}^4$, i.e., the coupling coefficients are normalized by the weak interaction mass scale $m_{weak} = (2G_F)^{(-1/2)}$ = 246.2 GeV. Therefore, if $c = 0.1$, the cross section is 1/100th of the weak interaction cross section. Fig. 12.8 shows that LUX has the best sensitivity, and is followed, in order, by PICO60-CF_3I, SuperCDMS and PICO60-C_3F_8. LUX appears to be more sensitive than the other experiments only due to its larger exposure; coupling wise, Xe does not have the highest coupling to $\mathcal{O}_5$. Looking back at Fig. 12.1, the Δ_n coupling is larger for Ge followed by Xe, while Iodine has the largest Δ_p coupling.

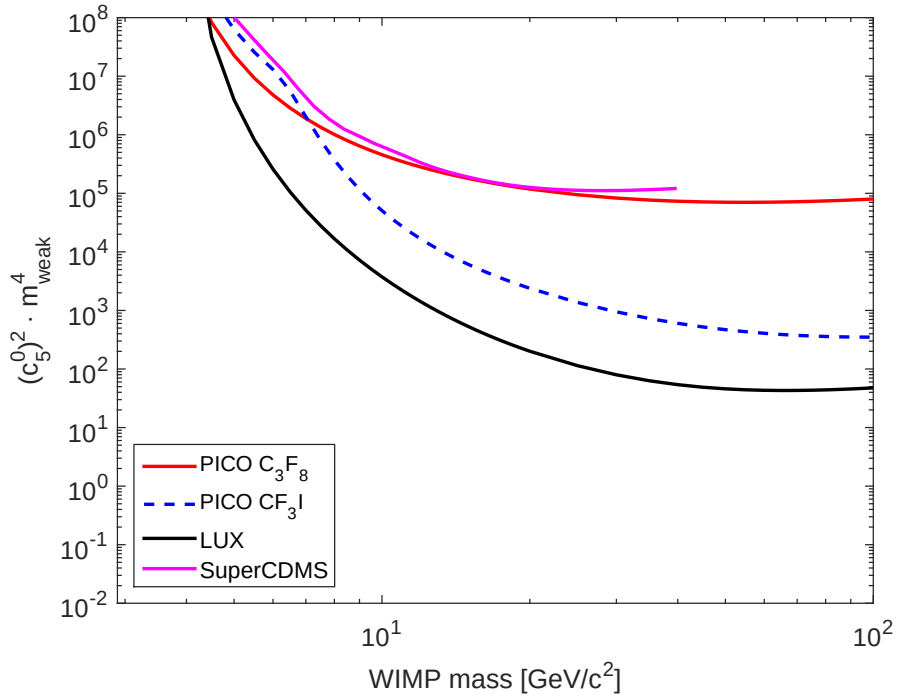

Figure 12.8 – Limit plot for an isoscalar coupling for the EFT operators $\mathcal{O}_5$ for the latest PICO 60 C_3F_8, LUX, SuperCDMS and a projected curve for a PICO 60 filled with CF_3I

12.4 Limits depending on isospin

Instead of assuming an isoscalar coupling, the combination for any given mixing angle between the couplings c^0 and c^1 can be calculated, which yields isospin limit plots very similar to the traditional a_p-a_n plots used in SD interactions, where a_p and a_n denote the respective coupling to proton and neutron, respectively. Such limits were calculated again for the $\mathcal{O}_5$ operator which couples to M and Δ interactions, and these limits are shown in Fig. 12.9.

The procedure to produce such a plot is to determine the c_5 limit for a given angle, e.g., as in Fig. 12.8 and then set $c_5^0 = c_5 \cdot \cos(\theta)$ and $c_5^1 = c_5 \cdot \sin(\theta)$. The calculation must be performed for a given value of WIMP mass. In this case, a 100 GeV/c^2 WIMP mass was used. The predicted limit for PICO60-CF_3I is more restrictive in some region

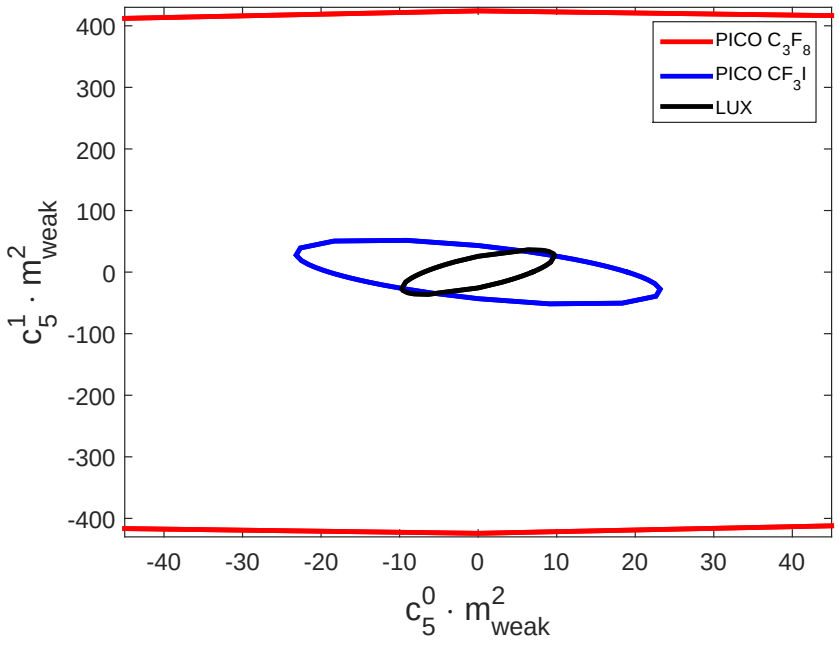

Figure 12.9 – Isospin limits for the EFT operator $\mathcal{O}_5$ for a 100 GeV/c^2 WIMP for PICO 60 C_3F_8 (red), LUX (black) and a projected curve for a PICO 60 filled with CF_3I (blue). The limits are obtained by determining $c_5^0 = c_5 \cdot cos(\theta)$ and $c_5^1 = c_5 \cdot sin(\theta)$ as a function of c_5 and θ.

than for LUX due to its stronger proton coupling, despite having a much lower exposure.

Recalling that a pure proton is obtained for $c^0 = c^1$ and pure neutron coupling for $c^0 = -c^1$, the orientation of the ellipse is explained by the fact that Xe has a higher coupling to neutrons than to protons, while for iodine the opposite applies. Both experiments are therefore complementary to each other.

12.4.1 Interference matrix

Rather than carrying out the full calculation of the isospin limit to infer the complementary of targets for individual EFT operators, the orientation of the destructive and constructive interference vectors for any EFT operator can be calculated directly. The orientation of the destructive (constructive) interference vector is given by the angle that yields the worst (best) limit. In order to calculate those orientations, one must calculate

the isospin interference matrix:

$$\begin{bmatrix} R_i^{00} & R_i^{01} \\ R_i^{10} & R_i^{11} \end{bmatrix}, \tag{12.18}$$

where $R^{\tau\tau'}$ is the observed rate for a given experiment for pure proton couplings R^{00}, neutron couplings R^{11}, isoscalar R^{10}, and isovector R^{10}, for a given WIMP mass, and for a given EFT operator i. The lowest (highest) eigenvalue corresponds to the destructive (constructive) vector. Using this method, the constructive vectors of each experiments shown in Fig. 12.8 as well as the for Si, Na and Ge targets were added to Fig. 12.9 as shown in Fig. 12.10.

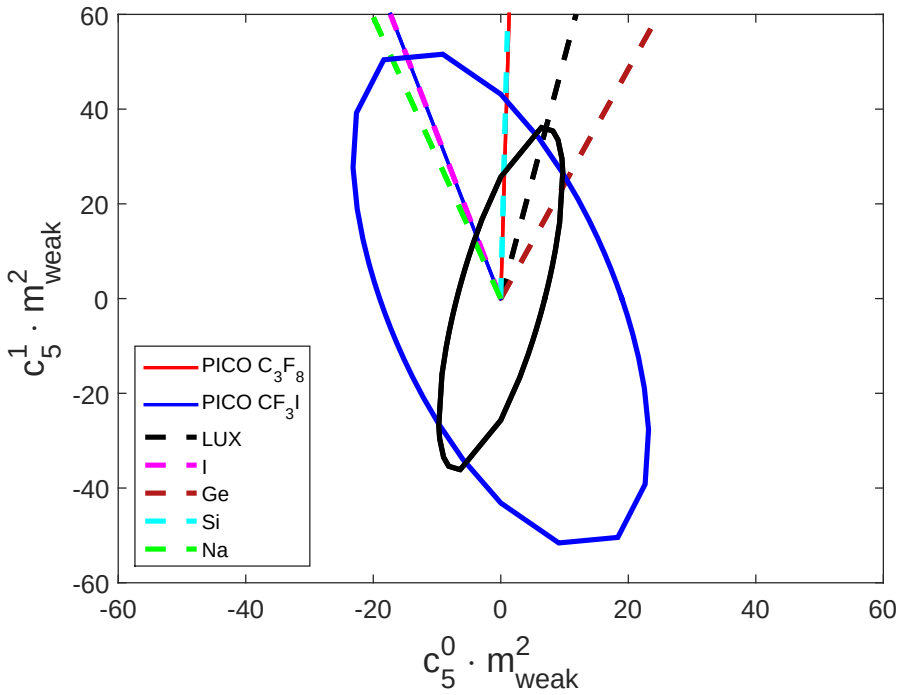

Figure 12.10 – Destructive interference vector for PICO 60 C_3F_8 (red), LUX (dotted black), hypothetical PICO 60 CF_3I (dotted blue), Iodine (dotted pink), Ge (dotted brown), Si (dotted teal), Na (dotted green), along with the isospin limit for LUX (black) and hypothetical PICO 60 CF_3I (blue). Iodine and CF_3I have the same vector because fluorine response is much lower than iodine (see Fig. 12.7)

This approach gets even more complex if interferences between EFT operators are also taken into account. Similarly to the isospin interference matrix, a 4x4 EFT operator interference matrix can be constructed to calculate obtain the eigenvalues and eigenvectors.

Eq. 12.11 has two interfering interactions (red terms), $\Delta\Sigma'$ and $\Phi'' M$, and they can significantly decrease the predicted rate in dark matter detectors which adds more complexity to fold in all these contributions. Thus while exploring them is instructive, it will be much more important to carry out this type of analysis once a WIMP signal is discovered.

12.5 EFT outlook and summary

The initial goal of this work was to study the relevance of a ^{19}F target in this theoretical framework. Despite the fact that ^{19}F favors largely SD-p interaction, such a target would be very useful when dark matter will be discovered. A priori, dark matter could have a coupling to SD and SI interactions or any of the other types of interactions in the framework of EFT. It is therefore desirable to measure all possible WIMP-nucleon couplings, and consequently, detectors using different targets are needed. In this context, an experiment with a ^{19}F target is optimal since it is the best way to measure SD couplings in the proton sector. Also, applying two different detector technologies using the same target would also be desirable in order to make sure that no systematic effects produce a false signal in one of the detector technology. Following this line of reasoning, there are currently several Xe and Ar detectors, as well as NaI crystal detectors, but there is only one type of detector that uses ^{19}F as an active target for dark matter searches.

The current list of targets planned for tonne-scale experiments that will search for WIMP masses higher than 10 GeV/c^2 is relatively short: F, Xe, Ar. The future SuperCDMS experiment, which uses Ge, cannot be added to this list since it will only contain $\sim$10 kg of Ge and Si and won't probe any cross sections not already explored by Xe or

Ar based experiments. With these 3 targets, the SD-p interaction is covered by F, while Ar is only sensitive to SI (paired number of protons and neutrons), and Xe is the most sensitive target to SI, SD-n, spin-orbit proton (SO-p), and spin-orbit neutron (SO-n) interactions. Consequently, if a Xe based experiment measures a WIMP signal, but no signal appears in F and Ar experiments, there is still an ambiguity concerning the nature of the interaction as it could be due to the SD-n, SO-p or SO-n interactions. If there is no isospin asymmetry, then SD-n can be eliminated as well, otherwise, a target strictly sensitive to SD-n interactions would be required such as ^{3}He. Finally, Ge being sensitive to the same interaction as Xe but with smaller coupling strengths could be used to confirm a signal seen by Xe, but would not add any information regarding the nature of the interaction.

To conclude, the EFT approach has the advantage of describing the complete set of WIMP-nucleus interactions while also allowing the calculation of limits on individual EFT operators and to produce isospin dependent limits. It also enables comparisons between direct detection experiments and highlights their complementarity. Unfortunately, due to the 24 free parameters and EFT operator interferences, the theoretical phase space is vast. This approach becomes useful once a discovery will be claimed since then it will allow the dark matter community to check whether or not a claim is already excluded by other experiments for one type of the possible interactions. Another critique of this approach is the lack of constraints regarding the 24 free parameters c_i. For example, a spin-orbit coupling much larger than a spin-independent coupling might be allowed by the EFT model, however, such a scenario would be unnatural from a physics point of view. Therefore, simplified dark matter models can sometimes be more useful since they already include physical constraints, but, on the other hand, they will be more restrictive than the EFT approach.

CHAPTER 13

R&D, OUTLOOK AND FUTURE PROSPECTS IN PICO

When the construction of PICO40L will be complete, the majority of the collaboration efforts will turn onto the development of the PICO500 design and its construction. In the meantime, GEANT4 simulations of the detector can be set up in order to predict the neutron and gamma background. The collaboration is also studying the possibility of using $C_2H_2F_4$ as an active liquid which would improve low mass WIMP sensitivity, and for establishing its feasibility, the UdeM group has filled PICO 0.1 with this freon. Another development that is ramping up within the collaboration concerns the development of a LAr scintillating bubble chamber. As of now, a LXe scintillating bubble chamber has been constructed, and the results of the first calibration measurements were recently published [163] . PICO500, due to its large mass, also opens up the possibility of detecting supernova neutrinos via elastic scattering. The capabilities for detecting supernova neutrinos were explored in details by the PICO Alberta group, and publishing recently [164].

13.1 PICO500

The PICO collaboration is currently working on the conceptual design of the PICO500. The first design sketch is shown in Fig. 13.1. The PV would be transported through the mine shaft in three parts that would be merged underground with two flanges, and the vessel would be suspended from the top of a platform. Essentially, the detector would be an RSU version of a PICO detector, similar to PICO40L. One modification consists of placing the accumulators outside of the PV instead of underneath the detector to increase space and accessibility under the detector. The thermal stability of PICO40L will also provide useful information regarding the corresponding design of PICO500.

The active volume will be enclosed by two quartz jars, but their diameter and espe-

cially their height are increased to contain at least 500 liters of freon. Consequently, their increased height will force the piezoelectric sensors to be farther away from the active liquid, and thus their sensitivity as a function of distance needs to be restudied to make sure that full alpha-neutron discrimination is maintained. Furthermore, there are more serious constraints on the tolerable neutron background for this detector which will, e.g., increase the minimum distance between the active freon and the (slightly radioactive) piezoelectric sensors. This problem among others will be investigated with GEANT4 simulations.

The possibility of increasing the amount of active liquid beyond 500 liters depends on the sizes of the quartz vessels and the PV, respectively, which are currently not yet determined. The currently projected sensitivity of PICO500 was shown in Fig. 12.5.

Figure 13.1 – Right: PICO500 detector inside the pressure vessel. Left: PICO500 detector design at SNOLAB inside the water tank and suspended from a platform.

13.2 Search for low WIMP masses with $C_2H_2F_4$

In the recent past, the PICO collaboration has been operating its detectors mostly with C_3F_8. The main reason for using this freon is the presence of fluorine which provides an important coupling to the SDp interaction as discussed in Sect. 4.2. $C_2H_2F_4$ (R134a) has similar WIMP couplings, but the presence of hydrogen would allow the detector to be sensitive to lower WIMP masses, while even increasing the SD proton coupling since hydrogen has a higher SDp coupling than ^{19}F. Its different thermodynamic parameters would require to run the detector at 30°C rather than 15°C which would still be in the operating range of, e.g., PICO40L. The current goal of the PICO collaboration is to test the new PICO40L design as soon as possible in order to be ready for the deployment of PICO500. In the future, when PICO500 will be running, PICO40L could then be filled with $C_2H_2F_4$. While there are no strong arguments suggesting models favoring low WIMP masses (0.1-10 GeV) over theories proposing high WIMP masses (10 GeV - 1 TeV), certain recent models, such as asymmetric dark matter [49], favor low mass WIMPs. In addition to an increased sensitivity to low mass WIMPs due to the H in the target, the current knowledge regarding gamma sensitivity of SHL suggests that target fluids of low atomic mass have lower gamma sensitivity due to the presence of fewer electrons. This means that a detector filled with $C_2H_2F_4$ could be operated at lower energy thresholds with respect to C_3F_8 which would increase the sensitivity to low mass WIMPs even further.

The PICO UdeM group started characterizing $C_2H_2F_4$ with the goal of performing the same neutron calibrations that were done with PICO 0.1 when it was filled with C_3F_8. As of now, calibrations were performed with a 22 keV neutron SbBe source and the count rates are shown in Fig. 13.2. In five measurements at fixed temperatures, the energy thresholds were scanned from $\sim$4 keV up to 40 keV. The lowest threshold was limited by the operating pressure which cannot be lower than 25 PSIA without compromising the detector stability. For pressures below 25 PSIA, the pressure system has difficulty in maintaining a constant pressure. Hence, the energy threshold cannot be low-

ered further by reducing the pressure, so the temperature has to be increased instead.

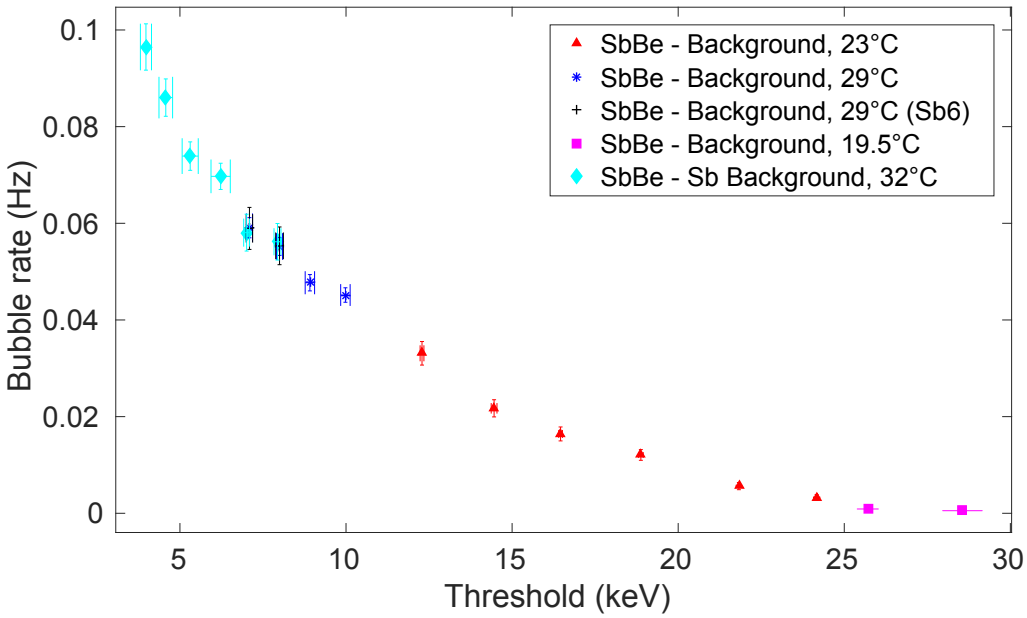

Figure 13.2 – SbBe 22 keV neutron calibration with PICO 0.1 chamber filled with $C_2H_2F_4$. Several data set were taken at different temperatures to cover a wide range of energy thresholds. Above ∼6 keV, only the elastic neutron scattering of hydrogen atoms can transfer enough energy to produce bubbles.

The obtained rate curve is smoothly rising with decreasing energy threshold which corresponds to the expected behavior. A measurable count rate above background appears at ∼22 keV which is due to the maximum recoil energy obtained for neutron-proton elastic scattering. Bubble events due to fluorine and carbon recoils occur at a maximum energy of ∼6 keV and ∼4 keV respectively and thus the 19.5°C, 23°C and 29°C datasets only contain proton recoils. These measurements proved for the first time the feasibility of hydrogen loaded fluid for dark matter searches.

Another interesting characteristic, which remains to be investigating, is the gamma sensitivity of $C_2H_2F_4$. Here the goal is to carry out gamma calibrations similar to the ones summarized in Fig. 8.28, and to verify that the gamma sensitivity is indeed lower

than in C_3F_8 as expected. Moreover, in the near future, PICO 0.1 will be brought back to the UdeM Tandem accelerator where monoenergetic neutrons will be used to complete the neutron calibration of this target fluid.

As an example, for the increased sensitivity to low WIMP masses, Fig. 13.3 shows a comparison between the limits obtained with PICO60 fill with C_3F_8 and $C_2H_2F_4$, respectively, assuming 1 keV and 2 keV threshold, an exposure of 1167 kg-day and 0 background events.

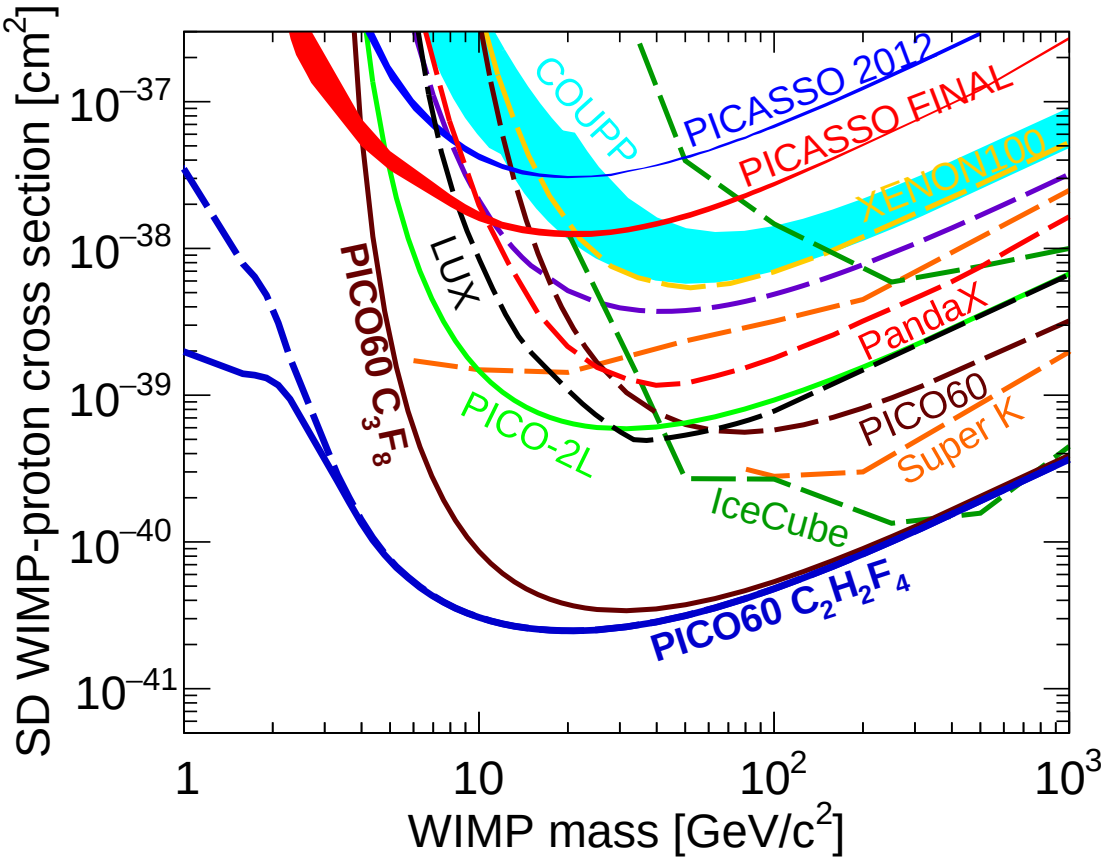

Figure 13.3 – PICO60 projected limit if filled with $C_2H_2F_4$ with an exposure of 1167 kg-day with no background events. The plain line and dotted line are for 1 and 2 keV energy threshold respectively.

13.3 LAr/LXe Scintillating Bubble chambers (SBC)

In the near future, the PICO collaboration plans to build a cryogenic bubble chamber filled with noble liquids such as LAr and LXe. An added advantage of the use of noble liquids is the possibility to observe scintillation photons. In the pioneering bubble experiment in 1958, Glaser observed no gamma-induced bubbles in pure LXe at a 1 keV threshold [165]. Bubble formation reappeared after quenching the scintillation with 2% ethylene. This historic observation led to the expectation that in LAr/LXe, sub-keV nuclear recoil detection might be possible without sensitivity to gammas. As of now, a prototype chamber containing LXe was built and operated at NorthWestern University. A schematic diagram of the detector is presented in Fig. 13.4.

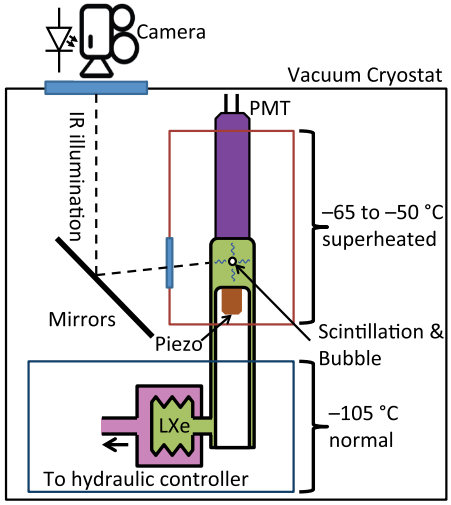

Figure 13.4 – Detector schematic of the LXe scintillation bubble chamber at NorthWestern University [163].

This detector is a cryogenic RSU PICO bubble chamber with the addition of a single PMT to measure the scintillation light. A calibration with a ^{57}Co source that produces 122 keV gamma rays was performed and published in [163]. In this measurement, scintillation light was observed as expected, but no evidence for gamma-induced bubble nucleation. Thus, a 90% C.L. upper limit of 6.3×10^{-7} on the bubble nucleation efficiency at a threshold of 4.2 keV could be placed. In striking contrast to the gamma

measurement, the exposure to neutrons from a calibration source showed scintillation in coincidence with bubble nucleation from nuclear recoils. For comparison, a gamma sensitivity of 6×10^{-6} was measured in CF_3I with PICO60 at the same energy threshold. The fact that the gamma sensitivity of a LXe operated bubble chamber is one order of magnitude lower than in CF_3I supports the hypothesis that the production of scintillation light reduces the heat available for bubble nucleation.

A subgroup of the PICO collaboration proposes to construct at 10 kg LAr bubble chamber at FermiLab. If the LAr bubble chamber shows the same reduced level of gamma sensitivity as of the LXe bubble chamber prototype, it could enable PICO to become also a leading experiment in the SI sector, and in particular to extend the sensitivity to sub-keV nuclear recoil detection and sub-GeV WIMP masses. Projected sensitivities in the SI sector with an argon SBC running at a 0.1 keV energy threshold for 5 kg-year and 1 ton-year are shown in Fig. 13.5. In the future, a similar detector could also be used to detect reactor neutrino via CEνNS similarly to the COHERENT experiment [166].

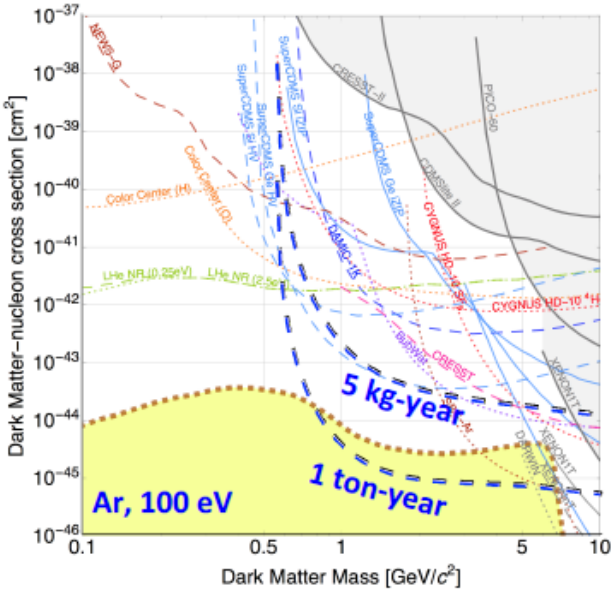

Figure 13.5 – LAr scintillation bubble chamber. Sensitivity in the SI sector assuming a 0.1 keV energy threshold for 5 kg-year and 1 ton-year along with current limits (grey) and other projected limits such as NEWS-G, CRESST, DAMIC and SuperCDMS.

13.4 Supernova detection with PICO500

The most important limitation for the next generation of direct dark matter experiments is the irreducible neutrino floor due to coherent scattering by atmospheric and solar neutrinos. By the same mechanism, dark matter detectors should also be sensitive to supernovae (SN) neutrinos. Consequently, a study of the possibility to detect SN neutrinos burst with PICO500 was carried out by the PICO Alberta group. The imprint of a SN neutrinos burst in a PICO detector would be a rapid sequence of bubble events within a time window of several seconds. In order to quantify the event structure, the number k of expected bubbles after the SN neutrino burst post-bounce time was calculated using the most recent SN models. Fig. 13.6 [164] shows the number of bubbles, $N_{CE\nu NS}$, as a function of post-bounce time for a SN at 10 kpc for different target liquids and a detector volume of 725 liters. Apparently, a detector lifetime interval of at least 2 seconds is required to observe at least two bubbles in a burst. While it was shown experimentally that C_3F_8 bubble chamber could be kept live for 2.5 s at a 2 keV threshold, this was not measured experimentally for LAr, LXe and CF_3I. Hence a conservative 10 keV threshold is applied for these liquids.

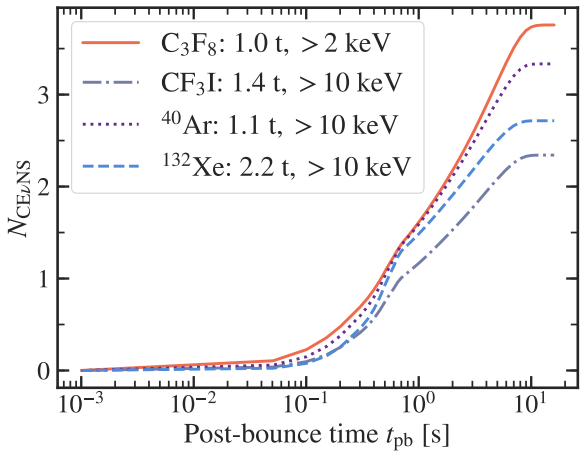

Figure 13.6 – Number of supernova neutrino events as a function of post-bounce time for a 725 liters bubble chamber filled with C_3F_8, CF_3I, Ar and Xe with their respective energy threshold.

CHAPTER 14

CONCLUSION

Despite the lack of any hints of dark matter observed with the ongoing experiments, it is an exciting time for direct dark matter detection considering that the first tonne-scale experiments are now taking data, while others are ramping up to the building or planning phase. These detectors will be able to probe cross sections at least two orders of magnitude smaller than the current best experiments while also reaching the neutrino floor for the first time. To this day, direct dark matter detectors have concentrated their efforts mostly on probing WIMP masses between $\sim 10\,\mathrm{GeV/c^2} - 1\,\mathrm{TeV/c^2}$, while fewer efforts were spent on WIMP searches at lower masses mostly due to theoretical biased towards higher WIMP masses by various models such as the MSSM, but also due to the increased difficulty of detecting recoils depositing less than 1 keV. The main experiments like LUX, XENON, etc., searching for high mass WIMPs are now established and are building tonne scale detectors, but it is only recently that experiments sensitive to low WIMP masses started deploying detectors containing a few kgs of active mass. Moreover, the neutrino floor is fast-approaching, and consequently, directional dark matter detectors might turn out to be the only viable method to discover dark matter.

The quest for dark matter is currently one of the most important global efforts in physics and one of the most active. The PICASSO collaboration has been part of this effort since 1994 and has held the world best SDp cross section limit until it merged with the COUPP collaboration to form the present PICO collaboration. The last PICASSO result has utilized its experimental setup in the most optimal way by introducing a fiducial volume cut obtained using acoustic 3D position reconstruction and by reaching a 1 keV energy threshold. To this day, this PICASSO result still holds the best SD cross section limits for WIMP masses below 5 $\mathrm{GeV/c^2}$, while PICO holds the world best SD cross section limit for any other WIMP masses and will continue to do so with the upcoming PICO40L and PICO500 detectors. Moreover, a future LAr bubble chamber, as well as

the possible use of $C_2H_2F_4$ will extend the physic reach of PICO towards lower mass WIMPs in the SI and SD sector, respectively. These new detectors might also broaden the scope of the experiment to new applications such as reactor neutrino and supernova neutrino searches.

The SHL detector technique for dark matter searches continues to improve especially regarding the understanding of the characteristics of the various types of backgrounds, of the bubble nucleation mechanism and of the WIMP detection efficiency at low energy thresholds. PICO40L is the first detector to implement detector design changes by using the knowledge acquired with PICO2L and PICO60 such as increased cleanliness requirements, improved material screenings, and, most noteworthy, the implementation of the RSU design to eliminate the water-particulate background. Another significant change is the increased size of the pressure vessel of PICO40L compared to PICO60 which will reduce the neutron background due to internal contamination by a factor of about $\sim$50. Furthermore, PICO40L will inform on the next crucial changes to meet the even more stringent background criteria PICO500.

One of the fundamental aspects of detecting dark matter is the complementary between direct detection, indirect detection and production of dark matter due to their different sensitivity to various WIMP and mediator masses. Moreover, the complementary between different targets used for direct detection is also crucial due to their unique coupling to the various possible types of WIMP-nucleon interactions, as it has been highlighted by the Effective Field Theory models of dark matter. In this theoretical context, by using a fluorinated target, PICO still remains the only experiment that is strictly sensitive to the SD proton sector and hence will continue to play a significant role in the collective search efforts to determine the nature of the dark matter.

BIBLIOGRAPHY

[1] E. Behnke et al., Astroparticle Physics 90 (2017) 85 – 92.

[2] C. Amole et al., Phys. Rev. D 100 (2019) 022001.

[3] N. Aghanim et al., arXiv (2018).

[4] F. Zwicky, Helvetica Physica Acta 6 (1933) 110–127.

[5] G. Bertone and D. Hooper, Rev. Mod. Phys. 90 (2018) 045002.

[6] C. CSÁKI, Modern Physics Letters A 11 (1996) 08 599–613.

[7] F. Zwicky, Astrophys. J. (1937) 86–217.

[8] V. C. Rubin and W. K. J. Ford, Astrophys. J. 159 (1970) 379–403.

[9] H. Ohanian and R. Ruffin, Gravitation and spacetime, Norton (1994).

[10] N. S. F. C. NASA/ESA Hubble Space Telescope, Gravitational lensing, https://svs.gsfc.nasa.gov/Gallery/HubbleSpaceTelescope.html (2019).

[11] D. Clowe et al., Astrophys. J. 648 (2006) 109–113.

[12] D. J. Fixsen, The Astrophysical Journal 707 (2009) 2 916–920.

[13] P. A. R. Ade et al., Planck 2013 results. I. Overview of products and scientific results (2013).

[14] E. Gawiser and J. Silk, Physics Reports 333-334 (2000) 4-6 245–267.

[15] G. Hinshaw et al., The Astrophysical Journal Supplement Series 208 (2013) 2 19.

[16] M. Tanabashi et al., Phys. Rev. D 98 (2018) 030001.

[17] Planck Collaboration, http://www.esa.int/spaceinimages/Images/2013/03/, PLANCK COSMIC RECIPE (2013).

[18] J. Beringer et al., The review of particle physics (2012).

[19] R. H. Cyburt, B. D. Fields and K. A. Olive, Phys. Lett. B 567 (2003) 227–234.

[20] B. D. Fields, Annual Review of Nuclear and Particle Science 61 (2011) 1 47–68.

[21] G. Jungman, M. Kamionkowski and K. Griest, Physics Reports 267 (1996) 5 195 – 373.

[22] E. W. Kolb and M. S. Turner, Front. Phys. 69 (1990) 1–547.

[23] J. R. Pritchard and A. Loeb, Reports on Progress in Physics 75 (2012) 8 086901.

[24] J. D. Bowman et al., Nature 555 (2018) 7694 67–70.

[25] G. B. Field, Proceedings of the IRE 46 (1958) 1 240–250.

[26] A. Cohen et al., Monthly Notices of the Royal Astronomical Society 472 (2017) 2 1915–1931.

[27] D. C. Price et al., Monthly Notices of the Royal Astronomical Society 478 (2018) 3 4193–4213.

[28] J. B. Peterson et al., Proceedings, 49th Rencontres de Moriond on Cosmology: La Thuile, Italy, March 15-22, 2014, 129–134 (2014).

[29] L. Philip et al., ArXiv e-prints (2018) arXiv:1806.09531.

[30] N. Patra et al., Experimental Astronomy 36 (2013) 1 319–370.

[31] R. Barkana et al., Phys. Rev. D 98 (2018) 103005.

[32] G. D'Amico, P. Panci and A. Strumia, Phys. Rev. Lett. 121 (2018) 011103.

[33] D. P. BENNETT et al., Annals of the New York Academy of Sciences 688 (1993) 1 612–618.

[34] Tisserand, P. et al., A&A 469 (2007) 2 387–404.

[35] G. Servant, Phys. Rev. Lett. 113 (2014) 171803.

[36] C. A. Baker et al., Phys. Rev. Lett. 97 (2006) 131801.

[37] J. E. Kim, Phys. Rev. Lett. 43 (1979) 103–107.

[38] M. Shifman, A. Vainshtein and V. Zakharov, Nuclear Physics B 166 (1980) 3 493 – 506.

[39] M. Dine, W. Fischler and M. Srednicki, Physics Letters B 104 (1981) 3 199 – 202.

[40] A. R. Zhitnitsky, Sov. J. Nucl. Phys. 31 (1980) 260, [Yad. Fiz.31,497(1980)].

[41] I. P. Stern, ADMX and A.-H. collaborations, AIP Conference Proceedings 1604 (2014) 1 456–461.

[42] N. Du et al., Phys. Rev. Lett. 120 (2018) 151301.

[43] L. Zhong et al., Phys. Rev. D 97 (2018) 092001.

[44] J. D. Bekenstein and R. H. Sanders, A primer to relativistic MOND theory (2005).

[45] G. W. Angus et al., The Astrophysical Journal 654 (2006) 1 L13–L16.

[46] P. F. de Salas and S. Pastor, JCAP 1607 (2016) 07 051.

[47] P. C. Divari and J. D. Vergados, Adv. High Energy Phys. 2018 (2018) 1479313.

[48] G. L. Kane and M. A. Shifman, arxiv (2001).

[49] K. PETRAKI and R. R. VOLKAS, International Journal of Modern Physics A 28 (2013) 19 1330028.

[50] J. D. Lewin and P. F. Smith, Astropart. Phys. 6 (1996) 87–112.

[51] S. University, Sheffield DRIFT-CYGNUS Group Dark matter research, https://www.hep.shef.ac.uk/research/dm/drift.php (2012).

[52] A. Kurylov and M. Kamionkowski, Phys. Rev. D 69 (2004) 063503.

[53] Y.-Z. Chen et al., Commun. Theor. Phys. 55 (2011) 1059–1064.

[54] D. R. Tovey et al., Phys.Lett. B 488 (2000) 17–26.

[55] P. Cushman et al., Community Summer Study 2013: Snowmass on the Mississippi (CSS2013) Minneapolis, MN, USA, July 29-August 6, 2013 (2013).

[56] P. Agnes et al., Phys. Rev. Lett. 121 (2018) 081307.

[57] P.-A. Amaudruz et al., Phys. Rev. Lett. 121 (2018) 071801.

[58] E. Aprile et al., Phys. Rev. Lett. 109 (2012) 181301.

[59] M. Szydagis et al., 10th International Symposium on Cosmology and Particle Astrophysics (CosPA 2013) Honolulu, Hawaii, USA, November 12-15, 2013 (2014).

[60] P. Agnes et al., Phys. Rev. Lett. 121 (2018) 081307.

[61] E. Armengaud et al., Journal of Instrumentation 12 (2017) 08 P08010–P08010.

[62] R. Agnese et al., Phys. Rev. D92 (2015) 7 072003.

[63] G. Angloher et al., Eur. Phys. J. C76 (2016) 1 25.

[64] CDMS Collaboration, Science 327 (2010) 1619–1621.

[65] R. Agnese et al., Phys. Rev. Lett. 121 (2018) 051301.

[66] A. Antonicci et al., Eur. Phys. J. C77 (2017) 11 752.

[67] S. Archambault et al., Phys. Lett. B 711 (2012) 153.

[68] E. Behnke et al., Phys. Rev. D 86 (2012) 052001.

[69] M. Felizardo et al., Phys. Rev. D 89 (2014) 7 072013.

[70] C. Amole et al., Phys. Rev. D 93 (2016) 061101.

[71] H. Jiang et al., Phys. Rev. Lett. 120 (2018) 241301.

[72] C. Amole et al., Phys. Rev. D (2015).

[73] C. Amole et al., Phys. Rev. Lett. 118 (2017) 25 251301.

[74] R. Agnese et al., Phys. Rev. Lett. 112 (2014) 241302.

[75] X. Cui et al., Phys. Rev. Lett. 119 (2017) 181302.

[76] D. S. Akerib et al., Phys. Rev. Lett. 118 (2017) 2 021303.

[77] E. Aprile et al., Phys. Rev. Lett. 121 (2018) 111302.

[78] R. Bernabei et al., Eur. Phys. J. C 56 (2008) 333–355.

[79] C. E. Aalseth et al., Phys. Rev. D 88 (2013) 012002.

[80] R. Agnese et al., Phys. Rev. Lett. 111 (2013) 251301.

[81] E. Aprile et al., Phys. Rev. D 94 (2016) 122001.

[82] C. Fu et al., Phys. Rev. Lett. 118 (2017) 071301.

[83] D. S. Akerib et al., Phys. Rev. Lett. 118 (2017) 251302.

[84] M. G. Aartsen et al., Phys. Rev. Lett. 110 (2013) 13 131302.

[85] T. Tanaka et al., Astrophys. J. 742 (2011) 78.

[86] L. Evans and P. Bryant, Journal of Instrumentation 3 (2008) 08 S08001–S08001.

[87] T. A. Collaboration et al., Journal of Instrumentation 3 (2008) 08 S08003–S08003.

[88] E. Focardi, Physics Procedia 37 (2012) 119 – 127, proceedings of the 2nd International Conference on Technology and Instrumentation in Particle Physics (TIPP 2011).

[89] ATLAS Collaboration, Eur. Phys. J. C 75 (2015) 299.

[90] O. Buchmueller, M. J. Dolan and C. McCabe, JHEP 01 (2014) 025.

[91] O. Buchmueller, M. J. Dolan and C. McCabe, Journal of High Energy Physics 2014 (2014) 1 25.

[92] K. Griestd, G. Jungmana and M. Kamionkowskib, Physics Report 267 (1996) 195–373.

[93] M. G. Aartsen and J. P. Yanez, The European Physical Journal C 77 (2017) 3 146.

[94] S. Adrian-Martinez et al., JCAP 1311 (2013) 032.

[95] D. A. Glaser, Phys. Rev. 87 (1952) 665–665.

[96] L. Bettelli, M. Bianchi-Streit and G. Giacomelli (1993).

[97] D. Haidt and A. Pullia, Riv. Nuovo Cim. 36 (2013) 08 335–395.

[98] S. Archambault et al., New J. Phys. 13 (2011) 043006.

[99] D. Baxter, Eliminating Backgrounds in the Search for Dark Matter with the PICO-60 Bubble Chamber, Ph.D. Thesis, NORTHWESTERN UNIVERSITY (2018).

[100] i. R. P. S. B C. Peyrou, Bubbles and Spark Chambers, Academic Press, New York (1967) pp. 19–58.

[101] F. Seitz, The Physics of Fluids 1 (1958) 1 2–13.

[102] N. I. for Standards et Technology, http ://webbook.nist.gov/.

[103] L. R. O. F.R.S., The London, Edinburgh, and Dublin Philosophical Magazine and Journal of Science 34 (1917) 200 94–98.

[104] M. S. Plesset and S. A. Zwick, Journal of Applied Physics 25 (1954) 4 493–500.

[105] A. J. Robinson and R. L. Judd, Heat MassTrans 47 5101 (2004).

[106] Y. N. Martynyuk and N. S. Smirnova, 1991 Sov. Phys. Acoust 37 76 (1991).

[107] A. Robinson, R. Judd and F. Lesage, Computational Thermal Sciences 2 (2010) 19–31.

[108] S. Archambault et al., New Journal of Physics 13 (2011) 4 043006.

[109] R. E. Apfel and F. D'Errico, Nucl. Instrum. Methods Phys. Res A 476 (2002) 298–303.

[110] F. Aubin, Caractérisation spatiale des évènements dans les détecteurs PICASSO, Mémoire de maîtrise, Département de physique, Faculté des arts et sciences, Université de Montréal (2007).

[111] A. Bellerive et al., Nuclear Physics B 908 (2016) 30 – 51, neutrino Oscillations: Celebrating the Nobel Prize in Physics 2015.

[112] D.-M. Mei and A. Hime, Phys. Rev. D 73 (2006) 053004.

[113] B. Aharmim et al., Phys. Rev. D 80 (2009) 012001.

[114] W. Davidson et al., SNO Collaboration Internal Report .

[115] https://www.dytran.com/ (1980).

[116] Nuclear Instruments and Methods in Physics Research Section A: Accelerators, Spectrometers, Detectors and Associated Equipment 506 (2003) 3 250 – 303.

[117] A. E. Robinson, Phys.Rev. C 89 (2014) 3 032801.

[118] J. Ziegleri, http ://www.srim.org/.

[119] R. V. D. Graaff, Nucl. Instrum. Methods 8 (1960) 2 195 – 202.

[120] Encyclopaedia Britannica, Tandem accelerator, https://www.britannica.com/technology/tandem-accelerator (2008).

[121] J. H. Gibbons, R. L. Macklin and H. W. Schmitt, Phys. Rev. 100 (1955) 167–168.

[122] J. Hunt, Nuclear Instruments and Methods in Physics Research 201 (1982) 2 533 – 534.

[123] S. A. Pozzi, E. Padovani and M. Marseguerra, Nucl. Instrum. Methods in Physics Research Section A: Accelerators, Spectrometers, Detectors and Associated Equipment 513 (2003) 3 550 – 558.

[124] C. D. Nesaraja, Nuclear Data Sheets 130 (2015) 183–252.

[125] International Atomic Energy Agencyy, Services Series, INTERNATIONAL ATOMIC ENERGY AGENCY, Vienna (2019).

[126] J. Billard, E. Figueroa-Feliciano and L. Strigari, Phys. Rev. D 89 (2014) 023524.

[127] C. A. J. O'Hare, Phys. Rev. D 94 (2016) 063527.

[128] J. Battat et al., Journal of Instrumentation 12 (2017) 10 P10009.

[129] Q. Riffard et al., Journal of Instrumentation 12 (2017) 06 P06021.

[130] T. Hashimoto et al., AIP Conference Proceedings 1921 (2018) 1 070001.

[131] N. Agafonova et al., The European Physical Journal C 78 (2018) 7 578.

[132] F. Mayet et al., Physics Reports 627 (2016) 1 – 49, a review of the discovery reach of directional Dark Matter detection.

[133] S. Archambault et al., Physics Letters B 682 (2009) 2 185 – 192.

[134] G. J. Feldman and R. D. Cousins, Phys. Rev. D 57 (1998) 3873–3889.

[135] F. James, CERN-D-506 (1994).

[136] E. Behnke et al., Phys. Rev. D 90 (2014) 079902.

[137] R. Agnese et al., Phys. Rev. Lett. 116 (2016) 7 071301.

[138] D. S. Akerib et al., Phys. Rev. Lett. 116 (2016) 16 161302.

[139] E. Aprile et al., Phys. Rev. D 94 (2016) 122001.

[140] M. G. Aartsen et al., Phys. Rev. Lett. 110 (2013) 131302.

[141] T. Tanaka et al., Astrophys. J. 742 (2011) 2 78.

[142] K. Choi et al., Phys. Rev. Lett. 114 (2015) 141301.

[143] S. Demidov and O. Suvorova, JCAP 1006 (2010) 018.

[144] A. D. Avrorin et al., Astropart. Phys. 62 (2015) 12–20.

[145] V. Khachatryan et al., Eur. Phys. J. C75 (2015) 5 235.

[146] G. Aad et al., Eur. Phys. J. C75 (2015) 7 299.

[147] L. Roszkowski, R. Ruiz de Austri and R. Trotta, JHEP 07 (2007) 075.

[148] S. Adrián-Martínez et al., Journal of Cosmology and Astroparticle Physics 2016 (2016).

[149] S. Adrián-Martínez et al., Physics Letters B 759 (2016).

[150] R. Agnese et al., Phys. Rev. Lett. 116 (2016) 071301.

[151] E. Collaboration", Astropart. Phys. 47 (2013) 1–9.

[152] D. Große et al., Fusion Engineering and Design 88 (2013) 9 2210 – 2214, proceedings of the 27th Symposium On Fusion Technology (SOFT-27); Liège, Belgium, September 24-28, 2012.

[153] K. Li et al., Nucl. Instrum. Methods in Physics Research Section A: Accelerators, Spectrometers, Detectors and Associated Equipment 908 (2018) 43 – 48.

[154] C. M. Poole et al., Australasian Physical & Engineering Sciences in Medicine 35 (2012) 3 329–334.

[155] W. B. Wilson et al. (Jan 2002) 127, lA-UR–02-1839.

[156] D. Gayer et al., Proc.SPIE 9914 (2016) 9914 – 9914 – 14.

[157] F. Fulkerson, SolidWorks Basics: A Project Based Approach, Industrial Press, Inc., New York, NY, USA (2015).

[158] A. L. Fitzpatrick et al., JCAP 1302 (2013) 004.

[159] A. L. Fitzpatrick et al., arXiv (2012).

[160] N. Anand, A. L. Fitzpatrick and W. C. Haxton, Phys. Rev. C 89 (2014) 065501.

[161] R. Thieberger, Nuclear Physics 2 (1956) 5 533 – 547.

[162] K. Schneck et al., Phys. Rev. D 91 (2015) 092004.

[163] D. Baxter et al., Phys. Rev. Lett. 118 (2017) 231301.

[164] T. Kozynets, S. Fallows and C. B. Krauss, Astropart. Phys. 105 (2019) 25–30.

[165] J. L. Brown, D. A. Glaser and M. L. Perl, Phys. Rev. 102 (1956) 586–587.

[166] D. Akimov et al., arXiv 1509.08702 (2015).

Astroparticle Physics 90 (2017) 85–92

Contents lists available at ScienceDirect

Astroparticle Physics

journal homepage: www.elsevier.com/locate/astropartphys

Final results of the PICASSO dark matter search experiment

E. Behnke[a], M. Besnier[b], P. Bhattacharjee[c], X. Dai[b,i], M. Das[c], A. Davour[b], F. Debris[d], N. Dhungana[e], J. Farine[e], M. Fines-Neuschild[d], S. Gagnebin[f], G. Giroux[b], E. Grace[a,l], C.M. Jackson[d,j], A. Kamaha[b], C.B. Krauss[f], M. Lafrenière[d], M. Laurin[d], I. Lawson[g], L. Lessard[d], I. Levine[a], D. Marlisov[f], J.-P. Martin[d], P. Mitra[f], A.J. Noble[b], A. Plante[d,*], R. Podviyanuk[e], S. Pospisil[h], O. Scallon[e], S. Seth[c,k], N. Starinski[d], I. Stekl[h], U. Wichoski[e], V. Zacek[d]

[a] Department of Physics & Astronomy, Indiana University South Bend, South Bend, IN 46634, USA
[b] Department of Physics, Queen's University, Kingston, K7L 3N6, Canada
[c] Saha Institute of Nuclear Physics, Centre for AstroParticle Physics (CAPP), Kolkata, 700064, India
[d] Département de Physique, Université de Montréal, Montréal, H3C 3J7, Canada
[e] Department of Physics, Laurentian University, Sudbury, P3E 2C6, Canada
[f] Department of Physics, University of Alberta, Edmonton, T6G 2G7, Canada
[g] SNOLAB, Lively ON, P3Y1N2, Canada
[h] Institute of Experimental and Applied Physics, Czech Technical University in Prague, Prague, Cz-12800, Czech Republic
[i] AECL Chalk River Laboratories, Chalk River, K0J 1J0, Canada
[j] Univ. of California, Berkeley, CA 94720, USA
[k] Tata Institute of Fundamental Research, Mumbai, 400088 Maharashtra, India
[l] Sterling College, Dep. of Natural Sciences & Mathematics, Sterling, KS 67579, USA

ARTICLE INFO

Article history:
Received 1 November 2016
Revised 5 February 2017
Accepted 17 February 2017
Available online 20 February 2017

Keywords:
Dark matter
WIMPs
Superheated droplets
SNOLAB

ABSTRACT

The PICASSO dark matter search experiment operated an array of 32 superheated droplet detectors containing 3.0 kg of C_4F_{10} and collected an exposure of 231.4 kgd at SNOLAB between March 2012 and January 2014. We report on the final results of this experiment which includes for the first time the complete data set and improved analysis techniques including acoustic localization to allow fiducialization and removal of higher activity regions within the detectors. No signal consistent with dark matter was observed. We set limits for spin-dependent interactions on protons of $\sigma_p^{SD} = 1.32 \times 10^{-2}$ pb (90% C.L.) at a WIMP mass of 20 GeV/c^2. In the spin-independent sector we exclude cross sections larger than $\sigma_p^{SI} = 4.86 \times 10^{-5}$ pb (90% C.L.) in the region around 7 GeV/c^2. The pioneering efforts of the PICASSO experiment have paved the way forward for a next generation detector incorporating much of this technology and experience into larger mass bubble chambers.

© 2017 Elsevier B.V. All rights reserved.

1. Introduction

Dark matter searches are the focus of underground laboratories all over the world. Even though the existence of dark matter is no longer controversial, the particle nature of dark matter has not been established so far. The class of particles best motivated theoretically are usually referred to as WIMPs, or Weakly Interacting Massive Particles [1–3]. The experimental signature of such particles can be searched for in production experiments at colliders and beam dumps, indirectly by looking for annihilation products from zones expected to have high dark matter densities, such as the galactic core, or by directly looking for interactions between ordinary matter and dark matter through the observation of nuclear recoils in large underground detectors.

The direct detection of dark matter through the observation of nuclear recoils requires detector technologies sensitive to keV nuclear recoils while able to discriminate against abundant backgrounds from conventional radioactivity. Successful technologies have been developed based on cryogenic solid state detectors, scintillating crystals, noble liquids and superheated liquids [4]. Historically, the interaction of dark matter with normal matter has been divided into two categories, spin independent and spin dependent. Since theory provides little guidance on WIMP masses or their couplings it is important to explore both sectors with a wide variety of targets.

* Corresponding author.
E-mail address: arthur.plante@umontreal.ca (A. Plante).

http://dx.doi.org/10.1016/j.astropartphys.2017.02.005
0927-6505/© 2017 Elsevier B.V. All rights reserved.

The highest sensitivity in the spin independent sector has been obtained by experiments using noble liquids and cryogenic crystals (e.g. LUX, XENON, PandaX, CDMS [5–8]). In the spin dependent (proton) sector the superheated detector technology has been at the forefront since several years, with the most stringent limits set by PICO (formed from a merger of PICASSO and COUPP) [9–11]. Other experiments using this technique are SIMPLE and MOSCAB [12,13]. Two primary types of detectors are in use: droplet detectors and bubble chambers, all using fluorinated halocarbons as target liquids.

The PICASSO experiment at SNOLAB used a superheated liquid droplet target of C_4F_{10}. A fluorine rich target such as C_4F_{10} is ideal for dark matter searches in the spin-dependent sector due to the very high spin enhancement factor from the single unpaired proton in ^{19}F and its natural isotopic abundance of 100% [14,15]. The low mass number also leads to a peak sensitivity in the low WIMP mass range of tens of GeV/c^2, an area of much recent interest in dark matter experiments [16–18]. In this mass region a competitive spin-independent search can also be performed.

2. Detection principle

The detection principle of PICASSO is a variant of the classical bubble chamber technique where a superheated liquid is held in a metastable state such that a deposition of a critical energy within a critical radius causes a phase transition and a droplet to change from liquid to gas [19–22]. The explosive bubble nucleation is accompanied by an acoustic signal in the audible and ultrasonic frequency range and gives information on the nature of the underlying event [11,23,24]. Since the detector observes phase transitions it performs as a threshold device, which can be controlled by setting the temperature and/or pressure.

With a boiling temperature of $T_b = -1.7\ ^0C$ at a pressure of 1.013 bar, the C_4F_{10} droplets in PICASSO are kept in a moderately superheated state at temperatures from 25 to 50 ^0C corresponding to thresholds in the range 1–60 keV. The precise relation between energy threshold and operating temperature in C_4F_{10} was determined by extensive measurements of ^{19}F-recoils using monoenergetic neutron beams and with alpha emitters of known energies in the droplets [24–26]. Since each temperature corresponds to a defined energy threshold, the spectrum of the particle induced energy depositions can be reconstructed by varying the threshold temperature. A summary of the detector response to different kinds of particles is shown in Fig. 1, where temperatures are converted into energy thresholds. For ^{19}F-recoils this energy scale corresponds directly to their detection thresholds.

Since WIMP induced recoil energies of ^{19}F nuclei are expected to be smaller than 100 keV they become detectable above 30 ^0C. At the normal operating thresholds of PICASSO above 1 keV, particles with low ionization densities, such as γ - rays and β - particles do not deposit sufficient energy to induce a phase change and these events are suppressed by more than a factor of 10^{-9}. Only alpha particles and neutrons can contribute particle induced backgrounds to the WIMP searches in this detector. The described responses depend exclusively on the thermodynamic parameters describing the degree of superheat of the droplet fluid and are independent of detector specific parameters (i.e. droplet size, loading fraction, transducer response).

Since α-particles induce phase transitions over the entire range of the WIMP sensitivity due to their large dE/dx, they are, together with neutrons an important background for this kind of detector in dark matter searches. However the shapes of the WIMP response, with count rates decreasing with increasing threshold energy, and of the α-response with constant rates in the region of interest, differ substantially, such that both contributions can be separated by fitting. In addition, PICASSO discovered that for alpha particles in the bulk fluid, it was possible to discriminate between alpha particles and nuclear recoils, an advantage best exploited in the next generation bubble chambers. A detailed discussion of the detector response is given in [24].

3. Detector set-up and operation

PICASSO started operating 4.5 L volume droplet detectors at SNOLAB in 2007 and published data with increasing exposure and sensitivity in 2009 and 2012 [25,27]. Being limited essentially by the alpha background in the gel components, continuous efforts were made to revise and improve the purification procedures and to replace higher rate modules with cleaner ones (Section 5). Data taking with the upgraded set of 32 detector modules started in March 2012 and concluded in January 2014 with a total exposure of 231.4 kgd, after applying fiducial volume and timing cuts (Section 6). This last run period was enhanced by the overall lower background rates and by an optimization of the data taking, concentrating on low energy threshold measurements between 1 and 2 keV.

The PICASSO detectors and their operation principle have been described in detail in [24,25]. The current generation of detectors consisted of cylindrical modules of 17 cm diameter and 40 cm height. They were fabricated from acrylic and were closed on top by stainless steel lids sealed with polyurethane O-rings. The acrylic walls of the cylinders had a thickness of 1.3 cm in order to provide sufficient mechanical strength and to minimize radon leakage. Each detector was filled with a water saturated polyacrylamide emulsion up to 30 cm in height and loaded with droplets of C_4F_{10} with an average diameter of 200 μm. The active part of each detector was topped by mineral oil, which is connected to a hydraulic manifold.

The emulsion of the droplets was created by a magnetic stirrer where the time and speed were adjusted to obtain a bell shaped droplet volume distribution centered on diameters of 200 μm and with a distribution width of about 150 μm (FWHM). The selected droplet size was found to maximize the amount of active fluid in the detectors. Much larger droplets would tend to imperil the structural integrity of the surrounding polymer during bubble formation in the gel; smaller droplets would increase the geometric efficiency for detection of alpha particles originating from the gel. Calibrations showed that the observed particle response was independent of the droplet size within the range considered and conformed to the response observed in bulk superheated liquids. Above 45 ^0C the polymer becomes increasingly softer; non-particle induced phase transitions appear due to shear and fractures and these events become a non-negligible, but still controllable background (Section 5).

The initial active mass of each detector was known with a precision of 1% from weighing during fabrication, but additional uncertainties arise due to potential losses during polymerization, diffusion into the gel matrix and surface leakage. Therefore the active detector mass and sensitivity were verified and monitored by measurements with a calibrated AmBe source at periodic intervals. No loss was observed over the run period defined, and the total mass of C_4F_{10} in the set-up was determined to be 2.97 ± 0.15 kg, corresponding to 2.37 ± 0.12 kg of ^{19}F.

The acoustic signal associated with an event was observed by 9 piezoelectric transducers (Ferroperm P27) uniformly distributed around each detector at three different heights on the container wall (one of the detectors had 6 piezos). This arrangement allowed the events to be localized by triangulation and the definition of fiducial volumes to avoid higher background regions near the container walls (Section 5). Triggering of any of the nine transducers causes all channels to acquire data. The trigger is fully sensitive over the entire threshold range [28].

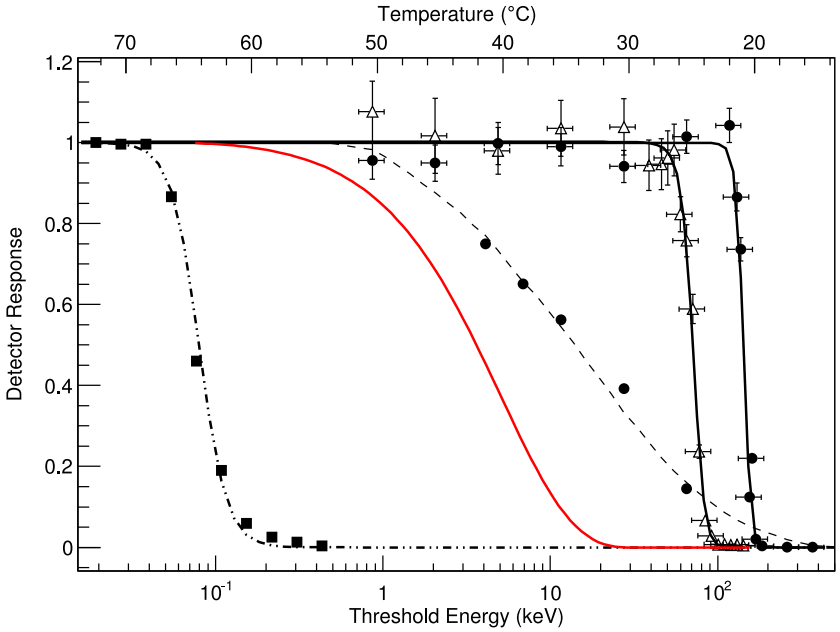

Fig. 1. Response to different kinds of particles in superheated C_4F_{10}. From left to right: 1.75 MeV γ-rays and MIPs (dot-dashed); ^{19}F recoils modeled assuming the scattering of a 50 GeV/c^2 WIMP (continuous red); poly-energetic neutrons from an AcBe source (dotted); α - particles at Bragg peak from ^{241}Am decays (open triangles); ^{210}Pb recoil nuclei from ^{226}Ra spikes (full dots). For ^{19}F and ^{210}Pb-recoils this energy scale corresponds directly to their detection thresholds. (For interpretation of the references to color in this figure legend, the reader is referred to the web version of this article.)

The detectors were typically operated for 40–50 h before being compressed by a hydraulic system to prevent damage to the gel matrix due to slow and continuing bubble growth. A compression phase which reduced the bubbles to the original liquid droplet state lasted 12 h at a pressure of 6.2 bar. This relatively long compression time was selected to assure complete curing of the gel and had no effect on the droplet size distribution and sensitivity which would have shown up during calibration runs.

The complete system of 32 detectors was housed in eight groups of four in thermally isolated boxes and was temperature controlled to roughly 0.1 ^{0}C to have a well-defined detection threshold. In order to preserve the sensitivity for annual rate modulations of an eventual signal, all detectors were operated at the same temperature at the same time. All 32 detectors met the data quality requirements and were used in the analysis.

The entire installation was surrounded by 50 cm of water contained in polyethylene tanks which served as neutron moderator and shielding. This shielding and setup represented a significant reduction in the background activity due to neutrons compared to the underground shielding used for previous PICASSO data sets. At the SNOLAB facility almost all neutrons are produced via (α, n) reactions due to natural U/Th radioactivity in the rock, with a remaining 10% from fission. A production rate of 4.0 neutrons g^{-1}y^{-1} was found from the relative abundance of isotopes in the surrounding Norite rock by computations using the SOURCES code [29,30]. These neutrons were further propagated by a GEANT4 simulation through the rock, the cavern and the water shielding to the detector location [31,32]. The performance of the simulation and the effectiveness of the shielding were checked by measurements with several ^{3}He counters (SNO NCDs [33]) which were surrounded by various thicknesses of dedicated polyethylene neutron moderator [29]. Measurements and simulations with and without water shielding showed that 99.66 ± 0.01 % of the incoming neutrons with energies above 5 keV were stopped in the shielding. Using the estimate of the fast neutron flux underground of (4 ± 2)× 10^3 neutrons m^{-2} d^{-1} in the cavern [34] and an average sensitivity of PICASSO detectors to neutrons of 0.1 cts per neutron g^{-1} cm^{-2} [26], the expected event rate induced by fast neutrons was determined to 0.14 cts kg^{-1} d^{-1}. This rate is still more than a factor ten smaller than the sensitivities of the best detectors in the set up.

The signals of each piezoelectric sensor were digitized using custom electronics with a sampling rate of 800 kHz and 16,384 samples per event. The data acquisition underwent a doubling of the sampling frequency since the previous runs [25] with the goal of improving the ability to reject alpha background. This important feature discovered by PICASSO was however not sufficiently efficient to be useful in this analysis due to the only partial containment of alpha events in the droplets [23]. The definition of a good event was determined by cut parameters on five acoustic variables described below. To determine these cuts the array of detectors was calibrated with a weak poly-energetic AmBe neutron source (68.71 ± 0.74 n s^{-1}) at every temperature that had a significant exposure. These calibration data were spread over the entire data taking period in order to follow temporal variations of the event selection parameters. A total of 53.8 kgd worth of neutron data was acquired for the calibrations.

4. Acoustic signatures for background discrimination

Calibrations with neutron test beams and fast neutrons from AcBe and AmBe sources showed that the waveforms associated with particle induced acoustic signals have characteristic frequency spectra (FFT) and time dependencies [26]. The signals have a short rise time, reaching a maximum after 20–40 μs, with slower oscillations following for several milliseconds. In addition, the amplitude distributions of the high frequency content (> 20 kHz) of the particle induced wave forms were concentrated in a well-defined peak. Tests on different known droplet samples showed that the amplitudes of particle induced events were not droplet size dependent, which is consistent with the current model of particle - induced sound generation in superheated liquids described in [24]. These features and others were used to construct variables which allowed the discrimination of particle induced events from non-particle background events. Since all event selection variables were dependent on the detector module and the operating temperature,

a set of variables and cut values were calculated using neutron calibration data averaged over all piezoelectric transducers. The cut values were determined by plotting the variable's distribution obtained in neutron calibrations and setting the cuts to retain 95% of neutrons. The values obtained were then fit with a polynomial to interpolate to all operating temperatures. The following are the main variables for event discrimination:

The acoustic energy EVAR is a variable calculated using the integrated energy in the recorded waveforms. The variable resolution was improved from the previous publication by reducing the signal time window used to calculate the variable to a length of 500 μs (starting 125 μs before the event trigger). This variable primarily isolates particle induced events and removes electronic noise which tends to have less acoustic energy than bubble events [29].

The signal rise time variable RVAR is calculated by taking the standard deviation of the time bins in the first 100 μs following the signal start time [29]. This primarily removes electronic noise and so-called "mystery" events, described later, which have a characteristically slow rise time.

The event shape/quality variable QVAR is calculated by taking the ratio of signal power within the first and second 10 ms of the recorded signal time window and this removes events where the signal power is distributed equally between the two time windows. These are events with unusual shapes, such as long ringing type signals, due to electronic noise.

The *event time variable TVAR* is calculated by finding the mean time bin of the signal squared and is used to identify events where the acoustic power is concentrated later in the signal. This was used to remove a class of repeating events due to delayed signals and electronic glitches.

A *wavelet based* frequency and time variable (*WFLVAR*) was constructed by taking ratios of parts of the decomposed continuous wavelet signal of the acoustic traces [29]. It replaced the older variable (*FVAR*) used in the previous publication which took ratios of energy contained within select frequency regions of the Fourier transformed signals.

5. Acoustic triangulation

Event localization by acoustic triangulation and fiducialization are a new feature introduced in this analysis and turned out to provide a powerful background discrimination especially against local alpha contamination and non-particle events happening at the container walls. This new technique uses the time differences between sound signals by different piezoelectric sensors to reconstruct the position of a bubble nucleation. First an event time for each piezoelectric sensor was found on raw and 18 kHz high-pass filtered signals from each piezoelectric sensor. Two methods were developed to find the event time: a comparison between two moving signal averages, averaged over 10 μs and 45 μs, respectively, and a cumulative shape indicator, where the cumulative time weighted average amplitude was compared with a uniform time integral to find the greatest separation, and hence the most likely signal start time. These arrival times were fit using a multi-parameter fit to obtain the localization point separately, giving four measurements of the bubble position. The results were then combined using a weighting that is inversely proportional to the fit quality χ^2 [35].

The performance was tested with 3 cm sized emulsion samples, suspended in a water filled detector module and a spatial resolution was found varying from ± 0.8 cm in the center of the detector up to ± 2 cm at the walls. The localization uncertainty increases near the detector walls due to sound propagation effects; no events are lost, but some are reconstructed slightly outside of the physical detector volume. The same measurements were used for a direct

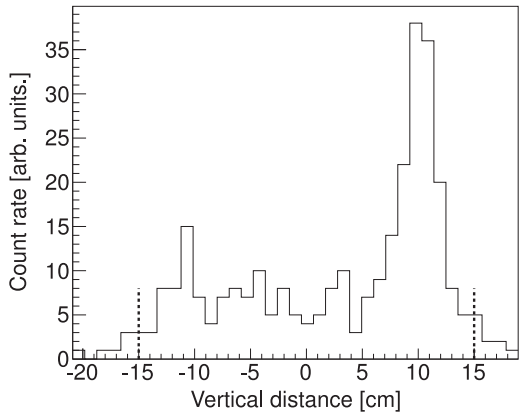

Fig. 2. Event localization by acoustic triangulation provides a powerful new tool for background discrimination. Shown here is the vertical profile of the count rate in one of the detector modules (# 145). The center of the droplet emulsion is located at 0 cm, top and bottom at ± 15 cm. A notable increase in α-decay events shows up at the top, close to the interface between the droplet emulsion and the mineral oil buffer.

determination of the speed of sound in the emulsion. These measurements were complemented by calibration data in 12 detectors at temperatures from 30 ^{0}C to 40 ^{0}C and where the speed was added as an additional fit parameter. The measured mean value v_s = 1507 ± 141 m/s at 40 ^{0}C agrees within uncertainties with the speed of sound in water v_s = 1528.88 m/s which constitutes 78% of the total mass of the detector.

Applying acoustic localization in data taking runs, an overabundance of events was observed in seven modules at the top of the detectors, close to the interface between emulsion and the hydraulic fluid for compression (mineral oil). This increase was not present in calibration runs and remained constant with operating temperature, so it was inferred that these were " hotspots" of alpha background contaminations on the surface, rather than an inhomogeneity in the droplet distribution.

In order to cope with this type of background a fiducial volume has been defined by an iterative process. Starting with a central volume of 5 cm radius and ± 8 cm in height, the count rate (in cts/gh) within this core volume was taken as a reference. Next, the active volume was gradually increased, as long as the count rate remained within one sigma of the core value, and this for all temperatures. An example is given in Fig. 2 which shows the vertical profile of the count rate in one of the "hot-spike"detector modules (# 145). For these modules a tighter fiducial cut was implemented, reducing the background rate substantially.

The event localization and wavelet analyses were also particularly useful for the discrimination of so called " mystery events": for high temperature runs above 45 ^{0}C (i.e. low recoil threshold) a new type of background was observed in the data especially for seven detectors with decreased intrinsic alpha-background ($<$ 10 cts kg^{-1} d^{-1}). This background was characterized by an increasingly large rate at high temperatures, similar in profile to a WIMP signal or neutron background. However, this background was not found in all detectors and when it was present had inconsistent and varying rates between modules. Data at 50 ^{0}C particularly exhibited this class of background events. By localizing the events it was noticed that they were concentrated at the edges of the detectors (both along the walls and at the top and bottom of the acrylic container). The most probable cause of these events are shear and stress effects at and in the vicinity of the emulsion interfaces. A typical fiducial cut of $r < 6$ cm around the center of the detector, together with the wavelet analysis, was able to remove the mystery events altogether. This allowed the inclusion of the 1 keV threshold data for the first time. The active mass

Table 1
Summary of the performance parameters of all detectors used in this analysis. The active masses refer to the mass content of ^{19}F in a module after application of individual fiducial volume cuts. Exposure values cover data taken over the entire temperature range from 30 ^{0}C < T < 50 ^{0}C. The quoted mass errors are: 5% systematic uncertainty in the determination of the active mass and a 3% uncertainty by introducing the fiducial volume cut.

Det	Fid. Mass g(F)	Exposure kg(F)d	Det	Fid. Mass g(F)	Exposure kg(F)d
106	21.63 ± 1.08	3.23 ± 0.16	153	34.64 ± 2.53	9.00 ± 0.66
108	26.30 ± 1.31	3.94 ± 0.20	154	32.48 ± 2.38	8.29 ± 0.61
110	70.86 ± 3.54	10.65 ± 0.53	155	31.65 ± 1.67	8.32 ± 0.44
112	11.74 ± 0.59	1.76 ± 0.09	156	52.61 ± 2.63	13.50 ± 0.68
123	32.06 ± 1.60	4.80 ± 0.24	157	60.78 ± 3.04	9.02 ± 0.45
131	33.14 ± 1.89	7.74 ± 0.44	158	41.86 ± 2.09	6.32 ± 0.32
136	81.88 ± 4.09	12.26 ± 0.61	159	48.21 ± 2.41	5.19 ± 0.26
137	16.10 ± 4.39	3.72 ± 1.02	160	73.37 ± 3.67	7.91 ± 0.40
141	31.64 ± 1.83	5.86 ± 0.34	161	66.44 ± 3.32	9.89 ± 0.49
144	59.56 ± 2.98	13.54 ± 0.68	162	31.71 ± 1.82	4.40 ± 0.25
145	41.15 ± 2.10	7.63 ± 0.39	163	28.26 ± 2.37	3.01 ± 0.25
146	31.67 ± 1.58	4.72 ± 0.24	164	27.86 ± 1.96	3.05 ± 0.21
147	41.23 ± 2.21	7.72 ± 0.41	165	56.39 ± 4.11	8.08 ± 0.59
148	91.74 ± 4.67	16.64 ± 0.85	166	60.61 ± 3.03	6.60 ± 0.33
150	25.52 ± 1.92	3.74 ± 0.28	167	65.00 ± 3.25	6.98 ± 0.35
151	36.59 ± 6.81	7.85 ± 1.46	168	43.61 ± 2.75	4.75 ± 0.30

contained within the restricted fiducial volume was measured using the AmBe calibration source runs, and it was found that each detector had its fiducial mass reduced by this radial cut by about 30%.

A summary of the final ^{19}F fiducial masses and exposures used in this analysis for each detector are given in Table 1. The integrated fiducial mass of the 32 detectors amounts to 1.41 ± 0.11 kg of ^{19}F and corresponds to 59.5 % of the total fluorine mass.

6. Analysis

The selection of good runs and of true particle induced events above electronic and mechanical noise backgrounds proceeded in the following order:

A list of golden runs was established for each detector. In order for a run to be good, at least six working acoustic readout channels were required; the duration of a run must have exceeded 15 h and the gauge pressure in the detector had to be within 0.1 bar with respect to ambient pressure.

Two pre-selection cuts were applied to remove electronic noise artifacts from the data. Events were discarded when the pre-trigger noise region was found to be large and when the peak amplitude normalized to the pre-trigger noise region was found to be small. These cuts were found to only remove electronic noise and no efficiency correction was necessary.

A time since last event cut was implemented to remove events thought to be caused by mechanical disturbances in the gel generated by fractures, deformation or gas bubble migration. The value used was 10 s during data taking runs and 0.1 s during calibration runs. The run exposure was corrected to account for this dead time.

After that the events had to pass the selections on *EVAR*, *RVAR*, *QVAR*, *TVAR* and *WFLVAR*, with the cut values chosen such that a 95% acceptance yield for calibration data was obtained. The event selection efficiency was estimated by accounting for variable correlations. The correlation matrix was measured from calibration runs and used as an input to a pseudo Monte Carlo simulation. For each detector and temperature the efficiency was extracted by testing the number of simulated events that passed all cuts and a polynomial fit to the efficiency was made. The fit value was used as the efficiency correction and was typically (detector and temperature dependent) in the range of 80–90 %.

Finally the fiducial volume cut was applied as described in Section 5. The active mass was corrected to account for the reduction in exposure.

Table 2
Effect of the applied cuts on the count rate in detector 153 at 30 ^{0}C and 50 ^{0}C.

Detector 153	30 ^{0}C	50 ^{0}C
Triggers/kgd	241.5 ± 8.4	5385.9 ± 32.1
After burst cut	36.9 ± 3.8	700.4 ± 49.2
After EVAR	19.2 ± 2.6	32.62 ± 3.4
After RVAR, QVAR, TVAR	19.1 ± 2.6	31.2 ± 2.7
After WFLVAR	18.3 ± 2.5	30.1 ± 2.7
After fid. cut	9.7 ± 3.1	8.6 ± 2.4

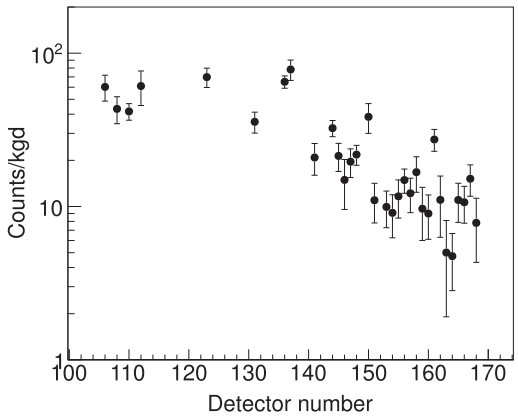

Fig. 3. Progressive reduction of background as a function of detector number. Shown is the count rate averaged over threshold energies in the range from 1 to 40 keV. The count rate after application of all cuts is flat in this region and indicative of the level of α - contamination in each detector.

The effects of the applied cuts for two temperatures on the trigger rates are illustrated for detector module 153 in Table 2. For this module the fiducial volume cut plays an important role in removing non-particle induced events and alpha particle “hot-spots”.

After correcting for cut acceptances and dead time the event rates for each detector at each temperature were normalized with respect to the active mass (^{19}F) and data taking time. The count rates of all detectors showed a flat plateau in the range from 1.05 to 40 keV (50–28 ^{0}C), similar to that observed in the presence of α - emitters (Fig. 1) in the droplets. The count rates averaged over the plateau range are shown in Fig. 3 and are indicative of the level of α - contamination in the individual detectors, ranging from

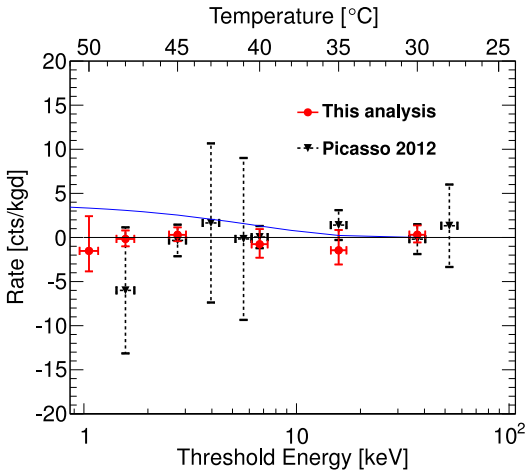

Fig. 4. Combined data from all detectors for WIMP runs for the present analysis. For each detector the average count rate was calculated over the temperature range 30 ^{0}C < T < 35 ^{0}C and subtracted from individual data points at the higher temperatures. Data for each detector and temperature are then combined in a weighted average. A hypothetical WIMP with $M_W = 15$ GeV/c^2 and $\sigma_p^{SD} = 3.2 \times 10^{-2}$ pb is shown by the continuous curve (blue). PICASSO 2012 results are shown for comparison (black dotted). (For interpretation of the references to color in this figure legend, the reader is referred to the web version of this article.)

80 cts kg^{-1} d^{-1} for earlier modules to 5 cts kg^{-1} d^{-1} for the best of the last set of detectors.

The progressive reduction in background was achieved by adding a 0.2 μm filtration stage for the monomer solution, by additional purification of the polymerizing agent (TEMED) and, for detectors 150 onward, by a doubling of all purification steps. In addition cover gas from LN_2 boil-off was used during all operations to mitigate radon diffusion from ambient air into the emulsion ingredients. This latter measure had no detectable effect on the detection sensitivity and threshold. The origin of the residual α - background is uncertain, but the acoustic signature of the events suggested that the activity was located primarily within the droplets. Detector 164 had the lowest background rate equivalent to a contamination level of 5×10^{-12} gU g^{-1} in the C_4F_{10} droplets.

In order to combine the data of all detectors for illustrative purposes in a single plot, we adopted the following procedure: for each detector the average count rate was calculated over the temperature range from 30 ^{0}C to 35 ^{0}C where WIMPS with masses $M_W < 15$ GeV/c^2 do marginally contribute; this count rate was taken as an approximation of the α - background level of the detector and was subtracted from individual data points at different temperatures; the data for each detector and temperature were then combined in a weighted average; and finally, the temperatures were converted into threshold energies by taking into account that due to the somewhat elevated mine pressure (1.2 bar) the measured temperature at the location of the experiment corresponded to a threshold with a temperature at surface (where the calibration was performed), reduced by 2 ^{0}C. The threshold dependence on pressure for a given temperature was measured by PICASSO with mono-energetic neutron test beams and is reported in [26].

The resulting threshold energy spectrum is shown in Fig. 4, where the error bars are dominated by statistics and reflect the time spent at each respective temperature. It is interesting to note that the count rates of all detectors as a function of recoil energy are essentially constant and that for modest changes in temperature from 30 ^{0}C to 50 ^{0}C the dynamic range in threshold energy sensitivity is large and covers the region from 1 keV up to 40 keV. No signal above background was observed.

7. Results

To search quantitatively for a dark matter signal the measured rates as a function of threshold energy have to be compared to those predicted for interactions of WIMPs in our galactic halo on ^{19}F nuclei in the presence of a constant alpha background in each of the detectors. We use the formalism described in [36] which approximates the recoil energy spectrum by an exponentially falling distribution and we use the standard halo parameterization with $\rho_D = 0.3$ GeVc^{-2} cm^{-3}, $v_0 = 220$ km s^{-1} and $v_{Earth} = 232$ km s^{-1}. Still following [36] we assume a nuclear form factor of $F(q^2) = 1$, justified by the light fluorine nucleus and the small momentum transfers involved.

Since our detectors operate as threshold devices, the observed rate at a given recoil energy threshold $E_{Rth}(T)$ is given by

$$R_{obs}(M_W, \sigma_F, E_{R_{th}}(T)) = \int_{E_{R_{th}}(T)}^{E_{R_{max}}} P(E_R, E_{R_{th}}(T)) \frac{dR}{dE_R} dE_R, \quad (1)$$

where $P(E_R, E_{R_{th}}(T))$ describes the effect of a finite resolution at threshold and dR/dE_R is the WIMP induced recoil energy spectrum; the integral extends to $E_{R_{max}}$ which is the maximum recoil energy a WIMP can transfer at its galactic escape velocity of $v_{esc} = 544$ km s^{-1}. The shape of the threshold curve is described by [26]:

$$P(E_R, E_{R_{th}}(T)) = 1 - \exp\left(a(T)\left(1 - \frac{E_R}{E_{R_{th}}(T)}\right)\right). \quad (2)$$

The parameter $a(T)$ describes the steepness of the energy threshold. It is related to the intrinsic energy resolution of the detection process and reflects the statistical nature of the energy deposition and its conversion into heat. It depends only on temperature and pressure and has to be determined experimentally. The larger a is, the steeper the threshold is. Our measurements with alpha emitters with well defined, mono-energetic recoil nuclei (^{210}Pb) indicate a sharp threshold that can be described with $a > 10$ at 146 keV (Fig. 1). Test beam measurements with mono-energetic neutrons at lower energies from 5 to 100 keV fall in the range of $1 < a < 10$, where decreasing energies favor smaller a. Poly-energetic AcBe neutron responses can be fit best with $a \approx 5$. As in [25] we adopt a principal value of $a = 5$ and let the parameter vary within the interval $1 < a < 7.5$ when estimating the uncertainty.

For WIMP masses smaller $M_W < 500$ GeV/c^2 the response curves differ in shape from the flat alpha background of each detector. By fitting the WIMP response curve and a flat alpha background, an upper bound on the WIMP-fluorine interaction cross section σ_F is obtained for each individual detector. For a given mass M_W the two parameters of the fit are the cross section σ_F and a scale factor describing the constant α-background. As an example, the result for each detector is shown in Fig. 5 for a WIMP mass of $M_W = 10$ GeV/c^2, the mass region of highest sensitivity.

The detector number follows the time of fabrication and the increasing sensitivity reflects the gradual reduction in alpha background by improvements in purification of the detector ingredients shown in Fig. 3. Combined in a weighted average, the maximum sensitivity occurs for WIMPs in the mass region around $M_W = 10$ GeV/c^2 and with a cross section of $\sigma_F = 0.083 \pm 0.448 \pm 0.039$ pb (1σ). The systematic error contribution was estimated as: an overall 5% uncertainty in the acceptance of the selection variables; a 3% uncertainty in the recoil detection efficiency inferred from the response to α-particles; a 5% uncertainty in the determination of the active mass; a 3% uncertainty by introducing the fiducial volume cut; a 1% uncertainty from energy scale shifts due to temperature uncertainties during neutron beam calibrations; the uncertainties due to atmospheric pressure changes were estimated < 1%, similar to the uncertainty of the hydrostatic pressure change along the vertical profile of the detectors.

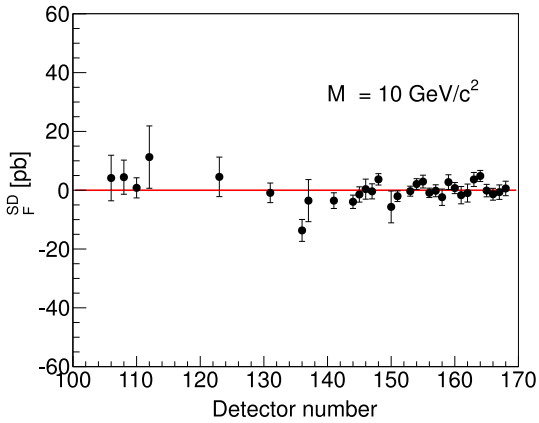

Fig. 5. Summary of the performance of all 32 detectors used in this analysis. Cross section values in pb for WIMP interactions on ^{19}F are quoted for a resolution parameter $a = 5$ and for a WIMP mass of 10 GeV/c^2, which is close to the maximum sensitivity. Systematic uncertainties are included as listed in the text. The detector number follows the time of fabrication.

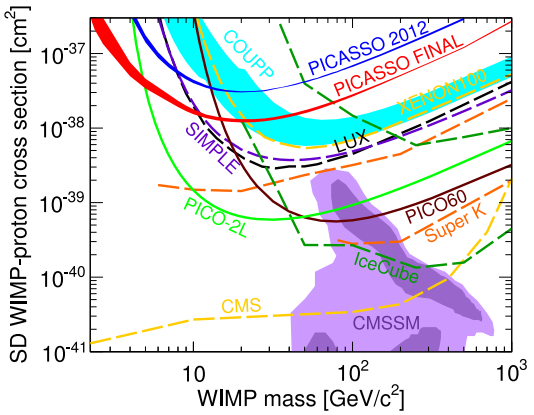

Fig. 6. Upper limits at 90% C.L. on SD-WIMP proton interactions. The final PICASSO limit is shown as a full red line along with limits from PICO-2L (green [9]), PICO60 (brown [10]), COUPP-4 (light blue [37]), SIMPLE (dashed purple [12]), XENON100 (dashed light orange [6]) and LUX (dashed black [38]). Indirect searches are represented by Ice-Cube (dashed dark green [39]), SuperK (dashed orange [40,41]) with comparable limits by ANTARES, Baikal and Baksan [42–44]. Limits from accelerator searches by CMS are shown in dashed light orange [45]. Comparable limits are set by ATLAS [46]. The purple region represents predictions in the framework of the CMSSM [47]. (For interpretation of the references to color in this figure legend, the reader is referred to the web version of this article.)

Assuming that scattering of dark matter is dominated by spin-dependent interactions with the unpaired proton in ^{19}F, the cross section σ_p^{SD} for scattering on free protons is related to the measured cross section σ_F by:

$$\sigma_p^{SD} = \sigma_F \left(\frac{\mu_p}{\mu_F}\right)^2 \frac{C_p^{SD}}{C_{p(F)}^{SD}}. \quad (3)$$

Here $\mu_{p(F)}$ are the WIMP-proton (fluorine) reduced masses, C_p^{SD} is the spin enhancement factor for scattering on the free proton and $C_{p(F)}^{SD}$ is the corresponding quantity for scattering on protons in the ^{19}F nucleus with the ratio $C_p^{SD}/C_{p(F)}^{SD} = 1.285$ [48,49]. The result for σ_F is then converted with Eq. (3) into a cross section on protons of $\sigma_p^{SD} = (1.39 \pm 8.46 \pm 0.72)\times 10^{-3}$ pb (1σ; $a = 5$), yielding a best limit of $\sigma_p^{SD} = 1.53 \times 10^{-2}$ pb (90% C.L.) for WIMP masses around 20 GeV/c^2. Adding the 114 kgd exposure of our 2012 data improves this limit slightly to $\sigma_p^{SD} = 1.32 \times 10^{-2}$ pb (90% C.L.) The resulting exclusion curve for the WIMP cross section on protons as a function of WIMP mass is shown in Fig. 6 together with published results in the spin-dependent sector. The broadening of the exclusion curve shows the effect of varying the energy resolution parameter a within its uncertainty.

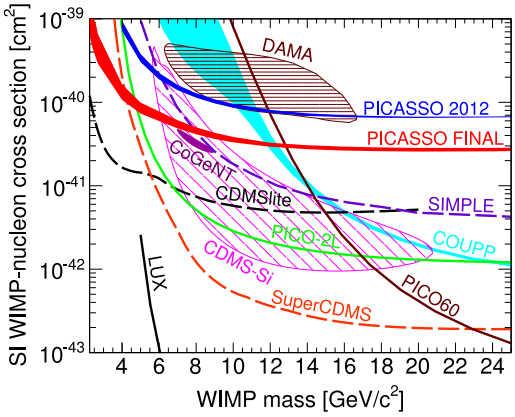

Fig. 7. Upper limits at 90% C.L. in the spin-independent sector. Only the region of interest in the range of low WIMP masses is shown. The closed contours are the allowed regions of DAMA (brown), CoGeNT (magenta) and CDMS-II Si (pink) [16–18]. The final PICASSO limit is shown in full red, along with PICO-2L (green [9]), PICO60 (brown [10]), COUPP-4 (light blue [37]), SIMPLE (dashed violet [12]), LUX (black [5]), CDMSlite (dashed black [50]) and SuperCDMS (dashed orange [8]). Similar limits (not shown) are set by XENON10, XENON100, CRESST and PandaX-II [6,7,51,52]. (For interpretation of the references to color in this figure legend, the reader is referred to the web version of this article.)

Similarly the limits on σ_F can be translated into an upper bound on the WIMP nucleon cross section in the spin-independent sector with a maximum sensitivity at $M_W = 20$ GeV/c^2 and $\sigma_p^{SI} = 2.8 \times 10^{-5}$ pb (90% C.L.). A summary of allowed regions and exclusion limits is shown in Fig. 7. We are aware of recent efforts to treat WIMP-nucleon interactions in a more complete and model independent way by using the approach of effective field theories [53] and it will be interesting to compare our ^{19}F results with other targets within this broader analysis framework.

8. Conclusions and outlook

PICASSO has operated a system of 32 superheated droplet detectors at SNOLAB with a combined exposure of 345.4 kgd. No indication of a WIMP signal was observed and a spin-dependent limit of 1.32×10^{-2} pb at $M_W = 20$ GeV/c^2 was set at a 90% confidence limit. In the spin-independent sector around 7 GeV/c^2, and close to the CoGeNT allowed region [17], a limit of 4.9×10^{-5} pb (90% C.L.) was extracted from the data. The use of the light target nucleus ^{19}F, combined with an increased exposure at the low detection threshold of 1 keV resulted in increased leverage in the low WIMP mass region. The main improvements with respect to our previous published results are: a substantial reduction in intrinsic α-background by up to a factor 10 in some modules and localization of events by acoustic triangulation.

The superheated droplet detector technique has proven to be a valuable technique for dark matter search especially in the spin-dependent sector and for low WIMP masses. The technique is easily scalable to multiple detectors; however the filling factor is only a few percent, the amount of surface area per active volume is much larger than in any other configuration of superheated liquid detectors and non-particle induced backgrounds start to become difficult to control in larger scale experiments. In addition the event by event α-recoil discrimination using the acoustic signal energy discovered by PICASSO can be much easier applied in bulk superheated liquids.

Without this important discrimination feature, a reduction in α-activity by more than a factor of 10^3 would be required in order to obtain a sensitivity which equals that already reached by

PICO-2L. This would not have been achievable with the existing purification technology for the components of the detector gel matrix. With this powerful acoustic discrimination tool the PICASSO group is now focused on large scale applications of superheated fluorinated halocarbons for dark matter detection using the more traditional bubble chamber technique as part of the broader PICO collaboration [9,10].

Acknowledgments

We wish to express our thanks to SNOLAB and its staff for providing an excellent infrastructure, as well as technical support and advice whenever needed. We especially thank SNOLAB for providing the water tanks for the improved shielding of the experiment. Many thanks go to Tina Shepherd and Naomi Tankersley (IUSB) for fabricating the acoustic transducers. We wish to acknowledge the support of the National Sciences and Engineering Research Council of Canada (NSERC) and the Canada Foundation for Innovation (CFI). This work is also supported by the National Science Foundation (NSF) under the Grants PHY-1205987 and PHY-1506377. We also acknowledge support from the Department of Atomic Energy (DAE), Govt. of India, under the project CAPP at SINP, Kolkata and the Czech Ministry of Education, Youth and Sports within the project MSM6840770029. We thank the members of the PICO collaboration for inspiring discussions and for providing the templates for the updated exclusion plots.

References

[1] K.A. Olive, Particle data group, Chin. Phys. C 38 (2014) 090001, doi:10.1088/1674-1137/38/9/090001.
[2] G. Jungman, M. Kamionkowski, K. Griest, Phys. Rep. 267 (5) (1996) 195, doi:10.1016/0370-1573(95)00058-5.
[3] M.W. Goodman, E. Witten, Phys. Rev. D 31 (1985) 3059, doi:10.1103/PhysRevD.31.3059.
[4] P. Cushman, et al., SNOWMASS CF1 summary: WIMP dark matter direct detection, arXiv:1310.8327v2 [hep-ex](2013).
[5] D.S. Akerib, et al., Phys. Rev. Lett. 118 (2) (2017) 021303, doi:10.1103/PhysRevLett.118.021303.
[6] E. Aprile, et al., Phys. Rev. D 94 (2016) 122001, doi:10.1103/PhysRevD.94.122001.
[7] A. Tan, et al., Phys. Rev. Lett. 117 (12) (2016) 121303, doi:10.1103/PhysRevLett.117.121303.
[8] R. Agnese, et al., Phys. Rev. Lett. 112 (2014) 241302, doi:10.1103/PhysRevLett.112.241302.
[9] C. Amole, et al., Phys. Rev. D 93 (2016a) 061101, doi:10.1103/PhysRevD.93.061101.
[10] C. Amole, et al., Phys. Rev. D 93 (5) (2016b) 052014, doi:10.1103/PhysRevD.93.052014.
[11] E. Behnke, et al., Phys. Rev. D 88 (2013) 021101, doi:10.1103/PhysRevD.88.021101.
[12] M. Felizardo, et al., Phys. Rev. D 89 (7) (2014) 072013, doi:10.1103/PhysRevD.89.072013.
[13] R. Bertoni, et al., Nucl. Inst. Meth. A 744 (2014) 61–68, doi:10.1016/j.nima.2014.01.026.
[14] J. Ellis, R. Flores, Phys. Lett. B 263 (1991) 259– 266.
[15] V.A. Bednyakov, H.V. Klapdor-Kleingrothaus, S.G. Kovalenko, Phys. Rev. D 55 (1997) 503–514, doi:10.1103/PhysRevD.55.503.
[16] R. Bernabei, et al., Eur. Phys. J. C 56 (2008) 333–355, doi:10.1140/epjc/s10052-008-0662-y.
[17] C.E. Aalseth, et al., Phys. Rev. D 88 (2013) 012002, doi:10.1103/PhysRevD.88.012002.
[18] R. Agnese, et al., Phys. Rev. Lett. 111 (2013) 251301, doi:10.1103/PhysRevLett.111.251301.
[19] D.A. Glaser, Phys. Rev. 87 (1952), doi:10.1103/PhysRev.87.665. 665–665
[20] R.E. Apfel, Nucl. Inst. and Meth. 162 (1–3) (1979) 603– 608, doi:10.1016/0029-554X(79)90735-3.
[21] H. Ing, R. Noulty, T. McLean, Radiat. Meas. 27 (1) (1997) 1–11, doi:10.1016/S1350-4487(96)00156-4.
[22] V. Zacek, Il Nuovo Cimento A 107 (1994) 291–298.
[23] F. Aubin, et al., New J. Phys. 10 (10) (2008) 103017.
[24] S. Archambault, et al., New J. Phys. 13 (4) (2011) 043006.
[25] S. Archambault, et al., Phys. Lett. B 711 (2) (2012) 153– 161, doi:10.1016/j.physletb.2012.03.078.
[26] M. Barnabé-Heider, et al., Nucl. Inst. Meth. A 555 (1–2) (2005) 184–204, doi:10.1016/j.nima.2005.09.015.
[27] S. Archambault, et al., Phys. Lett. B 682 (2) (2009) 185–192, doi:10.1016/j.physletb.2009.11.019.
[28] J.-P. Martin, N. Starinski, Designing data acquisition system for the PICASSO experiment, in: M. Vadursi (Ed.), Data Acquisition, Sciyo, 2010. isbn: 978-953-307-193- 0.
[29] A.C. Kamaha, Improved Limits on The Existence Of Dark Matter. The Final Results From The PICASSO Experiment, Queens University, 2015 Ph.D. thesis.
[30] W. Wilson, R. Perry, W. Charlton, T. Parish, Prog. Nucl. Energy 51 (45) (2009) 608– 613, doi:10.1016/j.pnucene.2008.11.007.
[31] S. Agostinelli, et al., Nucl. Inst. Meth. A 506 (2003) 250– 303.
[32] J. Allison, et al., IEEE Trans. Nucl. Sci. 53 (2006) 270–278.
[33] J. Amsbaugh, et al., Nucl. Inst. Meth. A 579 (2007) 1054–1080.
[34] W. Davidson, et al., Background Measurement in the Creighton Mine, SNO Collaboration Internal Report, 1987.
[35] F. Aubin, Localisation Spatiale des Événements dans les Détecteurs PICASSO, Université de Montréal, 2005 Master's thesis.
[36] J. Lewin, P. Smith, Astropart. Phys. 6 (1) (1996) 87–112, doi:10.1016/S0927-6505(96)00047-3.
[37] E. Behnke, et al., Phys. Rev. D 90 (2014) 079902.
[38] D.S. Akerib, et al., Phys. Rev. Lett. 116 (16) (2016) 161302, doi:10.1103/PhysRevLett.116.161302.
[39] M.G. Aartsen, et al., Phys. Rev. Lett. 110 (2013) 131302.
[40] T. Tanaka, et al., Astrophys. J. 742 (2) (2011) 78.
[41] K. Choi, et al., Phys. Rev. Lett. 114 (2015) 141301, doi:10.1103/PhysRevLett.114.141301.
[42] S. Adrian-Martinez, et al., JCAP 1311 (2013) 032, doi:10.1088/1475-7516/2013/11/032.
[43] S. Demidov, O. Suvorova, JCAP 1006 (2010) 018, doi:10.1088/1475-7516/2010/06/018.
[44] A.D. Avrorin, et al., Astropart. Phys. 62 (2015) 12–20, doi:10.1016/j.astropartphys.2014.07.006.
[45] V. Khachatryan, et al., Eur. Phys. J. C75 (5) (2015) 235, doi:10.1140/epjc/s10052-015-3451-4.
[46] G. Aad, et al., Eur. Phys. J. C75 (7) (2015) 299, doi:10.1140/epjc/s10052-015-3517-3, 10.1140/epjc/s10052-015-3639-7.
[47] L. Roszkowski, R. Ruiz de Austri, R. Trotta, JHEP 07 (2007) 075, doi:10.1088/1126-6708/2007/07/075.
[48] D. Tovey, R. Gaitskell, P. Gondolo, Y. Ramachers, L. Roszkowski, Phys. Lett. B 488 (1) (2000) 17–26, doi:10.1016/S0370-2693(00)00846-7.
[49] F. Giuliani, Phys. Rev. Lett. 93 (2004) 161301, doi:10.1103/PhysRevLett.93.161301.
[50] R. Agnese, et al., Phys. Rev. Lett. 116 (7) (2016) 071301, doi:10.1103/PhysRevLett.116.071301.
[51] J. Angle, et al., Phys. Rev. Lett. 107 (2011) 051301, doi:10.1103/PhysRevLett.107.051301.
[52] G. Angloher, et al., Eur. Phys. J. C76 (1) (2016) 25, doi:10.1140/epjc/s10052-016-3877-3.
[53] N. Anand, A.L. Fitzpatrick, W.C. Haxton, Phys. Procedia 61 (2015) 97–106, doi:10.1016/j.phpro.2014.12.017.

APPENDIX A

Table .I-.VII show the basic information regarding each components, i.e.: density, volume, fluence, ppb level and number of simulated neutrons.

Tables .VIII-.XII present the leakage probability for both single and multiple bubble events as well as the single and multiple rate per year for the three contaminants and for each detector components.

The last page of this Appendix contains the first and second order Seitz terms that were developed in section 5.2.2.

Component	Contaminent	Density	Volume	deltaVolume	Fluence	ppb	delta ppb	simulated
L-01-001-Fusedsilicajar	Th232	2.203	5278.194	0	6.314E-12	1.82e-6	6.3e-7	1e6
L-01-001-Fusedsilicajar	U235	2.203	5278.194	0	8.128E-13	8.6e-7	5.61e-7	1e6
L-01-001-Fusedsilicajar	U238	2.203	5278.194	0	2.727e-11	8.6e-7	5.61e-7	1e6
L-01-030-ShortFusedSilicaVessel	Th232	2.203	3622.51	0	6.314E-12	1.82e-6	6.3e-7	1e6
L-01-030-ShortFusedSilicaVessel	U235	2.203	3622.51	0	8.128E-13	8.6e-7	5.61e-7	1e6
L-01-030-ShortFusedSilicaVessel	U238	2.203	3622.51	0	2.727e-11	8.6e-7	5.61e-7	1e6
KaptonTop	Th232	1	91	0	2.031E-11	245.05	20.78	1e8
KaptonTop	U235	1	91	0	2.890E-12	147.90	80.63	1e8
KaptonTop	U238	1	91	0	6.318E-11	257.22	119.50	1e8
KaptonBot	Th232	1	91	0	2.031E-11	245.05	20.78	1e8
KaptonBot	U235	1	91	0	2.890E-12	147.90	80.63	1e8
KaptonBot	U238	1	91	0	6.318E-11	257.22	119.50	1e8
LensBot	Th232	2.675	89.8593674	0	4.203E-11	1450	160	1e8
LensBot	U235	2.675	89.8593674	0	4.831E-12	8.568	1.872	1e8
LensBot	U238	2.675	89.8593674	0	9.253E-11	340	40	1e8
LensTop	Th232	2.675	89.8593674	0	4.203E-11	1450	160	1e8
LensTop	U235	2.675	89.8593674	0	4.831E-12	8.568	1.872	1e8
LensTop	U238	2.675	89.8593674	0	9.253E-11	340	40	1e8
CameraTop	Th232	1	197.2	0	4.209e-11	371.30	14.97	1e8
CameraTop	U235	1	197.2	0	5.002E-12	30.734	6.74	1e8
CameraTop	U238	1	197.2	0	9.802e-11	61.13	6.113	1e8
CameraBot	Th232	1	197.2	0	4.209e-11	371.30	14.97	1e8
CameraBot	U235	1	197.2	0	5.002E-12	30.734	6.74	1e8
CameraBot	U238	1	197.2	0	9.802e-11	61.13	6.113	1e8

Table .I – Basic information regarding each detector component present in the PICO40L Geant4 GDML geometry which are the density, volume, fluence, ppb level and number of simulated neutrons.

Component	Contaminent	Density	Volume	ΔVolume	Fluence	ppb	delta ppb	simulated
PVReflector	Th232	8.0	48.9	0.8	6.726E-12	35.26	10.41	1e8
PVReflector	U235	8.0	48.9	0.8	2.094E-13	72.76	7.276	1e8
PVReflector	U238	8.0	48.9	0.8	1.932E-11	8.80	0.880	1e8
TopReflector	Th232	8.0	9.52	0.5	6.726E-12	35.26	10.41	1e8
TopReflector	U235	8.0	9.52	0.5	2.094E-13	72.76	7.276	1e8
TopReflector	U238	8.0	9.52	0.5	1.932E-11	8.80	0.880	1e8
BotReflector	Th232	8.0	11.8	0.6	6.726E-12	35.26	10.41	1e8
BotReflector	U235	8.0	11.8	0.6	2.094E-13	72.76	7.276	1e8
BotReflector	U238	8.0	11.8	0.6	1.932E-11	8.80	4.18	1e8
Oil	Th232	0.890	820420.63	0	5.048E-12	0.0000041	0	1e7
Oil	U235	0.890	820420.63	0	6.490E-13	0.0000040	0	1e7
Oil	U238	0.890	820420.63	0	2.480E-11	0.0000040	0	1e7
Oil	U238 low	0.890	820420.63	0	9.727E-12	1.0	0	1e7
Oil	Po210	0.890	820420.63	0	9.003E-13	1.0	0	1e7
Plastic shielding	Th232	1	287932.70	0	5.048E-12	0.12	0	1e8
Plastic shielding	U235	1	287932.70	0	6.490E-13	1.27	0	1e8
Plastic shielding	U238	1	287932.70	0	2.480E-11	0.94	0	1e8

Table .II – Basic information regarding each detector component present in the PICO40L Geant4 GDML geometry which are the density, volume, fluence, ppb level and number of simulated neutrons.

Component	Contaminent	Density	Volume	deltaVolume	Fluence	ppb	delta ppb	simulated
L-01-005-B-Titanium flange Top-Top	Th232	4.506	594.62	0	2.200E-11	4.32	1.25	1e8
L-01-005-B-Titanium flange Top-Top	U235	4.506	594.62	0	1.012E-12	5.05	8.60	1e8
L-01-005-B-Titanium flange Top-Top	U238	4.506	594.62	0	3.694E-11	3.99	8.65	1e8
L-01-006-B-Titanium flange Top-Bot	Th232	4.506	606.87	0	2.200E-11	4.32	1.25	1e8
L-01-006-B-Titanium flange Top-Bot	U235	4.506	606.87	0	1.012E-12	5.05	8.60	1e8
L-01-006-B-Titanium flange Top-Bot	U238	4.506	606.87	0	3.694E-11	3.99	8.65	1e8
L-01-008-B-Titanium flange Top-Mid	Th232	4.506	832.92	0	2.200E-11	4.32	1.25	1e8
L-01-008-B-Titanium flange Top-Mid	U235	4.506	832.92	0	1.012E-12	5.05	8.60	1e8
L-01-008-B-Titanium flange Top-Mid	U238	4.506	832.92	0	3.694E-11	3.99	8.65	1e8
L-01-036-A-Titanium flange Bot-Top	Th232	4.506	533.07	0	2.200E-11	4.32	1.25	1e8
L-01-036-A-Titanium flange Bot-Top	U235	4.506	533.07	0	1.012E-12	5.05	8.60	1e8
L-01-036-A-Titanium flange Bot-Top	U238	4.506	533.07	0	3.694E-11	3.99	8.65	1e8
L-01-037-A-Titanium flange Bot-Bot	Th232	4.506	405.76	0	2.200E-11	4.32	1.25	1e8
L-01-037-A-Titanium flange Bot-Bot	U235	4.506	405.76	0	1.012E-12	5.05	8.60	1e8
L-01-037-A-Titanium flange Bot-Bot	U238	4.506	405.76	0	3.694E-11	3.99	8.65	1e8
L-01-038-A-Titanium flange Bot-Mid	Th232	4.506	576.16	0	2.200E-11	4.32	1.25	1e8
L-01-038-A-Titanium flange Bot-Mid	U235	4.506	576.16	0	1.012E-12	5.05	8.60	1e8
L-01-038-A-Titanium flange Bot-Mid	U238	4.506	576.16	0	3.694E-11	3.99	8.65	1e8
L-01-039-A-Teflon ring bot bellows	Th232	2.200	15.68	0	1.999E-12	1	1	1e8
L-01-039-A-Teflon ring bot bellows	U235	2.200	15.68	0	5.249E-11	1	1	1e8
L-01-039-A-Teflon ring bot bellows	U238	2.200	15.68	0	8.809E-10	1	1	1e8

Table .III – Basic information regarding each detector component present in the PICO40L Geant4 GDML geometry which are the density, volume, fluence, ppb level and number of simulated neutrons.

Component	Contaminent	Density	Volume	deltaVolume	Fluence	ppb	delta ppb	simulated
L-01-040-A-Teflon ring top bellows	Th232	2.200	87.06	0	1.999E-12	1	1	1e8
L-01-040-A-Teflon ring top bellows	U235	2.200	87.06	0	5.249E-11	1	1	1e8
L-01-040-A-Teflon ring top bellows	U238	2.200	87.06	0	8.809E-10	1	1	1e8
L-01-041-A-Teflon ring top bellows	Th232	2.200	17.26	0	1.999E-12	1	1	1e8
L-01-041-A-Teflon ring top bellows	U235	2.200	17.26	0	5.249E-11	1	1	1e8
L-01-041-A-Teflon ring top bellows	U238	2.200	17.26	0	8.809E-10	1	1	1e8
L-01-042-A-Teflon ring top bellows	Th232	2.200	91.22	0	1.999E-12	1	1	1e8
L-01-042-A-Teflon ring top bellows	U235	2.200	91.22	0	5.249E-11	1	1	1e8
L-01-042-A-Teflon ring top bellows	U238	2.200	91.22	0	8.809E-10	1	1	1e8
O-ring 454-top bellows	Th232	1.000	77.974	0	8.625E-12	1	1	1e8
O-ring 454-top bellows	U235	1.000	77.974	0	9.077E-13	1	1	1e8
O-ring 454-top bellows	U238	1.000	77.974	0	3.076E-11	1	1	1e8
O-ring 2-452-bot bellows	Th232	1.000	71.874	0	8.625E-12	1	1	1e8
O-ring 2-452-bot bellows	U235	1.000	71.874	0	9.077E-13	1	1	1e8
O-ring 2-452-bot bellows	U238	1.000	71.874	0	3.076E-11	1	1	1e8

Table .IV – Basic information regarding each detector component present in the PICO40L Geant4 GDML geometry which are the density, volume, fluence, ppb level and number of simulated neutrons.

Component	Contaminent	Density	Volume	deltaVolume	Fluence	ppb	delta ppb	simulated
Bellows	Th232	8.000	276.794	0	6.726E-12	3.99	0.399	1e8
Bellows	U235	8.000	276.794	0	2.094E-13	17.26	21.13	1e8
Bellows	U238	8.000	276.794	0	1.932E-11	27.13	2.713	1e8
Bellows top flange	Th232	8.000	3958.92	0	6.726E-12	3.99	0.399	1e8
Bellows top flange	U235	8.000	3958.92	0	2.094E-13	17.26	21.13	1e8
Bellows top flange	U238	8.000	3958.92	0	1.932E-11	27.13	2.713	1e8
Bellows bot flange	Th232	8.000	2122.929	0	6.726E-12	3.99	0.399	1e8
Bellows bot flange	U235	8.000	2122.929	0	2.094E-13	17.26	21.13	1e8
Bellows bot flange	U238	8.000	2122.929	0	1.932E-11	27.13	2.713	1e8
PV	Th232	8.0	184200.73	0	6.726E-12	2.47	0.37	1e8
PV	U235	8.0	184200.73	0	2.094E-13	3.28	0.328	1e8
PV	U238	8.0	184200.73	0	1.932E-11	4.12	0.412	1e8
DishHead	Th232	8.0	10133.36	0	6.726E-12	2.47	0.37	1e8
DishHead	U235	8.0	10133.36	0	2.094E-13	3.28	0.328	1e8
DishHead	U238	8.0	10133.36	0	1.932E-11	4.12	0.412	1e8
Inner heating top copper plate	Th232	8.96	160.880	0	5.597E-15	0.00000311	9.22e-7	1e8
Inner heating top copper plate	U235	8.96	160.880	0	8.595E-15	0.0000275	0.0000055	1e8
Inner heating top copper plate	U238	8.96	160.880	0	1.542E-11	0.0000275	0.0000055	1e8
Inner heating bot copper plate	Th232	8.96	160.880	0	5.597E-15	0.00000311	9.22e-7	1e8
Inner heating bot copper plate	U235	8.96	160.880	0	8.595E-15	0.0000275	0.0000055	1e8
Inner heating bot copper plate	U238	8.96	160.880	0	1.542E-11	0.0000275	0.0000055	1e8
Outer thermal control copper disk	Th232	8.96	6471.82	0	5.597E-15	0.00000311	9.22e-7	1e8
Outer thermal control copper disk	U235	8.96	6471.82	0	8.595E-15	0.0000275	0.0000055	1e8
Outer thermal control copper disk	U238	8.96	6471.82	0	1.542E-11	0.0000275	0.0000055	1e8

Table .V – Basic information regarding each detector component present in the PICO40L Geant4 GDML geometry which are the density, volume, fluence, ppb level and number of simulated neutrons.

Component	Contaminent	Density	Volume	deltaVolume	Fluence	ppb	delta ppb	simulated
Piezo PZT	Th232	1	1	0	3.104E-12	56.32	31.99	1e7
Piezo PZT	U235	1	1	0	2.413E-13	686.92	562.84	1e7
Piezo PZT	U238	1	1	0	1.867E-11	619.68	964.04	1e7
Piezo PZT	Pb210	1	1	0	3.462E-08	1.66	0.166	1e7
Piezo PCB	Th232	1	15.8	0	5.048E-12	4.94	7.01	1e7
Piezo PCB	U235	1	15.8	0	6.670E-13	28.95	48.12	1e7
Piezo PCB	U238	1	15.8	0	2.522E-11	2.25	48.66	1e7
Piezo PCB	U238 low	1	15.8	0	2.522E-11	17.48	3.07	1e7
Piezo Copper	Th232	1	1160.6	0	5.597E-15	0.00000311	0.00000092	1e7
Piezo Copper	U235	1	1160.6	0	8.595E-15	0.0000275	0.0000055	1e7
Piezo Copper	U238	1	1160.6	0	1.542E-11	0.0000275	0.0000055	1e7
Piezo Cable Ver	Th232	1	237.55	0	5.893E-11	4.8	3.8	1e7
Piezo Cable Ver	U235	1	237.55	0	6.350E-12	8.8	2.3	1e7
Piezo Cable Ver	U238	1	237.55	0	1.160E-10	8.8	2.3	1e7
Piezo Cable Hor	Th232	1	14.91	0	5.893E-11	4.8	3.8	1e7
Piezo Cable Hor	U235	1	14.91	0	6.350E-12	8.8	2.3	1e7
Piezo Cable Hor	U238	1	14.91	0	1.160E-10	8.8	2.3	1e7

Table .VI – Basic information regarding each detector component present in the PICO40L Geant4 GDML geometry which are the density, volume, fluence, ppb level and number of simulated neutrons.

Component	Contaminent	Density	Volume	deltaVolume	Fluence	ppb	delta ppb	simulated
Piezo 84 PZT	Th232	1	13.828	0	3.104E-12	17.75	0.88	1e7
Piezo 84 PZT	U235	1	13.828	0	2.413E-13	17.42	1.77	1e7
Piezo 84 PZT	U238	1	13.828	0	1.867E-11	12.51	7.11	1e7
Piezo 84 PCB	Th232	1	15.8	0	5.048E-12	17.75	0.88	1e7
Piezo 84 PCB	U235	1	15.8	0	6.670E-13	17.42	1.77	1e7
Piezo 84 PCB	U238	1	15.8	0	2.522E-11	12.51	7.11	1e7
Piezo 84 Cable Ver	Th232	1	237.55	0	5.893E-11	17.75	0.88	1e7
Piezo 84 Cable Ver	U235	1	237.55	0	6.350E-12	17.42	1.77	1e7
Piezo 84 Cable Ver	U238	1	237.55	0	1.160E-10	12.51	7.11	1e7
Piezo 84 Cable Hor	Th232	1	14.91	0	5.893E-11	17.75	0.88	1e7
Piezo 84 Cable Hor	U235	1	14.91	0	6.350E-12	17.42	1.77	1e7
Piezo 84 Cable Hor	U238	1	14.91	0	1.160E-10	12.51	7.11	1e7
Piezo 84 Copper	Th232	1	1160.6	0	5.597E-15	0.00000311	0.00000092	1e7
Piezo 84 Copper	U235	1	1160.6	0	8.595E-15	0.0000275	0.0000055	1e7
Piezo 84 Copper	U238	1	1160.6	0	1.542E-11	0.0000275	0.0000055	1e7

Table .VII – Basic information regarding each detector component present in the PICO40L Geant4 GDML geometry which are the density, volume, fluence, ppb level and number of simulated neutrons.

Component	Contaminant	Single leak. prob.	Multiple leak. prob	Single/year	Mult./year
IV	U235	1.26E-02	2.79E-02	2.21E-09 ± 1.51E-09	4.92E-09 ± 3.35E-09
IV	U238	1.25E-02	2.78E-02	7.40E-08 ± 5.05E-08	1.64E-07 ± 1.12E-07
IV	Th232	1.26E-02	2.79E-02	3.64E-08 ± 1.45E-08	8.07E-08 ± 3.23E-08
OV	U235	7.29E-02	1.86E-01	1.87E-08 ± 1.28E-08	4.77E-08 ± 3.25E-08
OV	U238	7.28E-02	1.85E-01	6.26E-07 ± 4.27E-07	1.59E-06 ± 1.09E-06
OV	Th232	7.29E-02	1.86E-01	3.07E-07 ± 1.23E-07	7.82E-07 ± 3.13E-07
KaptonTop	U235	6.81E-05	1.86E-04	3.72E-05 ± 2.16E-05	1.02E-04 ± 5.90E-05
KaptonTop	U238	5.70E-05	1.53E-04	1.18E-03 ± 5.99E-04	3.18E-03 ± 1.61E-03
KaptonTop	Th232	7.83E-05	2.10E-04	4.98E-04 ± 1.08E-04	1.34E-03 ± 2.90E-04
KaptonBot	U235	6.76E-05	1.78E-04	3.69E-05 ± 2.15E-05	9.73E-05 ± 5.65E-05
KaptonBot	U238	5.49E-05	1.47E-04	1.14E-03 ± 5.76E-04	3.05E-03 ± 1.55E-03
KaptonBot	Th232	7.73E-05	2.01E-04	4.92E-04 ± 1.07E-04	1.28E-03 ± 2.77E-04
LensTop	U235	4.49E-06	1.37E-05	1.41E-06 ± 4.23E-07	4.28E-06 ± 1.27E-06
LensTop	U238	6.03E-06	1.92E-05	1.44E-03 ± 3.39E-04	4.57E-03 ± 1.06E-03
LensTop	Th232	6.98E-06	2.24E-05	3.22E-03 ± 7.47E-04	1.04E-02 ± 2.38E-03
LensBot	U235	4.48E-06	1.29E-05	1.41E-06 ± 4.22E-07	4.04E-06 ± 1.20E-06
LensBot	U238	6.72E-06	1.73E-05	1.60E-03 ± 3.77E-04	4.13E-03 ± 9.63E-04
LensBot	Th232	7.79E-06	2.07E-05	3.60E-03 ± 8.32E-04	9.58E-03 ± 2.20E-03
CameraTop	U235	6.99E-06	1.81E-05	6.10E-06 ± 1.82E-06	1.58E-05 ± 4.71E-06
CameraTop	U238	7.35E-06	1.87E-05	2.50E-04 ± 5.66E-05	6.36E-04 ± 1.43E-04
CameraTop	Th232	7.75E-06	2.12E-05	6.87E-04 ± 1.42E-04	1.88E-03 ± 3.87E-04
CameraBot	U235	6.38E-06	1.68E-05	5.57E-06 ± 1.67E-06	1.47E-05 ± 4.38E-06
CameraBot	U238	6.79E-06	1.80E-05	2.31E-04 ± 5.24E-05	6.14E-04 ± 1.38E-04
CameraBot	Th232	7.00E-06	1.89E-05	6.21E-04 ± 1.29E-04	1.68E-03 ± 3.44E-04
TopReflector	U235	4.44E-06	1.01E-05	1.62E-07 ± 3.81E-08	3.70E-07 ± 8.57E-08
TopReflector	U238	1.39E-05	3.46E-05	5.70E-06 ± 1.32E-06	1.41E-05 ± 3.25E-06
TopReflector	Th232	8.01E-06	2.01E-05	4.56E-06 ± 1.65E-06	1.15E-05 ± 4.14E-06

Table .VIII – Single/multiple event leakage probabilities and single/multiple rates per year for every component and each of the three contaminants.

Component	Contaminant	Single leak. prob.	Multiple leak. prob	Single/year	Mult./year
BotReflector	U235	2.59E-05	6.86E-05	1.17E-06 ± 2.70E-07	3.11E-06 ± 7.14E-07
BotReflector	U238	6.76E-05	1.74E-04	3.42E-05 ± 1.77E-05	8.81E-05 ± 4.57E-05
BotReflector	Th232	4.67E-05	1.26E-04	3.30E-05 ± 1.19E-05	8.87E-05 ± 3.20E-05
PVReflector	U235	1.14E-05	3.44E-05	2.13E-06 ± 4.82E-07	6.47E-06 ± 1.46E-06
PVReflector	U238	3.60E-05	1.02E-04	7.54E-05 ± 1.70E-05	2.14E-04 ± 4.80E-05
PVReflector	Th232	2.11E-05	6.42E-05	6.17E-05 ± 2.21E-05	1.88E-04 ± 6.71E-05
Oil	U235	4.14E-02	1.05E-01	2.48E-06 ± 4.95E-07	6.27E-06 ± 1.25E-06
Oil	U238	4.10E-02	1.05E-01	9.37E-05 ± 1.87E-05	2.40E-04 ± 4.79E-05
Oil	U238 low	4.10E-02	1.05E-01	3.68E-05 ± 7.35E-06	9.39E-05 ± 1.88E-05
Oil	Po210	3.71E-02	9.19E-02	7.70E-01 ± 7.85E-01	1.91E+00 ± 1.94E+00
Oil	Th232	4.22E-02	1.09E-01	2.01E-05 ± 4.02E-06	5.19E-05 ± 1.04E-05
Plastic Shield	U235	1.71e-04	3.68e-04	1.28e-03 ± 2.57e-04	2.75e-03 ± 5.51e-04
Plastic Shield	U238	1.24e-04	2.64e-04	2.62e-02 ± 5.24e-03	5.59e-02 ± 1.12e-02
Plastic Shield	Th232	1.68e-04	3.56e-04	9.23e-04 ± 1.85e-04	1.96e-03 ± 3.91e-04
L-01-005-B	U235	3.22E-05	6.76E-05	2.75E-06 ± 2.80E-06	5.78E-06 ± 5.90E-06
L-01-005-B	U238	3.93E-05	8.20E-05	1.23E-04 ± 1.25E-04	2.56E-04 ± 2.61E-04
L-01-005-B	Th232	5.13E-05	1.05E-04	9.54E-05 ± 9.73E-05	1.95E-04 ± 1.99E-04
L-01-006-B	U235	2.13E-05	4.52E-05	1.86E-06 ± 1.90E-06	3.94E-06 ± 4.02E-06
L-01-006-B	U238	2.60E-05	5.44E-05	8.28E-05 ± 8.44E-05	1.73E-04 ± 1.77E-04
L-01-006-B	Th232	3.38E-05	7.17E-05	6.42E-05 ± 6.55E-05	1.36E-04 ± 1.39E-04
L-01-008-B	U235	1.71E-05	3.57E-05	2.05E-06 ± 2.09E-06	4.28E-06 ± 4.37E-06
L-01-008-B	U238	2.16E-05	4.45E-05	9.43E-05 ± 9.62E-05	1.94E-04 ± 1.98E-04
L-01-008-B	Th232	2.73E-05	5.85E-05	7.11E-05 ± 7.25E-05	1.52E-04 ± 1.55E-04
L-01-036-A	Th232	6.00E-07	1.12E-06	1.00E-06 ± 1.03E-06	1.87E-06 ± 1.91E-06
L-01-036-A	U235	2.00E-08	2.00E-08	1.53E-09 ± 1.90E-09	1.53E-09 ± 1.90E-09
L-01-036-A	U238	3.10E-07	8.60E-07	8.67E-07 ± 8.98E-07	2.41E-06 ± 2.47E-06

Table .IX – Single/multiple event leakage probabilities and single/multiple rates per year for every component and each of the three contaminants.

Component	Contaminant	Single leak. prob.	Multiple leak. prob	Single/year	Mult./year
L-01-037-A	U235	8.00E-08	3.10E-07	4.67E-09 ± 5.04E-09	1.81E-08 ± 1.87E-08
L-01-037-A	U238	1.60E-07	4.00E-07	3.41E-07 ± 3.58E-07	8.52E-07 ± 8.79E-07
L-01-037-A	Th232	2.40E-07	5.80E-07	3.04E-07 ± 3.17E-07	7.36E-07 ± 7.56E-07
L-01-038-A	U235	2.20E-07	3.20E-07	1.82E-08 ± 1.90E-08	2.65E-08 ± 2.74E-08
L-01-038-A	U238	2.60E-07	4.90E-07	7.86E-07 ± 8.17E-07	1.48E-06 ± 1.53E-06
L-01-038-A	Th232	2.20E-07	5.80E-07	3.96E-07 ± 4.13E-07	1.04E-06 ± 1.07E-06
L-01-010-B	U235	5.02E-06	9.47E-06	1.27E-06 ± 1.57E-06	2.39E-06 ± 2.97E-06
L-01-010-B	U238	5.01E-06	9.50E-06	1.83E-04 ± 4.18E-05	3.48E-04 ± 7.86E-05
L-01-010-B	Th232	4.37E-06	8.45E-06	8.19E-06 ± 1.87E-06	1.58E-05 ± 3.58E-06
L-01-011-A	U235	5.70E-06	1.18E-05	2.06E-05 ± 2.55E-05	4.25E-05 ± 5.27E-05
L-01-011-A	U238	1.29E-05	2.64E-05	6.75E-03 ± 1.52E-03	1.38E-02 ± 3.11E-03
L-01-011-A	Th232	9.69E-06	2.12E-05	2.60E-04 ± 5.87E-05	5.67E-04 ± 1.27E-04
L-01-012-A	U235	1.90E-07	4.90E-07	3.68E-07 ± 4.64E-07	9.49E-07 ± 1.18E-06
L-01-012-A	U238	6.40E-07	1.26E-06	1.80E-04 ± 4.60E-05	3.54E-04 ± 8.51E-05
L-01-012-A	Th232	4.20E-07	9.40E-07	6.04E-06 ± 1.64E-06	1.35E-05 ± 3.33E-06
PV	U235	3.11E-06	9.56E-06	9.93E-05 ± 2.29E-05	3.05E-04 ± 6.89E-05
PV	U238	8.41E-06	2.31E-05	3.11E-02 ± 7.04E-03	8.54E-02 ± 1.92E-02
PV	Th232	5.69E-06	1.71E-05	4.39E-03 ± 1.11E-03	1.32E-02 ± 3.31E-03
DishHead	U235	8.00E-08	3.00E-07	1.40E-07 ± 5.88E-08	5.27E-07 ± 1.52E-07
DishHead	U238	6.70E-07	1.45E-06	1.36E-04 ± 3.47E-05	2.95E-04 ± 7.04E-05
DishHead	Th232	1.80E-07	6.10E-07	7.64E-06 ± 2.63E-06	2.59E-05 ± 7.27E-06
L-0301-023	U235	1.34E+00	3.20E+00	5.24E-04 ± 5.35E-04	1.25E-03 ± 1.28E-03
L-0301-023	U238	2.14E+00	6.51E+00	1.50E+00 ± 1.53E+00	4.56E+00 ± 4.65E+00
L-0301-023	Th232	6.22E-01	1.48E+00	1.58E-04 ± 1.61E-04	3.77E-04 ± 3.84E-04
L-0301-024	U235	1.20E+00	2.82E+00	4.68E-04 ± 4.78E-04	1.10E-03 ± 1.12E-03
L-0301-024	U238	1.99E+00	5.92E+00	1.40E+00 ± 1.43E+00	4.15E+00 ± 4.23E+00
L-0301-024	Th232	1.20E+00	2.82E+00	3.05E-04 ± 3.11E-04	7.17E-04 ± 7.31E-04

Table .X – Single/multiple event leakage probabilities and single/multiple rates per year for every component and each of the three contaminants.

Component	Contaminant	Single leak. prob.	Multiple leak. prob	Single/year	Mult./year
L-03-020	U235	7.39E-02	1.29E-01	1.16E-03 $\pm$ 1.18E-03	2.03E-03 $\pm$ 2.07E-03
L-03-020	U238	2.30E-01	4.91E-01	6.49E+00 $\pm$ 6.62E+00	1.38E+01 $\pm$ 1.41E+01
L-03-020	Th232	9.70E-02	1.72E-01	9.93E-04 $\pm$ 1.01E-03	1.76E-03 $\pm$ 1.79E-03
Piezo Copper	U235	1.09E-03	1.86E-03	6.73E-10 $\pm$ 1.91E-10	1.15E-09 $\pm$ 3.25E-10
Piezo Copper	U238	3.69E-03	7.65E-03	4.07E-06 $\pm$ 1.15E-06	8.45E-06 $\pm$ 2.39E-06
Piezo Copper	Th232	7.47E-04	1.10E-03	3.39E-11 $\pm$ 1.21E-11	4.97E-11 $\pm$ 1.78E-11
Piezo PCB	U235	5.62E-03	1.17E-02	5.41E-05 $\pm$ 9.06E-05	1.13E-04 $\pm$ 1.89E-04
Piezo PCB	U238	4.81E-03	9.97E-03	1.36E-04 $\pm$ 2.94E-03	2.82E-04 $\pm$ 6.10E-03
Piezo PCB	U238 low	5.52E-03	1.13E-02	1.15E-01 $\pm$ 3.06E-02	2.36E-01 $\pm$ 6.29E-02
Piezo PCB	Th232	5.62E-03	1.17E-02	6.99E-05 $\pm$ 1.00E-04	1.45E-04 $\pm$ 2.08E-04
Piezo PZT	U235	4.77E-03	1.01E-02	2.49E-05 $\pm$ 2.10E-05	5.29E-05 $\pm$ 4.46E-05
Piezo PZT	U238	4.09E-03	8.73E-03	1.49E-03 $\pm$ 2.34E-03	3.18E-03 $\pm$ 5.00E-03
Piezo PZT	Th232	4.95E-03	1.04E-02	2.73E-05 $\pm$ 1.64E-05	5.76E-05 $\pm$ 3.47E-05
Piezo Cable Ver	U235	7.51E-05	1.42E-04	3.14E-05 $\pm$ 1.04E-05	5.96E-05 $\pm$ 1.97E-05
Piezo Cable Ver	U238	8.61E-05	1.73E-04	6.58E-04 $\pm$ 2.18E-04	1.33E-03 $\pm$ 4.38E-04
Piezo Cable Ver	Th232	8.76E-05	1.73E-04	1.86E-04 $\pm$ 1.52E-04	3.67E-04 $\pm$ 3.00E-04
Piezo Cable Hor	U235	1.11E-03	2.35E-03	2.91E-05 $\pm$ 9.57E-06	6.17E-05 $\pm$ 2.03E-05
Piezo Cable Hor	U238	1.21E-03	2.57E-03	5.82E-04 $\pm$ 1.92E-04	1.23E-03 $\pm$ 4.06E-04
Piezo Cable Hor	Th232	1.54E-03	3.31E-03	2.05E-04 $\pm$ 1.67E-04	4.41E-04 $\pm$ 3.60E-04

Table .XI – Single/multiple event leakage probabilities and single/multiple rates per year for every component and each of the three contaminants.

Component	Contaminant	Single leak. prob.	Multiple leak. prob	Single/year	Mult./year
Piezo 84 Copper	U235	1.09e-03	1.86e-03	9.47e-12 $\pm$ 2.68e-12	1.61e-11 $\pm$ 4.55e-12
Piezo 84 Copper	U238	3.68e-03	7.65e-03	5.71e-08 $\pm$ 1.62e-08	1.19e-07 $\pm$ 3.36e-08
Piezo 84 Copper	Th232	7.50e-04	1.09e-03	4.78e-13 $\pm$ 1.71e-13	6.96e-13 $\pm$ 2.49e-13
Piezo 84 PCB	U235	5.63e-03	1.17e-02	3.26e-05 $\pm$ 7.31e-06	6.77e-05 $\pm$ 1.52e-05
Piezo 84 PCB	U238	4.81e-03	9.97e-03	7.56e-04 $\pm$ 4.56e-04	1.57e-03 $\pm$ 9.44e-04
Piezo 84 PCB	Th232	5.63e-03	1.17e-02	2.51e-04 $\pm$ 5.18e-05	5.20e-04 $\pm$ 1.07e-04
Piezo 84 PZT	U235	4.78e-03	1.01e-02	8.76e-06 $\pm$ 1.97e-06	1.86e-05 $\pm$ 4.16e-06
Piezo 84 PZT	U238	4.09e-03	8.72e-03	4.17e-04 $\pm$ 2.51e-04	8.89e-04 $\pm$ 5.35e-04
Piezo 84 PZT	Th232	4.95e-03	1.04e-02	1.19e-04 $\pm$ 2.45e-05	2.51e-04 $\pm$ 5.17e-05
Piezo 84 Cable Ver	U235	7.50e-05	1.42e-04	6.21e-05 $\pm$ 1.41e-05	1.18e-04 $\pm$ 2.67e-05
Piezo 84 Cable Ver	U238	8.60e-05	1.74e-04	9.35e-04 $\pm$ 5.64e-04	1.89e-03 $\pm$ 1.14e-03
Piezo 84 Cable Ver	Th232	8.62e-05	1.74e-04	6.75e-04 $\pm$ 1.41e-04	1.36e-03 $\pm$ 2.83e-04
Piezo 84 Cable Hor	U235	1.11e-03	2.35e-03	5.78e-05 $\pm$ 1.30e-05	1.22e-04 $\pm$ 2.74e-05
Piezo 84 Cable Hor	U238	1.21e-03	2.57e-03	8.27e-04 $\pm$ 4.98e-04	1.75e-03 $\pm$ 1.06e-03
Piezo 84 Cable Hor	Th232	1.54e-03	3.31e-03	7.59e-04 $\pm$ 1.57e-04	1.63e-03 $\pm$ 3.36e-04

Table .XII – Single/multiple event leakage probabilities and single/multiple rates per year for every component and each of the three contaminants.

$$Q_{0,h} = \frac{4}{3}\pi r_0^3 \rho_b (h_b - h_l) \tag{1}$$

$$Q_{0,s} = 4\pi r_0^2 \sigma_0 \tag{2}$$

$$Q_{0,ds} = -4\pi r_0^2 t \frac{\partial \sigma}{\partial t}\Big|_{\Delta p} \tag{3}$$

$$Q_{0,w} = -\frac{4}{3}\pi r_0^3 (P_b - P_l) \tag{4}$$

$$\tag{5}$$

$$Q_{1,h} = 8\pi r_0^3 \rho_b (h_b - h_l) \tag{6}$$

$$Q_{1,s} = 24\pi r_0^2 \sigma_0 \tag{7}$$

$$Q_{1,ds} = -16\pi r_0^2 t \frac{\partial \sigma_0}{\partial t}\Big|_{\Delta p} - \frac{4}{3}\pi r_0^3 \rho_b (h_b - h_l) \tag{8}$$

$$Q_{1,w} = -8\pi r_0^3 (P_b - P_l) \tag{9}$$